

Study of Diluted Magnetic Semiconductors: the Case of Transition Metal Doped ZnO

THÈSE N° 4728 (2010)

PRÉSENTÉE LE 24 JUIN 2010

À LA FACULTÉ SCIENCES DE BASE
LABORATOIRE DE PHYSIQUE DE LA MATIÈRE COMPLEXE
PROGRAMME DOCTORAL EN PHYSIQUE

ÉCOLE POLYTECHNIQUE FÉDÉRALE DE LAUSANNE

POUR L'OBTENTION DU GRADE DE DOCTEUR ÈS SCIENCES

PAR

Zlatko MICKOVIĆ

acceptée sur proposition du jury:

Prof. G. Meylan, président du jury
Prof. L. Forró, Dr A. Magrez, directeurs de thèse
Prof. O. Fischer, rapporteur
Prof. H. Ronnow, rapporteur
Prof. J. W. Seo, rapporteur



ÉCOLE POLYTECHNIQUE
FÉDÉRALE DE LAUSANNE

Suisse
2010

Abstract

Diluted magnetic semiconductors (DMS), semiconductors in which a fraction of non-magnetic sites have been replaced with their magnetic counterparts, have been in the limelight of the scientific community since the turn of the 21st century. The interest in these materials is spurred from their application in the spin electronics, the developing technology based on the usage of the fundamental property of every electron - its spin. Namely, diluted magnetic semiconductors have large spin-dependent properties that can be amplified in the presence of a magnetic field, thereby having the potential of achieving the external control of spin, which is the final goal of spintronics.

The Achilles heel of diluted magnetic semiconductors is the material's quality. The tendency of magnetic ions distributed in a non-magnetic matrix is to cluster and form magnetic islands leaving non-magnetic regions in the material with macroscopic properties of the sample completely different from originally envisaged.

The goal of this thesis was to develop novel synthesis methods to produce homogeneously doped ZnO with transition metal ions (TM = Mn, Ni, Co) and to check what magnetic transition temperatures (T_c) could be achieved in such conditions. The idea was to use homogeneous precursors synthesized at low temperatures. A synthesis method was elaborated using transition metal doped nitrates as precursors. The materials were decomposed in moderately oxidizing conditions of NO_2 formed during the synthesis. In the case of Mn as transition metal ion even this oxidation was strong enough to create a small quantity of Mn^{4+} and consequently, to form a small amount of parasitic magnetic phase ZnMnO_3 within the $\text{Zn}_{1-x}\text{Mn}_x\text{O}$ matrix.

Excellent material was produced by using a 2-step synthesis for DMSs based on inorganic precursor decomposition. The precursor was TM-doped hydrozincite, a zinc hydroxy carbonate salt, which is obtained by the oxidation of urea by Zn and Mn nitrates. This precursor undergoes a single-step decomposition to produce TM-doped ZnO at low temperatures. The detailed characterization of Mn-doped ZnO produced by this novel process demonstrates the high purity of its product. It is also compatible with Si-based device fabrication, because of the low-temperature nature of the process. In this case the formation of zinc manganate

impurities was avoided as the oxidation state of Mn cations is well controlled. ZnO doped with up to 1.8 % of Mn has been prepared, and a ferromagnetic signal has been observed below 40 K. Unfortunately, this is well below the desired room temperature ferromagnetism. The goal is further on to increase T_C with additional chemical manipulations.

Other TM dopants in hydrozincite precursor did not give satisfactory results . The case of $Zn_{1-x}Co_xO$ revealed that a strong ferromagnetism with $T_C > 260$ K can be achieved when the Co precipitates in the ZnO matrix and hence it is not intrinsic to the system. The case of $Zn_{1-x}Ni_xO$ has showed that NiO inclusions can lead to superparamagnetism.

Besides chemical methods, a large variety of experimental techniques were employed to characterize the materials, such as X-ray diffraction (XRD), transmission electron microscopy (TEM), energy dispersive X-ray spectroscopy (EDXS), selected area diffraction pattern (SADP), electron energy loss spectroscopy (EELS), low and high-field electron spin resonance (ESR), DC and AC conductivity, AC susceptibility and Superconducting Quantum Interference Device (SQUID).

Keywords: diluted magnetic semiconductors, spintronics, transition-metal doped ZnO, magnetism, Electron Spin Resonance, magnetic susceptibility

Version abrégée

Les semi-conducteurs magnétiques dilués (DMS), semi-conducteurs dans lesquels une fraction des sites non-magnétiques a été remplacée par leurs homologues magnétiques, sont sous le feu des projecteurs de la communauté scientifique depuis le début du 21ème siècle. L'intérêt pour ces matériaux est stimulé par ses applications dans l'électronique du spin, une technologie émergente basée sur le principe fondamental que chaque électron possède un spin. En effet, les semi-conducteurs magnétiques dilués ont d'importantes propriétés dépendantes du spin qui peuvent être amplifiées en présence d'un champ magnétique, ayant de ce fait comme débouché potentiel le contrôle externe du spin, but ultime de la spintronique. Cependant, le talon d'Achilles des DMS réside dans la qualité de ces matériaux. Les ions magnétiques distribués dans une matrice non-magnétique ont tendance à s'agglomérer ayant pour résultat d'induire des propriétés macroscopiques non-représentatives du matériau original dûe aux larges régions magnétiques ainsi formées. Le but de cette thèse a été le développement d'une nouvelle méthode de synthèse pour produire ZnO dopé avec des métaux de transition (TM = Mn, Ni, Co) et de déterminer quelles températures de transition magnétique pouvaient être atteintes dans de telles conditions.

Le principe de la méthode réside dans l'utilisation de précurseurs homogènes synthétisés à basse température. La synthèse est basée sur l'emploi de précurseurs tels que les nitrates dopés avec des métaux de transition comme précurseurs. Les matériaux sont ensuite décomposés sous atmosphère contrôlée. Dans le cas du Mn, son oxydation ne peut être empêchée et une faible quantité de Mn^{4+} est ainsi créée induisant la formation d'une phase parasite magnétique dans la matrice $Zn_{1-x}Mn_xO$.

D'excellents matériaux ont été produits en utilisant une méthode de synthèse en deux temps par un processus de décomposition d'un précurseur inorganique basé sur du DMS. Le précurseur était du hydrozincite TM-dopé, un hydroxy carbonate de zinc, qui est obtenu par l'oxydation d'urée par des nitrates de Zn et Mn. Ce précurseur subit une décomposition en une étape pour produire du ZnO TM-dopé à basse température. La caractérisation détaillée du ZnO Mn-dopé obtenu par ce nouveau processus démontre la grande pureté de ce produit.

Ce procédé est également compatible avec la fabrication de dispositifs basés sur la technologie du Si. Dans ce cas, la formation d'impuretés de manganate de zinc est évitée par le fait que l'état d'oxydation des cations de Mn est maîtrisée. Il a été possible de fabriquer ZnO dopé avec jusqu'à 1.8% de Mn. Un signal ferromagnétique a été observé pour des températures inférieures à 40 K: Néanmoins, cette température reste bien inférieure à la température ambiante désirée. Le but est d'accroître davantage le/la T_C grâce à des manipulations chimiques supplémentaires.

L'utilisation d'autres dopants magnétiques n'ont pas donné de résultats probants. Le cas du $Zn_{1-x}Co_xO$ a révélé qu'un fort ferromagnétisme avec $T > 260$ K peut être obtenu lorsque le Co précipite dans la matrice de ZnO et par conséquent le phénomène n'est pas intrinsèque au système. Le cas du $Zn_{1-x}Ni_xO$ a montré que des inclusions de NiO peuvent conduire à des propriétés superparamagnétiques.

En plus de méthodes chimiques employées pour la synthèse des matériaux, une grande variété de techniques expérimentales a été employées pour caractériser les échantillons, comme par exemple la diffraction de rayons X (XRD), la microscopie de transmission électronique (TEM), spectroscopie à énergie dispersive de rayons X (EDXS), Diffraction à zone sélectionnée (SADP), Spectroscopie de perte d'énergie (EELS), Résonance paramagnétique électronique (ESR), conductivité DC et AC, susceptibilité AC et susceptibilité mesurée par SQUID.

Mots-clés: semi-conducteurs magnétiques dilués, spintronique, ZnO dopé avec des métaux de transition, magnétisme, Résonance Paramagnétique Électronique, susceptibilité magnétique

Acknowledgments

The last four years of my life have been a once-in-a-lifetime experience, starting from the being a part of a top-notch research group in Ecole Polytechnique Fédérale de Lausanne, led by professor László Forró, to meeting new people, colleagues and friends. The first thanks goes to Materials with Novel Electronic Properties (MANEP) who have funded this Thesis research. The Professor László Forró, my thesis director, is the one that my deepest thanks go to, giving me the opportunity for a fruitful and thorough scientific work in an environment abundant with expertise and willingness to help. Special thanks goes to László, Livia, Zalan and Csaba for making me feel like home on many occasions I was invited to their home. A very big thanks and gratitude goes to Dr. Arnaud Magrez, with whose help this Ph.D. was streamlined from the very beginning and who was always willing to help to overcome any obstacle on the path of scientific progress. I owe immense gratitude to Dr. Duncan Alexander who worked meticulously on a great number of samples we were producing and gave us a clear path of where we should be going with the materials production. Great thanks goes to Dr. Andrzej Sienkiewicz, who greeted any question I might have had, no matter how silly, with patience and wisdom. The number of good friends I met here is incredible, and this is what I will cherish the most and how I will remember Lausanne. I thank the members of the group that I have worked most closely with, Martial, for giving a helping hand whenever I needed it and being a great friend, Marijana, for being a fighter and a guiding spirit. I can't find the words to thank my office mates, Anna and Kasia, who were close friends during my 2 years and helped me sail through many storms. Luka is a great friend and I hope he will remember the good laughs we have had as much as I will. To Goran I can only say, Cheers mate, for everything, you have been a great friend and support. Thanks for the help, warmth and understanding. Thanks to Dejan for showing me the discipline needed for success. Thanks to all the community from home that helped me when I came to Lausanne, Mimi, Ana, Iva and Branimir. Thanks to Jaćim and Stevan for giving me the competitive edge. Thanks to Endre for being a great guy and officemate. I wish to thank also my friends at home, Tomislav, Iva, Mario, Filip, Zec and Kristina for being great help and a proof that home and friendship

transcend the optical cable. Without your support and knowing where I am from and where I can always come back to, it would be difficult to accomplish this feat. As I said, the number of good friends I was blessed with is incredible, and due to the lack of space here I can only sincerely thank all the group members, past and present, for your support, your friendship and your help. Last but definitely not the least, I thank and dedicate this Thesis to my parents, Jasna and Zoran, not only for going through the difficult four years of being apart, but for their unconditional love and support throughout my life.

Contents

1	Introduction	1
2	Diluted magnetic semiconductors and application in spintronics	5
2.1	Magnetic interactions and their effect on measurable properties	6
2.1.1	Transition-metal ions in crystal fields	11
2.2	The fundamentals of spintronics	14
2.2.1	Materials for spintronics	18
2.2.2	Band scheme of common ferromagnets	20
2.2.3	Half-metallic ferromagnets	22
2.3	The basic notions on diluted magnetic semiconductors	23
2.4	Conclusion	28
3	Transition metal doped zinc oxide in spintronics	29
3.1	Zinc oxide - the host (II-VI) semiconductor	29
3.1.1	The Structural properties of ZnO	30
3.1.2	Defects in ZnO	31
3.1.3	The band structure, magnetic and transport properties of ZnO	31
3.1.4	Applications of ZnO	33
3.2	Synthesis methods of TM doped ZnO and DMS	34
3.2.1	Thin films deposition	35
3.2.2	Solid state reaction methods	36
3.2.3	Soft chemistry methods	36
3.2.4	Co-precipitation methods	38

3.2.5	Drawbacks of the synthesis methods	38
3.3	Room temperature ferromagnetism in Transition Metal doped Zinc Oxide . . .	39
3.3.1	Theoretical basis for ferromagnetism in TM doped ZnO	40
3.3.2	Observations of intrinsic ferromagnetism	48
3.3.3	Observations of extrinsic ferromagnetism	51
3.3.4	Conclusion	54
4	Synthesis and properties of transition metal doped ZnO precursors	56
4.1	TM doped zinc nitrates	56
4.2	The synthesis and properties of TM metal doped hydrozincite	60
4.2.1	Mn doped hydrozincite	62
4.2.2	Conclusion	69
5	Properties of $Zn_{1-x}Mn_xO$ produced from Mn doped zinc nitrates	72
5.1	Structural properties	72
5.2	Magnetic properties	76
5.3	Electronic properties	88
5.4	Properties of $ZnMnO_3$	90
5.4.1	Synthesis and Structural properties	92
5.4.2	Magnetic properties	94
5.4.3	High-field,high-frequency ESR study	96
5.4.4	Electronic properties	98
5.4.5	Thermopower and DC conductivity	99
5.4.6	Conclusion	102
6	Properties of $Zn_{1-x}TM_xO$ produced from TM doped hydrozincites	103
6.1	Hydrozincite decomposition	103
6.1.1	E-beam decomposition	108
6.2	Mn as a dopant	110
6.2.1	Oxygen rich environment	110

6.2.2	N_2H_2 environment	116
6.3	The (Mn, Li) co-doping	124
6.4	Co as a dopant	127
6.5	Ni as a dopant	137
7	Conclusion and outlook	144

Chapter 1

Introduction

The introduction of computers to the world's stage has had such huge influence on the everyday life that it is difficult to grasp a life without computers. No wonder than the old Olympic motto of Citius, Altius, Fortius is being modified to be Citius, Minor, Fortius, where "smaller" refers to the size of the electronic components. The time of finalizing the work on this Thesis has seen the computer power/size ratio reach new heights with the introduction of Apple's I-Pad to the market.

The working principle behind the new computers, including I-Pad, is based on the silicon semiconductor technology and the principle of transistor, transfer resistor, that has been developing since the 1950s. The silicon transistor/integrated circuit technology is working



Figure 1.1: The I-Pad computer, released in April 2010, sprawling a 1 GHz processor, a 64 Gb storage and the mass of 680 grams.

using the fundamental property of the electron charge. Electrons however have an additional fundamental property, *spin* that can have the value of $1/2$ or $-1/2$. If one would be able to control the spin states of the spins one would be in position to perform calculations several orders of magnitude faster than in conventional electronics, and the leap in power/size ratio would far supersede the leap that I-Pad made these days.

The spintronics has already made its way to I-Pad through its hard disk data storage drive using giant magnetoresistance effect, which is the 20-80 % change in resistance between the cases when the adjacent magnetic layers are under an applied field and without the applied field, respectively. Hence, by applying the magnetic field, one has the change of one to zero and a unit of information is created.

The spin of the electron is hence used in hard-disk technology, yet the challenge that remains is developing a spintronics device out of semiconductors, which could make the logical elements in computers function on the principle of measuring the spin state of the electrons and not whether the current is on or off.

This could finally achieve a computer that could boot-up instantaneously or be in stand-by state without any power needed, a significant step forward from the computers that we know today.

The aim of this thesis work is to present a systematic study of novel materials, based on a wide band gap zinc oxide, ZnO, that have potential application in spin electronics -spintronics. ZnO, a material with ubiquitous applications in piezoelectric transducers, varistors and as transparent electrodes [1] is fast becoming one of the most studied materials due mostly to the seminal work by Dietl et al. [2] who predicted ferromagnetic ground state of $Zn_{1-x}Mn_xO$ with $x = 5\%$ and hole doping of 3.5×10^{20} holes per cm^3 . Sato et al. further postulated that Fe, Co and Ni doped ZnO should have ferromagnetic ground state without any additional further carrier doping, while, corroborating analysis of Dietl et al. $Zn_{1-x}Mn_xO$ needs hole carriers to stabilize ferromagnetism from originally a spin-glass ground state present when there is no additional carrier doping.

Ferromagnetic electrodes are important for spintronics because they serve as reservoirs of

spin-polarized electrons from which non-equilibrium spin population is injected in a typically non-magnetic or insulating material. Polarized spins are then transferred within times typically shorter than their characteristic spin relaxation time through aforementioned non-magnetic or insulating material and finally detected at another ferromagnetic or superconducting electrode. ZnO and other (II-VI) as well as (III-V) semiconductors offer a high potential for nanostructure synthesis so an added ferromagnetism would allow for an unprecedented blend of properties with a strong stress on application.

The work by Dietl et al. [2] has however had strong roots in the field of diluted magnetic semiconductors (DMS), i.e. host non-magnetic (II-VI) and (III-V) semiconductors doped to a, typically, very dilute extent with magnetic elements from transition-metal 3d (TM) or rare-earth 4f (RE) series. A magnetic moment is endowed to the system from materials with unfilled 3d or 4f shells substituting for non-magnetic cations in structures.

The Achilles heel of this blooming field is the homogeneity of the material. This is why in this work we have put a special accent on the sample synthesis. This thesis work has strong foundations in the synthesis methods applied in order to synthesize a well characterized, quality bulk $\text{Zn}_{1-x}\text{TM}_x\text{O}$ with a special stress on $\text{Zn}_{1-x}\text{Mn}_x\text{O}$. As this Ph.D. work coincides temporally with several years in which importance of improvement of synthesis methods and analysis techniques has just started to be recognized, we have invented several novel synthesis methods with a stress on homogenous distribution of TM species in ZnO and single-phase character of $\text{Zn}_{1-x}\text{TM}_x\text{O}$ final product, with tracking down, with help of structural or magnetic signatures, possible nanoscale phase separation in final material. As analysis techniques we have typically used microscopical, magnetic resonance and techniques based on the Josephson's effect (Superconducting Quantum Interference Device - SQUID) for determining the structure and the magnetic properties of our samples as a function of their structure.

The structure of this work is as follows. First, basics of spintronics are introduced through a more pedagogical than chronological approach. The physics of diluted magnetic semiconductors with their spin-dependent properties as potential goldmine of materials for applications in spintronics is discussed subsequently. Zinc oxide, the host material for this thesis work

is the subject of the third Chapter. The focus of this work is on the improvement of the conventional synthesis methods of TM doped ZnO, hence they are listed after this. The possibility of room-temperature ferromagnetism in TM:ZnO is discussed in the following section. The next Chapter includes the discussion of the properties of TM doped nitrates and TM doped hydrozincite, $(\text{Zn}_{1-x}\text{Mn}_x)_5(\text{OH})_6(\text{CO}_3)_2$, the precursors developed and chosen for this study. Properties of the $\text{Zn}_{1-x}\text{Mn}_x\text{O}$ produced from nitrate precursors are discussed in the following Chapter. Following this, an essay on the properties of the parasitic phase ZnMnO_3 that defines very important properties of $\text{Zn}_{1-x}\text{Mn}_x\text{O}$ that contain even trace amounts of ZnMnO_3 , as established in this work, is given. Properties of $\text{Zn}_{1-x}\text{Mn}_x\text{O}$ produced from $(\text{Zn}_{1-x}\text{Mn}_x)_5(\text{OH})_6(\text{CO}_3)_2$ are a subject of the central Chapter, Chapter 6, with importance given to the atmosphere of the precursor decomposition. This Chapter includes essays of systems doped with other TM ions, such as Co, Ni and Mn system co-doped with Li. The thesis work is completed with conclusion and outlook, curriculum vitae, acknowledgements and list of references.

Chapter 2

Diluted magnetic semiconductors and application in spintronics

Spintronics is a novel technology based on usage of spins as information units that could possibly revolutionize the information technology as we know it today. Modern technologies are often developed in parallel or directly through the development of structures based on their flagship materials. The revolution of electronics with Si, optoelectronics with GaAs and display technology with liquid crystals are one of many examples. Spintronics is not an exception to this rule, scientists being constantly in search for suitable materials to achieve the goal of computing with individual spins. Materials for spintronics in general have to have the potential for amplification of spin-dependent properties. Diluted magnetic semiconductors are materials with properties such as giant Faraday rotation, the change in polarization of light when acting with the magnetic field and extremely large Zeeman splittings, the splittings of the energy states of the electrons in presence of a strong magnetic field, of both the band and impurity levels. ZnO by itself is already a promising material as it already easily finds its place in many demanding applications. It is used as a varistor, a variable resistor material used to e.g. protect sensitive pieces of electronic equipment by shunting the circuits [3], as a piezoelectric material, a material capable of generating electric potential when dangerously high current levels are present, etc. It can also be used as a nano-cantilever in Atomic Force Microscope

(AFM) [4, 5]. It is as well a high-k dielectric, i.e. a material with a high dielectric constant k compared to SiO_2 meaning that it could replace the silicon dioxide gate in conventional transistors and contribute to miniaturization of the electronic components which is essential to the optimization of their performance. In addition to all the mentioned characteristics, doping of n-doped ZnO with Co, Ni, V and Fe are predicted to render it ferromagnetic [6, 7], while doping of p-doped ZnO with Mn serves to the same effect [6, 7, 2]. Ferromagnetic semiconductors are essential candidates to make some or all of the (source, drain, channel, gate) components of a conventional spin-field effect transistor (spin-FET) [8]. One more reason then, to embark on the journey of ZnO, DMS and spintronics.

2.1 Magnetic interactions and their effect on measurable properties

This part of the Thesis is devoted to dealing with introducing the fundamental physical concepts that will be used throughout the remainder of this work. The interaction between two magnetic dipoles $\boldsymbol{\mu}_1$ and $\boldsymbol{\mu}_2$ separated by \mathbf{r} is defined by the energy that the system has respective to the values of the separation of the dipoles and the angles that the dipoles make. It is given by the Equation

$$E = \frac{\mu_0}{4\pi r^3} \left[\boldsymbol{\mu}_1 \cdot \boldsymbol{\mu}_2 - \frac{3}{r^2} (\boldsymbol{\mu}_1 \cdot \mathbf{r})(\boldsymbol{\mu}_2 \cdot \mathbf{r}) \right] \quad (2.1)$$

and is known as *magnetic dipolar interaction*. Two magnetic moments of size $\mu \approx \mu_B$ separated by $r \approx 1 \text{ \AA}$ would have energy of the order of $\mu^2/4\pi r^3 \sim 10^{-23} \text{ J}$ which translates to around 1 K, meaning that the magnetic dipolar interaction cannot be the sole responsible for the high temperature ordering effects of $\sim 1000 \text{ K}$.

The exchange interaction originates in the fermionic nature of the electron based on Pauli exclusion principle: no two fermions can occupy the same quantum state at the same time. As electrons are fermions, they are distinguishable, and the wave function of the system of two electrons has to be antisymmetric to the exchange of two electrons. This leaves two possible

spin states: an antisymmetric *singlet* state χ_S with $S=0$ (in the case of the symmetric spatial state) and a symmetric *triplet* state χ_T with $S=1$ (in the case of the antisymmetric spatial state).

$$\begin{aligned}\Psi_S &= \frac{1}{\sqrt{2}} [\psi_a(\mathbf{r}_1)\psi_b(\mathbf{r}_2) + \psi_a(\mathbf{r}_2)\psi_b(\mathbf{r}_1)] \chi_S \\ \Psi_T &= \frac{1}{\sqrt{2}} [\psi_a(\mathbf{r}_1)\psi_b(\mathbf{r}_2) - \psi_a(\mathbf{r}_2)\psi_b(\mathbf{r}_1)] \chi_T\end{aligned}\quad (2.2)$$

With the energies of the two possible spin states given by

$$E_S = \int \Psi_S^* \hat{H} \Psi_S d\mathbf{r}_1 d\mathbf{r}_2, \quad E_T = \int \Psi_T^* \hat{H} \Psi_T d\mathbf{r}_1 d\mathbf{r}_2 \quad (2.3)$$

The difference in energies of the singlet and triplet state is given by

$$E_S - E_T = 2 \int \psi_a^*(\mathbf{r}_1)\psi_b^*(\mathbf{r}_2)\hat{H}\psi_a(\mathbf{r}_2)\psi_b(\mathbf{r}_1)d\mathbf{r}_1d\mathbf{r}_2 \quad (2.4)$$

From this one can define the *exchange integral*

$$J = \frac{E_S - E_T}{2} = \int \psi_a^*(\mathbf{r}_1)\psi_b^*(\mathbf{r}_2)\hat{H}\psi_a(\mathbf{r}_2)\psi_b(\mathbf{r}_1)d\mathbf{r}_1d\mathbf{r}_2 \quad (2.5)$$

The basic properties of the spin operator require that, for a singlet state $\mathbf{S}_1 \cdot \mathbf{S}_2 = -\frac{3}{4}$ while for a triplet state $\mathbf{S}_1 \cdot \mathbf{S}_2 = \frac{1}{4}$. The effective Hamiltonian can hence be defined as

$$\hat{H} = \frac{1}{4}(E_S + 3E_T) - (E_S - E_T)\mathbf{S}_1 \cdot \mathbf{S}_2 \quad (2.6)$$

The effective spin Hamiltonian is then

$$\hat{H}_{spin} = -2J\mathbf{S}_1 \cdot \mathbf{S}_2 \quad (2.7)$$

If $J > 0$, $E_S > E_T$ the triplet $S = 1$ state is the lower energy, stable one. In the case of $J < 0$, $E_T > E_S$ and the singlet $S = 0$ state is the lower energy one. The generalization of Eq.

2.7 to more than 2 spins is not trivial, yet by assuming that Eq. 2.7 still holds in many-body systems we arrive at *Heisenberg Hamiltonian*

$$\hat{H}_{Heisenberg} = - \sum_{ij} J_{ij} \mathbf{S}_i \cdot \mathbf{S}_j \quad (2.8)$$

In systems where the electrons are localized on magnetic atoms, the interaction depicted by the Eqs. 2.7 and 2.8 is referred to as *direct exchange*. It requires, however, the strong overlap of the orbitals to be of considerable magnitude. As the electronic orbitals often extend less than one tenth of an interatomic spacing it is rarely a dominant magnetic interaction. Even in Fe, Co and Ni, that have 3d magnetic orbitals that extend quite far from the nucleus the interaction is not strong enough to explain the observed magnetic properties. As the Electron Spin Resonance (ESR) is one of the methods most extensively used in this Thesis work one has to quantify the effects that magnetic interactions have on ESR linewidth. ESR is, typically, a method of studying systems with unpaired electrons, often complexes possessing a transition metal ion. The electrons of the system are excited at a given frequency with the system being within a microwave cavity. Then the magnetic field is applied. Due to the Zeeman effect, the electronic states are separated by a gap proportional to the magnetic field. When the value of the Zeeman gap equals the energy of the radiation being absorbed or emitted when an electron changes between two states, the resonance condition is reached, the condition being $h\nu = g_e\mu_B B$. The net effect on the system in a microwave cavity is the absorption, but most spectrometers are designed to measure the first-derivative of the absorption.

From the experimentalist's point of view, the three main pieces of information one can obtain from the electron spin resonance measurement. The first is the value of the resonance field H_0 which is related by a simple formula to the electronic g-factor. The electronic g-factor is a measure of local magnetic fields that the electron "feels", being transferred to it through the spin-orbit coupling. The second is the value of the ΔH_{pp} ESR linewidth which is inversely proportional to the spin lifetime in the system, which in itself is important for relaxation effects and the third, the value of the spin susceptibility which is proportional to the intensity of the ESR signal, in this case the double integral of the signal. These elements are illustrated

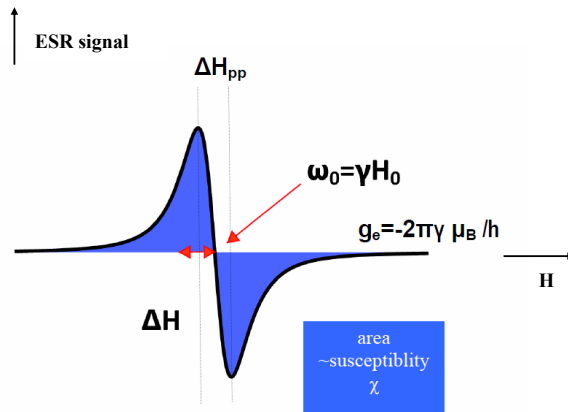


Figure 2.1: The main characteristics of the ESR signal, the resonance frequency ω_0 , related to the resonance field H_0 through the gyromagnetic factor γ , the ESR linewidth ΔH , between two peaks known as ΔH_{pp} where pp stands for peak-to-peak and finally, the double integral of the signal curve, proportional to spin susceptibility. Courtesy of D. M. Djokić.

at the Image 2.1.

We are now going to describe one of the most important pieces of information that we obtain from ESR measurements, the ESR linewidth ΔH_{pp} . Unlike the magnetic dipolar interaction, a strong exchange interaction can have for an effect a *narrowing* of the observed ESR lines measured. The work on *exchange narrowing* introduced here was initiated by Kittel [9, 10, 11] and developed by van Vleck [12] and Anderson [13], among others. Kittel considered a paramagnet far above transition temperature T_C and postulated that the width of the spin resonance line is narrower than expected for dipole-dipole interactions. He obtained

$$\Delta \cong \frac{\langle(\Delta\omega)\rangle_{dipole-dipole}}{J/\hbar} \quad (2.9)$$

Van Vleck studied the resonance in ferromagnetic materials, only to find that the Kittel's formula 2.9 still holds, in a first order perturbation theory, yet he noticed the presence of short-range dipolar interactions important in ferromagnets, of possible anisotropic exchange origin. This fact, however, did not have an influence to the form of Eq. 2.9. A classical work by Anderson and Weiss [13] based on a mathematical assumption that the ESR modulation function is the Gaussian function with the Gaussian noise has been able to explain why materials with very strong exchange narrowing effects still conform to 2.9.

Electron number	1	2	3	4
Electron is on ion	magnetic ₁	O ²⁻	O ²⁻	magnetic ₂
in orbital state	d ₁	p	p	d ₂
Magnetic state: singlet	spin up	(antiparallel)		spin down
		(no splitting because no 1-4 interaction)		
Magnetic state: triplet	spin up	(antiparallel)		spin up
Electron is on ion	magnetic ₁	O ²⁻	O ²⁻	magnetic ₂
in orbital state	d ₁	s ₁	p	d ₂
Magnetic state: singlet	(antiparallel)	spin up		spin down
		(splitting if 3-4 interact)		
Magnetic state: triplet	(antiparallel)	spin up		spin up

Table 2.1: Interaction scheme in superexchange (see text). Taken from [14].

An indirect exchange is a magnetic interaction that takes place between two magnetic ions, through, typically, a non-magnetic ion [15, 16]. It is of great importance in insulators, systems where there are no free electrons, i.e. in systems where band processes are unlikely to take place. The theory of *superexchange* was developed by Kramers [17] and Anderson [14]. Anderson developed a simple scheme, outlined in Table 2.1, to explain the interaction in Mn²⁺-O²⁻-Mn²⁺ system. He showed that there is an energy gap between a singlet and a triplet state of two d-shell electrons, one per Mn²⁺, that interact through a non-magnetic ion, e.g. oxygen O²⁻. He assumed that there is no direct overlap between the two d-wave functions. Further, he assumed that O²⁻ enters the interaction with 2 electrons both in the same p-state. There is then a finite probability that an electron will jump from the O²⁻ ion into a (possibly) s-state on one of the magnetic ions. This s-state has to be thought of as coupled by some strong spin dependent interaction with the d-electron that is already present on the magnetic ion. This is a necessary condition for the superexchange. As the p-spins are necessarily antiparallel due to Pauli principle ($\uparrow\downarrow$) the ground state can be either a singlet ($\uparrow\downarrow$) or a triplet ($\uparrow\uparrow$) with the same energy, i.e. there is no singlet-triplet energy splitting. If we assume, that the excited state, however, involves interaction of the two electrons on the same magnetic ion, the mutual antiparallel orientation of the involved spins is expected. The interaction between the remaining p-electron on the oxygen ion and the magnetic electron on the magnetic ion to which the electron has not been transferred can then contain an appreciable

exchange integral. This means that the singlet ($\uparrow\downarrow$) state is lower in energy, i.e. superexchange can bear an antiferromagnetic character.

However, according to the famous work by Goodenough and Kanamori [18, 19, 20] the superexchange can bear a ferromagnetic character, for example for the interaction between the d^2 and d^7 orbitals in the tetrahedral environment. It was Kanamori [20] who realized that the sign of the superexchange interaction is determined from symmetry relations. He studied the cases when magnetic cations are in octahedral environment and when the lines connecting the magnetic cations and the intervening anions are closing the angle of 90° or 180° . For magnetic cations in tetrahedral environment he found the definite relation between the superexchange and the symmetry of the cation electron orbitals, providing that the cation orbitals are s-state in nature.

An extension to the superexchange theory was developed by Dzyaloshinsky [21] and Moriya [22]. The interaction is very important in the field of diluted magnetic semiconductors [23]. Tackling the problem from the symmetry principles purely [24] Dzyaloshinsky predicted that the exchange interaction might also have an anisotropic term, a term $\hat{H} \propto \mathbf{D}_{ij} \cdot (\mathbf{S}_i \times \mathbf{S}_j)$ present in magnetic crystals with low symmetry. Moriya has managed to identify the spin-orbit interaction as the microscopic origin of the added term in the Hamiltonian, Eq. 2.10. Due to the spin-orbit interaction there occurs an *indirect* coupling through the spins, resulting in the Hamiltonian

$$\hat{H} = -\frac{1}{2} \sum_{ij} J_{ij} \mathbf{S}_i \cdot \mathbf{S}_j - \frac{1}{2} \sum_{ij} \mathbf{D}_{ij} \cdot (\mathbf{S}_i \times \mathbf{S}_j) \quad (2.10)$$

The added, second part of the Hamiltonian shown in Equation 2.10 is referred to as Dzyaloshinsky-Moriya interaction. An important issue to note here is that the Hamiltonian is no longer rotation invariant but depends on the direction of the spins ($\mathbf{S}_i \times \mathbf{S}_j$).

2.1.1 Transition-metal ions in crystal fields

The d orbitals can be classified into two classes [16], the t_{2g} orbitals that point between the x, y and z axes (referred to as d_{xy} , d_{xz} and d_{yz}) and the e_g orbitals that point along these

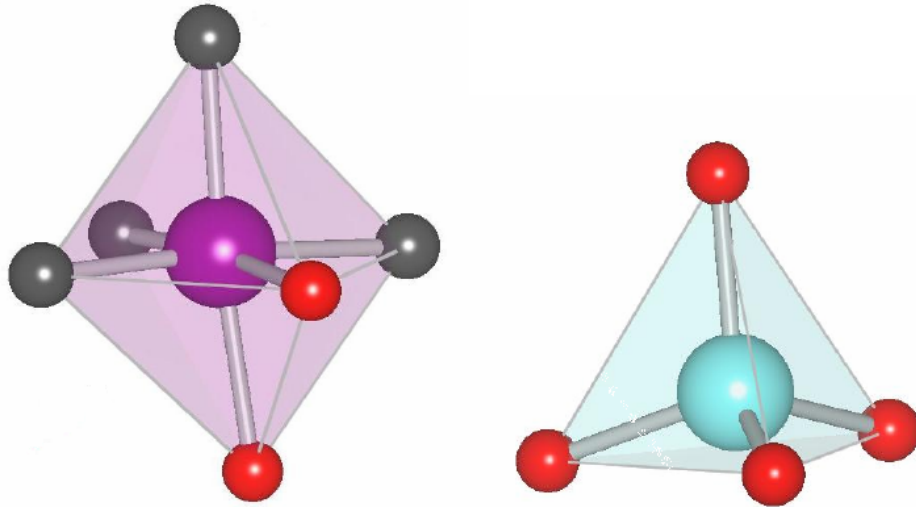


Figure 2.2: Mn ion (purple) in an octahedral environment of OH groups (grey) and oxygen (red) atoms in Mn doped hydrozincite $(\text{Zn}_{1-x}\text{Mn}_x)_5(\text{OH})_6(\text{CO}_3)_2$, one of the central materials in this Thesis work. Right: the Zn ion (cyan) in a tetrahedral environment of oxygen (red) atoms in ZnO, the host semiconductor in this study.

axes. The e_g orbitals are namely, the d_{z^2} orbital with lobes pointing along the z axis and the $d_{x^2-y^2}$ orbitals, with lobes pointing along both the x -axes and y -axes.

The *octahedral* environment is created by assuming that a cation containing ten d electrons is placed in the centre of a sphere of a radius r in which the charge on the sphere is collected into six discrete point charges. The total electronic energy of all the d orbitals will not change, but the d orbitals will no longer be degenerate. The *tetrahedral* environment is analogous taking only four discrete point charges.

The effect of the environment on the d orbitals is determined through the amount of overlap between the p orbitals and a given d orbital. For example, in octahedral environment the t_{2g} orbitals (d_{xy} , d_{xz} and d_{yz}), that point between the x , y and z axes will be lowered in energy, while the e_g orbitals d_{z^2} and $d_{x^2-y^2}$ will be raised in energy. The exact opposite situation is applicable for the case of tetrahedral environment where the orbitals which point along the axes (the e_g orbitals) are now maximally avoiding the charge density from the ligand atoms describing a tetrahedron, and the t_{2g} orbitals are maximally overlapping the ligand orbitals. These notions are summarized in Fig. 2.3.

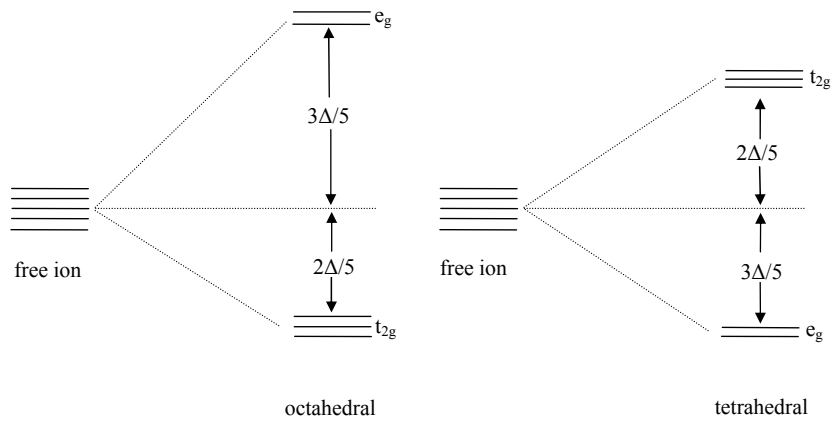


Figure 2.3: The crystal field in octahedral and tetrahedral environment.

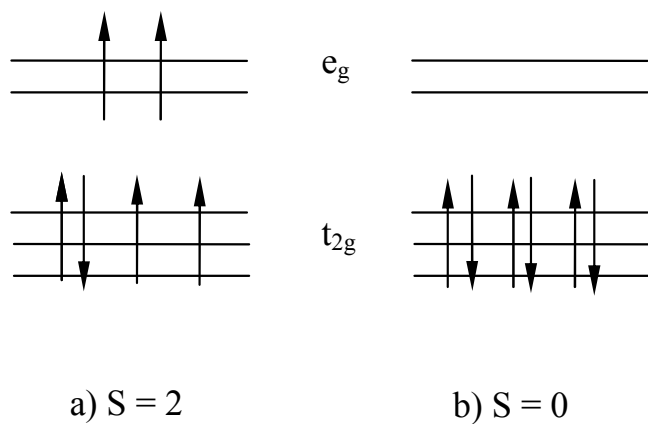


Figure 2.4: Electronic configuration for the (a) high-spin (weak-field) and (b) low-spin (strong-field) cases for a $3d^6$ ion, such as Fe^{2+} .

The transition metal ion that has less than 10 3d electrons will have its successive electrons fill the 3d states in order defined by the competition between the crystal field energy and the Coulomb energy cost of putting two electrons in the same orbital, the *pairing energy*. One distinguishes two cases, *weak-field case* where crystal field is lower than the pairing energy, in which the electrons first singly occupy each orbital before any orbital becomes doubly occupied and the case where crystal field is higher than the pairing energy, *strong-field case* and the electrons doubly occupy lower energy orbitals before occupying the higher energy ones. This is illustrated in the Fig. 2.4 where 3d⁶ ion, such as Fe²⁺ exhibits *high-spin* configuration in the case of the weak-field. In this case electrons fill each orbital once leaving one electron, that pairs up with a t_{2g} electron resulting in four unpaired spins, i.e. S = 2 state. Consequently, in the strong-field case the six electrons enter three t_{2g} orbitals leaving the e_g orbitals unfilled which results in a *low-spin* configuration with no unpaired electrons, i.e. S = 0 state.

2.2 The fundamentals of spintronics

The birth of spin electronics or spintronics [25] came in 1988. with the discovery of the giant magnetoresistance (GMR) effect by Baibich et al. [26] on Cr(001)/Fe(001) superlattices deposited on GaAs(001) substrates. A two-fold decrease in resistivity was found when the 60 bilayers of Cr(30Å)/Fe(9Å) structure were brought to saturation by an application of field of 20kG or higher. A tentative explanation by the authors is in "spin dependent transmission between ferromagnetic layers". The work relies on a multitude of earlier works on nonmagnet/ferromagnet/nonmagnet (N/F/N) sandwich structures in which I-V curves were found to be dependent on magnetic field. The first time magnetic field was observed in internal field emission (Fowler-Nordheim electron tunneling) was in the case of Eu chalcogenides such as EuS and EuSe [27]. Jullière et al. [28] were able to measure a change of conductance in ferromagnet/insulator/ferromagnet (F/I/F) sandwich structures when the ferromagnets were in antiferromagnetic and ferromagnetic configurations, respectively.

The work by Jullière et al. showed that in Fe/Ge/Pb and Fe/Ge/Co junctions a change of conductance at zero applied bias in FM and AFM configurations $(\Delta G/G)_{V=0}$ peaks at

14%. The $(\Delta G/G)$ value is actually the value of tunneling magnetoresistance (TMR) with G the value in the lower G (antiferromagnetic) configuration. The conductance itself was found to arise entirely due to electron tunneling between ferromagnetic electrodes hence being an entirely quantum mechanical effect. Assuming no spin-flip at the metal/barrier interface occurs the authors postulated a two-current model for the value of TMR which results in the value of conductance in FM configuration to be $G_{FM}=N_{M1}N_{M2}+N_{m1}N_{m2}$ while the $G_{AFM}=N_{M1}N_{m2}+N_{m1}N_{M2}$, N representing the density of states, M,m the majority and minority spin, respectively, while 1 and 2 are layer indices. As G_{FM} is typically much larger than G_{AFM} this system can be used as a spin-valve.

This is now known as the Jullière two-current model, as illustrated in Fig. 2.5. Significant tunneling occurs only when the spins in majority spin sub-bands are oriented mutually parallel, i.e. ferromagnetically.

The successful work of any spintronics device relies on creation of (1) non-equilibrium spin polarization in a ferromagnet or semiconductor, (2) injection of this population to an insulator, (3) the control of possible pathways to relaxation of spin population to equilibrium and (4) the detection of the spin-encoded signal at the detector. The explanation of these elements follows.

(1) Non-equilibrium spin polarization can be created electrically using Feher effect [29]. Feher effect is the creation of the dynamical nuclear spin polarization through strong hyperfine coupling between the electron and nuclear spins together with different temperatures of electron spin and electron velocity populations. Optical orientation uses transfer of angular momentum of circularly polarized light to electron orbital momenta. The spin of the electrons is then affected through spin-orbit interaction. The effect was first demonstrated on electrons in Si by Lampel et al. [30] as a verification of the theoretical proposition by Kastler et al. [31] who conjectured that one can optically change relative populations of electrons in Zeeman and hyperfine levels of the ground states of atoms. Magnetic resonance, scattering of unpolarized electrons in the presence of spin-orbit coupling, adiabatic and non-adiabatic quantum spin pumping and spin Hall effect are all alternatives to creating non-equilibrium spin polarization.

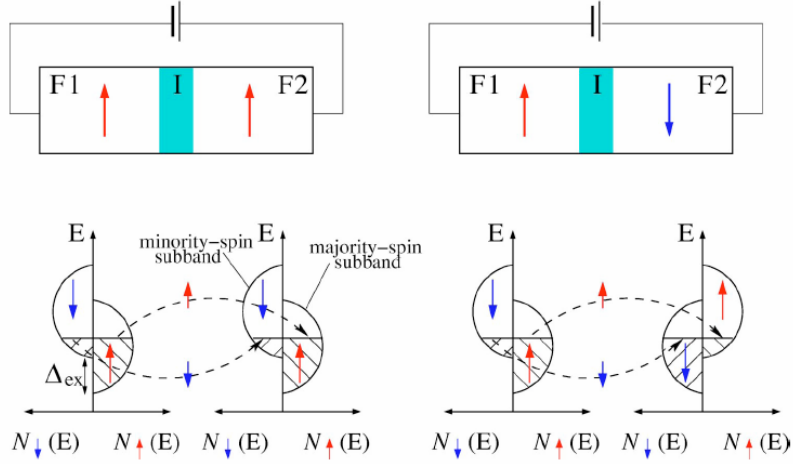


Figure 2.5: Electron tunneling in a ferromagnet/insulator/ferromagnet junction. Upper row: A scheme of the junction in ferromagnetic and antiferromagnetic configuration. Lower row: Spin-resolved density of the electronic d states of the two metals with spin densities split by an exchange field Δ_{ex} . The conductance is significantly higher in ferromagnetic configuration. Taken from [25].

Spin Hall effect is particularly interesting for possible applications, as it produces a spin layer at a surface of the sample, limited by spin relaxation. It was first described in a work by D'yakonov and Perel' [32] who hypothesized that the spin layer creation is a consequence of the creation of spin flux perpendicular to the current and directed from the interior to the periphery of the sample. The effect is illustrated in Fig. 2.6. Spin-orbit coupling is inducing an orbital momentum opposite in direction to the electron's spin, effectively separating a charge current which contains both types of spins into spin currents.

(2) The injection of spin population from ferromagnet into a nonmagnet through a F/N interface is based on a principle established by Aronov et al. who deduced that a charge current passing through a F/N interface will cause spin polarized carriers from a ferromagnet entering a non-metal thereby causing an injection of the non-equilibrium magnetization δM into a normal metal [34].

(3) In order for spin to cover macroscopic distances to get detected one has to take into account basic mechanisms of spin relaxation and spin dephasing. The four main relaxation mechanisms are Elliot-Yafet, Dyakonov-Perel', Bir-Aronov-Pikus and hyperfine interaction of

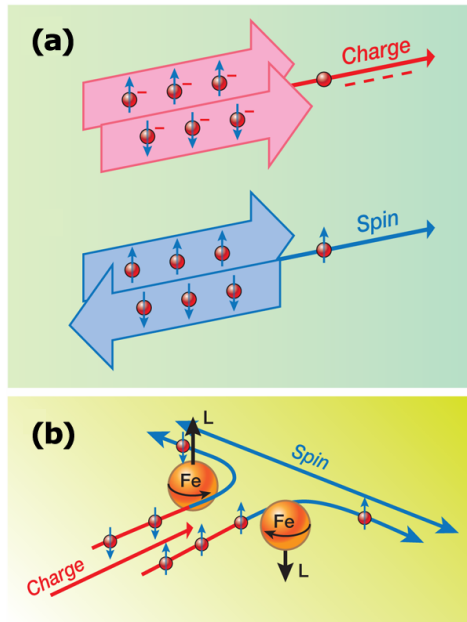


Figure 2.6: Spin Hall effect. (a) Charge current with both spin species equally populated , (b) Orbital momentum opposite to the direction of the electron's spin is induced by spin-orbit interactions. This results in a separation of charge current into spin currents. Taken from [33].

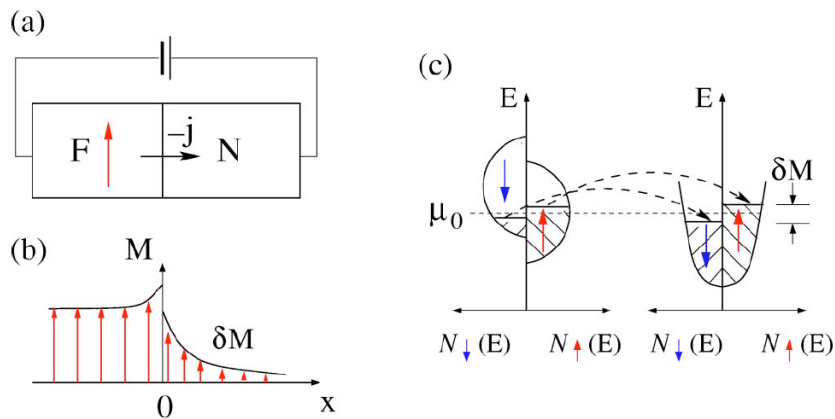


Figure 2.7: Spin injection from ferromagnet into a non-metal. (a) Device schematics , (b) Magnetization as a function of position - injected spins are the source of magnetization δM , (c) Spin resolved density contribution to charge and spin transport across the F/N interface. Taken from [25].

spins with nuclei. If the lattice ions can bring about spin-orbit interaction into the electron wave function then the electron can relax through defects and impurities, i.e. the ordinary momentum scattering. One speaks in this case of Elliot-Yafet relaxation mechanism. Dyakonov-Perel' mechanism is effective in materials where the inversion symmetry does not exist, e.g. when there are two or more distinct atoms in a primitive lattice, this being the case in (III-V) or (II-VI) semiconductors, such as GaAs or ZnSe, respectively. In this case spin-orbit interaction produces effective fields which are a function of \mathbf{k} , the electron wave vector. A field changing rapidly in time, a stochastic field, is created by scattering of the electron on defects and phonons [35]. The exposure to this stochastic field in turn causes spin relaxation. The spin relaxation due to Bir-Aronov-Pikus scattering channel occurs in p-type semiconductors due to the exchange interaction between the electrons in the conduction band and holes in the valence band [36]. This may be a significant effect in heavily p-doped semiconductors due to a large number of holes. The only mechanism that has an effect on localized electron spin is the hyperfine interaction of spins with nuclei [37]. The relaxation happens through the action of a random effective magnetic field produced by nuclei on the spin. Although of small corresponding relaxation rate, in systems with no itinerant electrons this effect gains importance.

(4) An ideal spin detection device would detect not only spin but the changes in spin states [25]. Due to the Silsbee-Johnson spin-charge coupling, in an F/N/F device, a change in relative orientations of the magnetization between the two ferromagnets will be followed by either a change in $V_S = \delta M \rightarrow -V_S$ in the case of high impedance of the circuit ($Z \rightarrow \infty$) or the reversal of charge current $j \rightarrow -j$ in the low impedance case ($Z \rightarrow 0$).

2.2.1 Materials for spintronics

From a material scientist's point of view there are several possible families of materials that satisfy criteria of successful implementation in spintronics [39]. In order to create a spin-polarized current a material is required to be half-metallic, i.e. to be metallic in one spin polarization and to have an energy gap in the other spin-polarization.

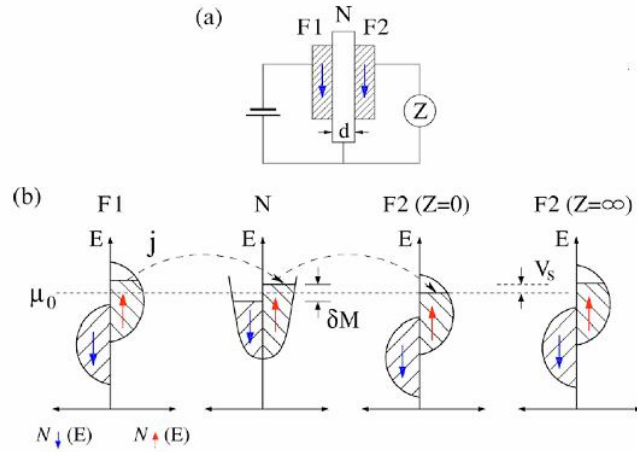


Figure 2.8: (a) A $F_1/N/F_2$ structure where F_1 and F_2 are ideal ferromagnets and N is a nonmagnet. (b) Spin injection from F_1 into N represented in an density-of-states diagram. The injection results in a spin accumulation, δM . Depending on the impedance of the circuit the spin is detected by measuring either the current across the N/F_2 interface ($Z \rightarrow 0$) or the voltage across the interface $V_S = \delta M \rightarrow -V_S$ (for $Z \rightarrow \infty$). Taken from [25].

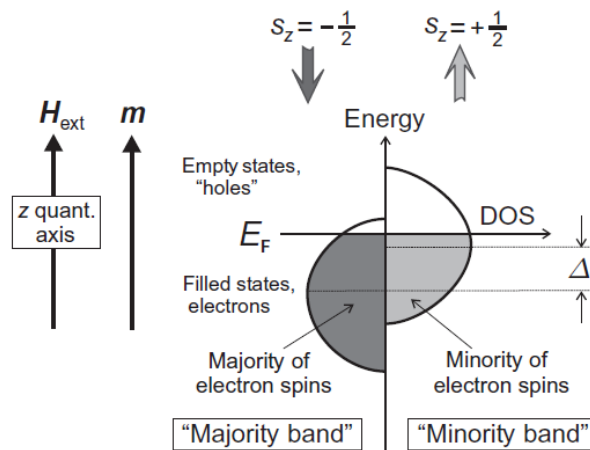


Figure 2.9: The band theory of ferromagnetism with majority and minority spin bands split by the exchange energy Δ . Taken from [38].

2.2.2 Band scheme of common ferromagnets

The band theories for ferromagnets are based on the famous Stoner-Wohlfarth model. A simple scheme is given in Fig. 2.9. The *majority spin* is the term used for the spin polarization which contains the higher number of electron spins, the *minority spin* denoting the species with the smaller number of electrons. The *spin-up* and *spin-down* appellation only has meaning when defined with respect to the quantization axis, here taken as the direction of the magnetic field. In the Stoner model, the spin polarizations are exchange split by the energy Δ .

The effect of the spin-polarized band structure on the magnetic properties of the compounds can be illustrated with the example of a weak ferromagnet, bcc-Fe and a stronger ferromagnet, hcp-Co. The general formula for the susceptibility of the system of interacting itinerant electrons is given by the formula 2.11 :

$$\chi = \frac{\chi_p}{1 - 2\mu_B^2 I_S N(E_F)} \quad (2.11)$$

Here, χ_p is the Pauli susceptibility, I_S is an effective interaction parameter, and $N(E_F)$ is the number of states at the Fermi energy. The factor multiplying the χ_p is $S = 1 - 2\mu_B^2 I_S N(E_F)$ and is known as the *Stoner enhancement factor*. As the susceptibility is the second derivative of the free energy of the system, the minimum in free energy for $M = 0$ corresponds to the positive value of the susceptibility. However, the existence of spontaneous ferromagnetic ordering will mean that the minimum in free energy is not at $M = 0$ and the susceptibility has to bare a negative value. In the case at hand, this is defined as the *Stoner criterion* (Eq. 2.12).

$$2\mu_B^2 I_S N(E_F) > 1 \quad (2.12)$$

The case of a weak ferromagnet bcc-Fe is given at the Fig 2.10(a). The Fermi energy in bcc-Fe is in the minimum of the spin-down density of states (DOS). For both spin projections the DOS is finite which leads to only a weak ferromagnetism. The DOS is also illustrated for the non-magnetic case where $N(E_F)$ follows the altered criterion (see [40] for details). The

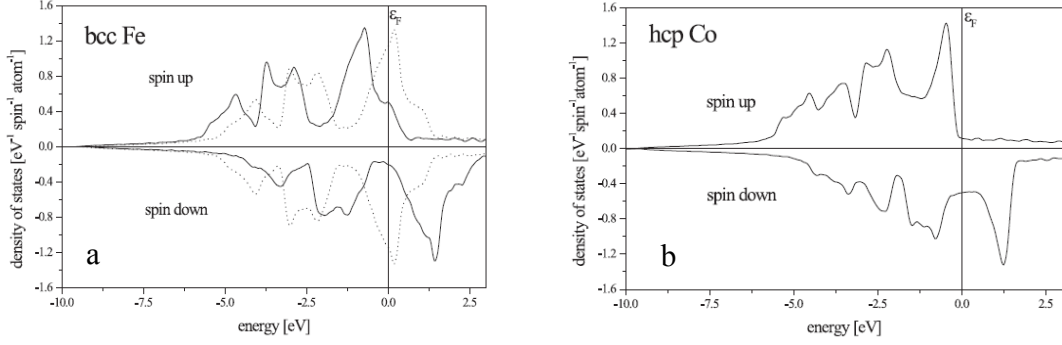


Figure 2.10: The density of states for bcc-Fe (a)(the non-magnetic case is delineated by a dashed line), a weak ferromagnet and hcp-Co (b), a strong ferromagnet (see text). Taken from [40].

high $N(E_F)$ means that the system is being brought back to the non-magnetic regime. What defines the spin splitting and the magnetic moment of bcc-Fe is the position of the Fermi energy in the minimum of the spin-down DOS, being energetically more favorable than having a full spin-up band that would lead to strong ferromagnetism.

$$\frac{2}{n}N(E_F)k_B\Theta \leq 1 - \frac{1}{3}c\zeta^2 \quad (2.13)$$

Here,

$$\zeta = \frac{M}{M_0}, \quad \Theta = \frac{\mu_B N M_0}{k_B} \quad (2.14)$$

$$c = \frac{1}{8} \frac{n^2}{N(E_F)^2} \left[\frac{N(E_F)''}{N(E_F)} - 3 \left(\frac{N(E_F)'}{N(E_F)} \right)^2 \right] \quad (2.15)$$

In hcp-Co the spin-up band is completely filled with the Fermi energy (see Fig 2.10(b)) being above the spin-up d band. This brings the hcp-Co a strong ferromagnetic character. The Fermi energy is in the region of low DOS where mainly s states exist. The low density of states means that the susceptibility of the material is small.

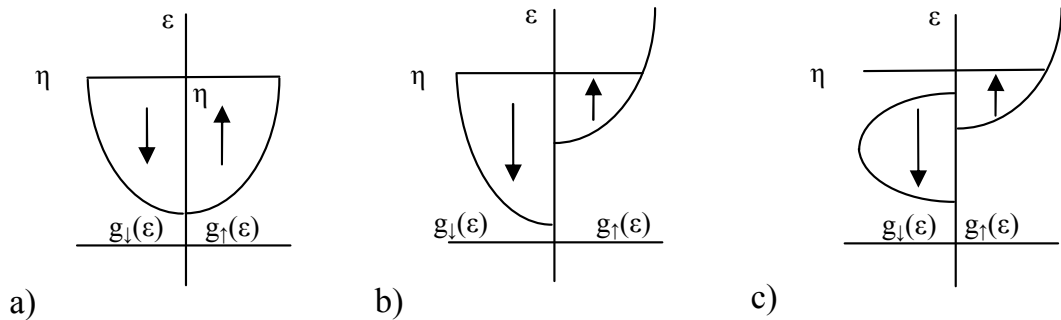


Figure 2.11: The energy bands of a nonmagnetic conductor (a), a ferromagnetic conductor (b), and half-metallic ferromagnet (c).

2.2.3 Half-metallic ferromagnets

The band scheme of a typical half-metallic ferromagnet is given in Fig. 2.11. This situation is equivalent to a filled majority spin band, with the conductivity happening only through the minority spin channel. ZnO was found to be half-metallic as well when doped with V, Cr, Fe, Co or Ni while the ferromagnetism in Mn-doped ZnO was found to necessitate p-type hole doping [41].

An example of a typical half-metallic ferromagnetic is given in the *ab initio* calculations of the electronic structure of 25% Co:ZnO, the diluted magnetic semiconductor with a high concentration of Co. These calculations are given in Fig. 2.12. Zn-3*d* states and O-2*p* states are approximately 7 and 4 eV below the Fermi level (E_F), respectively. Co-3*d* states are observed at approximately E_F , while the conduction band is mostly made up out of Zn-4*s* states. Co-3*d* states are exchange split with the *up* states being fully occupied. The Fermi energy E_F is in the minimum of the spin down states. When Ga atoms are doped into the systems, a portion of electrons occupy the Co 3*d* states. The electrons introduced through Ga interact through double exchange mechanism and lower the kinetic energy of the ferromagnetic states in $x=0.25$ Zn_{1-x}Co_xO. The origin of the stabilization of the ferromagnetic state by electron doping seems to stem from this interaction.

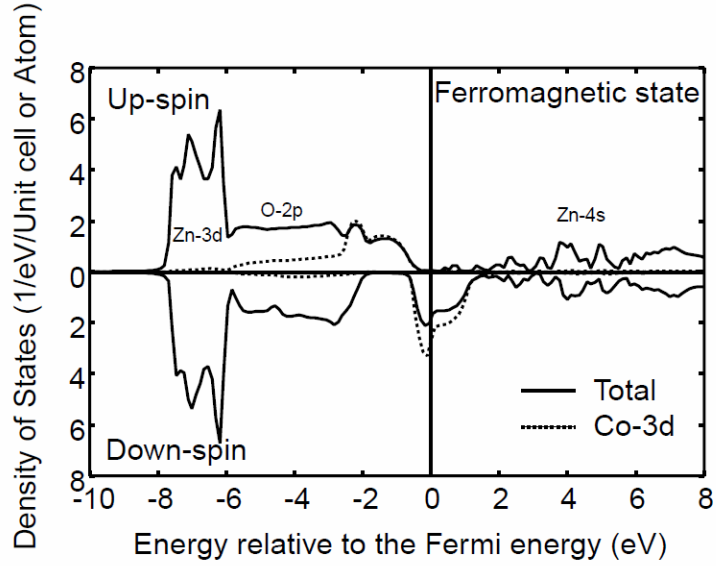


Figure 2.12: Total density of states per unit cell and local density of d states for Co doped ZnO per Co site. Taken from [7].

2.3 The basic notions on diluted magnetic semiconductors

For a long period of time [42] only few magnetic semiconductors have been known, such as europium based chalcogenides, e.g. EuO [43] or CdCr_2Se_4 [44]. It is with discovery of diluted magnetic semiconductors (DMS) that the situation and interest in these materials augmented drastically.

Furdyna's definition [45] of diluted magnetic semiconductors is that they ".. are semiconducting alloys whose lattice is made up in part of substitutional magnetic atoms". The DMS of the $\text{A}_{1-x}^{\text{II}}\text{Mn}_x\text{B}^{\text{VI}}$ gained interest because the possibility of tuning their lattice constants and band parameters by varying the material's composition. Originally it was realized that the random distribution of magnetic ions over the cation sublattice can lead to spin-glass-like phases at low temperatures. The sp band electrons can interact with the d electrons associated, with e.g. Mn^{++} that can lead to extremely large Zeeman splitting of band and impurity electronic properties and selective amplification of spin-dependent properties, which is an ideal criterium for application in spintronics.

Manganese doped DMS have a special interest due to the fact that Mn has a clearly defined

spin of $S = 5/2$ and does not alter significantly the band structure of the host material. They can be oriented by extremely small applied fields leading to the giant Zeeman splitting of the carrier bands of the order of tens of meV leading to a variety of magneto-electronic and magneto-optical effects. The low value of the ferromagnetic transition temperature in DMS was an impasse in the field, yet breakthrough was achieved in the 1990s, esp. in the (III-V) structures, such as InMnAs [46, 47] and subsequently, GaMnAs [48].

The electronic band structure of $A_{1-x}^{II}Mn_xB^{VI}$ can be summarized [45] as follows: (a) the band gap structure of $A_{1-x}^{II}Mn_xB^{VI}$ follows the one of $A^{II}B^{VI}$ and has a smooth transition with increasing x to a MnB^{VI} structure (b) the effects of the $3d^5$ Mn^{2+} electronic states the underlying band scheme can be summed up into the existence of majority (occupied) $e_d^{+\sigma}$ and minority (unoccupied) $e_d^{-\sigma}$ electronic states. The photoemission experiments, i.e. the experiments in which an electron is removed from the fully occupied $3d^5$ band at the Mn site have identified the position of the $e_d^{+\sigma}$ as being 3.5 eV higher than the valence band (c) the *intra-ion* transitions involving a spin-flip within a single $3d^5$ Mn^{2+} are occurring at energies about 2.2 eV and are key for determining the optical and electronic properties of DMS. The positions of $e_d^{+\sigma}$ and $e_d^{-\sigma}$ are however crucial for defining the *p-d interaction* that underlies both sp-d and d-d exchange interactions.

The magnetic properties of $A_{1-x}^{II}Mn_xB^{VI}$ can analytically be described only in limits of low Mn concentrations or high temperatures. In the *dilute limit*, for concentrations of Mn^{2+} $x < 0.01$ the Mn^{2+} spins can be treated independently with the magnetization M then being described by the Brillouin function

$$M = -xN_0g_{Mn}\mu_B\langle S_z \rangle = xN_0g_{Mn}\mu_B S B_S[g_{Mn}\mu_B S H / (k_B T)] \quad (2.16)$$

Here, $\langle S_z \rangle$ is the average spin per Mn site, N_0 is the number of cations per unit volume, B_S is the standard Brillouin function, H is the applied field, and $S=5/2$ for Mn^{2+} . When $g_{Mn}\mu_B S H / (k_B T) \ll 1$, i.e. in the low field or high-temperature limit, the static magnetic susceptibility defined by $M = \chi H$ is given by Curie law

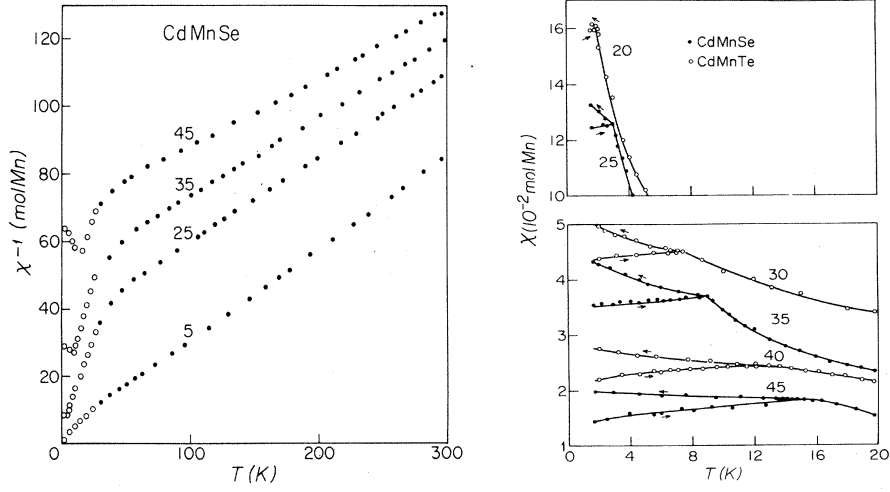


Figure 2.13: Left: Inverse of magnetic susceptibility against temperature for $\text{Cd}_{1-x}\text{Mn}_x\text{Se}$. Right: Irreversible thermoremanence effects observed in the magnetic susceptibility in $\text{Cd}_{1-x}\text{Mn}_x\text{Se}$ and $\text{Cd}_{1-x}\text{Mn}_x\text{Te}$. The arrow pointing to the right delineates zero-field-cooled data while the arrow pointing to the left corresponds to field-cooled-data. Taken from [49].

$$\chi = C_0 x / T, C_0 = N_0 (g_{Mn} \mu_B)^2 S(S+1) / (3k_B) \quad (2.17)$$

Experimentally, magnetic susceptibility was found to follow a Curie-Weiss behaviour

$$\chi = C(x) / [T - \theta(x)] \quad (2.18)$$

The original measured $\theta(x)$ were always found to be negative, indicating antiferromagnetic interactions between the spins.

Considering randomly dilute Heisenberg spins with antiferromagnetic interactions yields [50]

$$\chi = C_0 x / (T + \theta_0 x), \theta_0 = -\frac{2}{3} S(S+1) ZJ / k_B \quad (2.19)$$

In Eq. 3.2 Z is the nearest neighbor number, $Z = 12$ for wurtzite and zinc-blende structure, and J is the nearest-neighbor exchange integral.

A very universal feature of DMS is the departure from the Curie-Weiss law for higher x at low temperatures. Originally, this could only be understood qualitatively by including higher

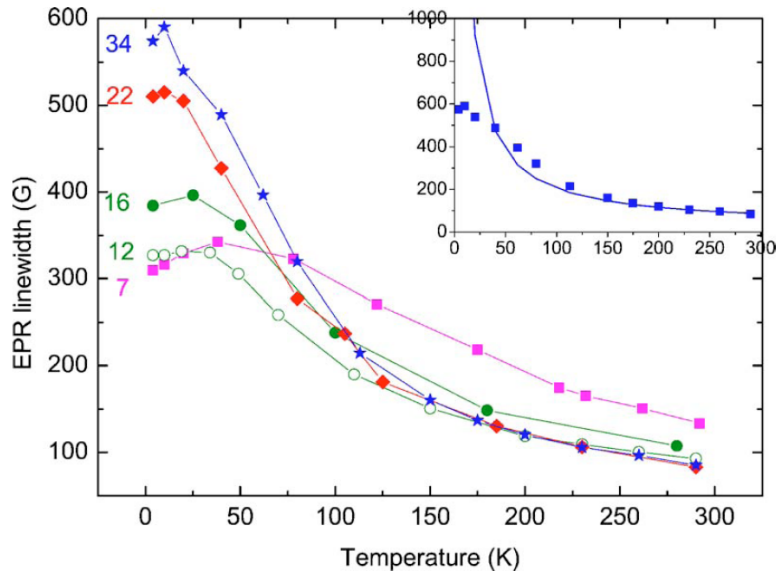


Figure 2.14: Variation of the peak-to-peak ESR linewidth in the $\text{Zn}_{1-x}\text{Mn}_x\text{O}$ thin films as a function of temperature for $x = 0.07, 0.12, 0.16, 0.22, 0.34$. The inset is a $1/(\Theta + T)$ fit to $x = 0.34$. Taken from [51].

order expansion terms in the calculation of χ . Three key elements can be discerned from the figure 2.13 (a) the linear Curie-Weiss behaviour above 40 nK, (b) the downturn of χ^{-1} at lower temperatures and the cusp in $x = 0.25, x = 0.35$ and $x = 0.45$ indicative of a spin-glass transition.

The transition at a T_g at which a well-defined cusp occurs serves to define the boundary between the high-temperature paramagnetic phase and the low temperature frozen state. The frozen state shows many of the characteristic of a spin-glass state. The occurrence of the irreversible phenomena is visible in the magnetic signatures observed below T_g , especially in the difference between field-cooled (FC) and zero-field-cooled (ZFC) susceptibility data (see Fig. 2.13). Zero-field cooled measurements refer to the measurement taken after initially cooling down the samples from room temperature to the lowest temperature without magnetic field. The field cooled measurement refers to the measurement taken after the second cooling down of the sample, this time in the applied magnetic field. The same value of magnetic field is typically used throughout all of the phases of the measurement. In addition to the (ZFC-FC) splitting several other magnetic signatures can confirm the presence of spin-glass

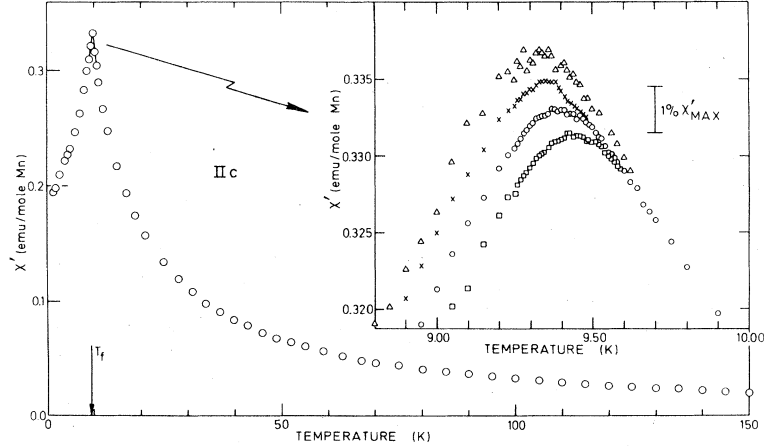


Figure 2.15: Zero-field susceptibility χ' as a function of temperature for $\text{Cu}_{1-x}\text{Mn}_x$, $x=0.0094$. Measurement frequencies are given by : square - 1.33 kHz, circle - 234 Hz, cross - 10.4 Hz, triangle - 2.6 Hz Taken from [52].

order at low temperatures in DMS. The ΔH_{pp} , the linewidth as measured in the Electron Spin Resonance (ESR) experiment experiences saturation when the system is cooled below the freezing temperature T_g . The constant line width corresponds to a state of frozen spins with different regions of the sample having different magnetic orders. The different regions will then have resonance frequencies determined by a combination of the local exchange field and the local anisotropy field. In the spin-blocked system these fields are both independent of the temperature, resulting in a line width of the system independent of temperature [51].

The alternating current susceptibility measurements enable us to measure the in-phase and out of phase components of the susceptibility χ_T . χ'_T is the component of χ_T in phase with the ac field applied, while the χ''_T is the out-of-phase component. χ'_T is expected to be dependent on the frequency ν and the applied field H . The temperature dependence of χ'_T for several measurement frequencies in the case of the canonical spin-glass CuMn [52] is given in Fig. 2.15. $\chi'_T(T, \nu)$ show a shift to higher freezing temperatures T_F . The shift ΔT_F is minute, $\Delta T_F = 0.14$ K for $\Delta\nu = 10^3$ Hz. Although ΔT_F increases significantly when the Mn content x augments, the normalized frequency shift $\Delta T_F/T_F$ remains constant, and for CuMn is equal to $\frac{\Delta T_F}{T_F(\Delta \log_{10} \nu)} = 0.005$.

2.4 Conclusion

The purpose of this Chapter was to introduce the basic principles of spintronics, and to introduce the family of diluted magnetic semiconductors to which our material of choice for the study during this doctoral work, TM doped ZnO, belongs. Spintronics is a technology based on a spin control of magnetism or an electrical or optical control of spin or magnetism [42] and diluted magnetic semiconductors. While the spintronics often works with non-magnetic semiconductors where the control of spin is achieved through the only spin-dependent interaction, the spin-orbit coupling, ferromagnetic semiconductors are used as essential elements of spintronics designs, most notably as ferromagnetic sources and drains. Likewise, they offer unprecedented blend of magnetic and electronic properties, due to the strongly spin-dependent properties and high Curie-temperatures that peak for TM doped ZnO. In the next Chapter we shall learn more about the work on ZnO, already a universally used material, the synthesis and properties of TM doped ZnO, the theoretical predictions and experimental realizations of the room-temperature ferromagnetism of ZnO, and finally the controversies about the results that fuel further research.

Chapter 3

Transition metal doped zinc oxide in spintronics

This Chapter will cover the transition metal doped zinc oxide in spintronics, starting from the depiction of the zinc oxide, most notably its electronic structure and the defects chemistry, followed by a short overview of the synthesis methods employed to synthesize ZnO, and to conclude the Chapter, the differentiation between the results on ferromagnetism of $\text{Zn}_{1-x}\text{TM}_x\text{O}$ coming from intrinsic materials, i.e. materials without precipitation of parasitic phases or materials in which the parasitic phase did precipitate.

3.1 Zinc oxide - the host (II-VI) semiconductor

The physics of the host semiconductor ZnO has been developing since 1935. since Bunn et al. studied the ZnO lattice parameters. The development occurred with a tempo determined with possible applications of ZnO in different fields of science and technology. For these applications there are a number of reasons. To begin with, ZnO possesses a very large exciton binding energy of ≈ 60 meV, significantly higher than similarly well studied (III-V) semiconductor GaN (≈ 24 meV). The two semiconductors are both direct band-gap and have $E_g \approx 3.3$ eV (3.4 eV) making them suitable for a range of optoelectronic applications. A large-band-gap materials have higher breakdown voltages, lower noise generation, operation at high-power

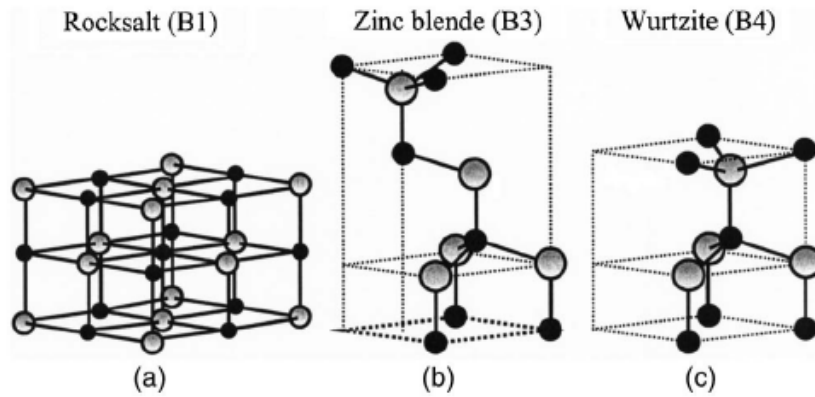


Figure 3.1: The crystal structures of ZnO. ZnO crystallizes in (a) B1, cubic rocksalt structure, (b) B2, hexagonal zinc-blende structure and (c) B4, $P6_3mc$ wurtzite. Only the B4 wurtzite structure is thermodynamically stable in bulk samples.

and they can sustain large electric fields.

3.1.1 The Structural properties of ZnO

Zinc oxide crystallizes in a $P6_3mc$ wurtzite hexagonal structure, space group B4, while it can exist in B1, cubic rocksalt structure and B2, hexagonal zinc-blende structure, the latter two not being thermodynamically stable in bulk samples. The structure of ZnO can be most readily described as two interconnected sublattices of Zn^{2+} and O^{2-} , each of the two ions being in tetrahedral environment of the other one. It has a hexagonal Bravais lattice with four atoms per unit cell. It is completely defined by the length of the hexagonal edge a_0 , the height c_0 of the prism and a microscopic dimensionless parameter u , defined as the length of the bond parallel to the c axis, in units of c . The structure is given in Fig. 3.1(c). Tetrahedral environment is causing ZnO to be polar with respect to hexagonal axis, the trait that is behind its properties such as piezoelectricity and spontaneous polarization. While expected to have sp^3 hybridized orbitals due to its tetrahedral configuration, the ZnO actually scores very high on the Philips' ionicity scale, $f_i=0.616$ revealing its nature of an ionic crystal.

3.1.2 Defects in ZnO

The native ZnO is n-doped, due to high presence of the donor type point defects, mainly Zn interstitials and oxygen vacancies within the structure. However, hydrogen can serve as a powerful n dopant as well. The theory behind oxygen vacancy state reveals a deep state but also a 100 meV shallow energy state attributable to an oxygen vacancy. Acceptor type point defects include the O interstitial O_I and Zn vacancy V_{Zn} . V_{Zn} is a dominant point defect, a negatively charged vacancy produced in oxygen rich environments. The most controversial issue in the ZnO defect chemistry is the nature of the predominant donor defect [53]. According to several authors the dominant defect are zinc interstitials occurring through the Frenkel reaction $Zn_{Zn} \rightleftharpoons Zn_i^x + V_{Zn}^x$ with a reaction constant K_F . Other literature points to oxygen vacancies as the main donor defect. They are created in a Schottky process $0 \rightleftharpoons V_{Zn}^x + V_O^x$ (reaction constant K_S). As oxygen vacancies induce the similar electronic properties it is difficult to distinguish between the two. The work of Han et al. [53] indicates that $K_F > K_S$ hence Zn interstitials dominate below 1573 K while at higher temperatures oxygen vacancies tend to be more important.

A complete list of defect chemical reactions in ZnO was published by Han et al. [53]

3.1.3 The band structure, magnetic and transport properties of ZnO

The calculation of the electronic band structure of ZnO has reproduced the correct band-gap established in measurements only when self-interaction-corrected pseudopotentials (SIC-PP) method was used in combination with local density approximation (LDA). The resulting scheme is presented at 3.2. As the valence band maxima and the lowest conduction band point minima occur at the Γ point ($k = 0$) ZnO is a direct band gap semiconductor. The bottom 10 bands ($\approx -9\text{eV}$) are the Zn 3d levels, the middle 6 bands (from $\approx -5\text{ eV}$ to 0 eV correspond to O 2p bonding states) while the first two conduction band states are empty Zn 3s levels and are strongly Zn localized. The O 2s bands are the core-like energy states and occur around -20 eV . The method gives 3.77 eV for the value of gap (3.4 eV measured) yet the value of the anion p-valence bandwidth obtained by local-density approximation self-interaction-corrected

Reaction	Constant	Sukker et al.	Han et al.
$\text{ZnO}(\text{g}) \rightleftharpoons \text{Zn}(\text{g}) + 1/2\text{O}_2(\text{g})$	$K_{\text{ZnO}} = P_{\text{Zn}} P_{\text{O}_2}^{1/2}$	$1.50 \times 10^{10} \exp(-4.89/\text{kT})$	$1.50 \times 10^{10} \exp(-4.89/\text{kT})$
$1/2\text{O}_2 \rightleftharpoons \text{O}_\text{O} + \text{V}_{\text{Zn}}^\times$	$K_\text{O} = [\text{V}_{\text{Zn}}^\times] P_{\text{O}_2}^{-1/2}$	$1.2 \times 10^{17} \exp(-1.9/\text{kT})$	$1.15 \times 10^{16} \exp(-1.86/\text{kT})$
$\text{ZnO}(\text{g}) \rightleftharpoons \text{Zn}_\text{i}^\times + 1/2\text{O}_2(\text{g})$	$K_\text{R} = [\text{Zn}_\text{i}^\times] P_{\text{O}_2}^{1/2}$	$1.6 \times 10^{28} \exp(-5.57/\text{kT})$	$1.56 \times 10^{29} \exp(-5.57/\text{kT})$
$\text{Zn}_{\text{Zn}} \rightleftharpoons \text{Zn}_\text{i}^\times + \text{V}_{\text{Zn}}^\times$	$K_\text{F} = K_\text{O} K_\text{R}$	$1.8 \times 10^{45} \exp(-7.47/\text{kT})$	$1.8 \times 10^{45} \exp(-7.43/\text{kT})$
$\text{O}_\text{O}^\times \rightleftharpoons \text{V}_\text{O}^\times + 1/2\text{O}_2(\text{g})$	$K_{\text{O}_2} = \text{V}_\text{O}^\times P_{\text{O}_2}^{1/2}$	-	-
$\text{Ni}_\text{l} \rightleftharpoons \text{V}_{\text{Zn}}^\times + \text{V}_\text{O}^\times$	$K_\text{S} = K_\text{O} K_{\text{O}_2}$	-	-
$\text{Zn}_\text{i}^\times \rightleftharpoons \text{Zn}_\text{i}^\bullet + e'$	$K_1 = [\text{Zn}_\text{i}^\bullet]_\text{n} / [\text{Zn}_\text{i}^\times]$	$1.2 N_\text{C} \exp(-0.05/\text{kT})$	$1.2 N_\text{C} \exp(-(0.052 - 5.5 \times 10^{-6} \text{T})/\text{kT})$
$\text{Zn}_\text{i}^\bullet \rightleftharpoons \text{Zn}_\text{i}^{\bullet\bullet} + e'$	$K_2 = [\text{Zn}_\text{i}^{\bullet\bullet}]_\text{n} / [\text{Zn}_\text{i}^\bullet]_\text{n}$	$2 N_\text{C} \exp(-0.20/\text{kT})$	$2 N_\text{C} \exp(-(0.207 - 5.5 \times 10^{-6} \text{T})/\text{kT})$
$\text{V}_\text{O}^\times \rightleftharpoons \text{V}_\text{O}^\bullet + e'$	$K_3 = [\text{V}_\text{O}^\bullet]_\text{n} / [\text{V}_\text{O}^\times]$	$1/2 N_\text{C} \exp(-0.50/\text{kT})$	$1/2 N_\text{C} \exp(-(0.331 - 3.5 \times 10^{-5} \text{T})/\text{kT})$
$\text{V}_\text{O}^\bullet \rightleftharpoons \text{V}_\text{O}^{\bullet\bullet} + e'$	$K_4 = [\text{V}_\text{O}^{\bullet\bullet}]_\text{n} / [\text{V}_\text{O}^\bullet]_\text{n}$	$2 N_\text{C} \exp(-2.0/\text{kT})$	$2 N_\text{C} \exp(-(2.066 - 2.2 \times 10^{-4} \text{T})/\text{kT})$
$\text{V}_{\text{Zn}}^\times \rightleftharpoons \text{V}'_{\text{Zn}} + h^\bullet$	$K_5 = [\text{V}'_{\text{Zn}}]_\text{p} / [\text{V}_{\text{Zn}}^\times]$	$1/2 N_\text{V} \exp(-(-0.9 \sim 1.0)/\text{kT})$	$1/2 N_\text{V} \exp(-(-1.033 - 1.1 \times 10^{-4} \text{T})/\text{kT})$
$\text{V}'_{\text{Zn}} \rightleftharpoons \text{V}''_{\text{Zn}} + h^\bullet$	$K_6 = [\text{V}''_{\text{Zn}}]_\text{p} / [\text{V}'_{\text{Zn}}]$	$2 N_\text{V} \exp(-(>2.0)/\text{kT})$	$2 N_\text{V} \exp(-(-2.892 - 3.1 \times 10^{-4} \text{T})/\text{kT})$
$\text{Ni}_\text{l} \rightleftharpoons e' + h^\bullet$	$K_i = np$	$N_\text{C} N_\text{V} \exp(-E_\text{g}/\text{kT})$	$N_\text{C} N_\text{V} \exp(-E_\text{g}/\text{kT})$
	m_e^*	0.28 m_0	0.28 m_0
	m_h^*	0.60 m_0	0.60 m_0
	$E_\text{g} = E_\text{g}(0) - \beta_\text{g} \text{T}$	3.45-3.7 $\times 10^{-4} \text{T}$	3.45-3.7 $\times 10^{-4} \text{T}$

Table 3.1: Defect chemical reactions and related constants for ZnO in the work by Sukker et al. and Han et al. Taken from [53]

pseudopotential W_p (-5.2 eV) is very close to the measured one (-5.3 eV).

As discussed in the part 3.1.2 the dominant defects in ZnO are the oxygen vacancies V_O and zinc interstitials Zn_{Zn} . An important consequence on conductivity can, however, also be brought on by hydrogen. Contrary to the belief that a typical role of hydrogen is the one of an amphoteric impurity [55], i.e. acting as a donor in a p-type doped material by incorporating H^+ and as an acceptor in n-type materials incorporating an H^- it is actually exclusively in a positive charge state and responsible for the n-type conductivity in ZnO.

The electrical conductivity and charge mobility of ZnO are limited by scattering mechanisms [56], including (I) polar-optical-phonon scattering, (II) acoustic-phonon scattering through deformation and piezoelectric potentials and (III) scattering on Coulomb potentials from ionized impurities or defects. At 8 K the conductivity was found to be hopping mediated due to the freezing of carriers, above 40 K the standard statistical model (charge-balance equation) involving conduction only through conduction band has been applicable while the intermediate $15 \text{ K} < T < 40 \text{ K}$ region the transport was the combination of the hopping/conduction

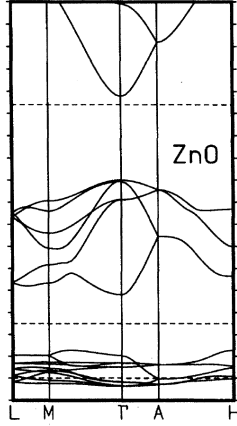


Figure 3.2: The band structure of ZnO as calculated by Vogel et al. [54] using the SIC-PP method (see text). The method slightly overestimates the band gap (3.77 eV calculated as compared to 3.4 eV measured).

band mechanisms.

3.1.4 Applications of ZnO

Applications of zinc oxide are numerous. The dielectric properties of humidity sensors based on $\text{Li}_2\text{O-ZnO}$ [57] have been investigated at frequencies from 1Hz to 1MHz at room temperature. The resistivity was found to be dependent significantly on the relative humidity levels. The mechanism for this behaviour is related to adsorption of water molecules at grain surfaces [58], especially at the Li sites, with hydrogen bonds between adjacent layers of molecular water forming at progressively higher humidity levels. The electronic conduction happens through, primarily, proton hopping.

Among the tetrahedrally bonded semiconductors, ZnO has the highest piezoelectric tensor [59, 60]. In hexagonal wurtzite phase the piezoelectric tensor has three independent components which characterize the full piezoelectric tensor [61]. The polarization induced along the c axis at zero electric field by a uniform strain in the basal plane or along the c axis is measured by two of these components. The value of the induced polarization constant is

$$P_z^{piezo} = \gamma_{33}\epsilon_z + e_{31}(\epsilon_1 + \epsilon_2) \quad (3.1)$$

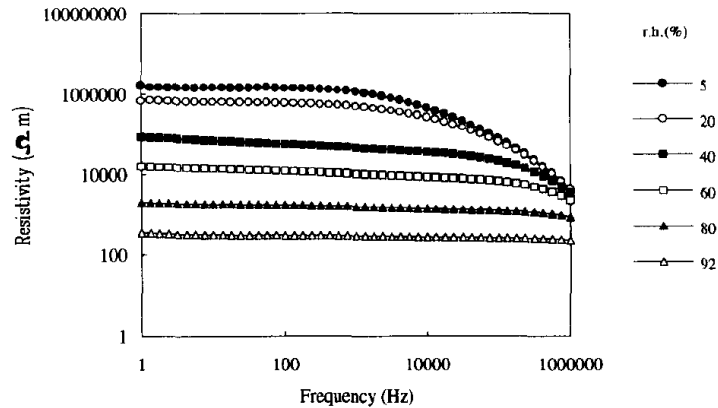


Figure 3.3: The resistivity of gas sensors based on $\text{Li}_2\text{O-ZnO}$ as a function of frequencies for different relative humidity values [57].

Here, $\epsilon_z=(c-c_0)/c_0$ is the strain along the c axis while the $\epsilon_{1,2}=(a-a_0)/a_0$ is the strain in the basal plane, and γ_{33}, γ_{11} are the piezoelectric coefficients. It was found [62] that the piezoelectric constant is strongly sensitive to both temperature and stress (Fig. 3.4). This arises due to a strong hybridization between the O 2p and Zn 3d electrons which is in itself strongly dependent on bond lengths.

3.2 Synthesis methods of TM doped ZnO and DMS

The predicted and experimentally observed high ferromagnetic Curie temperature (T_C) in transition metal doped zinc oxide (TM:ZnO) together with the fact that the host material ZnO is currently being ubiquitously applied in electronics, and in chemical and biosensor applications, make this material one of the most promising compounds for the usage in the fast-growing technology of spintronics. The spatial distribution of the TM ion species within the host semiconductor matrix is essential to the magnetic properties of the system [63]. The physical complexity of real systems due to complicated physics only often makes them too hard of a task for conventional *ab initio* calculations [64]. One has to therefore insist on avoiding TM ion clustering and formation of magnetic nanoprecipitates in actual materials to be as close as possible to the original theory that caused the ongoing vigor in the field.

Different synthesis methods have been applied and will be listed here with their advantages

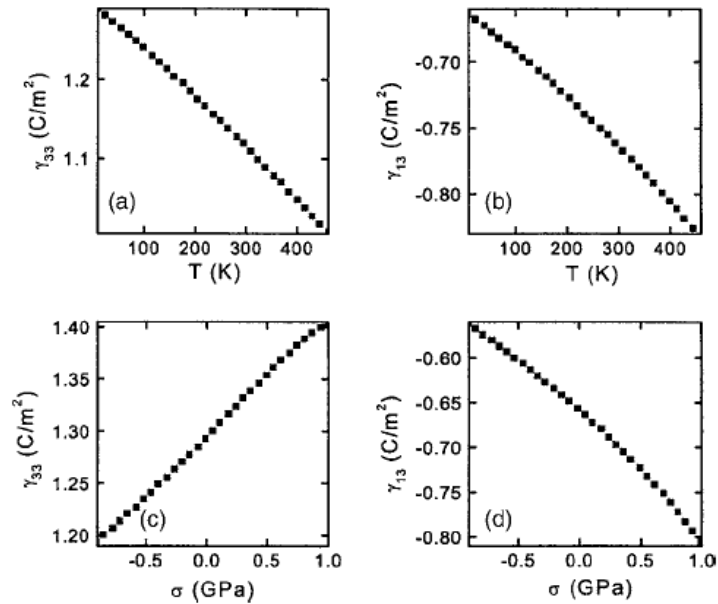


Figure 3.4: The dependence of the piezoelectric constants γ_{33} and γ_{11} on temperature (a) and (b) and stress (c) and (d). Taken from [59].

and their downsides.

3.2.1 Thin films deposition

TM-doped ZnO films are frequently deposited [65] by pulsed laser deposition (PLD) [66], magnetron co-sputtering that can be direct current (dc) reactive [67] and radio-frequency (rf) [68], ultrasonic-assisted solution [69] and plasma enhanced [70], chemical vapor deposition (CVD), combinatorial laser molecular beam epitaxy (laser MBE) [71], ion-beam sputtering [72] and sol-gel methods [73]. A high degree of ambiguity exists in thin films produced by these methods, such as in the example of Co doped ZnO films that alternatively exhibit room temperature ferromagnetism and room temperature paramagnetism, the difference being in the synthesis method, PLD or magnetron sputtering. An example of an epitaxial thin film of $\text{Zn}_{1-x}\text{Mn}_x\text{O}$ ($x \approx 0.25$) grown on (0001) sapphire substrate ($\alpha\text{-Al}_2\text{O}_3$) by pulsed laser deposition technique is given at 3.5. The films were found to be ferromagnetic with the coercive field of 6.2 mT and the saturation magnetic moment of $0.42 \mu_B = 0.42/\text{Mn}^{2+}$ ion at a field of 0.5 T at 10 K.

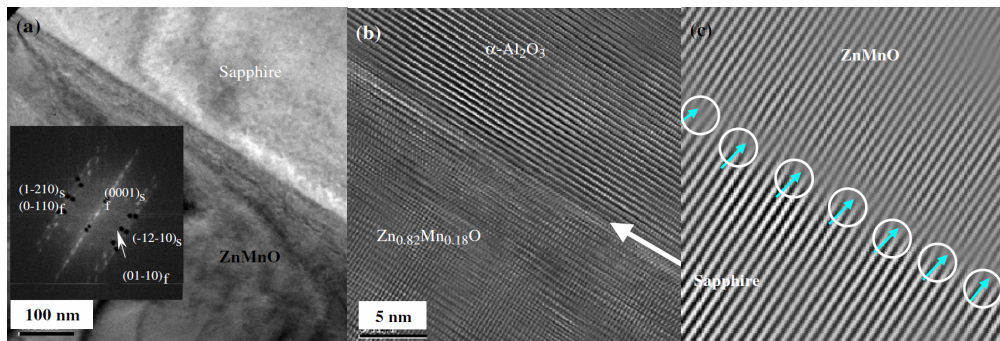


Figure 3.5: The thin films of $\text{Zn}_{1-x}\text{Mn}_x\text{O}$ produced by the pulsed laser deposition method grown on sapphire (Al_2O_3) substrates. Taken from [74].

3.2.2 Solid state reaction methods

Basic solid state reaction, consisting in the heat treatment of ZnO and transition metal oxide at high temperature has been among the first methods used to produce TM doped ZnO. However, the use of high temperature combined with poor homogeneity of the starting mixture yielded the production of inhomogeneous materials. The results of the magnetic properties of materials produced by solid state reaction are therefore controversial. Peiteado et al. [75] studied the reaction between ZnO and MnO_x at different temperatures using the diffusion couple technique. They found that below 973 K no Mn diffusion into ZnO actually occurs, while at the higher temperature Mn^{4+} reduces to Mn^{3+} thereby forming Mn_2O_3 . This substantiates the need to develop synthesis based from homogenous starting materials prepared by low temperature process.

3.2.3 Soft chemistry methods

Numerous soft chemistry processes have been developed to produce at low temperature homogenous precursors aiming at circumventing the diffusion issues of the solid state reaction. As an example, Thota et al. [76] developed zinc oxalate precursors doped with transition metal by adding oxalic acid to ethanolic solution in which Zn and TM acetates have been previously dissolved. This yielded to the gelification of the solution. Once dried, TM doped Zn oxalates are obtained and undergo decomposition to produce TM doped ZnO. Materials obtained by this process have different properties depending on the dopant. In the case of Ni

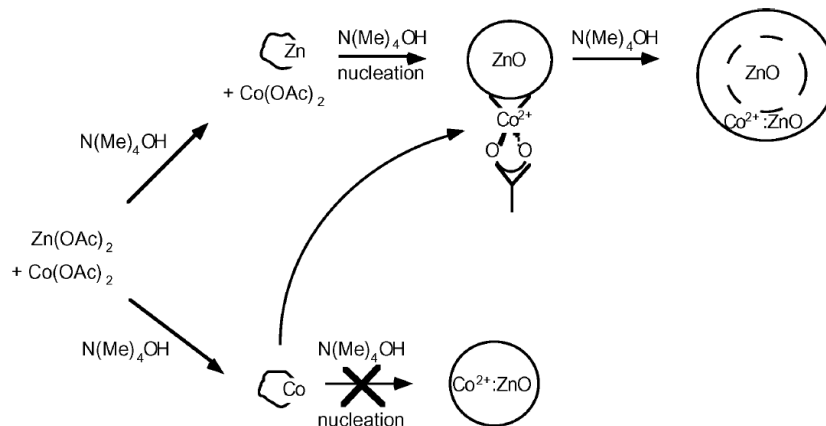


Figure 3.6: The scheme depicting the formation of Co:ZnO in a synthesis by Schwartz et al. [77].

ferromagnetic state was obtained by observing hysteresis loops at 10 K and 320 K. Manganese and cobalt doped ZnO do not reflect any hysteresis loops and their magnetization is found to decrease with Mn or Co content.

Schwartz et al. [77] have developed a method of the preparation of colloidal ZnO-diluted magnetic semiconductor quantum dots by alkaline-activated hydrolysis and condensation of zinc acetate solutions in dimethyl sulfoxide (DMSO). The scheme depicting the formation of Co:ZnO in a synthesis by Schwartz et al. is given in Fig. 3.6.

From the electronic absorption spectra and in the ZnO band gap and Co²⁺ ligand field energy regions of the system collected by titration of 0.2 equivalent aliquots of N(Me)₄OH to a DMSO solution of 98 % Zn(OAc)₂ / 2 % Co²⁺(OAc)₂ the authors conclude that Co²⁺ ions in solution remain octahedrally coordinated until the nucleation of ZnO crystallites. When Co²⁺ ions bind to the nanocrystal surfaces they do so in tetrahedral geometries either as monomers or within basic acetate clusters. Reaction with OH⁻ liberates acetate and yields substitutionally doped Co:ZnO.

Auto-combustion synthesis method have been developed by Deka et al. [78]. High-purity Zn is dissolved in dilute nitric acid and mixed with a water solution of Co(NO₃)₂ · 6H₂O. Glycine is added to the solution which is placed on a hot plate until a thick mass is formed. The final solution which was made by adding water solution of glycine to the solution of the

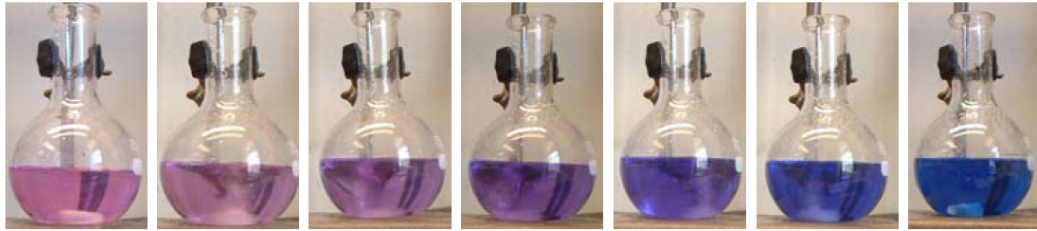


Figure 3.7: Images of colloidal nanocrystals of $\text{Co}^{2+}:\text{ZnO}$ DMS- quantum dots. The increase of OH^- concentration is from left to right. Adapted from the presentation by professor Scott Chambers, held at Krakow, Poland, 9th July, 2009. Part of this image was published in [77].

metal nitrates was subsequently put on a hot plate till it formed a thick mass that subsequently underwent auto-combustion by the exothermic oxidation of the glycine by the nitrates. A fine powder is obtained.

3.2.4 Co-precipitation methods

Bouloudenine et al. [79] reported on the preparation of Co doped Zn oxalate by co-precipitation in aqueous medium. Pink oxalate precursors turned green when exposed to high temperature. Magnetization measurements reveal a paramagnetic behaviour. Numerous different organometallic salts, such as acetates [80] and citrates [81] prepared by co-precipitation have also been used to produce TM doped ZnO. However, for the same nominal composition different types of magnetic behaviour have been observed depending on the decomposition as well as on the choice of the precursor salt used [82].

3.2.5 Drawbacks of the synthesis methods

There are several drawbacks of the synthesis methods which corroborate the inconsistency listed previously in the magnetic properties of TM doped ZnO. The high temperature methods are found to be inadequate in producing single-phase with homogeneously distributed TM species $\text{Zn}_{1-x}\text{TM}_x\text{O}$ [83, 84, 85] often leading to the formation of TM in higher oxidation states and impurities. This is in a big part due to poorly mixed starting materials. As previously mentioned the mixture quality of the starting materials is the key to obtaining homogeneous TM doped ZnO. Although it has been dramatically improved by the use of organometallic

precursors, this is not believed to be adequate. Because of the low intrinsic oxygen content of the organometallic salts, oxygen is usually added to complete the oxidation of organic carbon during the decomposition. However, this can make the TM ions prone to oxidation, in turn leading to the formation of TM rich impurities.

Other drawbacks exist. First, organic precursors undergo multistep decomposition processes, forming intermediate organic salts having dissimilar Zn or TM solubilities compared to the original precursor material(s). Second, the character of different decomposition steps is heavily influenced by environmental factors like the atmosphere, and so can change between endothermic and exothermic [86, 87]. As a result, sample temperature may fluctuate dramatically during the decomposition. The variations of Zn and TM solubility within the organic matrix, combined with temperature fluctuations, can yield chemical gradients within the final products, and, hence, the formation of TM rich impurities.

3.3 Room temperature ferromagnetism in Transition Metal doped Zinc Oxide

The theoretical bases for the ferromagnetism in transition metal doped ZnO has been developed by Dietl et al. [2] who used a theory originally developed for metals by Zener [88, 89].

The thrilling consequence of Dietl's work is the fact that the p-d coupling, the coupling between the magnetic ions and the holes in the host semiconductor in contrast to the s-d coupling between the magnetic ions and the host semiconductor electrons is strong enough to achieve ferromagnetism mediated through holes. The ferromagnetic interactions are in this case sufficiently strong to overcome superexchange induced antiferromagnetic interactions. Spin polarization of localized magnetic moments causes redistribution of holes among spin subbands. The resulting lowering of holes' energy surpasses the increase in the spin-free energy associated with short-range superexchange and spin entropy which, in turn, causes ferromagnetism.

The ferromagnetism was experimentally confirmed in bulk pellets, in transparent films with a thickness of 2-3 μm and in powders of $\text{Zn}_{1-x}\text{Mn}_x\text{O}$ with $x < 4\%$ [83]. An impasse

in the field occurred through a dispute about the real origin of room-temperature ferromagnetism. Unlike the favorable scenario of uniform solution of Mn in ZnO being created at low temperature processing, an explanation favoured by Sharma et al., Kundaliya et al. showed that a metastable ferromagnetic phase forms by diffusion of Zn into Mn oxide, suggesting the $\text{Mn}_{2-x}\text{Zn}_x\text{O}_{3-\delta}$ as the molecular formula of the ferromagnetic compound. Works suggesting intrinsic ferromagnetism, such as in p-doped $\text{Zn}_{1-x}\text{Mn}_x\text{O}$ through doping with nitrogen [90] gave importance to defects as the possible mediators of ferromagnetic interaction [91]. One of the strongest arguments is the possibility to turn the magnetism "on and off", as it was seen in a work by Kittilstved et al. who annealed ZnO successively in Zn vapour and oxygen. Films being alternatively treated in reducing and oxidizing atmospheres showed similar behaviour. The origin of the room temperature ferromagnetism in $\text{Zn}_{1-x}\text{Mn}_x\text{O}$ is therefore not known, despite the abundant literature on the subject.

3.3.1 Theoretical basis for ferromagnetism in TM doped ZnO

The theory of ferromagnetism in (II-VI) and (III-V) semiconductors by Dietl et al. [2] is based on Zener's model of ferromagnetism [88, 92] in (II-VI) $\text{Zn}_{1-x}\text{Mn}_x\text{Te}$ and (III-V) $\text{Ga}_{1-x}\text{Mn}_x\text{As}$. Dietl et al. consider ferromagnetic correlation mediated by shallow acceptors in the ensemble of localized spins in doped magnetic semiconductors. Zener based his theory on three main postulates [88]. As the first one, the incomplete d-shells have the highest possible net electron spin, in accordance with Slater's theory based on the principle that electrons with similar spin automatically avoid close proximity. The second principle it is that the exchange integral between d shells of adjacent atoms is of such a sign that tends to favor antiferromagnetic interactions. The third principle views the strong coupling of an incomplete d shell to the spin of the conduction electrons. The coupling tends to align the spins in a ferromagnetic manner. Zener was of the opinion that the ferromagnetism is possible only when the indirect coupling dominates over the direct coupling between adjacent d shells. The reason why Zener's model was not extensively used in the decades to come was that it was ignoring the itinerant character of the magnetic electrons [2] and the Friedel oscillations of the electron spin polarization around

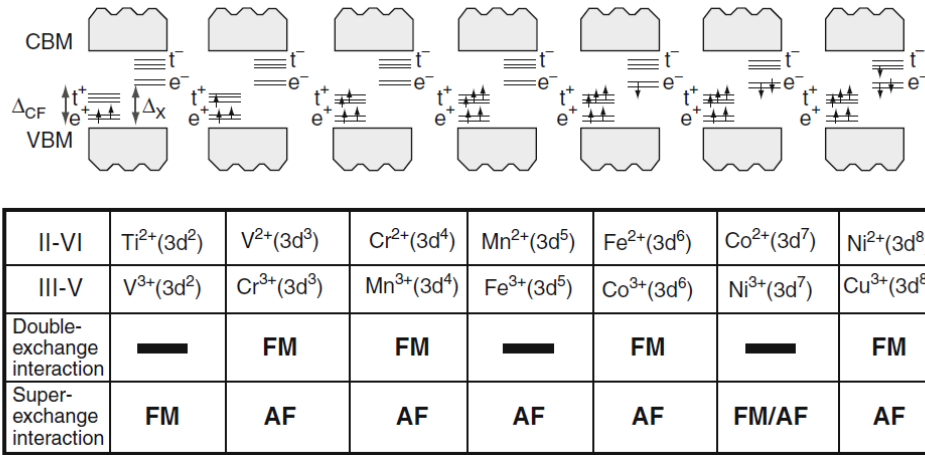


Figure 3.8: Electron configuration of magnetic impurities in diluted magnetic semiconductors with a high-spin ground state. Taken from [93].

the localized spin. Dietl et al. realized that in semiconductors the Friedel effect averages out due to the fact that the mean distance between the itinerant carriers is bigger than the mean distance between the localized spins, Zener model in semiconductors becoming equivalent to the RKKY theory.

Dietl et al. have used the empirical data for $\text{Ga}_{1-x}\text{Mn}_x\text{As}$ as a model for (III)-(V) DMS and $\text{Zn}_{1-x}\text{Mn}_x\text{Te}$ as its (II)-(VI) counterpart. The values of the p-d exchange interaction were taken as $\beta N_0 = -1.1\text{eV} \pm 0.1\text{ eV}$ and $-1.2\text{eV} \pm 0.2\text{ eV}$ for $\text{Zn}_{1-x}\text{Mn}_x\text{Te}$ and $\text{Ga}_{1-x}\text{Mn}_x\text{As}$, respectively. In the equations above β is the p-d exchange integral and N_0 is the concentration of the cation sites. This is the *carrier* contribution to the standard Ginzburg-Landau free-energy functional F , $F_C[M]$. The *localized spins* contribution depends upon the $H(M_0)$, the inverse function of the experimental dependence of the magnetization of the magnetic field H in the absence of the carriers. The Brillouin function, that conveniently parameterizes this dependence, has two input parameters, the effective spin concentration, $x_{eff}N_0 < xN_0$ and $T_{eff} > T$. These two parameters account for the antiferromagnetic superexchange interactions. The determination of the Curie temperature by this model is through determining the competition between the ferromagnetic and antiferromagnetic interactions, with Curie temperature calculated through

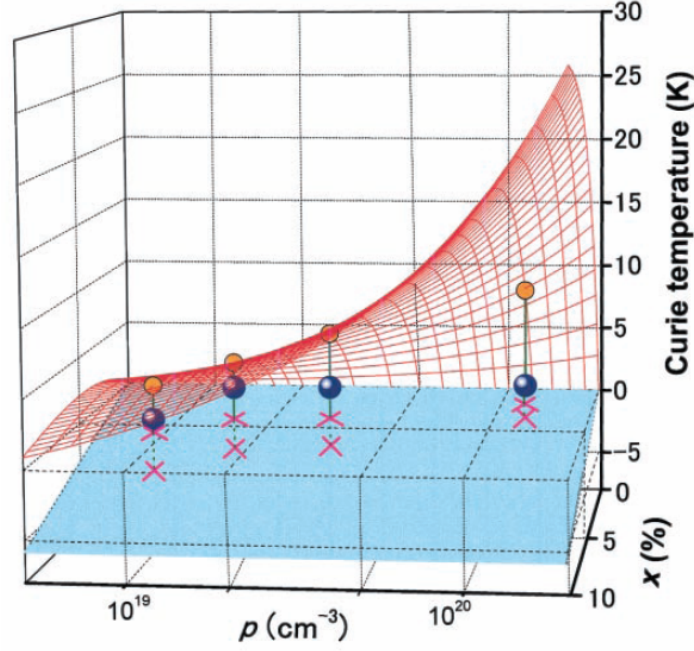


Figure 3.9: Curie temperature T_C in $\text{Zn}_{1-x}\text{Mn}_x\text{Te:N}$ for various Mn contents x and hole concentrations p . Taken from [2].

$$T_C(x) = A_F(x_{eff}/0.05)(\beta N_0[\text{eV}])^2 [N_0(\text{GaAs})/N_0] T_F^{nor} - T_{AF}(x) \quad (3.2)$$

The ferromagnetic interactions are hole-induced. To be more pictorial, see Figure 3.9. The theoretical prediction for the Curie temperatures T_C is given by a red mesh with attached yellow spheres. Two sorts of red crosses delineate the $T_C=0$ plane (upper crosses) and the T_{AF} plane (lower crosses). The experimental values are given by blue spheres. Dietl et al. got a very good agreement between the Curie temperature T_C of the $(\text{Zn,Mn})\text{Te:N}$ except for the samples with the smallest x . In the case of the smallest x the effects of the Friedel oscillations and Kondo correlation could not be neglected.

For the description of electronic states in the vicinity of the Anderson-Mott metal-insulator transition (MIT) the *two-fluid model* is applied. Moving to the insulating direction by increasing disorder, this model assumes that the conversion of itinerant electrons with increasing disorder into singly occupied impurity states occurs gradually. This leads to a separation of

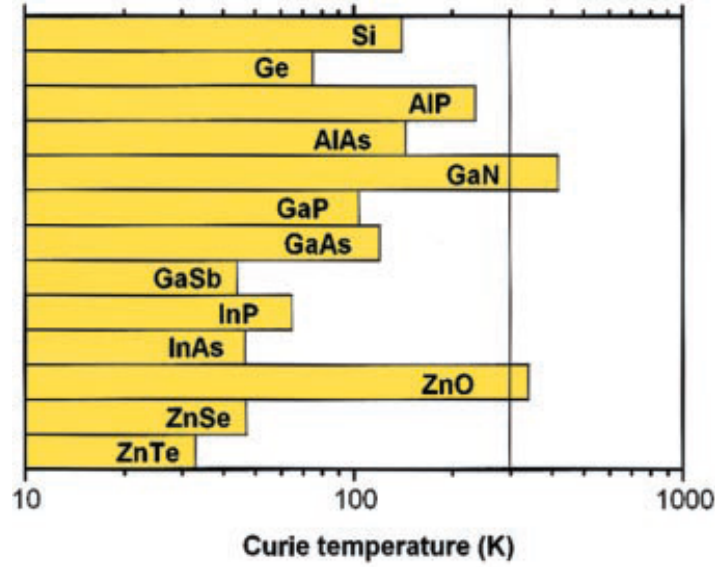


Figure 3.10: Computed values of Curie temperature T_C for p-doped semiconductors with 3.5×10^{20} holes per cm^3 and 5% of Mn. Taken from [2].

the material into a region where electrons are extended states and one in which electrons are in singly occupied impurity-like states. However, the extended states electrons are becoming localized only gradually, leaving the wave function having an extended character within the localization radius ξ . It is thought that the weakly localized states are at the origin of the static longitudinal and Hall conductivities of doped semiconductors. The singly occupied impurity-like states are controlling the magnetic response of doped non-magnetic semiconductors, giving the rise to *bound magnetic polarons* in magnetic semiconductors on both sides of the MIT transition.

Laying firmly on the aforementioned principles, the authors suggested holes in the extended or the weakly localized states to mediate the long-range interaction between the localized spins on both sides of the MIT. The values of T_C calculated for various semiconductors at the doping of 5% of Mn and 3.5×10^{20} holes per cm^3 are given in the Fig. 3.10.

The authors assumed the same value of $\beta = \beta(\text{GaMnAs})$ for all the group (IV) and all the III-V semiconductors. The β was also found to scale as a_0^{-3} where a_0 is the lattice constant. This is a trait common for the II-VI semiconductors. From the Fig 3.10 it is clear that the T_C is higher than room temperature for GaN and ZnO and that the lighter elements seem

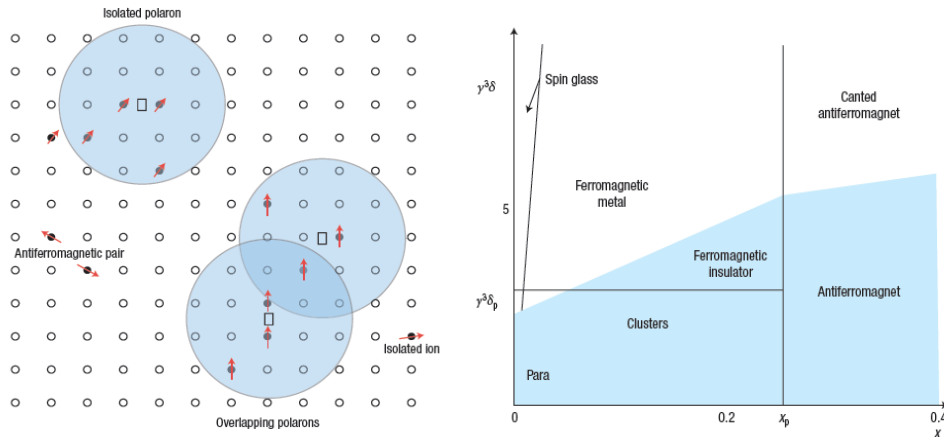


Figure 3.11: The magnetic phase diagram for diluted ferromagnetic semiconductors. Taken from [94].

to be more prone to the occurrence of high-temperature ferromagnetism. This can be readily understood by noticing that the p-d hybridization is stronger and the spin-orbit coupling is weaker in these materials.

Electron configuration of magnetic impurities in DMS in a high-spin ground state is given at the Fig 3.8. As mentioned in Section 2.1.1, for the high-spin to be the ground energy state, the exchange splitting has to be larger than the crystal field splitting between t_{2g} and e_g orbitals. The double-exchange mechanism stabilizes the ferromagnetic state by the kinetic energy gain of electron or hole hopping. The superexchange contribution is effectively defined by the Goodenough-Kanamori rules (see Section 2.1).

A theory for high k dielectrics, diluted ferromagnetic oxides, was developed by Coey et al. [94]. Coey proposed that the ferromagnetic exchange is mediated by shallow donor electrons that form bound magnetic polarons that overlap to create a spin-split impurity band. He further postulated that high Curie temperatures arise only when empty minority-spin or majority-spin d states lie at the Fermi level in the impurity band. He considered that an electron associated with a particular donor defect will find itself in a hydrogenic orbital of radius $r_H = \epsilon(m/m^*)a_0$ where ϵ is the high-frequency dielectric constant, m is the mass of the electron, m^* is the mass of the donor electron and a_0 is the Bohr radius. As the donor concentration δ is increased the $1s$ orbitals $\psi(r) = (\pi r_H^3)^{-1/2} \exp(-r/r_H)$ overlap to form

an impurity band. After a critical donor concentration n_{\square}^{crit} the impurity band states become delocalized and metallic conduction sets in. The critical donor concentration is given by $(n_{\square}^{crit})^{1/3}r_H \cong 0.26$. The corresponding value of $\delta^{crit} = n_{\square}^{crit}/n_O$. Here, the oxygen density is given for oxides with a close-packed oxygen lattice. This gives finally

$$\gamma^3 \delta^{crit} \cong 2.2 \quad (3.3)$$

Here, radius of the orbital is $r_H = \gamma a_0$, where $\gamma = \epsilon(m/m^*)$. The bound magnetic polarons are created to form from the donor ions, whereby the $3d$ moments of the TM ions are coupled within their (donor) orbits. As x increases the cations present an extra random potential which extends the localized region as x increases. When the radius of the donor orbital is sufficiently large there occurs a ferromagnetic exchange coupling between the donor electron and the TM ion electron which is known as the s - d exchange, given by

$$-J_{sd} \mathbf{S} \cdot \mathbf{s} (|\psi(r)|)^2 \Omega \quad (3.4)$$

Here \mathbf{S} is the spin of the $3d$ cations that have volume Ω , while \mathbf{s} is the donor electron spin. The coupling between the cation and the donor electron is ferromagnetic when the $3d$ shell is less than half full, and antiferromagnetic when the $3d$ shell is half full or more. The coupling between two TM impurities is in either case ferromagnetic. With the increase in n_{\square} , assuming the hydrogenic orbitals are spherical, the percolation will occur when the orbitals take up $\approx 16\%$ of space. Expressing the above in terms of $\delta = n_{\square}/n_O$ the appearance of long range ferromagnetic order is expected for $\gamma^3 \delta_p \cong 4.3$. Taking δ_p and x_p as parameters the ferromagnetism occurs when $\delta > \delta_p$ and $x < x_p$. When $x > x_p$ the antiferromagnetism or ferrimagnetism can appear due to the continuous nearest-neighbour paths interacting antiferromagnetically appearing through the crystal.

Coey further develops the model by assuming that the DMS system is analogous to a Néel two-sublattice magnet, one sublattice being composed of dopant cations and the other of donor electrons. The main result for the ferromagnetic ordering temperature T_C is

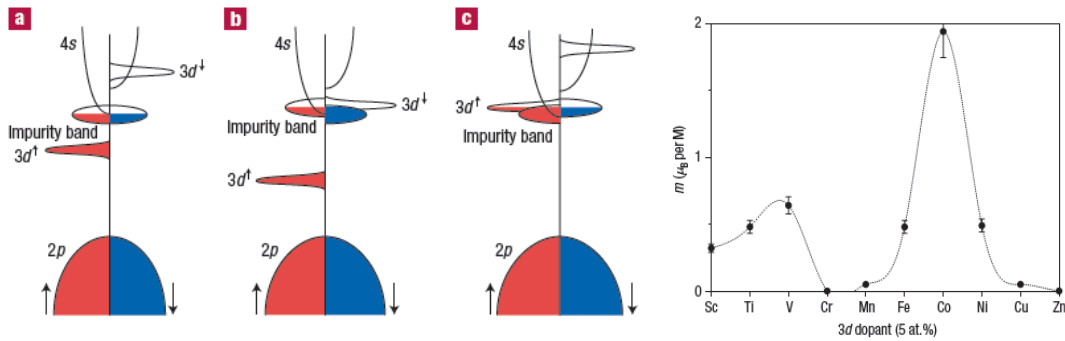


Figure 3.12: Left: The proposed model to explain the high temperature ferromagnetism of diluted magnetic oxides of the 3d series. Right: The magnetic moment of the $\text{Zn}_{1-x}\text{TM}_x\text{O}$ films produced by pulsed laser deposition, measured at room temperature. Taken from [94].

$$T_C = [\mathbf{S}(\mathbf{S} + 1)s^2x\delta n/3]^{1/2} J_{sd}\omega_c/k_B \quad (3.5)$$

Here ω_c is the product of cation/anion volume ratio. The T_C for a typical case, Co doped ZnO can be calculated by introducing $n = 1$, $n_O = 6.10^{28} \text{ m}^{-3}$, $x = 0.1$, $\mathbf{S} = 3/2$, $\mathbf{S} = 1/2$, $r_c = 0.06 \text{ nm}$ and $\delta = 0.01$. J_{sd} can be established from the red shift of the band gap with the cobalt doping to be 1.5 eV.

Calculated, this amounts to T_C of 18 K, an order of magnitude too low to explain the observed high-temperature ferromagnetism in $\text{Zn}_{1-x}\text{Co}_x\text{O}$. The only way that the T_C can increase is if the donor electron density ($|\psi(r)|^2$) is increased in the vicinity of the magnetic impurities. Translated to the band energy scheme, empty 3d states, i.e. $3d_{\downarrow}$ in the case of the $3d^7$ impurity ($\mathbf{S} = 3/2$) have to hybridize with the donor states at the Fermi level. As moving along the 3d series the d-levels move down in energy approaching the oxygen 2p band there are two opportunities for hybridizing to happen (1) at the beginning of the series when $3d_{\uparrow}$ hybridize with the impurity band and respectively, (2) at the end of the series when $3d_{\downarrow}$ crosses the Fermi level. The authors have confirmed this by observing peaks in magnetic moments for Ti, V and Co members of the 3d series.

Sato et al. [6] have used the local spin density approximation methods to study the stability of the ferromagnetic state of Mn doped ZnO. The results are shown in the Fig. 3.13. The p-doping of $\text{Zn}_{1-x}\text{Mn}_x\text{O}$ was simulated by adding N to the superlattice, while the Ga was

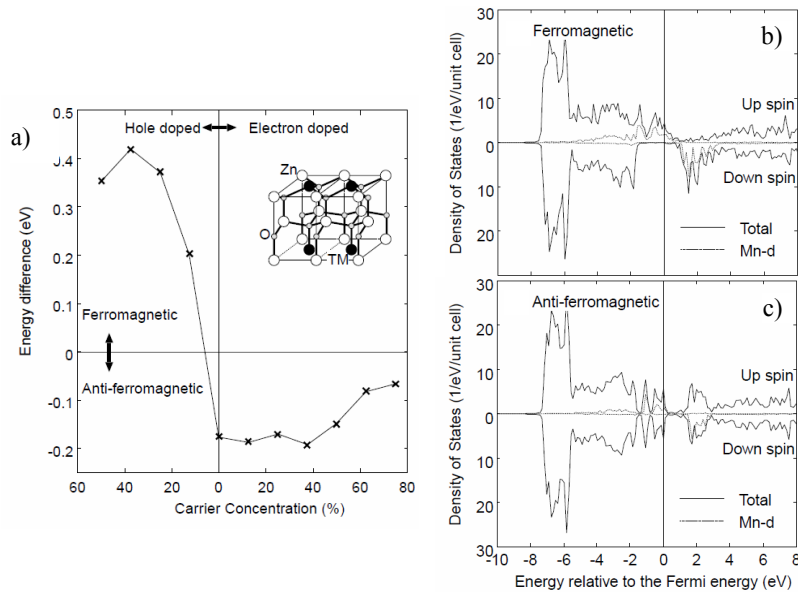


Figure 3.13: Stability of the ferromagnetic state in Mn doped ZnO as a function of the carrier concentration (a). Calculation of the local spin density of states for the ferromagnetic (b) and anti-ferromagnetic (c) configuration. Taken from [6].

used to simulate n-doping.

In Fig. 3.13(a) the difference in energy $E(\text{antiferromagnetic configuration}) - E(\text{ferromagnetic configuration})$ was plotted as a function of hole (N) doping or electron (Ga) doping of $\text{Zn}_{1-x}\text{Mn}_x\text{O}$. Stability of the ferromagnetic state is evident for the ferromagnetic configuration of the system. The doping of ZnO with Mn does not introduce carriers into the system so the system is expected to be anti-ferromagnetic in this case. With the addition of holes into the system the system becomes ferromagnetic. The origin of ferromagnetism is illustrated in Fig. 3.13(b). The spin-up 3d states of Mn hybridize well with the N 2p (hole) states at Fermi energy, while the spin-down 3d states are strongly exchange split and are too far in energy to hybridize with the p states of N. The half-metallic ferromagnetic state is realized with spins at the Fermi energy being exclusively in one spin (up) polarization. In the anti-ferromagnetic case Fig. 3.13(c) the most important difference from the ferromagnetic case is the fact that the Mn spin-up and spin-down electrons have equal DOS at Fermi energy.

3.3.2 Observations of intrinsic ferromagnetism

One of the landmark works in favour of the intrinsic ferromagnetism in TM doped ZnO is the work by Kittilstved et al. [95] who observed that addition of nitrogen to $\text{Zn}_{1-x}\text{Mn}_x\text{O}$ induces strong 300 K ferromagnetism, while the ferromagnetism was suppressed for $\text{Zn}_{1-x}\text{Co}_x\text{O}$ in accordance with theory that predicts ferromagnetism in p-type doped $\text{Zn}_{1-x}\text{Mn}_x\text{O}$ and n-type doped $\text{Zn}_{1-x}\text{Co}_x\text{O}$. The addition of nitrogen/oxygen was induced by the following procedure. The capping with oxygen was achieved through treatment of as-prepared $\text{Mn}^{2+}:\text{ZnO}$ nanocrystals with trioctylphosphine oxide (TOPO)/stearyl phosphate. TOPO is actually R_3PO , with R being C_8H_{17} . N capped samples were produced by treating the nanocrystals with dodecylamine ($\text{R}'\text{NH}_2$, $\text{C}_{12}\text{H}_{25}$ represented by R') instead of TOPO, yielding a clear suspension of amine-capped nanocrystals. N-capped colloids were ferromagnetic in the case of $\text{Mn}^{2+}:\text{ZnO}$ and paramagnetic for $\text{Co}^{2+}:\text{ZnO}$. The exactly opposite magnetic signature was observed for O-capped colloids (paramagnetic for Mn, ferromagnetic for Co). The strongest part of the message of the work by Kittilstved et al. is shown in the right part of the Figure 3.14. It regards the external "ex-situ" treatment of nanocrystals. This consisted of n-perturbation which was done by exposing the sample to Zn vapor, resulting with Zn interstitials in the structure, Zn_i a known shallow donor, i.e. n-dopant. The p-perturbation consisted of absorbing the N containing molecules directly on the surface of the doped ZnO film. The N containing molecules were deposited in form of 0.1 mL of 0:5M $\text{Zn}(\text{NO}_3)_2/\text{R}'\text{NH}_2$ (1:1) in ethanol. The p-perturbation was found to induce the ferromagnetism in $\text{Mn}^{2+}:\text{ZnO}$ and paramagnetism in $\text{Co}^{2+}:\text{ZnO}$, while the n-perturbation favoured the ferromagnetism in $\text{Co}^{2+}:\text{ZnO}$ and paramagnetism in $\text{Mn}^{2+}:\text{ZnO}$. This is in perfect agreement with the theory [6, 7].

Another interesting work in favour of intrinsic ferromagnetism in $\text{Zn}_{1-x}\text{TM}_x\text{O}$ occurred through work on free-standing nanocrystals of $\text{Zn}_{1-x}\text{Mn}_x\text{O}$ by Ochsenbein et al. [96]. The authors generated conduction band electrons e_{CB}^- through anaerobic ultraviolet (UV) photoexcitation. From the Figure 3.15 (a) it is clear that in $d=5.6\text{nm}$ 0.25% $\text{Mn}^{2+}:\text{ZnO}$ nanocrystals the Mn^{2+} hyperfine structure broadens upon charging, i.e. the introduction of e_{CB}^- . ESR signal of the oxidized (as prepared) system is given as a red line and the signal of the system

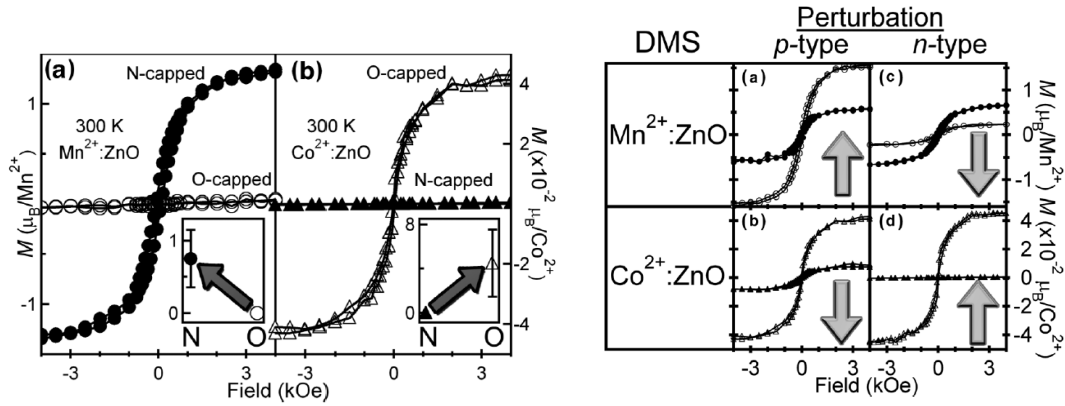


Figure 3.14: Left: 300 K magnetization vs field loops for (a) 0.20% $\text{Mn}^{2+}:\text{ZnO}$ and (b) 3.5% $\text{Co}^{2+}:\text{ZnO}$ films prepared from N-capped or O-capped colloids. Insets: statistics for 300 K ferromagnetic saturation moments obtained from 10 independent films for each case. Right: 300 K magnetization vs field loops for 0.20% $\text{Mn}^{2+}:\text{ZnO}$ and (b) 3.5% $\text{Co}^{2+}:\text{ZnO}$ films before and after various n- or p-type perturbations. Arrows indicate the increase (up) or decrease (down) of 300 K ferromagnetism upon perturbation. Taken from [95].

in which e_{CB}^- have been photoinjected is given as the blue line. The re-oxidized system is presented with a dotted grey line. The broadening is due to the $\text{Mn}^{2+} - e_{CB}^-$ exchange interaction and not to the superposition of the signals of Mn^{2+} and e_{CB}^- . As the authors suggest, the ESR spectra do not show superimposed sharp and broad Mn^{2+} features, hence all the Mn^{2+} ions are affected by the added electrons. It is demonstrated further that upon exposure to air, the oxidation reverts the ESR spectra to their original shape. The oxidation/regeneration process has been shown to occur in a multitude occasions with no degradation to the sample. The spectra are also shown in the ESR absorption mode (Fig. 3.15 (b)).

To corroborate these results using an alternative measurement technique the authors used SQUID to measure the magnetization data for the 0.25% $\text{Mn}^{2+}:\text{ZnO}$ nanocrystals in the 2 - 300 K temperature interval. The results are given at Fig. 3.15 (c). Magnetization of the as-prepared (red triangles), charged (filled blue triangles) and the difference of magnetization between charged and as-prepared samples (filled blue diamonds) is given. The magnetic moment before charging was shown to be $3.4 \mu_B$, significantly under $5 \mu_B$ expected if all the Mn^{2+} contributed. The nominal antiferromagnetic superexchange interaction is active within nearest-neighbour $\text{Mn}^{2+}-\text{Mn}^{2+}$ pairs. As outlined before the Heisenberg-type dimer

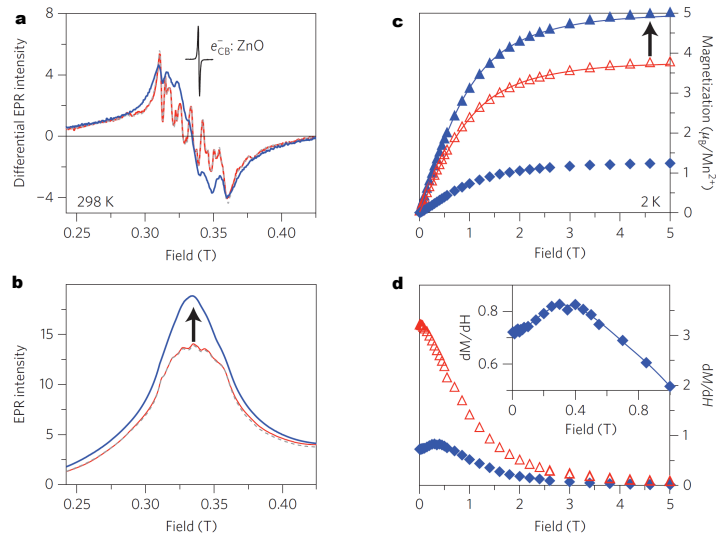


Figure 3.15: Reversible charge controlled ferromagnetism in free-standing $\text{Mn}^{2+}:\text{ZnO}$ nanocrystals. Derivative-mode (a) and absorption-mode (b) EPR spectra of as-prepared (solid red line), photochemically charged (solid blue line) and re-oxidized (dotted grey line) colloidal $\text{Mn}^{2+}:\text{ZnO}$ nanocrystals (with diameter $d=5.6$ nm and Mn^{2+} concentration $x=0.25\%$, 298 K). (c) Field dependence of the magnetization of as-prepared (open red triangles) and charged (filled blue triangles) colloidal $\text{Mn}^{2+}:\text{ZnO}$ nanocrystals ($d=5.6$ nm, $x=0.25\%$, 2 K). The activated fraction (filled blue diamonds) is the difference between the magnetization of the charged and the as-prepared nanocrystals. (d) The numerical derivative dM/dH of the as-prepared (open red triangles) and the activated fraction (filled blue diamonds) of the $\text{Mn}^{2+}:\text{ZnO}$ nanocrystals. The expanded low-field region of the activated fraction is shown in the inset. Taken from [96].

spin Hamiltonian can be described by

$$H = -2J\mathbf{S}_1 \cdot \mathbf{S}_2 \quad (3.6)$$

As the J is of the order of some $30 \text{ J} \approx 48 \text{ meV}$, hence Mn^{2+} in dimers are not expected to contribute to the magnetic moment measured expected in the room-temperature X-band ESR scans or even at $2 \text{ K} / 5 \text{ T}$ measurements. Upon studying the effect for several concentrations ranging up to 0.4% of Mn the authors conclude that the addition of Mn decreases the relative ESR intensity through formation of higher number of antiferromagnetic dimers, yet charging with e_{CB}^- always reverted the ESR intensity to the maximum expected, i.e. $5 \mu_B$. The typical energy of the s-d ($\text{Mn}^{2+} - e_{CB}^-$) interaction energy is shown to be $+0.19 \text{ eV}$ which translates to a J_{FM} of about 0.01 eV per unpaired electron. This is about 2 orders of magnitude lower than what is estimated to be J_{FM} in the system deduced from the inflection point in dM/dH measured curves (details in [96]). In Fig. 3.15(d) the differential magnetization of the as-prepared (red triangles) and charged (filled blue diamonds) is given. The inset is the zoom of the low-field region for the charged sample. The authors presented a model that takes into account ferromagnetic interactions between distant Mn^{2+} ions amounting to a correct J_{FM} . The work by Ochsenbein et al. [96] is hence in favour of the reversible charge controlled magnetism in free-standing colloidal nanocrystals.

3.3.3 Observations of extrinsic ferromagnetism

As outlined in the section 3.3 Sharma et al. [83] have observed ferromagnetism in different forms of $\text{Zn}_{1-x}\text{Mn}_x\text{O}$. They have used low temperature processing of MnO_2 - ZnO mixture as the synthesis method for producing $\text{Zn}_{1-x}\text{Mn}_x\text{O}$. They have observed ferromagnetic signature in 2% $\text{Zn}_{1-x}\text{Mn}_x\text{O}$ pellets with a ferromagnetic Curie temperature $T_C > 420 \text{ K}$ in samples sintered below 700°C . Although very small, a hysteretic effect was observed in samples produced below $T < 700^\circ\text{C}$. Room-temperature $-10 \text{ kOe} - 10 \text{ kOe}$ sweeps performed in SQUID are given in Fig. 3.16. Along with hysteresis in samples produced below 700°C one can observe that above 900°C the hysteresis disappears. Additionally, the sample produced at 900°C was

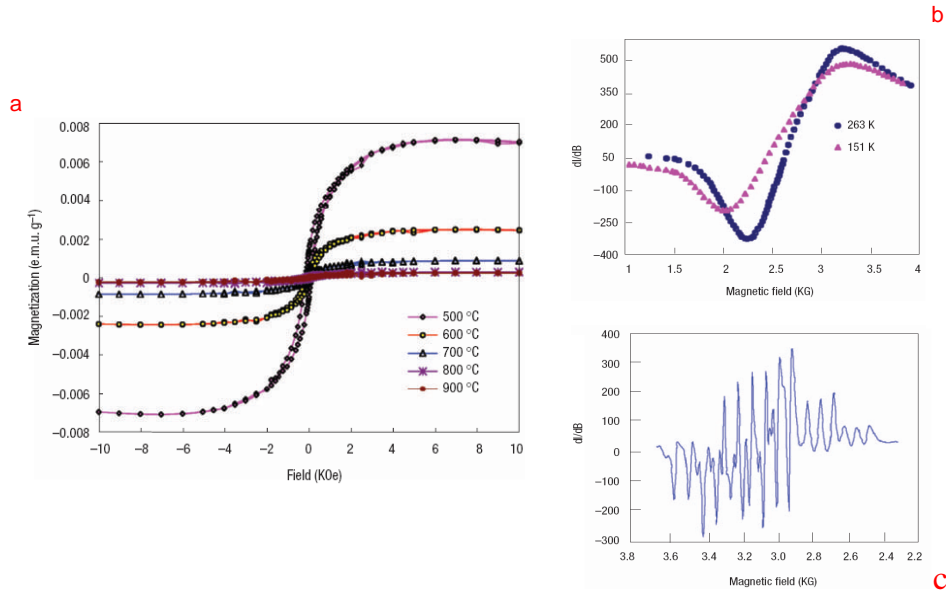


Figure 3.16: (a) The field sweep of Mn:ZnO bulk materials revealing ferromagnetic signatures in samples produced below 700°C curves in the work by Sharma et al. [83] (b) A broad FMR line with g-factor higher than the free electron value as a proof of ferromagnetism of $Zn_{1-x}Mn_xO$ synthesized at 500°C (c) A signal of paramagnetic Mn^{2+} in the sample synthesized at 900°C. Adapted from [83].

found to have T_C of 40 K. The authors suggested that the formation of antiferromagnetic Mn clusters is to be responsible for the disappearance of ferromagnetism at sintering temperature higher than 700°C. To corroborate this hypothesis, the authors performed ferromagnetic resonance - FMR measurement on samples sintered below and above 700°C. In the absence of detailed analysis, the authors were content to state that the paramagnetic signal observed for the 900°C was reminiscent of Mn^{2+} (Fig 3.16(c)). The 500°C signal showed a line with g-factor different from the free electron value even at 425°C (Fig 3.16 (b)), the maximum temperature they were able to use, pointing to the ferromagnetism in the sample with T_C higher than 425°C. The authors claimed to have measured a very small low Mn mean concentration of only 0.3 at.% instead of the nominal 2 at.%

The work by Kundaliya et al. [85] tried to explain the results obtained by Sharma et al. [83] through a significantly more detailed sample analysis. They were able to demonstrate, that the ferromagnetism in samples produced in almost the exact same way as in [83] originates as a signature of a metastable $Mn_{2-x}Zn_xO_{3-\delta}$ and not of Mn homogeneously distributed in

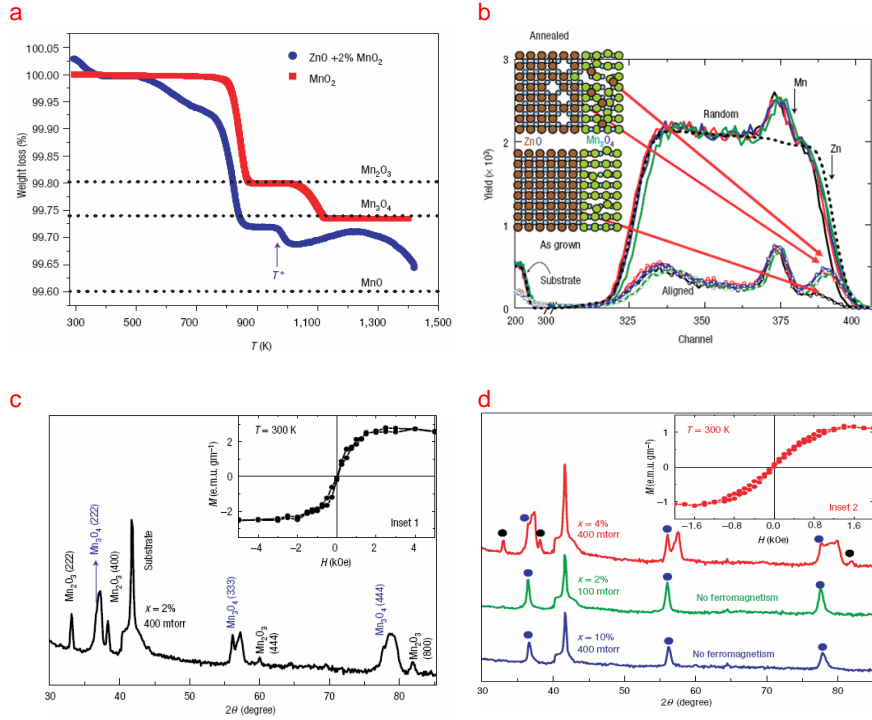


Figure 3.17: Identification of $\text{Mn}_{2-x}\text{Zn}_x\text{O}_{3-\delta}$ as the ferromagnetic phase in $\text{Zn}_{1-x}\text{Mn}_x\text{O}$ samples. See text. Taken from [85].

ZnO. By performing thermo-gravimetric analysis on a ZnO - 2% MnO₂ powder mixture they have observed a signal indicated as a blue line in the Figure 3.17. The red curve, the referent MnO₂ signal experiences three plateaus in 300 K < T < 1500 K regime. The first plateau represents MnO₂ while the second and third plateau represent the material present after the transformation of the original MnO₂ to Mn₂O₃ at 809 K and Mn₃O₄ at 1040 K, respectively. The descent of the blue curve, referring to 98 % ZnO with 2% of MnO₂, which begins around 450 K is due to the loss of oxygen upon incorporation of Zn into Mn⁴⁺ sites in MnO₂, because of the principle of charge neutrality. At 780 K the blue curve experiences a sharp drop with the weight loss stabilizing itself just below the value for Mn₃O₄. At 980 K, the temperature at which the magnetization of the system disappears, another drop is present, this time followed by an intake of oxygen, resulting in an decrease of the value of the weight loss again. Realizing that with introduction of Zn²⁺ into Mn₂O₃ matrix one loses half oxygen atom per Zn atom and furthermore, taking into account the fact that if one removes one oxygen per three molecular

units of Mn_2O_3 one obtains a Mn_3O_4 , the authors suggested that the ferromagnetic phase is indeed $\text{Mn}_{2-x}\text{Zn}_x\text{O}_{3-\delta}$ that at T^* transforms into a non-magnetic Mn_3O_4 phase.

In a different experiment Kundaliya et al. deposited Mn_3O_4 on a ZnO surface and then post-annealed the system for 3h, 9h and 18 hours. They have noticed that the RBS signal did not resemble the signal of Mn homogenously distributed in ZnO in every sample, even after the longest time of annealing. The worsening of the ZnO ion channeling in the top surface layers of ZnO together with broadening of the surface profile outwards Mn_3O_4 data indicate diffusion of around 10%-15% of Zn into Mn_3O_4 matrix. The fact that most of the decrease of channeling is noticed in the early, and not in the late stages of the heat-treatment corroborates the diffusive mechanism, i.e. diffusion of and solubility limitation of Zn into Mn_3O_4 matrix. The ferromagnetic components were the 3h and 9h annealed ones, while the 18 hours one showed a decrease in magnetization probably due to the increase in Zn concentration or oxygen related transformations from the surface side of the thin film. This is a proof that ferromagnetism is not caused by a homogenous distribution of Mn in ZnO but Zn diffusing into Mn oxide.

The final nail to the coffin of the work of Sharma et al. was put by an experiment in which the authors using thin films produced from $\text{Zn}_{3-x}\text{Mn}_x\text{O}_4$ sintered at high temperatures probed the magnetism of samples with Mn introduced into the sample during the thin film deposition. As a summary, ferromagnetic signals were observed only in the condition of low Zn concentration / high oxygen pressure and only in the cases when Mn_2O_3 was present in the structure (shown as black circles at the Fig 3.17, while blue circles represent Mn_3O_4 reflections). The Mn_2O_3 reflections in ferromagnetic samples confirm $\text{Mn}_{2-x}\text{Zn}_x\text{O}_{3-\delta}$ as the ferromagnetic phase, while Zn doped Mn_3O_4 do not exhibit ferromagnetic properties.

3.3.4 Conclusion

The purpose of this Chapter was to get acquainted with the basic properties underlying ZnO, our host semiconductor. The basic energy band scheme, the chemistry of defects, the most common applications have been laid out. The basic theoretical predictions regarding the high temperature ferromagnetism in ZnO have been introduced, especially focusing on the different

predictions for n-doped and p-doped ZnO. The main subgroups of the synthesis methods of TM doped ZnO have been listed. Finally, recently observed ferromagnetic signatures as well as the different camps of thought regarding the intrinsic nature of the ferromagnetism have been elucidated.

Chapter 4

Synthesis and properties of transition metal doped ZnO precursors

As outlined in the previous Chapters, the past decade, the first in the development of the $\text{Zn}_{1-x}\text{TM}_x\text{O}$ has seen difficulties in the production of single-phase materials, with well characterized intermediate and final products. We have found that the use of inorganic precursors like nitrates or carbonates for the synthesis of TM doped ZnO offers unique opportunities over existing synthesis processes. In this Chapter, we report on the synthesis of the precursors as well as on their characterization.

4.1 TM doped zinc nitrates

Transition metal doped zinc nitrates offer an interesting precursor for the $\text{Zn}_{1-x}\text{TM}_x\text{O}$ synthesis due to their low melting temperatures (Table 4.1) , low cost and simplicity of usage. The steps of the synthesis of TM doped zinc nitrates are illustrated in the Fig. 4.1. Typically, transition metal doped zinc nitrates are synthesized by mixing stoichiometric ratios of $\text{TM}(\text{NO}_3)_2 \cdot x\text{H}_2\text{O}$ and $\text{Zn}(\text{NO}_3)_2 \cdot x\text{H}_2\text{O}$ hydrated nitrates , melting the nitrates at temperatures close to 100°C in order to get a homogenous liquid mixture of the nitrates. Such a homogeneity is preserved by quenching the solution with liquid nitrogen. This results in a powder that we refer to as transition metal doped zinc nitrate precursor, $\text{Zn}_{1-x}\text{TM}_x(\text{NO}_3)_2 \cdot x\text{H}_2\text{O}$. The color

Material	Melting point (°C)
Zn(NO ₃) ₂	105
Mn(NO ₃) ₂	116
Co(NO ₃) ₂	75

Table 4.1: The melting temperatures of TM doped nitrates used in this study.

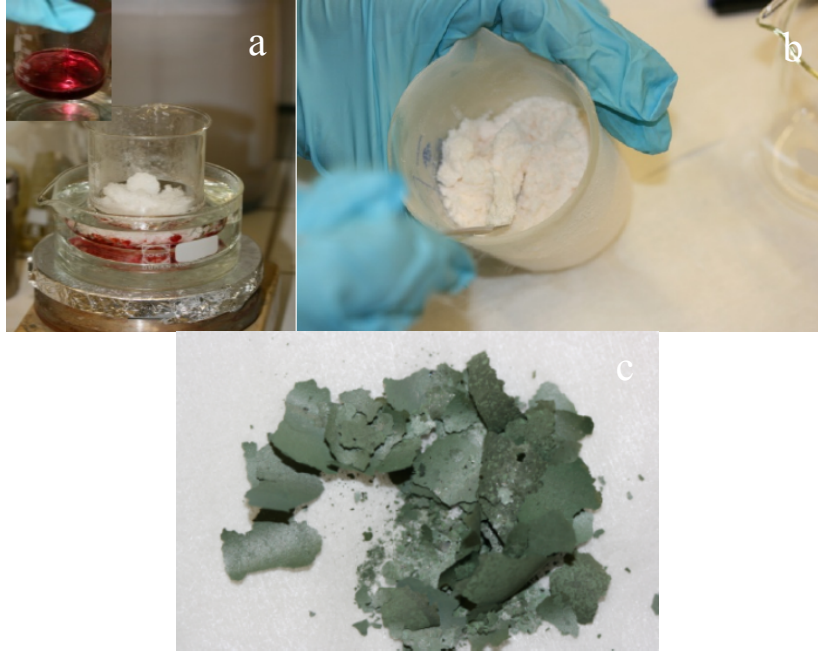


Figure 4.1: Three steps of $Zn_{1-x}TM_xO$ synthesis from nitrate precursors: (a)melting, (b)quenching and (c)thermal decomposition, here shown for $TM=Co$.

of the powders is whitish, with a slight tint corresponding to the dopant, being yellow for Mn and red for Co.

The homogeneity of the distribution of Mn within the nitrate matrix was inferred through Electron Spin Resonance measurements. The ESR measurements were performed using a standard X-band ($\nu \approx 9.4GHz$) Bruker spectrometer in the field ranging from 100 G to 12000 G. The signal of the Mn doped nitrate precursors is given in Fig 4.2. The paramagnetic Mn^{2+} ion has a half-filled d-shell ($S=5/2$) with an orbital quantum number equal to $L=0$ (${}^6S_{5/2}$) and a nuclear orbital quantum number equal to $I=5/2$, giving a spectrum of 30 lines (5 fine structure lines each separated into 6 hyperfine structure lines). The central six lines due to $|-1/2,m\rangle - |1/2,m\rangle$ transition are normally the lines with the strongest intensity. One observes

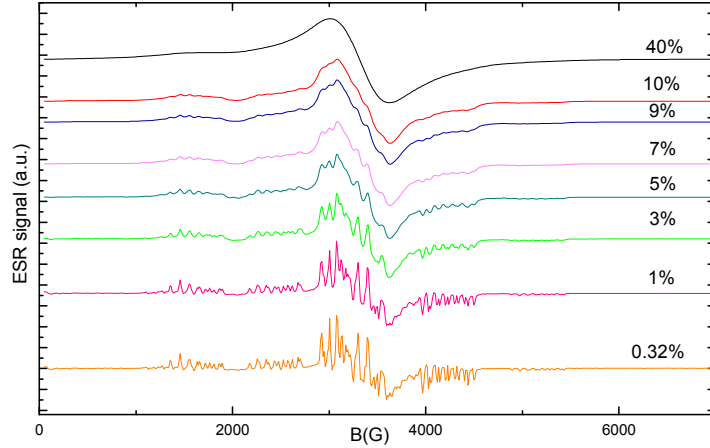


Figure 4.2: Electron spin resonance measurements on the series of Mn doped Zn nitrate precursors with Mn content from 0.32% to 40% .

in Figure 4.2 such a spectrum of Mn^{2+} . A series of narrow lines attributed to the hyperfine structure of the Mn^{2+} was observed in the span of 1000 G to 5600 G. It persists down to approximately 10% percent of Mn:nitrate and gets gradually "washed away" as the proportion of the non-interacting, paramagnetic centers goes to zero. The similar effect was seen in the studies on Mn doped materials [97, 98, 99]. More recent work and spectra simulations can be found in the work of Chikoidze et al. [100]. As the hyperfine structure persists up to almost 10% of Mn we can estimate that the precursor is homogeneous for concentrations as high as 10 percent, at higher concentrations Mn ions starting to interact due to the higher statistical probability of encountering Mn ions at close distances.

In electron spin resonance, the selection rule is $\Delta m_J = \pm 1$, which is the dipole selection rule. The $S=5/2$ Mn^{2+} ion is, at an applied magnetic field B , then exposed to a number of possible transitions, all the same size given by $g\mu_B B$ hence one line could be expected at the frequency $h\nu = g\mu_B B$. In reality a solid containing the Mn^{2+} ion is complicating the picture with the crystal field. The hyperfine coupling between the electron and the nucleus results in a term in the Hamiltonian equal to $A\mathbf{I} \cdot \mathbf{J}$. Each m_J level is split into $2I+1$ hyperfine levels depending on the value of m_I . This results in an added rule for the ESR transition of $\Delta m_I = 0$. The situation for the free Mn^{2+} ion in the magnetic field is illustrated in the Fig. 4.3. The situation depicted there, hence the absence of the crystal field would result with 6 ESR

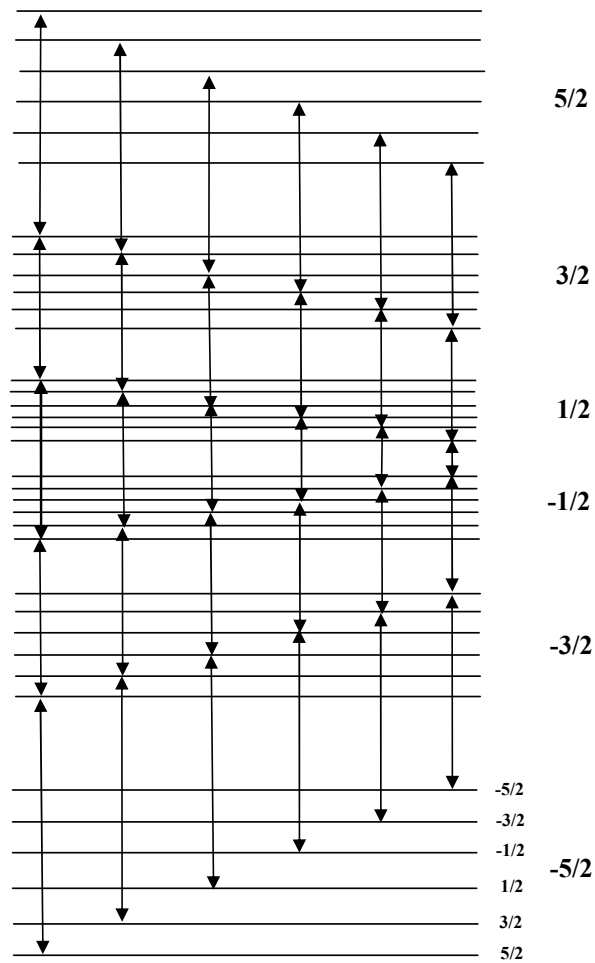


Figure 4.3: The hyperfine splitting of the free Mn^{2+} ion in the magnetic field, illustrating the $\Delta m_J = \pm 1$, $\Delta m_I = 0$ selection rule for the ESR transitions.

lines, yet the crystal field makes Δm_J transitions nonequivalent which results in a total of 30 ESR lines. Nitrates make for excellent precursors in terms of homogeneity but they are unstable with respect to time, due to the effect of hydration. Their long-term instability due to the hydration effect narrows down the chances for their successful application. This is why we have not pursued their characterization to great lengths as we have done for hydrozincite, which is the subject of the next Section.

4.2 The synthesis and properties of TM metal doped hydrozincite

The crystal structure of hydrozincite, $\text{Zn}_5(\text{OH})_6(\text{CO}_3)_2$, has been determined by Subrata Ghose in 1964. [101] (see Fig 4.4). The structure is monoclinic with $a_0=13.62$, $b_0=6.30$, $c_0=5.42$ Å, $\beta = 95^\circ 50'$, the space group is $C2/m$. There are two Zn sites, one in octahedral and one in tetrahedral coordination as shown in Figure 4.4. The octahedral sites outnumber the tetrahedral in the 3:2 ratio. Zinc atoms in tetrahedral coordination occur above holes that are present in sheets of octahedral zinc atoms. CO_3 groups are binding the sheets parallel to (100). Out of the three oxygen atoms in the CO_3 group the first is bonded to an octahedral, the second to the tetrahedral oxygen site while the remaining one is hydrogen bonded to three OH groups. The tetrahedral Zn-O distance is limited to 1.95 Å and is significantly smaller than the octahedral Zn-O distance at 2.10 Å.

Experimentally, stoichiometric amounts of $\text{Zn}(\text{NO}_3)_2$, $\text{TM}(\text{NO}_3)_2$ and urea, $\text{CO}(\text{NH}_2)_2$ are dissolved in distilled water, producing a clear solution. The solution is poured into a Teflon vessel and given a hydrothermal treatment at autoclave temperatures ranging from 100-150°C for 1 day. The solid samples obtained are then filtered and dried. The reaction proceeds along the following Equation:

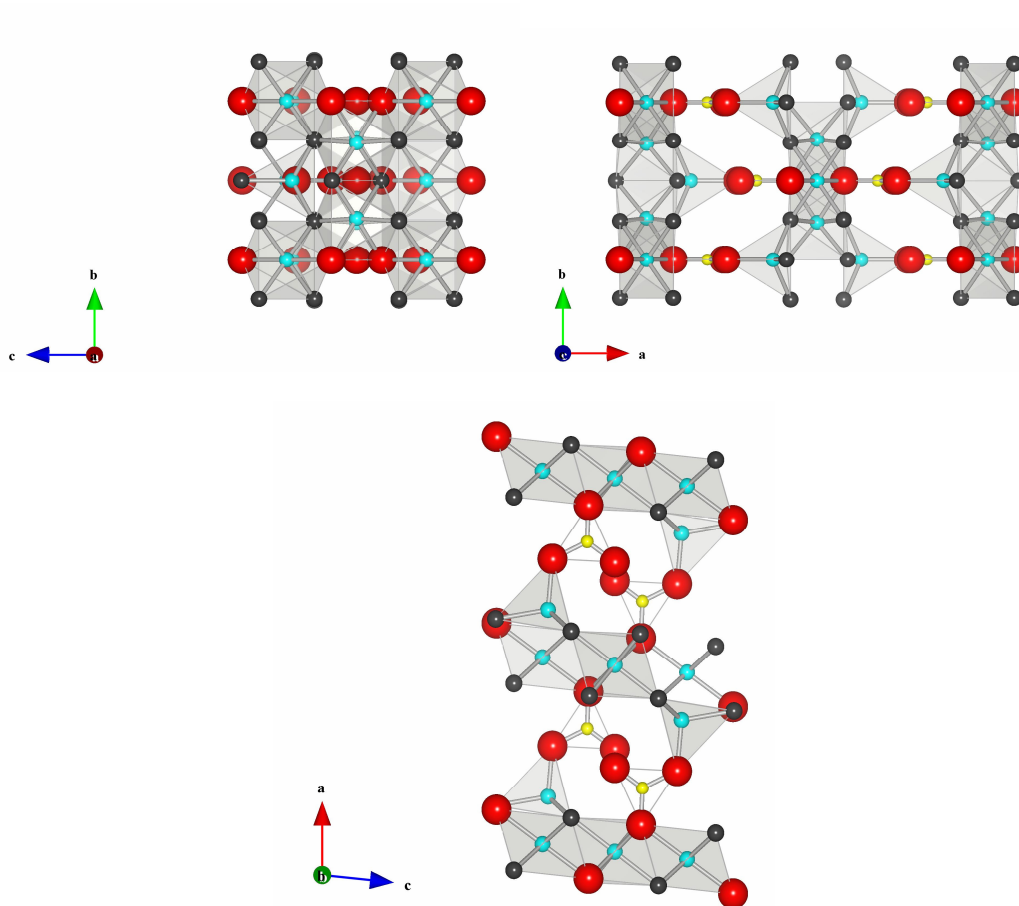
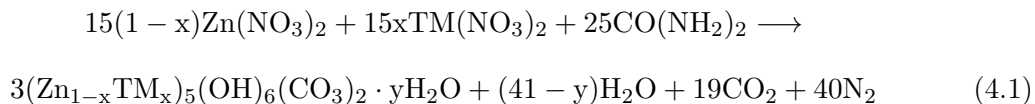


Figure 4.4: The crystal structure of $\text{Zn}_5(\text{OH})_6(\text{CO}_3)_2$. The atoms of Zn are represented with cyan balls and they can be in octahedral and tetrahedral environment, as can be seen from the outline of the polyhedra shaded in gray. The atoms of O (red balls) are at the vertices of the polyhedra either stand-alone or bound with a hydrogen atom into an OH bond depicted as a black ball. The atom of C is shown as a yellow ball and finds itself in CO_3 group bridging the $\text{Zn}(\text{OH})_2$ that grow parallel to (100).



The reaction 4.1, that successfully ends with the synthesis of $(\text{Zn}_{1-x}\text{TM}_x)_5(\text{OH})_6(\text{CO}_3)_2$, the TM doped hydrozincite, is based on the concept of propellant chemistry. This process is of particular interest due to its simplicity and to the high degree of homogeneity and purity of the reaction product. As it will be shown in this Section, the XRD shows that hydrozincite materials of high purity are made and the transmission electron microscopy (TEM) studies similarly show the hydrozincite purity $> 99.9\%$. The purity in excess of $> 99.9\%$ was established by random sampling of the hydrozincite nanoparticles. That is, less than 1 in 1000 particles observed were found to be a possible impurity phase, with an estimated volume fraction even lower. The synthesis produces a population of nanoparticles, hence instead of sectioning from a potentially inhomogeneous bulk material, random sampling of the population gives the correct purity value.

4.2.1 Mn doped hydrozincite

Mn doped hydrozincite materials are whitish powders gaining a brown tint with the increase in the nominally introduced Mn concentration. The structure and purity of Mn doped hydrozincite have been characterized by X Ray Diffraction (XRD) and Transmission Electron Microscopy (TEM). As shown in the Figure 4.5, XRD confirms that our materials crystallize with $C2/m$ space group.

Distribution of magnetic species within the non-magnetic matrix has been proven essential in determining the magnetic properties of a DMS compound [63]. Kuroda et al. have shown that the ferromagnetism of $(\text{Zn,Cr})\text{Te}$, together with magneto-optical and magnetotransport functionalities are dominated by the formation of Cr-rich $(\text{Zn,Cr})\text{Te}$ metallic nanocrystals embedded in the Cr-poor $(\text{Zn,Cr})\text{Te}$ matrix. The authors showed that if one looks at the spatially resolved Energy Data Spectroscopy (EDS) of a series of $\text{Zn}_{0.95}\text{Cr}_{0.05}\text{Te}$ thin films,

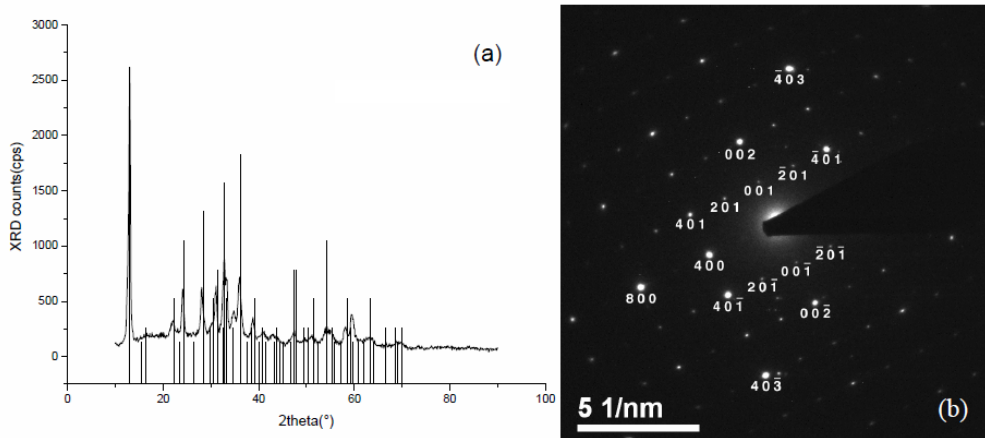


Figure 4.5: (a) The θ - 2θ XRD spectra of Mn doped hydrozincite precursors exhibiting $\text{Zn}_5(\text{OH})_6(\text{CO}_3)_2$ reflections, PDF number 19-1458. (b) Reflections of the SADP pattern can be indexed using the $C2/m$ space group of hydrozincite.

given in Fig. 4.6, one notices that the co-doping and deviations from stoichiometry affect the spatial distribution of Cr over the zinc-blende lattice. The uniform distribution of the Cr was found in the films doped with nitrogen (f) and prepared in the Te rich conditions (e). On the contrary, clustering of Cr has been noticed in the iodine-treated (a-c) and samples produced in Zn-rich conditions (d).

The magnetization data of the aforementioned films are given in the Fig. 4.7. As a very educational example, three characteristic temperatures pertaining to the magnetization behaviors are introduced. The apparent Curie temperature, T_C^{app} (red circles) was deduced from the Arrott plot analysis. The blocking temperature, T_B (blue squares) is defined as the temperature at which the magnetization measured in 500 Oe attains a maximum. In the case of the plateau nature of the maximum, the width of the maximum is represented as an error bar. The third temperature is the Θ_p (green triangles), the paramagnetic Curie-Weiss temperature.

As can be seen from the Fig. 4.7 with the letters assigned to different samples, in the case of the homogenous distribution, i.e. the nitrogen co-doped sample (case f) all the three magnetic temperatures went to zero, i.e. there are no ferromagnetic signatures or signatures pertaining to a different magnetic order. The authors conclude that the high-temperature

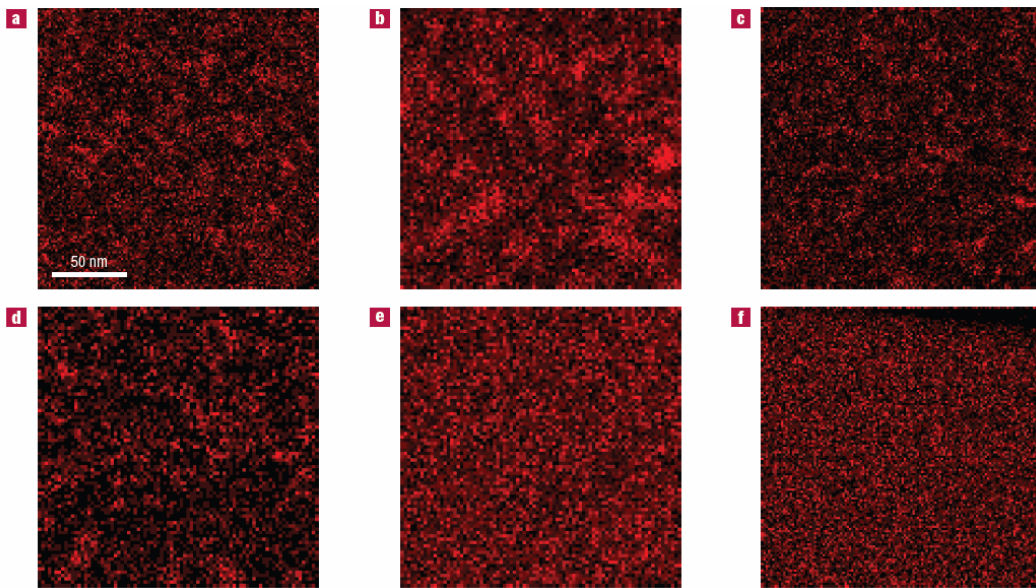


Figure 4.6: A work by Kuroda et al. [63] illustrates the importance of clustering effects on magnetic properties of DMS. Cross-sectional mapping images of the Cr K_α emission intensity for a series of $Zn_{1-x}Cr_xTe$ films with the same Cr composition of $x = 0.05 \pm 0.005$ but differing in co-doping or stoichiometry. The samples (a)-(c) have been treated in iodine and show significant clustering effect. The sample (d) has been produced in Zn-rich conditions and also manifests clustering. The samples free of clustering were (e) produced in Te rich conditions, while the sample (f) was N doped. Taken from [63].

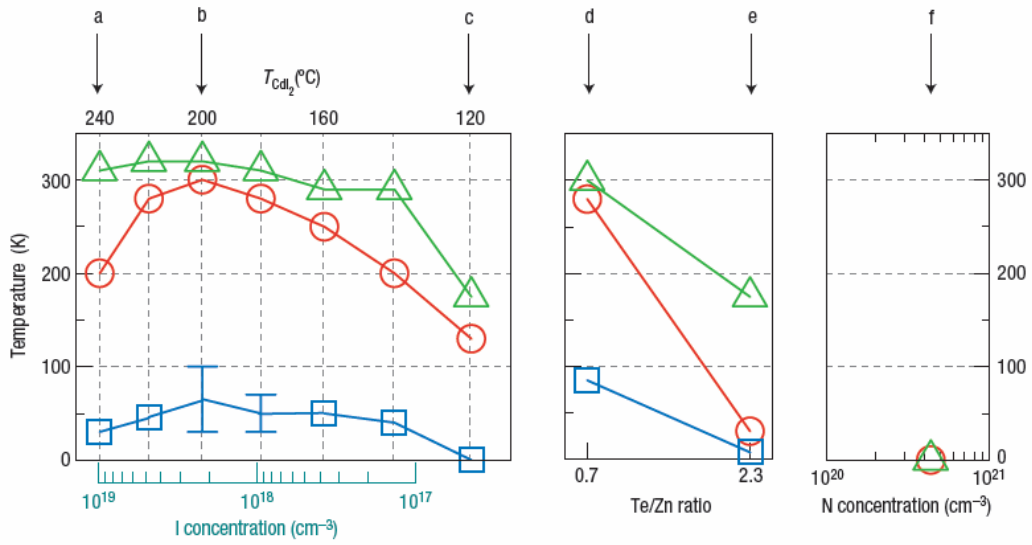


Figure 4.7: Characteristic magnetic temperatures of $\text{Zn}_{1-x}\text{Cr}_x\text{Te}$ films. Red circles represent the apparent Curie temperature T_C^{app} , the blue squares represent blocking temperatures T_B , and the paramagnetic Curie-Weiss temperature Θ_p is given in green triangles. The samples exhibiting clustering are iodine treated $(\text{Zn,Cr})\text{Te}$ (a-c) and zinc rich materials (d). They exhibit high values of all the three characteristic temperatures. The homogenous samples exhibiting clustering are Te treated $(\text{Zn,Cr})\text{Te}$ (e) and iodine treated $(\text{Zn,Cr})\text{Te}$ (f) and they exhibit significantly lower or zero values of all the three temperatures. Taken from [63].

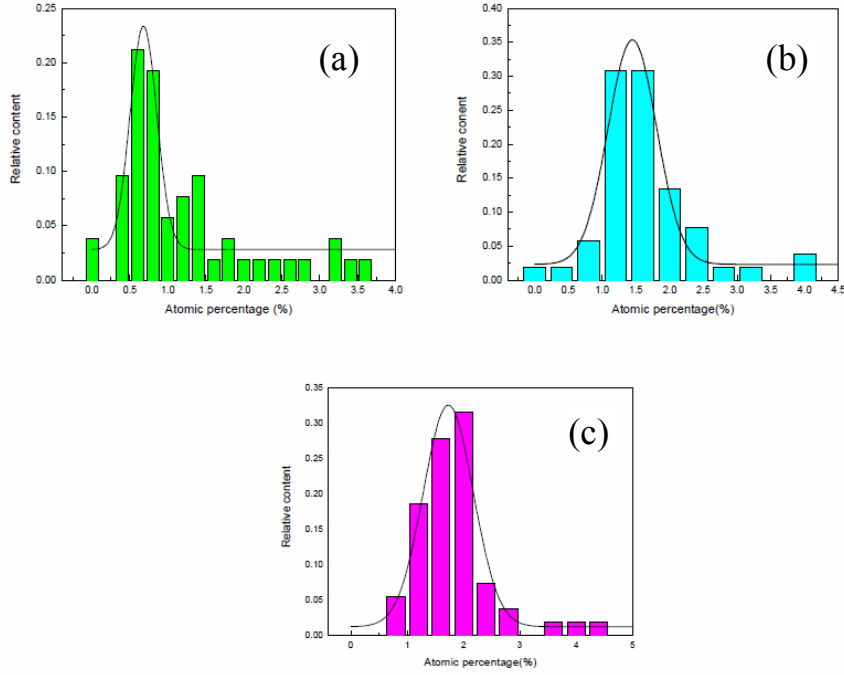


Figure 4.8: Mn/Zn concentration ratios found by random, per-particle EDXS profiling of $(\text{Zn}_{1-x}\text{Mn}_x)_5(\text{OH})_6(\text{CO}_3)_2$ particles, for nominal $x=0.02$ (a), $x=0.04$ (b) and $x=0.08$ (c) resulting with $x=0.012$ (a), $x=0.016$ (b) and $x=0.018$ (c) effective concentrations.

ferromagnetism can be easily brought upon by clustering effects, i.e. through the existence of Cr-rich (Zn,Cr)Te nanocrystals in a Cr-poor (Zn,Cr)Te matrix.

Using random, per-particle EDXS profiling, we have obtained a narrow Mn distribution in $(\text{Zn}_{1-x}\text{Mn}_x)_5(\text{OH})_6(\text{CO}_3)_2$. The dispersion is given in Fig. 4.8. On nominal $x=0.02$ (green), 0.04 (cyan) and 0.08 (magenta) Mn:hydrozincite powders the real values of concentration were calculated to be $x=0.012$, 0.016 and 0.018 through taking the value of the arithmetic mean of the actual Mn/Zn concentration ratios found. The discrepancy between the nominal input values and the effective values found in the products are in the nature of the method, with some of initial quantity of Mn remaining in the solution and not entering the precipitate. Discrepancy also arises due to the existence of the solubility limit of Mn in hydrozincite. We estimate the solubility limit in Mn:hydrozincite to be close to 2% as inferred from EDXS profiling of the higher nominal Mn concentration samples. The homogeneity of the Mn distribution in hydrozincite is preserved in ZnO as it will be shown in Chapter 6.

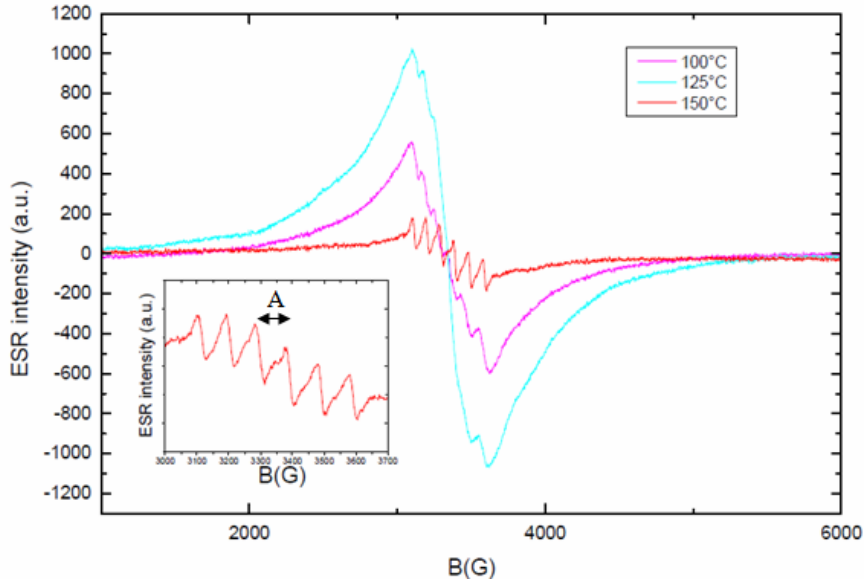


Figure 4.9: Room-temperature X-band ESR spectra of $(\text{Zn}_{0.988}\text{Mn}_{0.012})_5(\text{OH})_6(\text{CO}_3)_2$ synthesized at 100°C (magenta), 125°C (cyan) and 150°C (red). Inset: 6-peak hyperfine structure of Mn^{2+} measured for the 150°C sample with the value of hyperfine splitting $A=(87 \pm 1)\times 10^{-4} \text{ cm}^{-1}$.

Magnetic properties of $(\text{Zn}_{1-x}\text{Mn}_x)_5(\text{OH})_6(\text{CO}_3)_2$ have been investigated via ESR and SQUID measurements. The initial work on the synthesis of $(\text{Zn}_{1-x}\text{Mn}_x)_5(\text{OH})_6(\text{CO}_3)_2$ concerned the study of the impact of the temperature used during the synthesis method on the properties of the product. Three temperatures were used: 100°C, 125°C and 150°C. The ESR spectra of the samples produced at these temperatures are given in Fig. 4.9. The inset shows the 6-peak hyperfine structure of Mn^{2+} in hydrozincite, with the value of the hyperfine coupling constant $A=(87 \pm 1)\times 10^{-4} \text{ cm}^{-1}$ being roughly determined as the average value of the adjacent peak spacings.

The characteristic hyperfine structure corresponding to 6 lines, most conspicuous for the sample synthesized at 150°C, confirms the presence of paramagnetic Mn^{2+} ions distributed in the hydrozincite matrix. The structure is due to the central $J=1/2$ to $J=-1/2$ Mn^{2+} electronic transition. Due to the interaction between Mn ions the hyperfine structure gets washed away into a Lorentzian derivative line, the line stemming from Mn-Mn interaction. In the case of the

sample produced at 125°C, where the smearing out has proven to be the most advanced the peak-to-peak ESR linewidth was found to be $\Delta H_{pp} = (439 \pm 5) \text{G}$. The sample with the largest $\Delta H_{pp} = (481 \pm 5) \text{G}$ among the three is incidentally the sample produced at 150°C which shows the least degree of smearing out (the most undistorted hyperfine structure) among the three samples studied. Taking the fundamental effect of isotropic Mn-Mn exchange narrowing of the ESR linewidth one can hint that the isotropic Mn-Mn exchange is the dominant interaction in $(\text{Zn}_{1-x}\text{Mn}_x)_5(\text{OH})_6(\text{CO}_3)_2$ at room-temperature (see Section 2.1) with the sample with stronger interaction being represented by the narrower line and more distorted hyperfine structure, simultaneously. As for the proof of purity of the material, one can add that no additional sextets are present, which corroborates the absence of Mn with valence state higher than 2 in the hydrozincite precursor. Therefore Mn is not oxidized during the synthesis of hydrozincite. The obtained ESR signal is also equivalent to the signal observed for Mn^{2+} in $\text{Zn}(\text{OH})_2$ by Zhou et al. [102] (Fig. 4.10 where the authors observed $g=2.001$ and $A=89 \times 10^{-4} \text{cm}^{-1}$ for their sample). The existence of the equivalent signal as a component of the joint signal of ZnO in the work by Zhou et al. was explained as a presence of Mn^{2+} in $\text{Zn}(\text{OH})_2$ shells surrounding ZnO particles. The observed value of the hyperfine constant, A, that we have obtained for Mn in hydrozincite is $A=(87 \pm 1) \times 10^{-4} \text{cm}^{-1}$, as seen in the Inset to Fig. 4.9. This makes it slightly lower than that of Mn^{2+} in $\text{Zn}(\text{OH})_2$.

To infer on the macroscopic magnetic properties of the $\text{Zn}_5(\text{OH})_6(\text{CO}_3)_2$ produced at 100°C, 125°C and 150°C SQUID ZFC-FC measurements were performed. The results are shown in the Fig. 4.11. The $100 \text{ K} < T < 300 \text{ K}$ linear fit of the high-temperature inverse susceptibility is given in the inset to the Fig. 4.11. The samples were found to observe the Curie-Weiss behaviour of the magnetization with T_{CW} given to be -65 K in the case of the sample synthesized at 125°C, -35 K for the 100°C and finally, -18 K for the sample synthesized at 150°C. From the negative value of all the three Curie-Weiss temperature observed we can deduce that the dominant magnetic interactions in the samples are antiferromagnetic. Also, as a perfect fit to the ESR measurements given in Fig. 4.11 the strongest interactions are in the sample with the most-smearred out hyperfine structure (T_{CW} highest in absolute value),

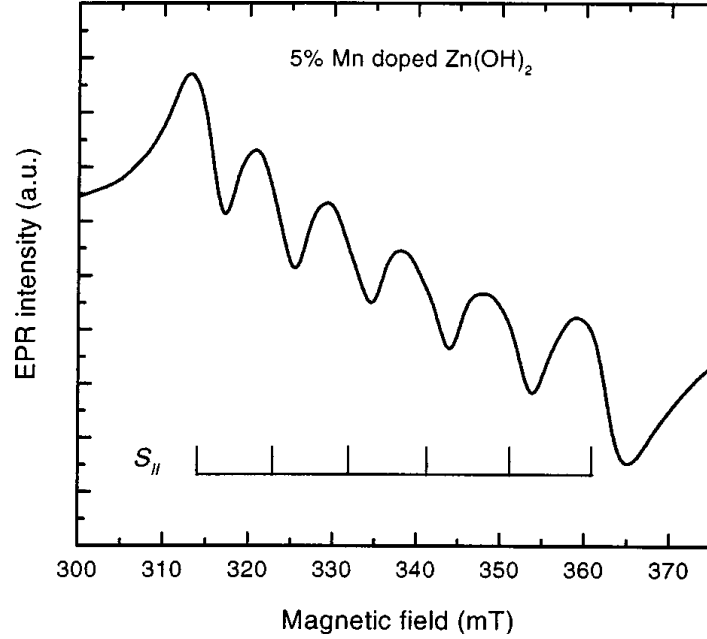


Figure 4.10: The ESR signal of the 5% Mn doped Zn(OH)₂ with $g=2.001$ and $A=89 \times 10^{-4} \text{ cm}^{-1}$. Taken from [102].

while the "least-smeared-out sample" exhibits the behaviour closest to paramagnetism (T_{CW} closest to zero).

When choosing the temperature of the synthesis for the hydrozincite that we fixed for all the future samples during this Thesis work we were lead by the condition of interaction, with the final aim in mind of achieving room temperature ferromagnetism in the final product. This is why we chose the "most-smeared-out sample", i.e. the sample synthesized at 125°C as our material for future syntheses. The fact that the sample is "most-smeared-out", means that in it the Mn-Mn interactions are strongest. One needs strong Mn-Mn interactions either direct, or through itinerant carriers to have a material that is a ferromagnet on a large scale.

4.2.2 Conclusion

As shown in this Chapter, we have synthesized new precursors of ZnO homogeneously doped with TM. TM doped zinc nitrates offer an interesting choice for precursors of $\text{Zn}_{1-x}\text{TM}_x\text{O}$ due to their low melting temperature and possibility of intrinsic homogeneity of the distribution of the magnetic species within the nitrate matrix. The nitrates were studied to infer their

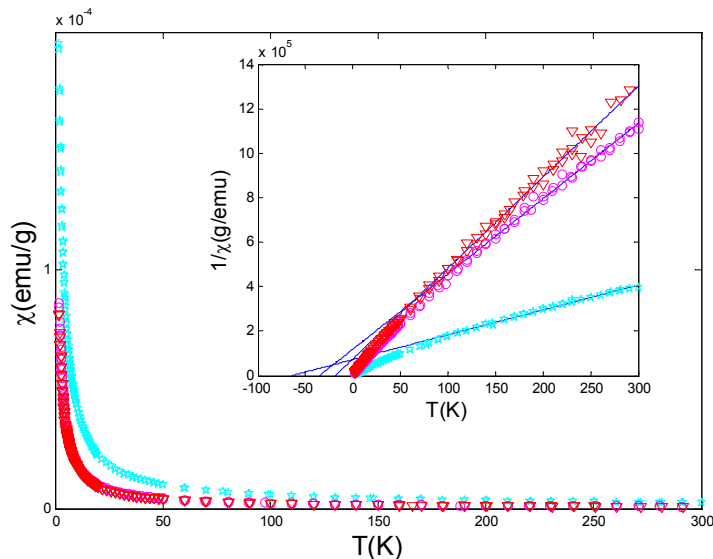


Figure 4.11: The ZFC-FC SQUID curves of $(\text{Zn}_{1-x}\text{Mn}_x)_5(\text{OH})_6(\text{CO}_3)_2$ synthesized at 100°C (magenta) , 125°C (cyan) and 150°C (red). No signs of ferromagnetic order coming from ZFC-FC splitting are present, with antiferromagnetic interactions being dominant, as inferred from the negative T_{CW} temperatures.

homogeneity through the ESR method and were found to allow for up to 10% of Mn in the structure without showing a significant smearing out of the ESR line, i.e. interaction between the Mn spins. Hence, in the next Chapter, Chapter 5, we will present the results on $\text{Zn}_{1-x}\text{Mn}_x\text{O}$ synthesized by thermal decomposition of TM doped zinc nitrates to see whether this homogeneity is kept in the oxide $\text{Zn}_{1-x}\text{Mn}_x\text{O}$ samples.

We have as well characterized the structural and magnetic properties of Mn doped hydrozincite, the second generation of our precursors. Measurements of magnetic properties have revealed that $(\text{Zn}_{1-x}\text{Mn}_x)_5(\text{OH})_6(\text{CO}_3)_2$ exhibits Curie-Weiss behaviour with antiferromagnetic interactions dominant for $\text{Mn} = \text{TM}$.

As outlined in Section 4.2, $(\text{Zn}_{1-x}\text{TM}_x)_5(\text{OH})_6(\text{CO}_3)_2$ has numerous advantages in comparison to a growing group of precursors for $\text{Zn}_{1-x}\text{TM}_x\text{O}$, avoiding caveats present for precursors used for solid-state and co-precipitation synthesis methods. Single step decomposition process at low temperatures, high TM solid state solubility and, as it will be apparent from Chapter 6, tunable properties of the $\text{Zn}_{1-x}\text{TM}_x\text{O}$ dependent on the atmosphere of the decomposition, are some of the upper hands that $(\text{Zn}_{1-x}\text{TM}_x)_5(\text{OH})_6(\text{CO}_3)_2$ offers. The Chapter

6 will begin with an overview of the properties of the $\text{Zn}_{1-x}\text{Mn}_x\text{O}$, one of the most studied materials in the DMO field, continue with $\text{Zn}_{1-x}\text{Co}_x\text{O}$, a sister material, yet with its own peculiarities, advance to $\text{Zn}_{1-x}\text{Ni}_x\text{O}$, a product likewise predicted to be ferromagnetic and conclude with the co-doping of $\text{Zn}_{1-x}\text{Mn}_x\text{O}$ with Li, intended to dope the material with holes and achieve the predicted ferromagnetism, for which the foundation was laid out in this Chapter.

Before Chapter 6, however, we turn our attention to the properties of materials synthesized from TM doped nitrates.

Chapter 5

Properties of $\text{Zn}_{1-x}\text{Mn}_x\text{O}$ produced from Mn doped zinc nitrates

This Chapter covers the main elements of the synthesis of $\text{Zn}_{1-x}\text{Mn}_x\text{O}$ from the nitrate precursors, which were presented in Chapter 4. As it will be explained in this Chapter, a small amount of a parasitic phase, ZnMnO_3 , coexistent with the produced $\text{Zn}_{1-x}\text{Mn}_x\text{O}$ was observed. ZnMnO_3 was found to exhibit a significant impact on the magnetic and electronic properties of $\text{Zn}_{1-x}\text{Mn}_x\text{O}$ system.

5.1 Structural properties

$\text{Zn}_{1-x}\text{Mn}_x\text{O}$ is synthesized by decomposing the nitrate precursor into a $\text{Zn}_{1-x}\text{Mn}_x\text{O}$ and nitric oxide NO_2 . The reaction is given as the Equation 5.1. This was done at low temperatures (typically 400°C), because the low temperature should disfavor clustering, but more importantly, oxidation of Mn into higher oxidation states and from there, formation of parasitic phases (ZnMnO_3 - the Mn is in 4+ state). Avoiding oxidation of Mn was also the reason behind performing the synthesis in reducing atmospheres of flowing Ar and H_2 (typically at flow rates of 100 sccm (standard cubic centimeter per minute) and 50 sccm for Ar and H_2 , respectively), under constant pumping to out-pump the produced NO_2 . The typical duration of the synthesis was 10 minutes.

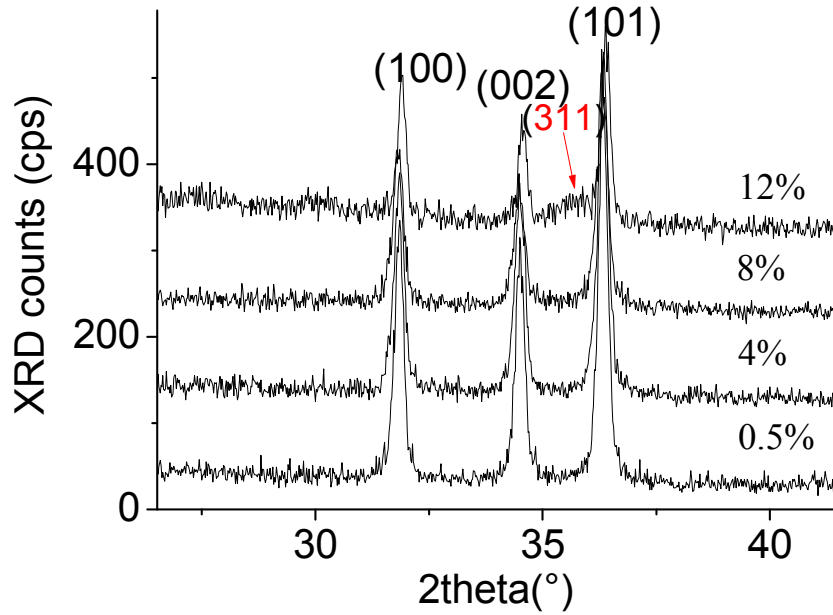
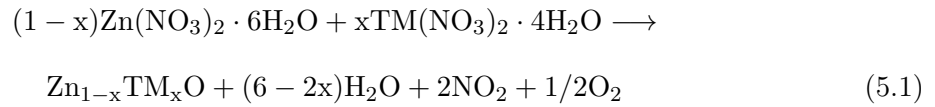


Figure 5.1: XRD θ - 2θ spectra of 0.5%, 4%, 8% and 12% Mn:ZnO powders. The red arrow shows the position of the reflection of the (311) ZnMnO_3 .



An initial check of the single phase nature of the sample, a standard procedure described in Section 4.2, was performed. The XRD spectra of 0.5%, 4%, 8% and 12% Mn:ZnO powders is given in Fig. 5.1. Although the signal to noise ratio in this series of samples is not as high compared to the samples produced by decomposition of $(\text{Zn}_{1-x}\text{Mn}_x)_5(\text{OH})_6(\text{CO}_3)_2$, as shall become clear from the Chapter 6, the absence of other phases is clear in the three samples with lower Mn concentration. The 12% Mn:ZnO powder revealed a (311) reflection of ZnMnO_3 .

In sharp contrast with the XRD analysis, the TEM analysis revealed a high degree of structural inhomogeneity of the $\text{Zn}_{1-x}\text{Mn}_x\text{O}$ powders even in samples with the nominally low Mn content. A clear disparity between equiaxed particles and sharp-like structures that we refer to as "needles" for a $\text{Zn}_{1-x}\text{Mn}_x\text{O}$, $x=0.04$ particle is evident from Figure 5.2. Analysis

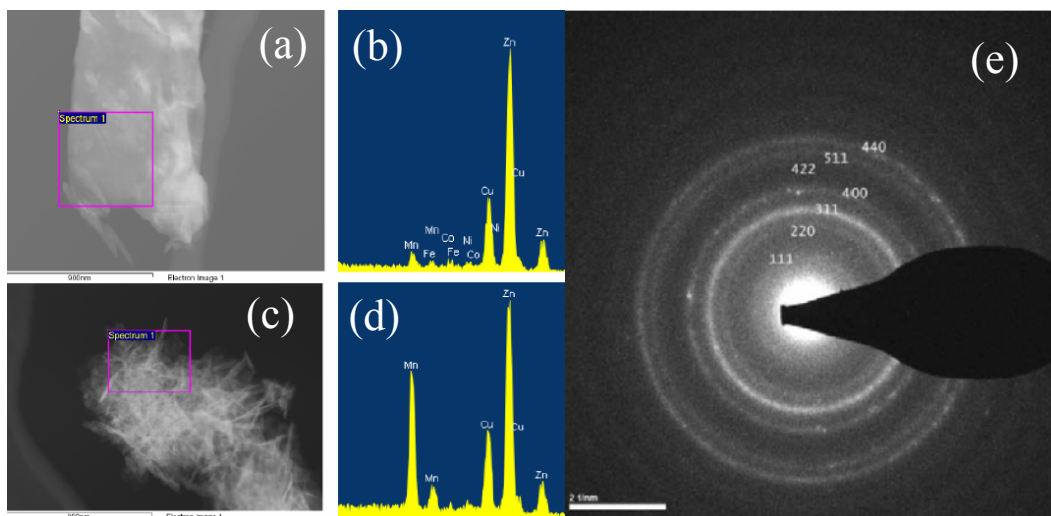


Figure 5.2: STEM-EDX spectra of a 4% Mn:ZnO particle shows different structural characteristics and significantly different Mn content throughout different regions of the particle. The portion of the particle not-rich in manganese (a) and the corresponding EDX scan (b). "Needle-like" portions of particles rich in manganese (c) and the corresponding EDX scan (d). SADP analysis of the portion of the Mn rich portion of the particle (e).

of chemical composition of the samples was performed using STEM-EDX giving us the locally determined relative ratio of Zn-Mn atomic species, as described for $(\text{Zn}_{1-x}\text{Mn}_x)_5(\text{OH})_6(\text{CO}_3)_2$ in section 4.2. Distinctly different values of Mn concentration were established for different portions of the particle. The section shown in Figure 5.2(a) showed measured Mn/Zn concentration ratio close to 0.026 as obtained from the spectra given in Fig. 5.2(b), while the value in the region 5.2(c) was as much as 0.55 as measured from the spectra shown in Fig. 5.2(d). We can therefore conclude that our powders consist of at least two phases with two distinctly different values of the dopant concentration, judging from the difference in morphology and an order of magnitude different Mn/Zn ratio.

In order to identify the parasitic phase in question, the measurement of the selected area diffraction pattern (SADP) has been performed on a Mn-rich portion of 4% $\text{Zn}_{1-x}\text{Mn}_x\text{O}$ particle. The results of the SADP scan are shown in Fig. 5.2 (e). We have established the existence of diffused rings corresponding to crystalline lattice reflections of ZnMnO_3 . The literature is still very scarce on the Zn-Mn-O compounds synthesized at low temperatures, yet Blasco et al. [103] were able to claim that these reflections coincide well with cubic spinels of

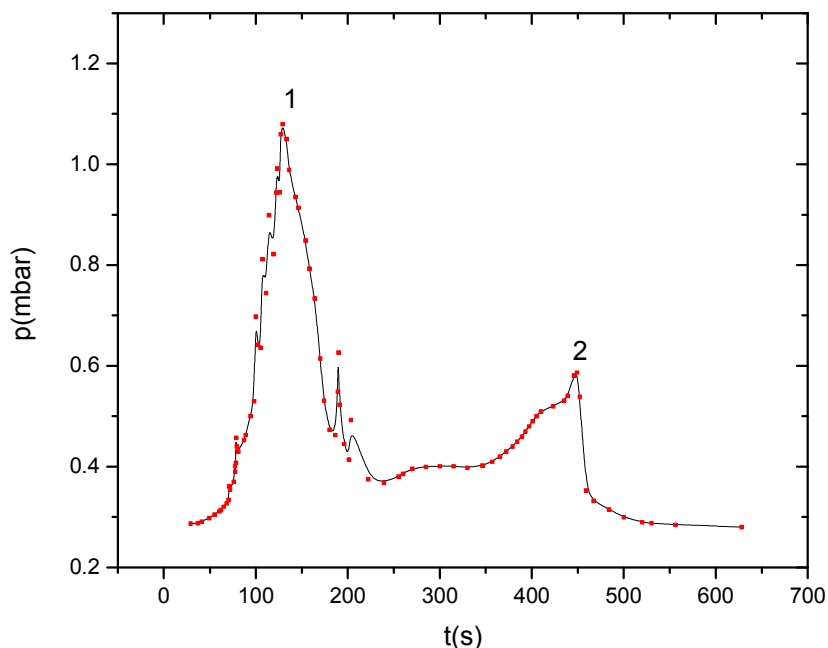


Figure 5.3: Pressure variation within the quartz tube during the typical $\text{Zn}_{1-x}\text{Mn}_x\text{O}/\text{ZnMnO}_3$ synthesis. The two-peak structure is relevant to the parasitic phase co-formation.

the stoichiometry $\text{Mn}_{3-x}\text{Zn}_x\text{O}_4$. The spinels of this structural formula, the authors speculate further, were in past being mistaken for ZnMnO_3 .

Additionally, the pressure variations inside the quartz tube indicate the intricacy of the mechanism behind the synthesis of $\text{Zn}_{1-x}\text{Mn}_x\text{O}$. The variation of the quartz tube pressure is a measure of the NO_2 produced during the synthesis reaction. The synthesis of single-phase $\text{Zn}_{1-x}\text{Mn}_x\text{O}$ should then involve only one peak in the pressure within the quartz tube-time curve shown in the Fig 5.3. However, the curve exhibits two peaks, with the first peak having a satellite structure. This points to the probability that one of the peaks is related to the formation of a parasitic phase ZnMnO_3 . To infer more on the chronology of the phase separation we have performed the synthesis by ending the process at the time defined by the disappearance of the first peak. The sample had similar morphology to the $\text{Zn}_{1-x}\text{Mn}_x\text{O}/\text{ZnMnO}_3$ phase system, pointing that the phase separation $\text{Zn}_{1-x}\text{Mn}_x\text{O}/\text{ZnMnO}_3$ probably happens during the initial stages with the slower diffusion processes happening later.

The ambiguity about the true molecular formula of the parasitic phase does not influence the fact that the goals of homogeneity and single phase nature of the sample have not been ful-

filled. However, the sample offers the opportunity to quantify the contribution of the ZnMnO_3 to the magnetic properties of $\text{Zn}_{1-x}\text{Mn}_x\text{O}$ as there exists a high chance of ZnMnO_3 going unnoticed in the XRD analysis and yet to give non-negligible contribution to the magnetic signal of $\text{Zn}_{1-x}\text{Mn}_x\text{O}$ in the samples produced by different synthesis methods.

Mn, Co and Cu doped ZnO produced at high temperatures are likely to contain the very same parasitic phases as Mn, Co and Cu doped ZnO produced in better (low temperature, less oxidative reaction byproducts) conditions. This is why we have performed the XRD scans of the products of the synthesis of $\text{Zn}_{1-x}\text{TM}_x\text{O}$, where $\text{TM} = \text{Mn, Co, Cu}$, synthesized at 700°C from the nitrate precursors. The scans are given in Fig. 5.4. The parasitic phases found to form were ZnMnO_3 in the case of Mn as a dopant, ZnCo_2O_4 in the case of Co as a dopant and CuO in the case of Cu.

Interestingly enough, the $\text{Zn}_{1-x}\text{Cu}_x\text{O}$ is a material with significantly higher solid state solubility of Cu as there are no compounds containing the combination of Zn, Cu and O atoms. The faint reflections of CuO therefore start to occur only at as much as 40 % percent of Cu in the sample. This experiment gives a good guess about the identification of possible of second phases that can form in far smaller amounts in (TM,Zn)O systems produced from hydrozincite precursors.

5.2 Magnetic properties

As explained in the Section 2.1 the principal information that one can observe from the ESR spectra are, firstly, the ESR linewidth which is inversely proportional to the spin relaxation time and can give valuable information about the spin dynamics of the system. The linewidth is the field span between the positive and negative peak in the ESR signal curve, commonly known as ΔH_{pp} where H is the field and pp signifies "peak-to-peak". Secondly, the ESR intensity is proportional to the number of paramagnetic spins in the sample. Thirdly, the electron g-factor serves as a measure of the local field experienced by the electrons in the system.

The Hamiltonian of a Mn^{2+} ion in powder samples of ZnO can be written as [102].

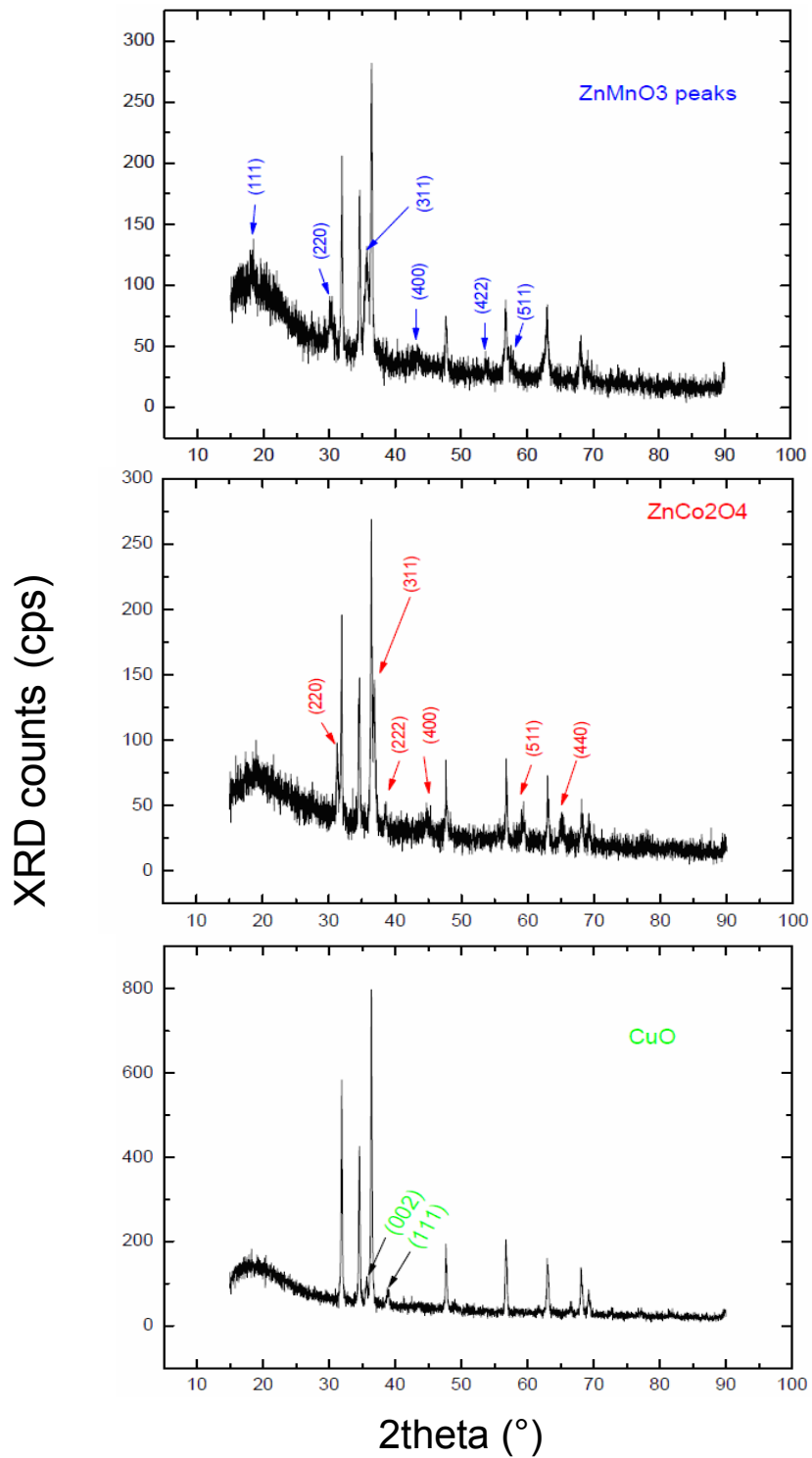


Figure 5.4: XRD scans of $Zn_{1-x}TM_xO$, $TM = Mn, Co, Cu$ synthesized at $700^\circ C$, with $ZnMnO_3$, $ZnCo_2O_4$ and CuO reflections of second phase marked with arrows.

$$H = g\beta HS + \frac{1}{6}a(S_x^4 + S_y^4 + S_z^4) + D[(S_z^2 - \frac{1}{3}S(S+1))] + ASI \quad (5.2)$$

Here, the first term is the Zeeman contribution, the middle two terms are due to axial fine structure splitting quantified by the factors a and D while the last term results from the hyperfine interaction and is given by the value of the hyperfine constant, A .

The ESR spectra of the heat-treated (oxide) samples are shown in Figure 5.5. The signals of $\text{Zn}_{1-x}\text{Mn}_x\text{O}$ of all concentrations consist of a broad resonance line stemming from interacting spins (order of magnitude ≈ 1000 G) and a set of hyperfine structure lines originating in the presence of the non-interacting (paramagnetic) Mn^{2+} ions described by the Hamiltonian (5.2). The latter lines are very narrow, with a linewidth of the order of magnitude of ≈ 1 G. The dependence of intensity and the linewidth of the ESR line on the temperature is given in Fig 5.5 (b) and (c), respectively. The intensity grows linearly with the concentration of Mn pointing to the fact that most of the Mn centers in the samples are paramagnetic. The broad line stemming from Mn-Mn interaction has a linewidth that increases from 980 G to 2300 G in the 1% to 15% interval and subsequently saturates (cf. Fig. 5.5). These properties can be explained by supposing that the broad line actually stems from the parasitic phase, ZnMnO_3 that has a room-temperature linewidth of close to 2000 G, as explained and shown in Section 5.4. In Section 5.4 we have synthesized the parasitic phase ZnMnO_3 and established its magnetic and electronic properties. The hyperfine part of the spectra, the signal roughly in the region of roughly 2800 - 3800 G, as seen in Fig. 5.6 shows the presence of Mn^{2+} lines and a sextet shifted to lower g-factors. The dominant sextet is marked with black arrows and is stemming from the Mn^{2+} ions. The shifted sextet, marked in red, together with being shifted to lower g-factors is also smaller in intensity. It is attributed to Mn in 4+ valence state. This was found to be the case for Mn in PbTiO_3 [104] where the g-factor of Mn^{4+} was as well slightly shifted to lower values.

Zero-field cooled - field cooled scans using SQUID have been performed on the same batch of 2%, 4%, 6% and 8% Mn:ZnO powder samples. Measurements were performed in heating up, with the samples first time (ZFC) being cooled down from room temperature to 5 K

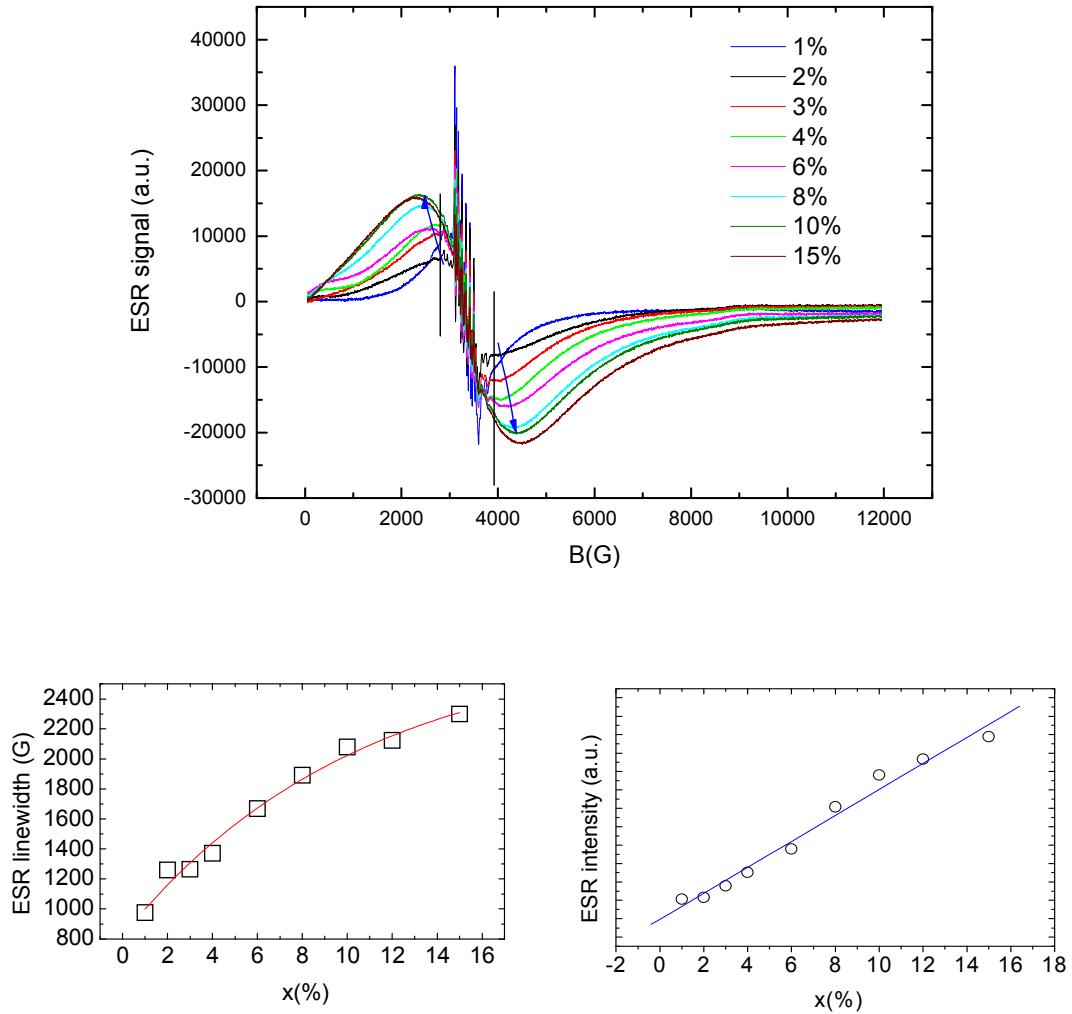


Figure 5.5: Electron spin resonance measurements on the series of Mn:oxide samples, with a complicated central sextet of lines representing different paramagnetic species of Mn, corresponding to different valence states and coordinations together with a broad background stemming from a phase with highly interacting Mn ions. ESR linewidth is experiencing saturation at ≈ 2400 G, while the ESR intensity grows almost linearly with concentration, pointing to the dominant paramagnetic nature of Mn centers.

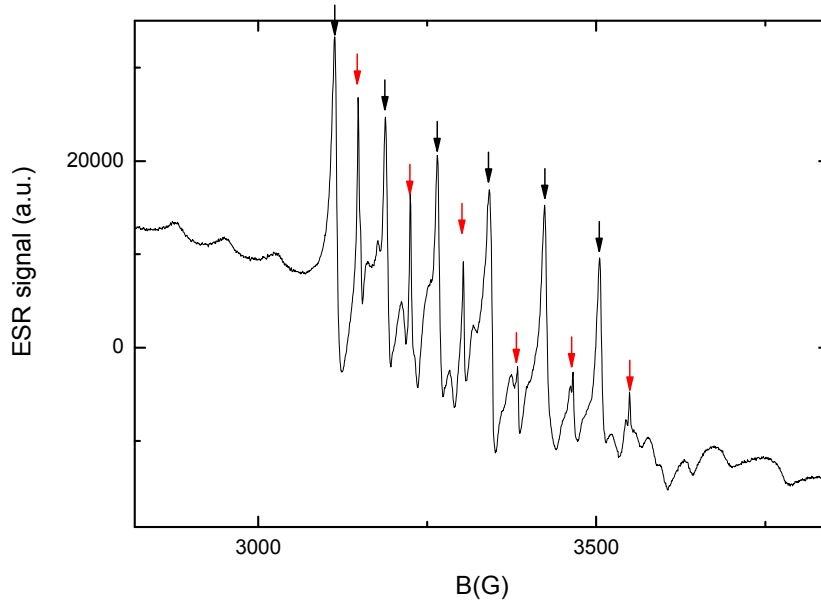


Figure 5.6: The complicated hyperfine signal of paramagnetic Mn species in ZnO. While the dominant ESR contribution is attributed to Mn^{2+} (black), the shifted sextet corresponding to Mn^{4+} is outlined in red arrows.

without magnetic field, and second time in the magnetic field, as explained in earlier Sections. The same value of magnetic field in which the sample was cooled was used for measuring the magnetization of samples while heating up. Here we have used two typical fields, 100 Oe and 1000 Oe. The results of the measurements performed at 100 Oe are given in Fig. 5.7. The dependence of magnetization on temperature for 2%, 4%, 6% and 8% Mn:ZnO measured at 1000 Oe is given in Fig. 5.8. Measurements performed at two measuring fields have revealed similar behaviour that can be summed up by confirming that 2%, 4%, 6% and 8% Mn:ZnO produced by the decomposition of the TM doped nitrates (a) experience a splitting at low temperatures, typically $T < 10$ K, with the blocking temperatures given in Table 5.1 (b) experience Curie-Weiss behaviour with the $100 \text{ K} < T < 300 \text{ K}$ fit giving positive values of the Curie-Weiss temperature T_{CW} independent of the concentration. This effectively means that ferromagnetic interactions are dominant for all four samples studied. One has to notice from the values of the blocking temperatures given for all the four samples measured at 100 Oe that the blocking temperature advances slightly to higher values with the addition of Mn, approximately 1 K for fourfold increase in concentration.

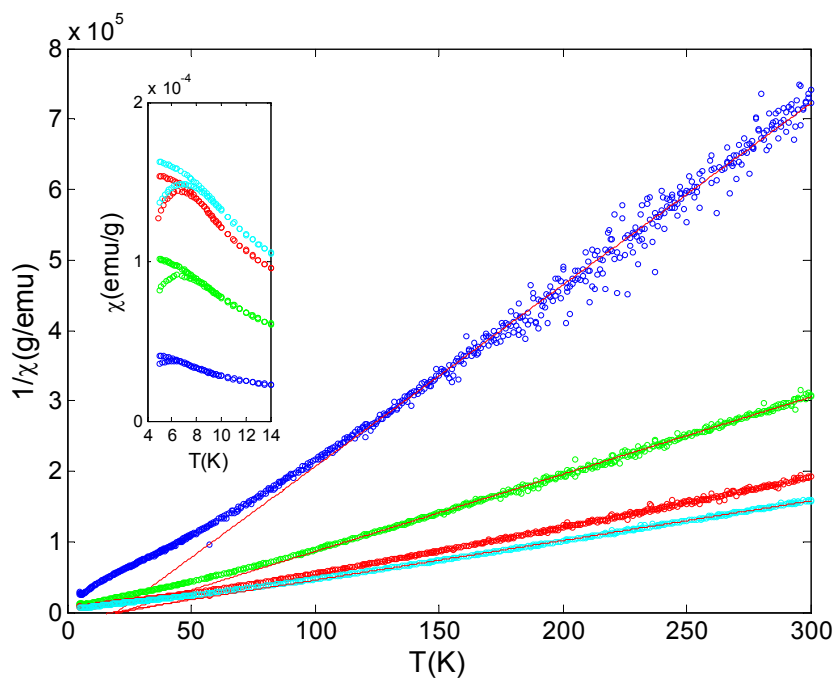


Figure 5.7: Inverse susceptibility and low temperature susceptibility of 2% (blue), 4% (green), 6% (red) and 8 % (cyan) $\text{Zn}_{1-x}\text{Mn}_x\text{O}$ powders measured at 100 Oe. Inset: closer look on a behavior of the susceptibility curve in a region below 14 K. Clear splitting is observed, pointing to a existence of a paramagnetic-superparamagnetic transition.

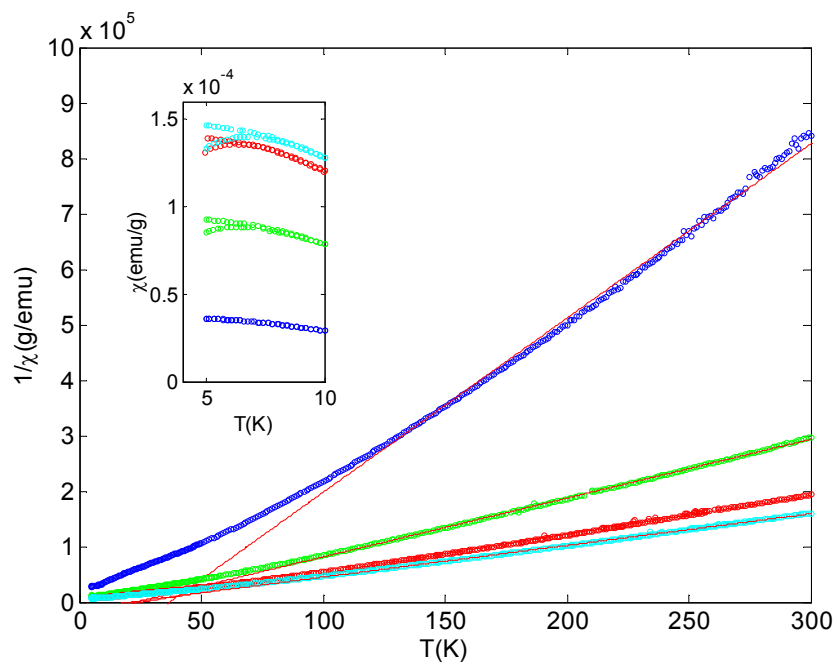


Figure 5.8: Inverse susceptibility of 2% (blue), 4% (green), 6% (red) and 8 % (cyan) $\text{Zn}_{1-x}\text{Mn}_x\text{O}$ powders with a corresponding Curie-Weiss fit measured at 1000 Oe. Inset: closer look on a behavior of the susceptibility curve in a region below 10 K. Clear splitting is observed, pointing to a existence of a paramagnetic-superparamagnetic transition.

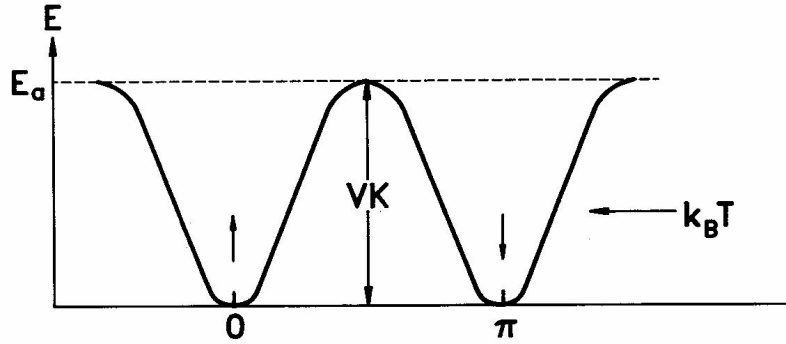


Figure 5.9: Anisotropy barrier for an up/down superparamagnet. Note that the thermal activation energy ($k_B T$) is too small to cause rapid barrier hopping. Taken from [105].

More specifically, at temperatures typically below 10 K, a splitting between ZFC and FC curves occurs, with the ZFC curve experiencing a characteristic maximum - a "cusp" - at the superparamagnetic blocking temperature T_B . In the same temperature range FC curve increases monotonically continuing Curie-Weiss-like behavior. To explain this behaviour we evoke the classic text by J. A. Mydosh [105] which employs an energy-barrier model as depicted in Fig. 5.9.

Due to the magnetic anisotropy which can occur due to many possible sources, magnetocrystalline, shape, dipolar, surface, to name only few, in the particles of $ZnMnO_3$ an energy barrier is formed with a height $E_a = KV$, the anisotropy constant multiplied by the particle volume inducing the formation of a system with two easy orientations of magnetization, shown in Fig. 5.9. This energy can be overcome with either field $\mathbf{M} \cdot \mathbf{H}$ or temperature $k_B T$. The relaxation time of the magnetization between these two states is given by Arrhenius law explaining thermal activation, $\tau = \tau_0 \exp(E_a/k_B T)$ where E_a is the energy barrier separating the states and τ_0 is the microscopic limiting relaxation time of the order of 10^{-9} s. The values of T_B are given in Table 5.1. A slight increase in the T_B with the increase in the Mn concentration from 2% to 8% is visible. The blocking temperature has a simple dependence on anisotropy constant and the volume of ferromagnetic particles, as given by Equation 5.3. The increase in the blocking temperature, assuming that the anisotropy constant is the same, can only mean that the average volume of the particle is increasing. This means that further

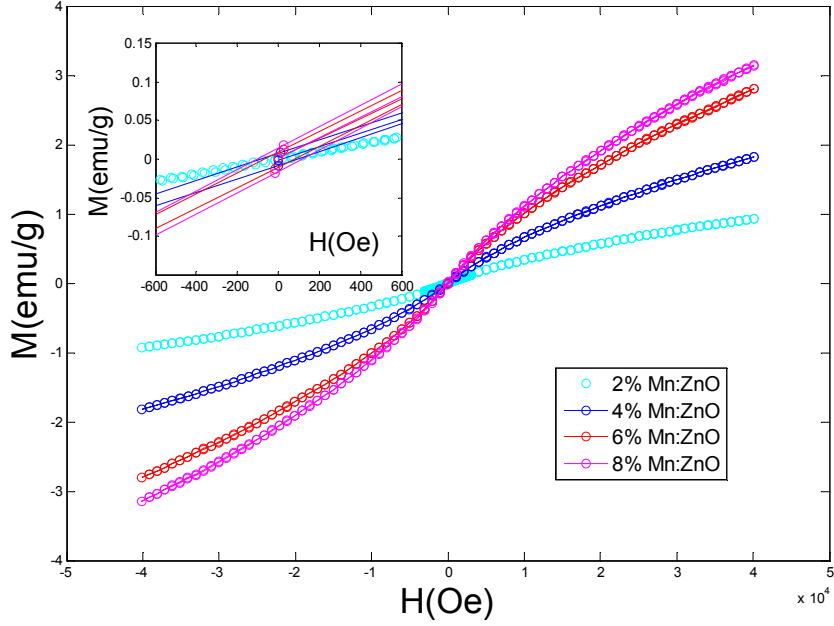


Figure 5.10: (-4T)-4T field sweeps of 2% (cyan), 4% (blue), 6% (red) and 8 % (magenta) Mn:ZnO. Inset: behavior of $M(H)$ curves around zero, showing very small hysteresis for 4%, 6 and 8% Mn:ZnO powders. 2% Mn:ZnO has much smaller splitting at 5 K, hence hysteresis is much harder to observe, cf. Figure 5.11.

addition of Mn to the $\text{Zn}_{1-x}\text{Mn}_x\text{O}/\text{ZnMnO}_3$ system is increasing the average volume of the ZnMnO_3 particles.

$$T_B \approx \frac{K_{Eff}V}{30k_B} \quad (5.3)$$

In the research done so far ZnMnO_3 has been established as the source of the observed blocking behavior [106, 103]. In a series of samples of the same nominal composition, but synthesized by a different method, which were proven to be free of second phases, we do not observe superparamagnetic behavior, corroborating that ZnMnO_3 is responsible for blocking.

Calculated $\Theta(x)$ from fits given in Figs. 5.7 and 5.8 are given in Table 5.1. We conclude that the value of $\Theta(x)$ inferred from the fit of the high-temperature part of the $1/\chi(T)$ shows the value that is independent of the concentration. A homogeneous diluted magnetic semiconductor, with randomly distributed Heisenberg spins, according to a classic paper by Spalek et al. would exhibit an antiferromagnetic behaviour [50] in which the Curie-Weiss temperature is

Sample	T_B at 100Oe	$\Theta(x)$ at 1000Oe	$\Theta(x)$ at 100Oe	H_C at 5 K
2% Mn:ZnO	5.89 K	37 K	20 K	≈ 0 Oe
4% Mn:ZnO	6.5 K	23 K	22 K	70 Oe
6% Mn:ZnO	6.55 K	26 K	23 K	83 Oe
8% Mn:ZnO	6.71 K	21 K	19 K	105 Oe

Table 5.1: Values of Curie-Weiss temperature $\Theta(x)$ measured at 100 Oe and 1000 Oe, together with blocking temperatures T_B measured at 100 Oe for 2% - 8% Mn:ZnO powders. Coercive fields at 5 K deduced from Figure 5.10 are given in the last column.

expected to scale with the concentration as $\Theta(x) = \Theta_0 \cdot x$ where Θ_0 is the concentration independent temperature. However, we have measured Curie-Weiss temperatures independent of the concentration, consistent with $ZnMnO_3$ governing the magnetic interactions with blocking temperature determined by the size of the individual "needle" that only slightly increases with a fourfold increase in the Mn nominal concentration.

It is known that for magnetic nanoparticles, the formation of domain walls is energetically unfavorable [107], below a certain size particle staying in a single-domain configuration. The blocking temperature is alternatively defined as a particular temperature above which the thermal fluctuations dominate and there is no possibility of determining the preferred magnetization direction. The coercivity H_C and remanence M_R of such particle are both equal to zero. The actual transition is evident, yet gradual. The slow disappearance of the hysteresis above the blocking temperature is visible for the 6% Mn:ZnO sample and is shown in Fig. 5.10. The values of the coercive fields for the three temperatures are given at Table 5.2. Hysteresis is much more strongly pronounced in the case of the scan performed at 5 K (below $T_B = 6.55$ K) than at 15 K and 25 K (above T_B). A good example from the literature is the work by Shinde et al. [108] where the effect of the disappearance of the hysteresis is illustrated in the view of both the magnetic remanence M_R and the coercive field H_C going to zero. The authors have also noticed that the magnetization curves lie on top of each other at temperatures above the blocking temperature (Fig. 5.12).

In our samples, magnetic behavior can be further elucidated from field sweep measurements done using SQUID. We have done (-4T)-4T field scans of the 2% - 8% Mn:ZnO powders at the constant temperature of 5 K. As outlined above, as 5 K is lower than the ZFC-FC splitting

Temperature	H_C
5 K	83 Oe
15 K	10 Oe
25 K	16 Oe

Table 5.2: Values of coercive field for a 6% Mn:ZnO powder measured at temperatures of 5 K, 15 K and 25 K.

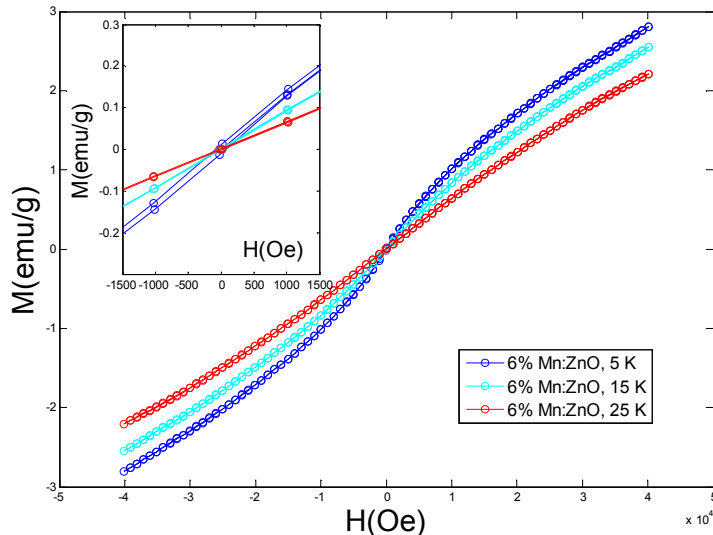


Figure 5.11: (-4 T)-4 T field sweeps of the 6% Mn:ZnO measured at 5 K (blue), 15 K (cyan) and 25 K (red). Inset: behavior of $M(H)$ curves around zero, showing an almost complete disappearance of hysteresis for 15 K (cyan) and 25 K (red) line.

temperature we expect to see a very small hysteresis superimposed on a paramagnetic Brillouin function representing a response of the dominantly paramagnetic, yet containing a small frozen part, system to the applied magnetic field. The field scans are shown in Figure 5.10. What is observed is the existence of hysteresis for the 4%, 6% and 8% samples. The 2% Mn:ZnO sample, however, shows none or a very small hysteresis cycle as visible from its very small coercive field, as noted on Table 5.1. This is due to the smaller average value of the $ZnMnO_3$ particles in the sample with lowest nominal Mn concentration.

The behavior of the system around the blocking temperature was more closely inspected by employing the AC field of different frequencies and observing the real part of the susceptibility, shown in Fig. 5.13. From the experimental work performed on an archetypal spin glass, CuMn [52] we know that a minute shift of the AC susceptibility peak is to be expected for the spin

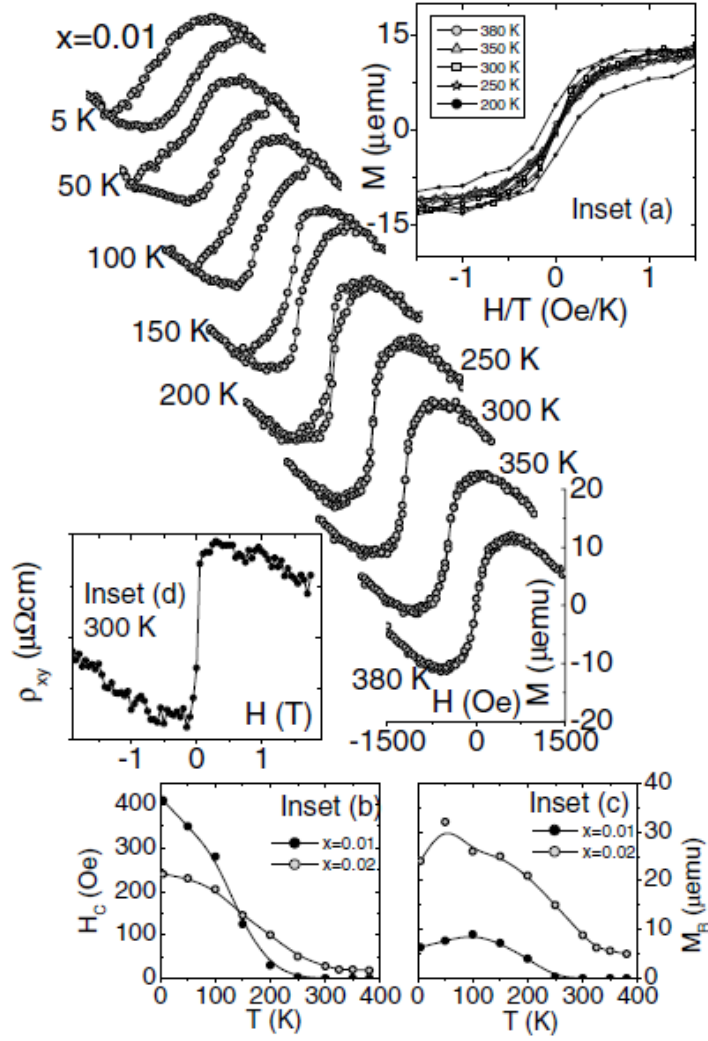


Figure 5.12: M-H curves for $\text{Ti}_{0.99}\text{Co}_{0.01}\text{O}_{2-\delta}$ film measured at different temperatures. Magnetization as a function of H/T for different temperatures is given in the inset (a). The temperature dependences of H_C and M_R for $\text{Ti}_{0.99}\text{Co}_{0.01}\text{O}_{2-\delta}$ and $\text{Ti}_{0.98}\text{Co}_{0.02}\text{O}_{2-\delta}$ films are shown in (b) and (c) respectively. Inset (d) shows the magnetic field dependence of Hall resistivity of the $\text{Ti}_{0.99}\text{Co}_{0.01}\text{O}_{2-\delta}$ film. Taken from [108].

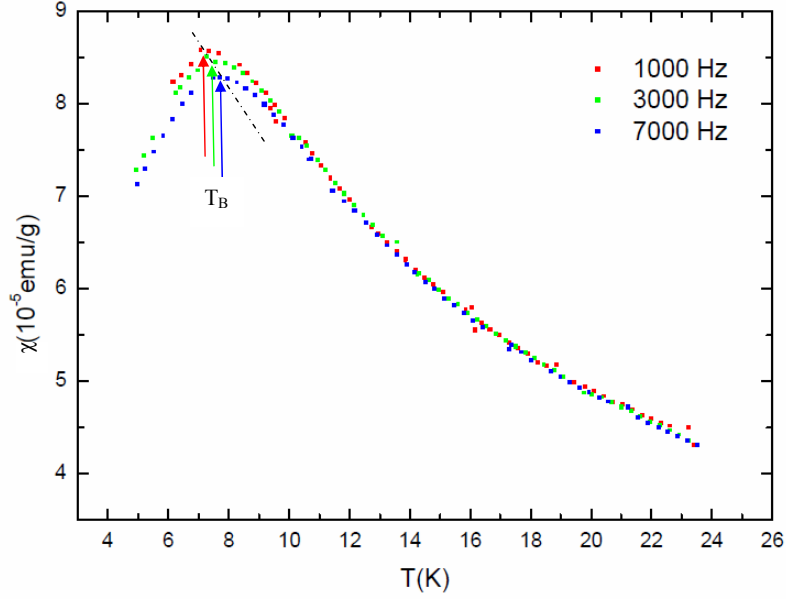


Figure 5.13: The real part of the susceptibility for a 4% Mn:ZnO powder under different AC excitation frequencies. A shift of the susceptibility peak at the blocking temperature is observed, indicated with the arrows.

glass - like system. The peak shift is realized through positive change in the position of the T_B as well as in the decrease of the corresponding peak value of the susceptibility. What distinguishes superparamagnetism from a canonical spin-glass is the shape of the field curve (FC) in the measurements done by SQUID, but also indirectly, the actual numerical value of the frequency shift $\Delta T_B/[T_B \Delta(\log \omega)]$ [105]. For our 4% Mn:ZnO sample, the expected behavior of the peak was observed, with the value of $\Delta T_B/[T_B \Delta(\log \omega)]$ calculated for the frequencies of 1000 Hz, 3000 Hz and 7000 Hz to be 0.042, which puts our 4% Mn:ZnO sample in between the documented superparamagnets such as $\alpha\text{-(Ho}_2\text{O}_3\text{)}(\text{B}_2\text{O}_3)\text{S}$ and canonical spin glasses such as CuMn or AuMn.

5.3 Electronic properties

The electronic properties of TM doped ZnO have been extensively studied in the past. As the electronic structure of substitutional Mn^{2+} is $[\text{Ar}]3d^54s^2$ and the s-electrons are the valence electrons, i.e. they go into the sp^3 bonding with oxygen giving Mn^{2+} in a tetrahedral

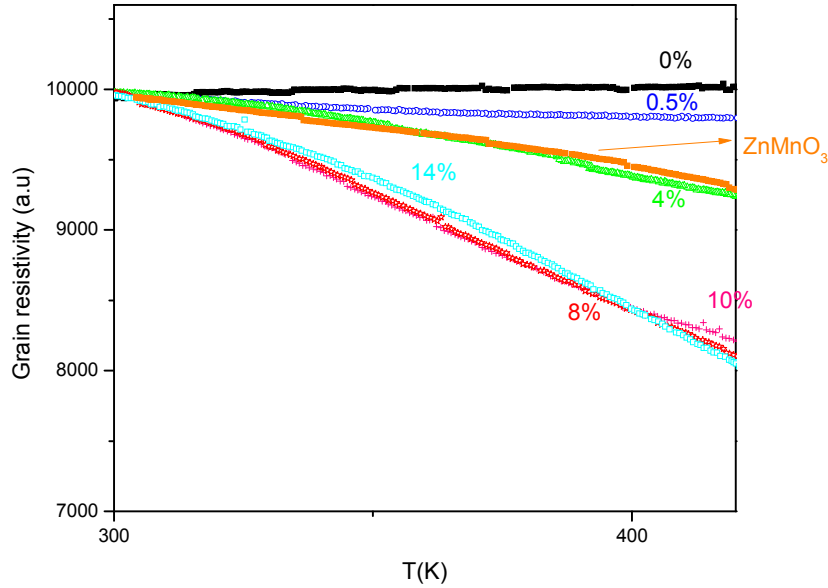


Figure 5.14: The AC conductivity measurements on 0.5% (blue), 4% (green), 8% (red), 10% (magenta), 14% Mn:ZnO (cyan) and ZnMnO₃ parasitic phase (orange). The referent undoped ZnO sample is given in black.

environment, typical of wurtzite structure materials, we do not expect an increase in activated conductivity when we are below solid state solubility limit of Mn in ZnO, suggested by some authors to be 13% for a bulk material [109]. Mn in different oxidation states, such as Mn³⁺ or Mn⁴⁺ n-dopes the system by providing one or two electrons, respectively, in the conduction band of the ZnO. Experimentally, Mn:ZnO doped ceramic powders were found to exhibit lower conductivity compared to the nominally undoped powders, a behavior confirmed in Mn:ZnO samples sintered at high temperatures [53], and in samples prepared by low-temperature processing [110].

In order to probe the electronic properties of the materials microwave (AC) conductivity measurements have been performed on 0.5 - 14% powder samples. The results are shown in Figure 5.14. Increase of the activated conductivity is well visible from the temperature dependence for up to 8% of the Mn in the sample. Higher doping seems not to result in an increase of the activated conductivity, but rather with the saturation of the conductivity.

5.4 Properties of ZnMnO_3

As the development of true, single-phase diluted magnetic semiconductors $\text{Zn}_{1-x}\text{TM}_x\text{O}$ is plagued by the formation of parasitic phases with a high TM/Zn ratio as soon as the solid state solubility limit is reached, special importance is starting to be awarded to the study of magnetic properties of materials where TM and Zn concentrations are of the same order of magnitude. The phases which oxidated Mn ions can form with Zn and O are numerous, such as ZnMnO_3 [106], $\text{Mn}_{2-x}\text{Zn}_x\text{O}_{3-\delta}$, Mn_3O_4 [85]. Other catalogued phases include haeterolite ZnMn_2O_4 [103, 111] and chalcopanite ZnMn_3O_7 .

Blasco et al. [103] have explored the Zn-Mn-O phase diagram at low temperature by using starting materials in a nano-size scale. They have synthesized nominal $\text{Mn}_{3-x}\text{Zn}_x\text{O}_4$ samples ($1 \leq x \leq 2$) following a *sol-gel* method that permitted the formation of crystal compounds at a relatively low temperature. The citrate route was used, whereby the stoichiometric amounts of ZnO and MnCO_3 were dissolved in nitric acid solution. The citric-acid and ethylene-glycol were added to obtain light-yellow solutions. These were then heated up to gel formation. The gel was subsequently fired at 210°C overnight. The resulting brown resin was calcined in air at 400°C for 6 h. The powder was then pressed into pellets and heated at temperatures ranging from 450°C to 800°C .

Peiteado et al. have extended Blasco et al.'s study to higher temperature by using co-precipitation as the synthesis method, referring to the method originally developed by Bouloudenine et al. [79], and given in Section 3.2.

Blasco et al. obtained a diagram of phases given in Fig. 5.15. This diagram can be entitled $\text{Mn}_{3-x}\text{Zn}_x\text{O}_4$ $1 < x < 2$ phase-diagram at temperatures up to 750°C . Summarizing the Fig. 5.15, at temperatures $T < 670^\circ\text{C}$ $1 < x < 1.05$ the system is roughly an "H phase" - haeterolite ZnMn_2O_4 , a tetragonally distorted spinel, isomorphic to Mn_3O_4 . For $1.05 < x < 1.55$ the system is a mixture of an H phase and C phase, where C phase is a cubic spinel isomorphic to ZnMnO_3 . Blasco et al. further concluded that for $1.55 < x < 1.72$ the system consists of almost pure C-phase while for $1.72 < x < 2$ the system is a mixture of the C-phase and ZnO.

Peiteado et al. [111] obtained the phase diagram of the Zn-Mn-O given in the Fig. 5.16.

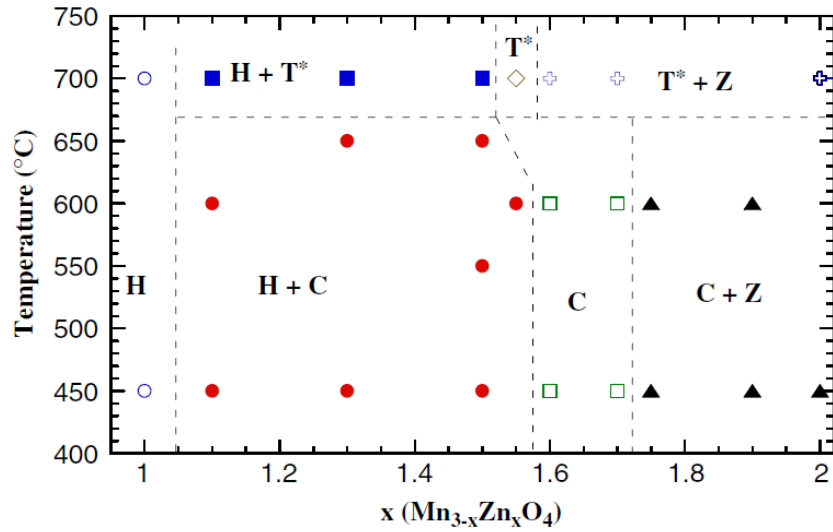


Figure 5.15: The low temperature phase diagram of Zn-Mn-O as proposed by Blasco et al. [103]. The T, Z, C and H denote tetragonal spinel, zincite, cubic phase and haeterolite, respectively. Taken from [103].

The low-temperature phase diagram coincides fairly well with the phase diagram obtained by Blasco et al. The system consists of two phases depending on the quantity of Zn and is either a T_1 (standard haeterolite) + C, or C + Z phase. Above 650 °C the cubic phase C gets tetragonally distorted creating a new tetragonal phase, T_2 meaning that the two fields are now $T_1 + T_2$ and $T_2 + Z$. Above 1300°C T_2 gets transformed into a T_1 phase, leaving the whole Zn concentration range to $T_1 + Z$ phase. The authors explain all the results obtained through the quantity of Mn^{3+} in $Mn_{3-x}Zn_xO_4$. Mn^{3+} has a d^4 electronic configuration which makes it a strongly active Jahn-Teller ion. Effectively, the distortion leads to the change of symmetry, from cubic at the low temperature to highly distorted tetragonal at high temperatures. This suggests that an octahedron of ligands around Mn(III) is distorted in such a way that $c/a > 1$. For compositions with $x > 1$ above 650 °C Mn^{4+} gets reduced to Mn^{3+} leading to the subsequent distortion of the structure and formation of the T_2 phase, a new tetragonal spinel with the space group $I41/amd$. With the increase in temperature the additional distortion of the T_2 phase occurs resulting with the change of the final precipitation of the T_2 phase to the maximally distorted T_1 phase and the high-temperature phase diagram effectively consisting of the $T_1 + ZnO$ phase.

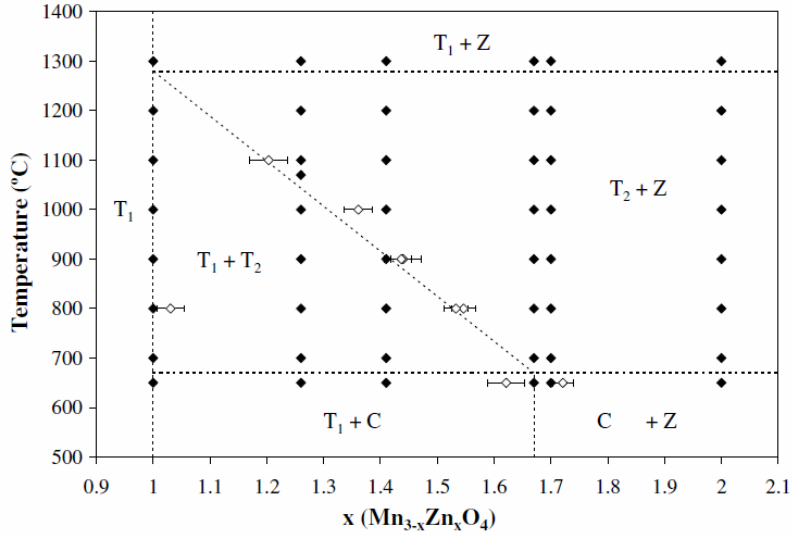


Figure 5.16: The high temperature phase diagram of Zn-Mn-O as proposed by Peiteado et al. [111]. The T_1 phase is the tetragonal spinel, haeterolite $ZnMn_2O_4$, T_2 is the tetragonal spinel, C is the cubic spinel and Z is ZnO.

5.4.1 Synthesis and Structural properties

Using low-temperature decomposition of Mn and Zn nitrates, we have synthesized $Zn_{1-x}Mn_xO$ $0.02 < x < 0.08$, as described in Section 5.1. At 400°C and 700°C , in all the concentration range probed the additional presence of a phase isomorphic to $ZnMnO_3$ with $(1-x):x$ at 0.6:0.4 was noted. Morphologically the particles resembled "needles", hence they were a lot longer than thick (Fig. 5.17(a)). Supposing $Mn_{3-x}Zn_xO_4$ is the right stoichiometry this puts us in the phase diagram region with $x=1.2$ (H+C phase). The 700°C decomposition temperature also saw the presence of $(1-x):x=0.5:0.5$ particles (Fig. 5.17(b)), but with an equiaxed shape, reserving the $(1-x):x=0.6:0.4$ composition for needle morphology. At 900°C we have observed the $(1-x):x$ ratio move to 0.4:0.6 (Fig. 5.17(c)), hence $x=1.8$ in the Blasco picture (C phase+ZnO). The morphology of our samples was also highly dependent on the temperature used. Decomposition at 300°C (Fig. 5.17(d)) was not sufficient to produce ZnO fully decomposed and it appears that a Mn-rich shell of Mn ($0.08 < x < 0.11$, points B and C) was found to be encircling the core of the particles with a significantly lower Mn-concentration ($x=0.003$, point A).

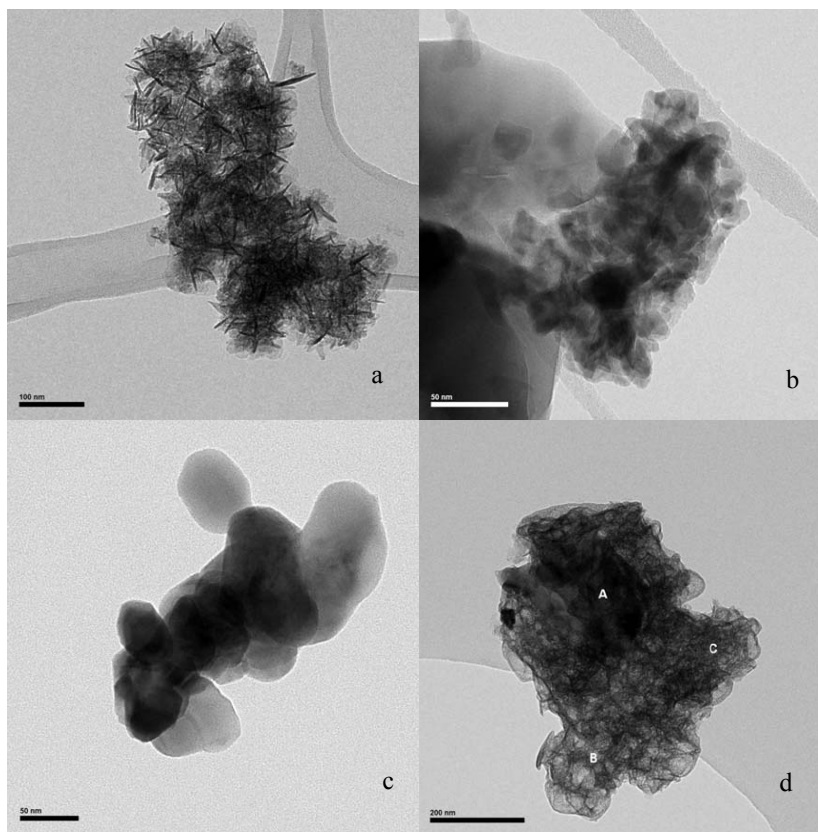


Figure 5.17: TEM images of Mn-Zn-O phases produced by high-temperature decomposition of Mn:Zn nitrates at (a) 400 °C, (b) 700 °C, (c) 900 °C and (d) 300 °C.

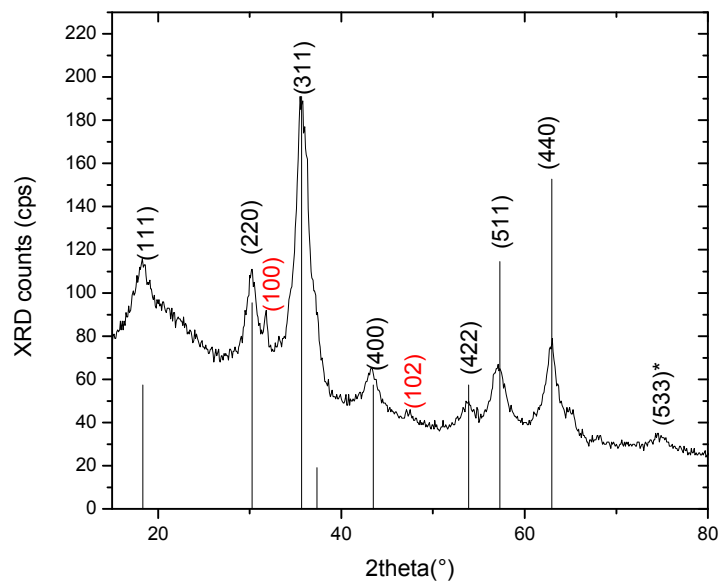


Figure 5.18: XRD of the ZnMnO₃ powder, showing reflections of the Fd-3m ZnMnO₃ structure (black) and ZnO wurtzite structure (red).

In the literature ZnMnO_3 - like phase has been found to invoke spin-glass behaviour in $\text{Zn}_{1-x}\text{Mn}_x\text{O}$ samples found to contain it [106] and on its own [103]. As demonstrated in Section 5.2, we have observed the analogue behaviour for our $\text{Zn}_{1-x}\text{Mn}_x\text{O}/\text{ZnMnO}_3$ samples, evident in the frequency shift of the ZFC curve maximum to lower values and higher temperatures. The detailed characterization of the macroscopic magnetic properties of the ZnMnO_3 obtained as a pure phase was however, still lacking. First, a pure ZnMnO_3 had to be synthesized. In order to oxidize an as high as possible proportion of Mn^{2+} into Mn^{4+} in our sample, we have heat-treated the powder produced using the method described in Section 5.1 at 400°C for 11 hours under oxygen flow. The temperature of 400°C was used in order to avoid any temperature driven morphological changes. The XRD of the sample produced is given in 5.18. All the major reflections of ZnMnO_3 are present together with a reflection indicating a small amount of ZnO present.

The equivalent XRD scan has recently been found by Saraf et al. [112] as synthesized by the sol-gel method. The structure of ZnO was found to evolve gradually from ZnO through $\text{Zn}_{1-x}\text{Mn}_x\text{O}$ to $\text{Zn}_{1-x}\text{Mn}_x\text{O}/\text{ZnMnO}_3$ to finally ZnMnO_3 .

5.4.2 Magnetic properties

The powder obtained was measured using SQUID ZFC-FC measurement as described in the Section 5.2. The temperature interval in which we measured the magnetization of ZnMnO_3 was 2 K to 300 K. As outlined earlier, the existence of low-temperature splitting between these two curves is attributed to either spin-glass freezing or the appearance of superparamagnetism. Such splitting was observed in our sample. The SQUID magnetization measurements show the splitting which begins at 12 K with a characteristic maximum in ZFC curve susceptibility close to 4 K. The sudden drop in the magnetization is attributed to the artefact that the SQUID measurements often exhibit at 4.2 K, the boiling temperature of liquid helium. This behaviour is very similar to the magnetization profile obtained by Blasco et al. for their $\text{Mn}_{1.3}\text{Zn}_{1.7}\text{O}_4$ sample confirming that the glassy transition originates from a high Mn concentration phase isomorphic to ZnMnO_3 .

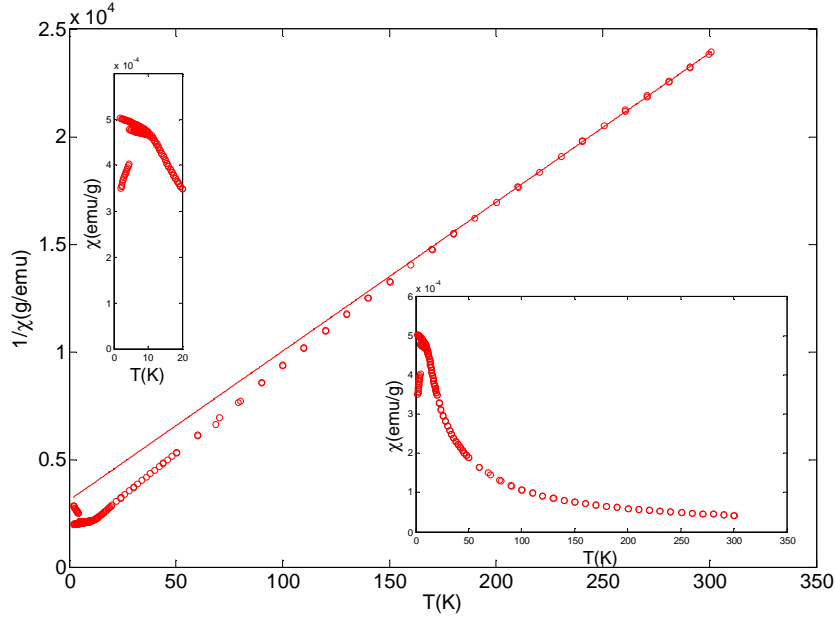


Figure 5.19: ZFC-FC SQUID measurements of a ZnMnO_3 phase. The splitting which begins at 12 K together with a characteristic maximum in ZFC curve susceptibility close to 4 K are observed.

Magnetization measurements of the aforementioned $\text{Mn}_{1.3}\text{Zn}_{1.7}\text{O}_4$ as well as the Curie-Weiss fit to the inverse susceptibility of $\text{Mn}_{1.4}\text{Zn}_{1.6}\text{O}_4$ produced in the study of Blasco et al. are given, for comparison in the Fig. 5.20. As can be seen from the Figure 5.20 the ZFC-FC splitting of the $\text{Mn}_{1.3}\text{Zn}_{1.7}\text{O}_4$ sample is attributed to the spin-glass behaviour but the line between the superparamagnetism and the spin-glass is known to be a thin one in the literature and is actually determined from the value of the shift of the peak with the frequency of the AC field applied, as discerned from the inset to the Fig. 5.20 (a).

Like our ZnMnO_3 , the material here exhibits Curie-Weiss behaviour with an antiferromagnetic Curie-Weiss temperature. The splitting is present at the similar temperature of 14 K, while the T_{CW} of our sample of -33 K which is close to the given value for the $\text{Mn}_{1.3}\text{Zn}_{1.7}\text{O}_4$ sample, which is -35.5 K.

We have performed the measurements on a standard X-band ($\nu \approx 9.4\text{GHz}$) Bruker spectrometer on the ZnMnO_3 sample in the temperature range of $4 < T < 300$ K. The measurements are given in the Fig. 5.21. We were able to fit the signal to a single Lorentzian line for all the temperatures studied. From the fit we deduced, principally, the linewidth of the signal, as

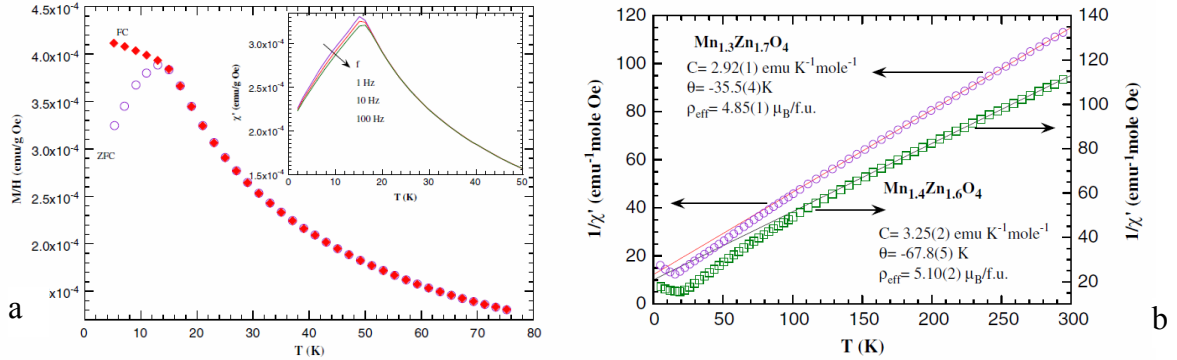


Figure 5.20: (a) ZFC-FC SQUID measurements on a $\text{Mn}_{1.3}\text{Zn}_{1.7}\text{O}_4$ phase synthesized by Blasco et al. [103] Inset: The peak shift when applying AC field of frequencies of 1, 10 and 100 Hz (b) The inverse of the magnetic susceptibility for $\text{Mn}_{1.3}\text{Zn}_{1.7}\text{O}_4$ and $\text{Mn}_{1.4}\text{Zn}_{1.6}\text{O}_4$ yielding to antiferromagnetic Curie-Weiss temperatures. Taken from [103].

given in Fig. 5.23. It has been shown to exhibit a divergence of linewidth at the temperature of 15 K. Another very valuable information is the room temperature linewidth in the vicinity of 2000 G, which is close to the saturation value of the linewidth in the $\text{Zn}_{1-x}\text{Mn}_x\text{O}/\text{ZnMnO}_3$ samples ($\Delta H_{pp} \approx 2400$ G). We have hence proven the existence of the transition at the temperature close to 15 K which was seen in the SQUID measurements. Moreover, we have proven that the saturation ESR linewidth of the $\text{Zn}_{1-x}\text{Mn}_x\text{O}/\text{ZnMnO}_3$ series of samples with the addition of Mn (See Fig. 4.2) approaches the room temperature ESR linewidth of the ZnMnO_3 phase corroborating that ZnMnO_3 phase is responsible for the broad line component of the $\text{Zn}_{1-x}\text{Mn}_x\text{O}/\text{ZnMnO}_3$ spectra, which hence does not come from diluted Mn interacting in the ZnO matrix.

The extracted data are shown in the next Section together with the ESR data obtained through measurements performed using the high-field ESR setup.

5.4.3 High-field,high-frequency ESR study

Together with the low-field ESR data, the high-field ESR data were as well successfully fitted to a single Lorentzian line in Wolfram Mathematica 7.0. , as illustrated in Fig. 5.22.

The ESR linewidth(G) vs temperature(K) for low and high field measurements of the ZnMnO_3 powder is given in Fig. 5.23. One quickly observes a move of the linewidth to very

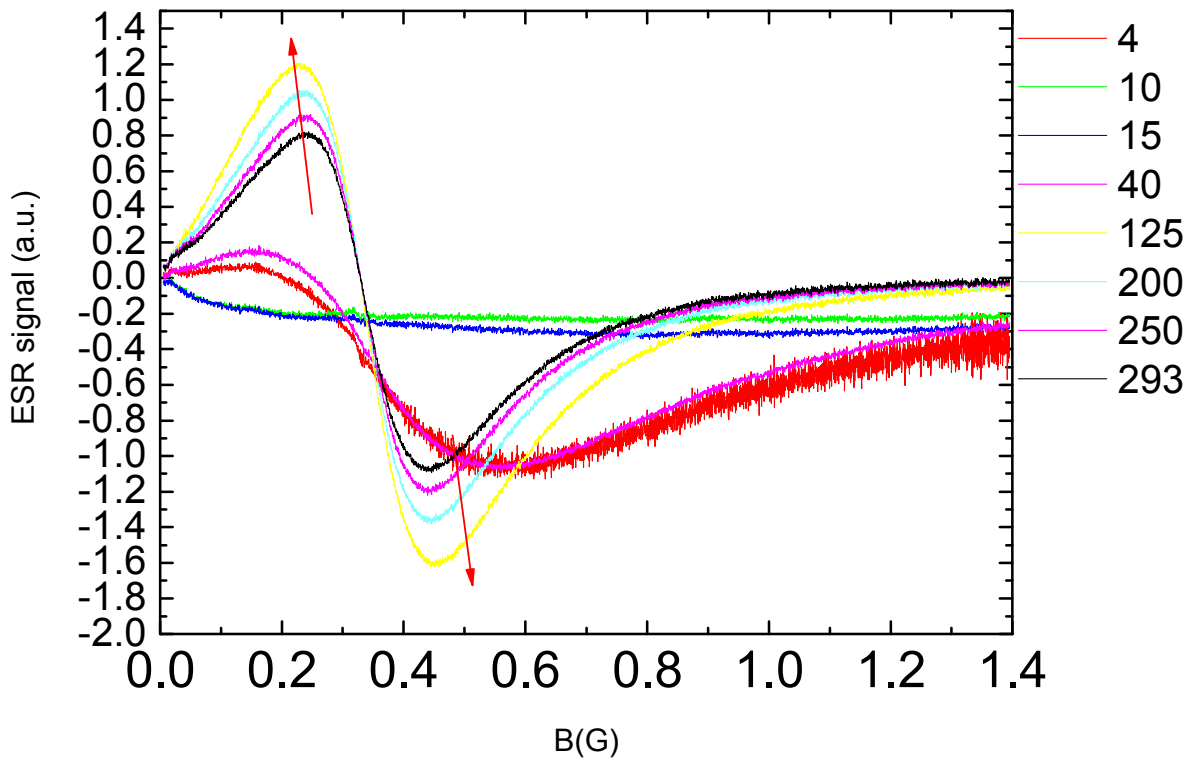


Figure 5.21: 4 - 300 K ESR measurement done on the ZnMnO_3 phase revealing a divergence of the linewidth at 15 K together with the room-temperature linewidth $\Delta H_{pp} \approx 2000$ G, which is a similar value to the value of the saturation ESR linewidth obtained in the $\text{Zn}_{1-x}\text{Mn}_x\text{O}/\text{ZnMnO}_3$ system ($\Delta H_{pp} \approx 2400$ G).

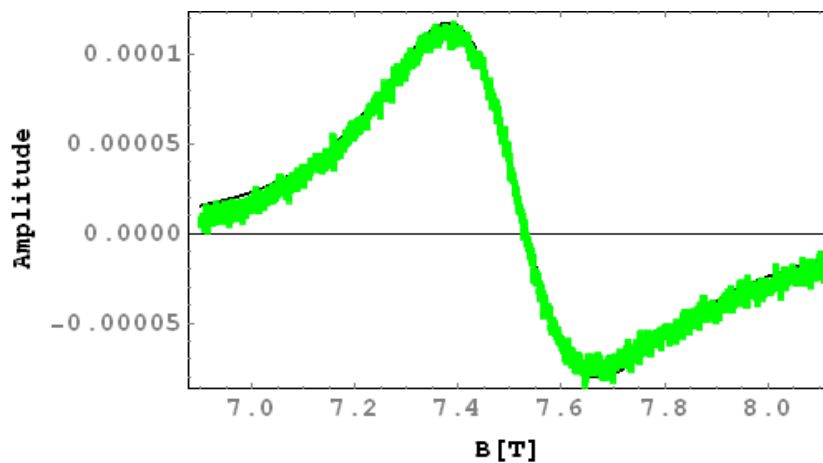


Figure 5.22: An example to the signal of the ZnMnO_3 in a high-field ESR setup at the measuring frequency of 210 GHz, together with a fit to a derivative Lorentzian.

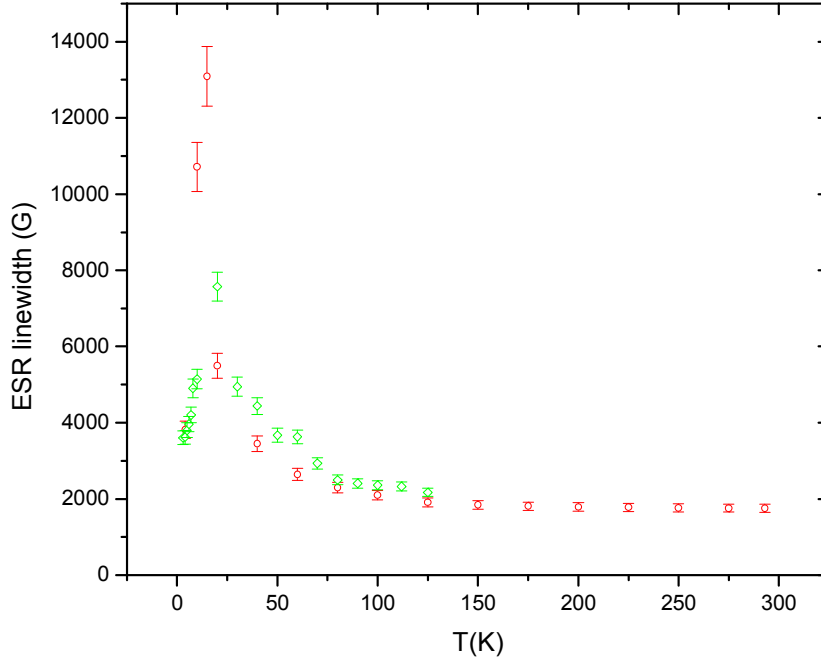


Figure 5.23: The ESR linewidth of the ZnMnO_3 measured in a conventional 9.4 GHz X-band spectrometer (red) and the high-field ESR setup at the measuring frequency of 210 GHz (green). The divergence of the ESR linewidth is present at the temperature close to 15 K for both frequencies used.

high values in the 10-20 K temperature regime, pointing to the fact that the actual magnetic transition temperature is higher than 5 K and that the temperature to focus on is the onset of ZFC-FC splitting (cf. Fig 5.19. - onset of splitting 12 K , while a sudden drop in susceptibility is close to 4 K). The diverging nature of the linewidth for 10 K and 15 K is pointing to an antiferromagnetic nature of the transition, however, this is not a unique signature for antiferromagnets as spin-glasses can exhibit a similar behaviour [113]. In combination with the results of SQUID measurements we attribute this transition to a spin-glass-like one.

5.4.4 Electronic properties

The electronic conductivity of $\text{Zn}_{1-x}\text{Mn}_x\text{O}$ was measured by measuring the temperature dependence of the quality (Q) factor of the microwave cavity used in the standard electron spin resonance (ESR) measurement. As described in Section 5.3 it was found that $\text{Zn}_{1-x}\text{Mn}_x\text{O}$ powders produced by the nitrate decomposition method show an increase in conductivity with

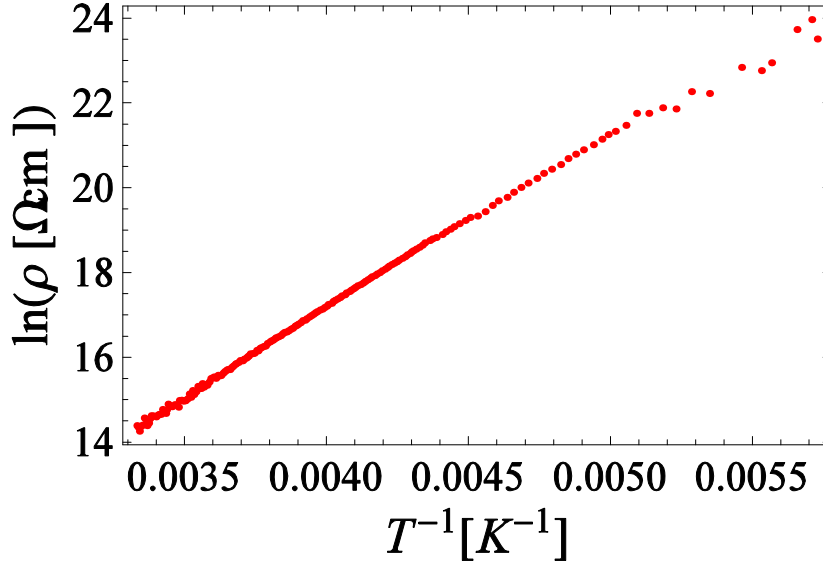


Figure 5.24: A logarithm of the resistivity of $ZnMnO_3$ plotted against the inverse of the temperature. The fit to the exponential dependence of resistivity on T yields the activation energy $\Delta = (0.7 \pm 0.1)$ eV.

an increase in x until the saturation is reached at $x \approx 0.08$. By measuring the AC conductivity of the $ZnMnO_3$ we were able to quantify the contribution of $ZnMnO_3$ parasitic phase to the magnetism of $Zn_{1-x}Mn_xO/ZnMnO_3$ produced by the decomposition of $Zn_{1-x}Mn_x(NO_3)_2$. The results are given in the Figure 5.14. The $ZnMnO_3$ was found to induce the observed increase in conductivity with temperature dependence of the conductivity analogous to the one noticed in $Zn_{1-x}Mn_xO$ samples. One has to note that the mass of the powder, itself proportional to the change in the Q factor samples is 8 fold lower in the case of $ZnMnO_3$ than in the remaining $Zn_{1-x}Mn_xO$ powders synthesized. The actual conductivity of $ZnMnO_3$ is hence even higher, making it plausible that it is the phase responsible for the conductivity increase in the $Zn_{1-x}Mn_xO/ZnMnO_3$ system.

5.4.5 Thermopower and DC conductivity

The fundamental experimental data concerning the transport study of $ZnMnO_3$ are the resistivity and thermo-electric power (TEP) as a function of temperature. The measurements were performed on a pressed pellet of $ZnMnO_3$. Resistivity was measured by a four probe DC

method with TEP compensation, and TEP was measured by DC and AC method. The sample was shaped in a rectangular bar (typical dimensions $0.8 \times 0.6 \times 0.15 \text{ mm}^3$) and placed horizontally on a ceramic heater and subsequently contacted with silver paste on pre-deposited gold pads. This configuration allows a simultaneous measurement of resistivity (in a four probe configuration), and thermo-electric power. In the TEP measurements the temperature gradient was measured by a calibrated chromel/constantan differential thermocouple. All measurements were performed in the 170-300 K temperature range at ambient pressure. Due to the very high resistance of the sample we have not been able to measure below the temperature of 170 K since the measured resistivity exceeded $10^{12} \Omega$.

In Figure 5.24 the logarithm of the resistivity of the sample is plotted as a function of the inverse temperature. The dependence is linear, indicating the activated nature of the conductivity, which can be described by the theoretically well-founded relation, established by Wilson [114] for the case of semiconductors:

$$\rho = \rho_0 e^{-\Delta/2k_B T} \quad (5.4)$$

where the activation energy, Δ was found to be 0.7 eV (8100 K). This can be interpreted as the ionization energy of an impurity level, since the gap of pure ZnO is about 3.3 eV [115]. Eq. 5.4 is only valid if the number of charge carriers is much lower than the number of impurities, which means that the temperature should be much lower than the gap, and that there should be only one type of impurity present: $N_A \gg n_0 \gg N_D$, where N_A is the number of acceptors, n_0 the number of excited carriers and, N_D that of the donors. The fact that the activation energy is rather high assures the applicability of 5.4.

In order to determine the sign of the charge carriers we have measured thermo-electric power (TEP) in the same temperature interval as we did for the resistivity. The result is shown in Fig. 5.25. The positive sign of TEP points to hole-like charge carriers and therefore to the acceptor nature of impurities. The high value of TEP even at room temperature indicates a very low number of charge carriers and a further decrease of that number with decreasing temperature. The temperature dependence of TEP in Fig. 5.25 is a typical illustration of

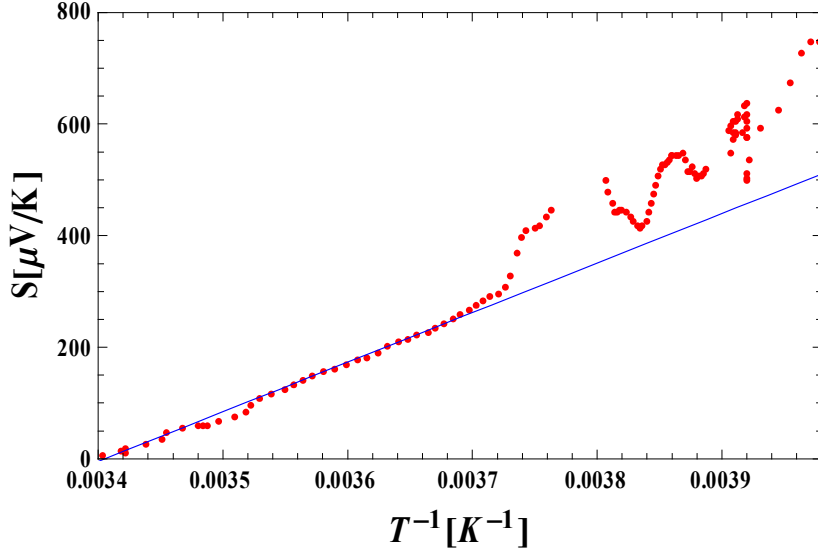


Figure 5.25: Thermopower measurements on ZnMnO_3 sample. The value obtained for the activation energy from the thermopower measurements is $\Delta = (0.8 \pm 0.1)$ eV, consistent with the conductivity measurements (cf. Fig. 5.24).

semiconducting behavior: $S \propto 1/T$. Below 260 K, the resistance of the sample exceeded $10^9 \Omega\text{cm}$. The huge sample resistance as well as contact resistances during measurements caused noise comparable to the signal. This is the explanation of the scattering of the measured TEP values. Nevertheless, the obtained trend is still similar to the one observed at higher temperatures. One way to verify consistency of the results is to compare resistivity and TEP results. Theory [116] predicts that TEP for the case of semiconductors should vary as:

$$S = \frac{-k_B}{e} \left(r + \frac{5}{2} + \frac{\epsilon_F}{k_B T} \right) \quad (5.5)$$

where, ϵ_F is the Fermi energy, and r describes deformation potential scattering. Furthermore, theory [116] says that when temperature is moderate, ϵ_F can be approximated by the following relation:

$$\epsilon_F \longrightarrow E_v + E_a \quad (5.6)$$

Once we verified the position of the Fermi level, one can immediately determine the band gap by using the relation 5.5. Fitting TEP results in the 260-300 K temperature range (where

smooth data were observed) we have found $\Delta = (0.8 \pm 0.1)$ eV.

5.4.6 Conclusion

In this Chapter we have shown that starting from high-quality precursors with homogeneously distributed TM species does not have to be the recipe for success. Oxidative conditions in the case of Mn as TM ion have led to the formation of a number of Mn in the 4+ oxidation state. The Mn in the 4+ oxidation state formed a ZnMnO_3 second phase which caused the low-temperature superparamagnetic freezing. We have however used this method to synthesize the ZnMnO_3 and to qualify exactly which magnetic properties this phase attributes to the system of $\text{Zn}_{1-x}\text{Mn}_x\text{O}/\text{ZnMnO}_3$. The increase of conductivity through the smaller energy band-gap of 0.7 eV, the $\Delta H_{pp} \approx 2000$ G room-temperature ESR line, the ZFC-FC splitting at 12 K are all properties of ZnMnO_3 that can explain the presence of the broad line in ESR spectra, the ZFC-FC splitting in the SQUID scan and the increase in the conductivity of the $\text{Zn}_{1-x}\text{Mn}_x\text{O}/\text{ZnMnO}_3$ system.

The method hence has to be improved to synthesize single-phase materials that we can use to probe the inherent magnetism. This is the subject of the next Chapter.

Chapter 6

Properties of $\text{Zn}_{1-x}\text{TM}_x\text{O}$ produced from TM doped hydrozincites

As described in Chapter 4 we have synthesized highly homogeneous $(\text{Zn}_{1-x}\text{TM}_x)_5(\text{OH})_6(\text{CO}_3)_2$ precursors for TM = Mn, Co and Ni for the synthesis of $\text{Zn}_{1-x}\text{TM}_x\text{O}$. This Chapter will explain the methods of synthesizing $\text{Zn}_{1-x}\text{TM}_x\text{O}$ from $(\text{Zn}_{1-x}\text{TM}_x)_5(\text{OH})_6(\text{CO}_3)_2$ by the ways of thermal decomposition or e-beam decomposition. It will also consider the structural characterization of the final products, $\text{Zn}_{1-x}\text{Mn}_x\text{O}$, $\text{Zn}_{1-x}\text{Co}_x\text{O}$ and $\text{Zn}_{1-x}\text{Ni}_x\text{O}$. The Chapter will give the most important results on the magnetic properties of these diluted magnetic oxides.

6.1 Hydrozincite decomposition

In Chapter 4 we have introduced the novel precursor, $(\text{Zn}_{1-x}\text{TM}_x)_5(\text{OH})_6(\text{CO}_3)_2$, the TM doped hydrozincite, and named its many advantages, such as the homogeneous distribution of TM species and the low temperature synthesis. TM doped ZnO can be produced from TM doped hydrozincite in two principal ways.

Thermal decomposition

Hydrozincite materials undergo decomposition when heated at 400°C along the reaction

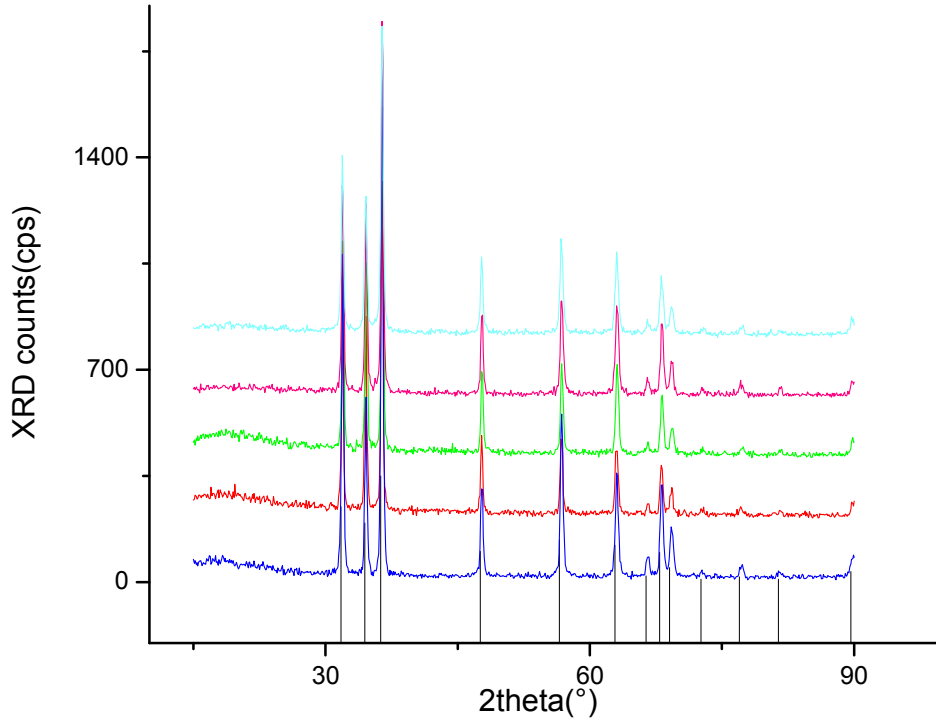
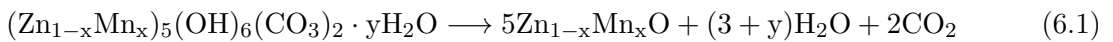


Figure 6.1: The XRD measurements on the $x=0$ (blue), $x=0.005$ (red), $x=0.1$ (green), $x=0.4$ (magenta) and $x=0.8$ (cyan) $Zn_{1-x}Mn_xO$ produced by thermal decomposition of $(Zn_{1-x}Mn_x)_5(OH)_6(CO_3)_2$ in air at $400^\circ C$ revealing only $P6_3mc$ wurtzite reflections of ZnO, indicating the likely single-phase nature of the final $Zn_{1-x}Mn_xO$ product.



We have followed the strategy employed in the section 4.2 to determine the structure of the product. The single phase nature of the sample, the phase being the one of the host semiconductor was first checked using XRD. The space group in which ZnO crystallizes is $P6_3mc$ (See Section 3.1.1). The Graph showing the XRD performed on a series of samples produced in air is given in Fig. 6.1. One can infer only the $P6_3mc$ wurtzite reflections of ZnO, hinting to the single-phase nature of the final ZnO product.

As the properties of the $Zn_{1-x}Mn_xO$ produced by this method have proven susceptible to changes in synthesis parameters, with the atmosphere of decomposition being among the most

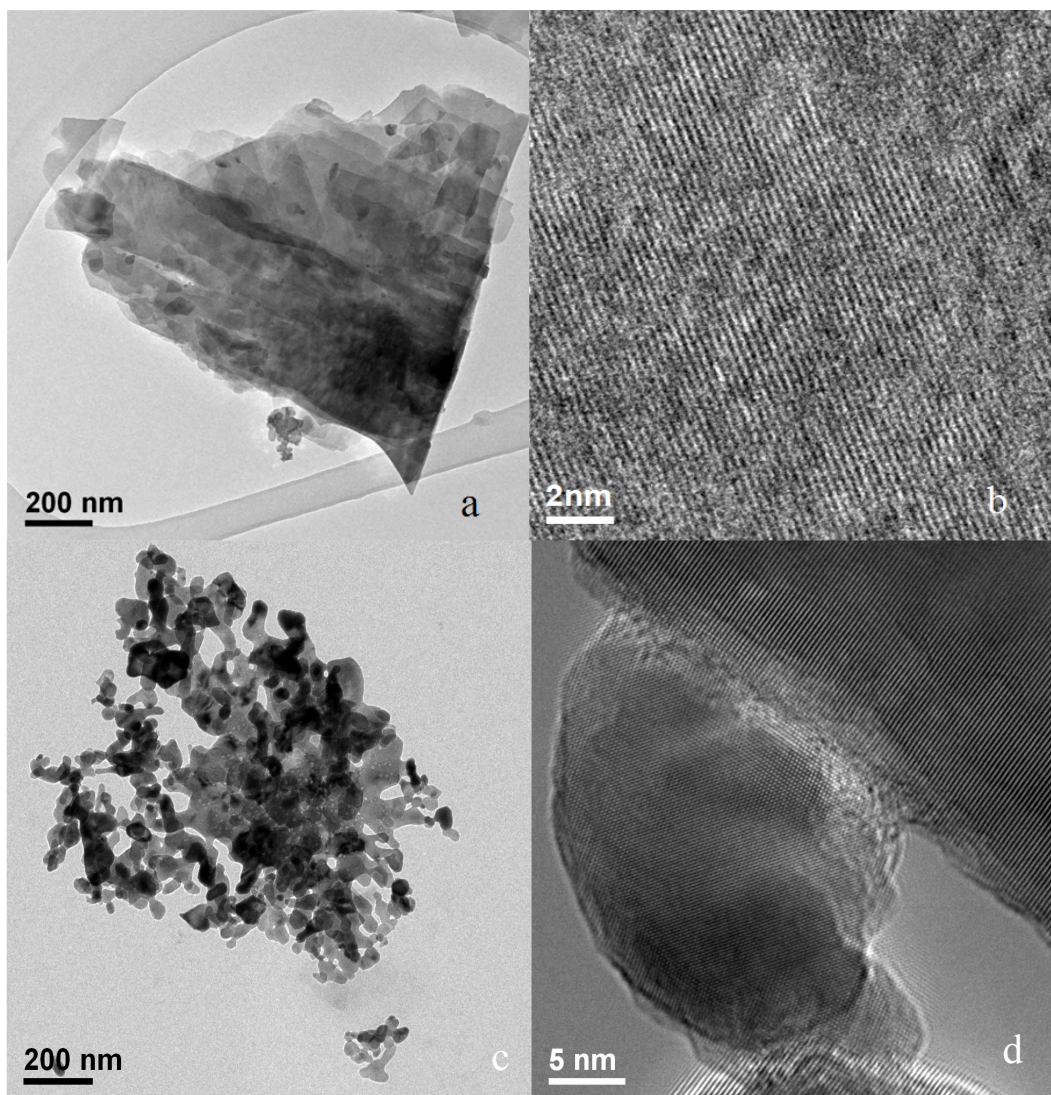


Figure 6.2: Thermal decomposition of $(\text{Zn}_{1-x}\text{Mn}_x)_5(\text{OH})_6(\text{CO}_3)_2$ to produce $\text{Zn}_{1-x}\text{Mn}_x\text{O}$. A reference TEM (a) and HRTEM (b) image of hydrozincite precursor. TEM micrographs of $x=0.012$ $\text{Zn}_{1-x}\text{Mn}_x\text{O}$ thermally decomposed under $\text{N}_2\text{-H}_2$ (c). A range of lattice fringes in the HRTEM image shows the nanocrystallinity of the Mn-doped ZnO (d).

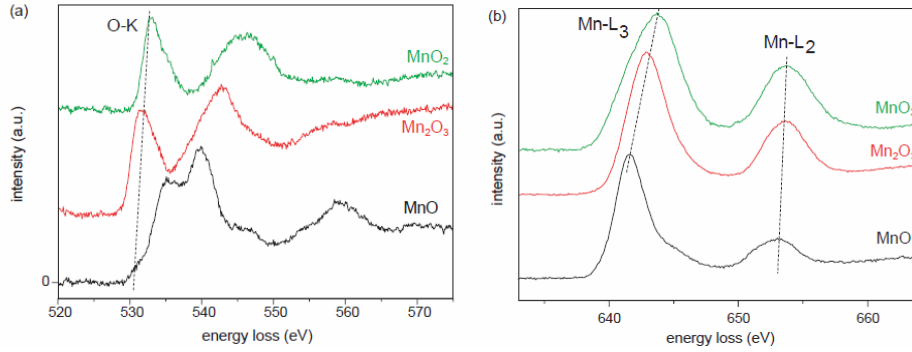


Figure 6.3: Comparison of ELNES data deduced from EELS measurements for sets of three manganese oxides, MnO, Mn₂O₃ and MnO₂ with the characteristic oxygen edge (a) and manganese edge (b) shown by vertical lines vertically displaced for clarity. Taken from [117].

important factors we have as well studied Zn_{1-x}Mn_xO produced in reducing atmosphere of N₂-H₂. TEM images of the samples produced at 400°C in N₂-H₂ were taken and they are given in the Figure 6.2 (c,d). The sample synthesized at 400 °C in N₂-H₂ showed purely Mn doped ZnO phase with grains about 20-100 nm in diameter. This signifies that the 400°C is the optimal temperature where one can consider the synthesis of Zn_{1-x}Mn_xO being accomplished. It was this temperature that was fixed as the synthesis temperature for the remainder of Zn_{1-x}TM_xO synthesis.

Electron energy loss spectroscopy, or EELS, technique is an important tool for inferring the valence state of the dopant, typically elements of the transition metal ion series [118]. Upon traversing a TEM specimen, a significant number of electrons have lost energy to core excitations or plasmons, leaving the specimen with energies less than the energy of the incident electrons, E₀. Electrons with equal energy are dispersed by magnetic field to trajectories with equal curvatures. Applied to systems important for us EELS is used coupled with electron energy-loss near-edge structure (ELNES). When wanting to infer the oxidation state, of, e.g. Mn, we perform the near-edge EELS measurement close to the L_{2,3} edge of manganese Mn. The different oxidation states of Mn will then result in a shifted L_{2,3} structure. This is illustrated [117] in the ELNES EEL spectra for the Mn in three typical manganese oxides, MnO, Mn₂O₃ and MnO₂, with the spectra taken at O-K edges and Mn-L_{2,3} edges, vertically displaced for clarity.

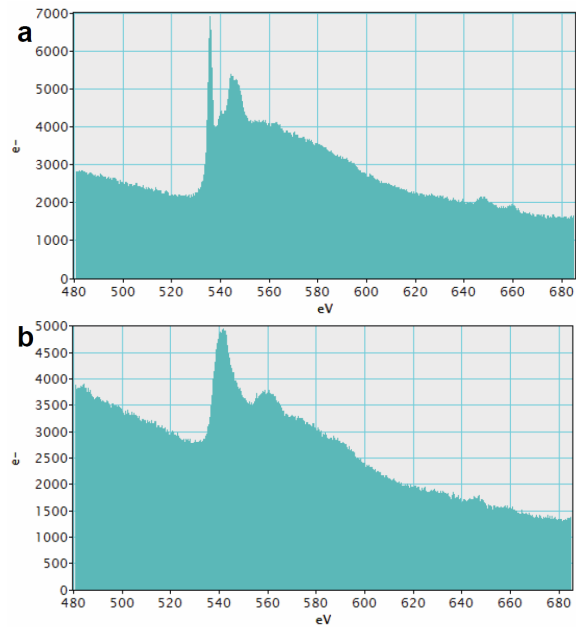


Figure 6.4: An EELS signal as observed on (a) $(\text{Zn}_{1-x}\text{Mn}_x)_5(\text{OH})_6(\text{CO}_3)_2$ and (b) $\text{Zn}_{1-x}\text{Mn}_x\text{O}$, where $\text{Zn}_{1-x}\text{Mn}_x\text{O}$ was produced by decomposing $(\text{Zn}_{1-x}\text{Mn}_x)_5(\text{OH})_6(\text{CO}_3)_2$ using a high-energy TEM electron beam. A significant change in the ≈ 530 eV O K-edge fine structure bears witness to the achieved crystallization. This effect allows for Mn content to be directly correlated to the precursor phase.

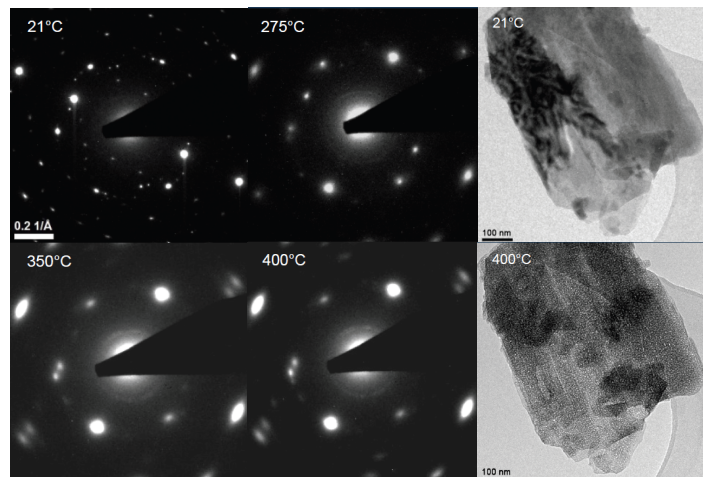


Figure 6.5: The effects of in-situ heating of $(\text{Zn}_{1-x}\text{Mn}_x)_5(\text{OH})_6(\text{CO}_3)_2$, producing a defected form of $\text{Zn}_{1-x}\text{Mn}_x\text{O}$ structurally based on the hydrozincite lattice. A gradual loss is visible in the SADP from 21°C (a), over 275°C (b) and 350°C (c) to 400°C (d).

The EELS technique was used in team with scanning transmission electron microscope (STEM) to analyze the compositional uniformity of Mn dopant in hydrozincite matrix. This was performed using the 640-660 eV Mn-L₃ and Mn-L₂ lines, as previously explained. The scanned beam was able to recrystallize the hydrozincite to ZnO, as manifested by a significant change in the 530 eV O K-edge fine structure as can be inferred from the Fig. 6.4 shown in (a) to (b) above. This allows us to relate the Mn content directly to the precursor phase, avoiding possible influences of transformation-induced Mn diffusion on the compositional analysis.

As the structure of the hydrozincite is not changed when it is exposed to a low electron flux we have performed in-situ heating experiments, with the results given in Fig. 6.5. At temperatures from 275°C to 400°C, hydrozincite reflections present at 21 °C were gradually lost. The resulting SADP was however, not fully consistent with the structure of ZnO, with the form of the product different to that of the ZnO nanocrystals. Holding the temperature at 400°C did not cause significant change in structure. The conclusion is that the vacuum/low p(O₂) conditions within the TEM stabilize a defected form of ZnO that is structurally based on the hydrozincite lattice.

6.1.1 E-beam decomposition

There is, however, an interesting alternative to the synthesis of Zn_{1-x}Mn_xO by thermal decomposition. We have noticed that when hydrozincite is exposed to an intense electron beam it transforms into nanocrystals of Zn_{1-x}Mn_xO. The nanocrystals of Zn_{1-x}Mn_xO were significantly smaller with ≈ 5 nm in diameter. We have repeated this experiment at -170°C using a cold stage and observed that this is not simply an ionization-induced effect. The experiment showed that the transformation rates for both syntheses were around ≈ 1 s. As a digression, silicon technology is based on low temperatures. The low temperature nature of this synthesis methods could hence be proven to be vital for applications. The TEM electron diffraction patterns of hydrozincite and decomposed oxide are given in Fig 6.6 (a) and (c) respectively. High resolution TEM image of the same compounds is given in Fig 6.6 (b) and (d), correspondingly. One can see in bright field TEM images shown in Fig. 6.6 (a) and (c) that hydrozincite

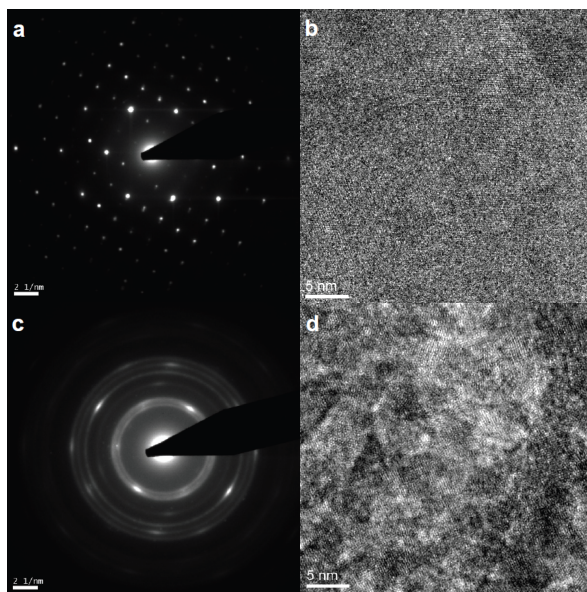


Figure 6.6: The e-beam induced decomposition of hydrozincite $(\text{Zn}_{1-x}\text{Mn}_x)_5(\text{OH})_6(\text{CO}_3)_2$ into $\text{Zn}_{1-x}\text{Mn}_x\text{O}$. TEM electron diffraction showing a diffraction pattern of hydrozincite (a) giving way to polycrystalline reflections of ZnO, corresponding to an average diameter of 5 nm (c). High-resolution TEM showing real space image of the transformation taking place from hydrozincite (b) to Mn doped ZnO (d), correspondingly.

gives way to polycrystalline ZnO. High resolution TEM gave us the real space imaging of the transformation from $(\text{Zn}_{1-x}\text{Mn}_x)_5(\text{OH})_6(\text{CO}_3)_2$ to $\text{Zn}_{1-x}\text{Mn}_x\text{O}$.

As outlined in Section 4.2, $(\text{Zn}_{1-x}\text{TM}_x)_5(\text{OH})_6(\text{CO}_3)_2$ has numerous advantages in comparison to a growing group of precursors for $\text{Zn}_{1-x}\text{TM}_x\text{O}$, avoiding caveats present for precursors used for solid-state and co-precipitation synthesis methods. Single step decomposition process at low temperatures, high TM solid state solubility and, as it will be apparent from this Chapter, tunable properties of the $\text{Zn}_{1-x}\text{TM}_x\text{O}$ dependent on the atmosphere of the decomposition, are some of the upper hands that $(\text{Zn}_{1-x}\text{TM}_x)_5(\text{OH})_6(\text{CO}_3)_2$ precursor offers. The Chapter begins with an overview of the properties of the $\text{Zn}_{1-x}\text{Mn}_x\text{O}$, one of the most studied materials in the DMO field, continues with $\text{Zn}_{1-x}\text{Co}_x\text{O}$, a sister material, yet with its own peculiarities, $\text{Zn}_{1-x}\text{Ni}_x\text{O}$, a product likewise predicted to be ferromagnetic and concludes with the co-doping of $\text{Zn}_{1-x}\text{Mn}_x\text{O}$ with Li, intended to dope the material with holes and achieve the predicted ferromagnetism.

6.2 Mn as a dopant

The original prediction for the ferromagnetism in ZnO was given by Dietl et al. [2] and streamlined a significant part of this Thesis work towards $\text{Zn}_{1-x}\text{Mn}_x\text{O}$. The defining and differing mark for Mn as a dopant in ZnO is that it was originally predicted to have hole (p) doping as a necessity for observed ferromagnetism.

6.2.1 Oxygen rich environment

The samples that were produced in oxygen rich environment were actually fabricated by thermal decomposition of $(\text{Zn}_{1-x}\text{Mn}_x)_5(\text{OH})_6(\text{CO}_3)_2$ at 400°C under air. As the atmosphere of decomposition critically determines the oxidation state of Mn species we have tried both reducing and oxidizing atmosphere for synthesis in order to see the effect on the magnetic properties of the final product.

The literature, however, considers examples of materials produced by a given synthesis method and then focuses on the post-heat-treatment in different atmospheres. The effect of the chemical defect balance within the $\text{Zn}_{1-x}\text{Mn}_x\text{O}$, notably the oxygen vacancy content was studied in the work of Rubi et al. [119]. They concluded that the ferromagnetism in $\text{Zn}_{1-x}\text{Mn}_x\text{O}$ can be switched on and off by heat-treatment of $\text{Zn}_{1-x}\text{Mn}_x\text{O}$ in N_2 and O_2 , respectively. The opposite tendency was found in the case of $\text{Zn}_{1-x}\text{Co}_x\text{O}$. One can see, in the Fig. 6.7 that the hysteresis curves, although weak, were found to be suppressed together with the value of magnetization during the heating process in N_2 while reinstated in O_2 . As suggested, the exact opposite effect was noticed in the case of Co.

Motivated to obtain a single-phase $\text{Zn}_{1-x}\text{Mn}_x\text{O}$ material and compare its properties to a referent sample produced in different atmosphere we have pursued the synthesis of $\text{Zn}_{1-x}\text{Mn}_x\text{O}$ and $\text{Zn}_{1-x}\text{Co}_x\text{O}$ in oxidizing and reducing atmosphere, accordingly. Additional motivation were the aforementioned works by Rubi et al. [119] together with the pivotal work of Kittilstved et al. [90, 95, 120] listed in the Section 3.3.2. The results of our measurements follow.

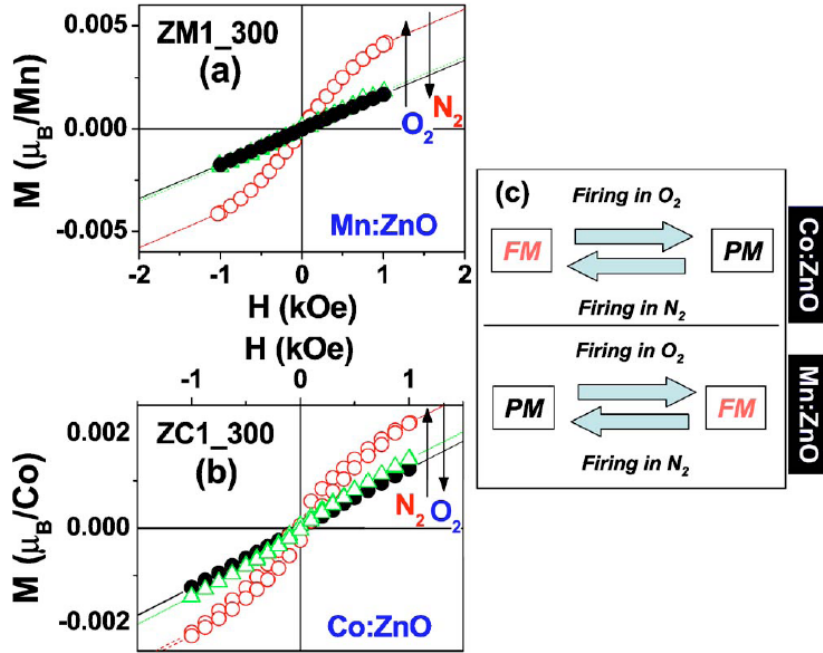


Figure 6.7: Room-temperature measurements of magnetization on $Zn_{1-x}Mn_xO$ (a) and $Zn_{1-x}Co_xO$ (b) fired under N_2 and O_2 resulting with the summary of the effects of the N_2 and O_2 annealing on the properties of $Zn_{1-x}Mn_xO$ and $Zn_{1-x}Co_xO$ (c). Taken from [119].

Structural properties

The structural properties of $Zn_{1-x}Mn_xO$ produced under air were, consistently with the remainder of this work, inferred through XRD and TEM microscopy coupled with SADP. The optimal temperature found for successful synthesis of $Zn_{1-x}Mn_xO$ and $Zn_{1-x}Co_xO$ was $400^\circ C$, with the results of the synthesis given in Section 6.1. The XRD scans of the $Zn_{1-x}Mn_xO$ series are given in the Fig. 6.1. The conclusions can be summarized by stating that the samples exhibit only the $P6_3mc$ reflections, and that the SADP does not exhibit the rings other than those coming from the host ZnO. The TEM measurement further referred to the random sampling of the nanoparticles. Analogously as for the Mn doped hydrozincite precursor, based on TEM observations, the sample purity was estimated to be higher than 99.9 %. As outlined in the Section 4.2 random sampling of the nanoparticle population acquires the correct purity. In conclusion the results of the three methods of structural investigation concerning XRD/TEM/SADP structural measurements confirm that the samples are structurally clean

and no presence of secondary phases is documented.

Magnetic and electronic properties

With the single-phase nature of $\text{Zn}_{1-x}\text{Mn}_x\text{O}$ samples in mind (Section 6.2.1) we have performed the measurements of magnetic properties as described in Section 5.4.2, with the principle of the ZFC-FC measurement given in Section 2.3. The $\text{Zn}_{1-x}\text{Mn}_x\text{O}$ with concentrations $x=0.012$, 0.016 and 0.018 obtained through procedure explained in Sections 2.3 and 5.4.2 all show the ZFC-FC splitting at 4.4 K, as can be seen in the Figure 6.8. This effect is more visible in the enlarged spectra of the left inset to the Figure 6.8. This means that, contrary to the results and resulting conclusions from the preceding Section, we have probably obtained a minute quantity of $\text{Zn}_{1-x}\text{Mn}_x\text{O}$ into the sample that was enough not to have the supporting broad ESR line, yet the quantity was enough to cause the observed 4.4 K ZFC-FC splitting. We will continue to describe the delicate differences in properties between the samples produced by these two synthesis methods.

Unlike for results of the $\text{Zn}_{1-x}\text{Mn}_x\text{O}$ samples produced by the nitrate method explained in Chapter 5, there is no decrease of ZFC susceptibility with decreasing temperature below 4.4 K for all the samples studied. This is another preliminary hint that the quantity of ZnMnO_3 that precipitated in these samples, deduced by analogy with the samples produced by heat-treatment of Mn doped nitrates (Section 5.2) is significantly smaller. This does not come as a surprise, as the hydrozincite synthesis method can be thought of dealing with the impasse of the nitrate synthesis method by employing urea, $\text{CO}(\text{NH}_2)_2$ as a material to be oxidized by the oxidative species during the synthesis. This protects the significant proportion of Mn^{2+} ions to be oxidized into Mn^{4+} . The Mn^{2+} in $\text{Zn}_{1-x}\text{Mn}_x\text{O}$ produced by the nitrate method do not have this kind of "protection" so the quantity of the ZnMnO_3 produced is larger enough to be seen in the XRD, to exhibit a broad ESR line in the ESR experimental results and to observe the full ZFC-FC splitting due to the average larger size of the ZnMnO_3 precipitates.

The high-temperature behaviour of the susceptibility reveals that the samples produced by decomposition of $(\text{Zn}_{1-x}\text{Mn}_x)_5(\text{OH})_6(\text{CO}_3)_2$ in air in the 2-300 K temperature regime, exhibit

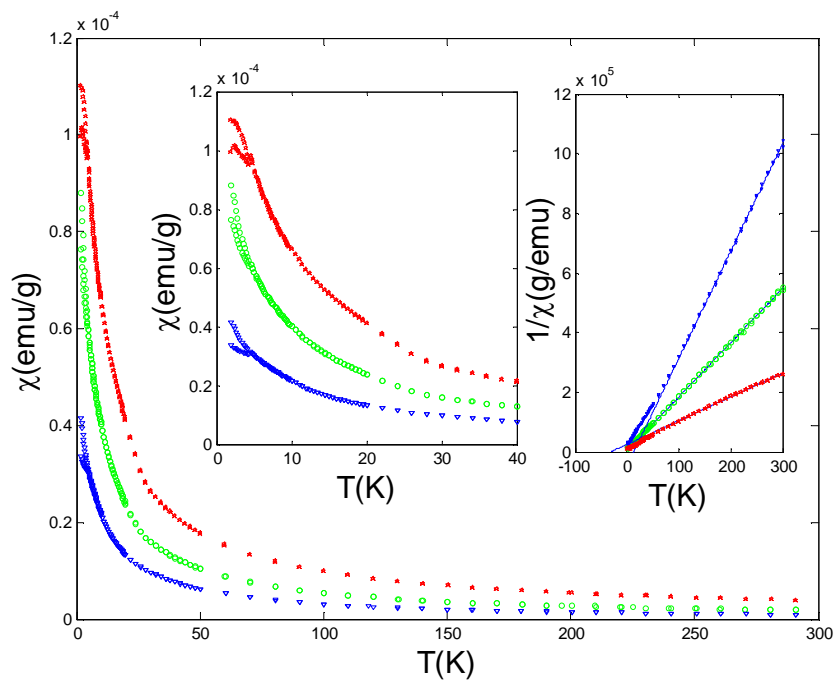


Figure 6.8: SQUID-measured magnetic susceptibility for $\text{Zn}_{1-x}\text{Mn}_x\text{O}$ samples produced by the thermal decomposition of the $(\text{Zn}_{1-x}\text{Mn}_x)_5(\text{OH})_6(\text{CO}_3)_2$ precursor in air, having three different Mn contents, x , of 0.012 (blue triangle), 0.016 (green circle), 0.018 (red star). Inset A (left): Blow-up of the low-temperature region; Inset B (right): The inverse magnetic susceptibility plots as a function of temperature.

Sample	HZ- air	HZ N ₂ -H ₂
1.2% Mn,	13 K	-57 K
1.6% Mn,	-1 K	-58 K
1.8% Mn,	-31 K	-35 K

Table 6.1: Values of Curie-Weiss temperature $\Theta(x)$ for $x=0.012$, $x=0.016$ and $x=0.018$ $\text{Zn}_{1-x}\text{Mn}_x\text{O}$ samples produced under reducing (HZ-N₂-H₂) and oxidizing atmosphere (HZ-air) as inferred from ZFC-FC SQUID measurements at 0.1 T.

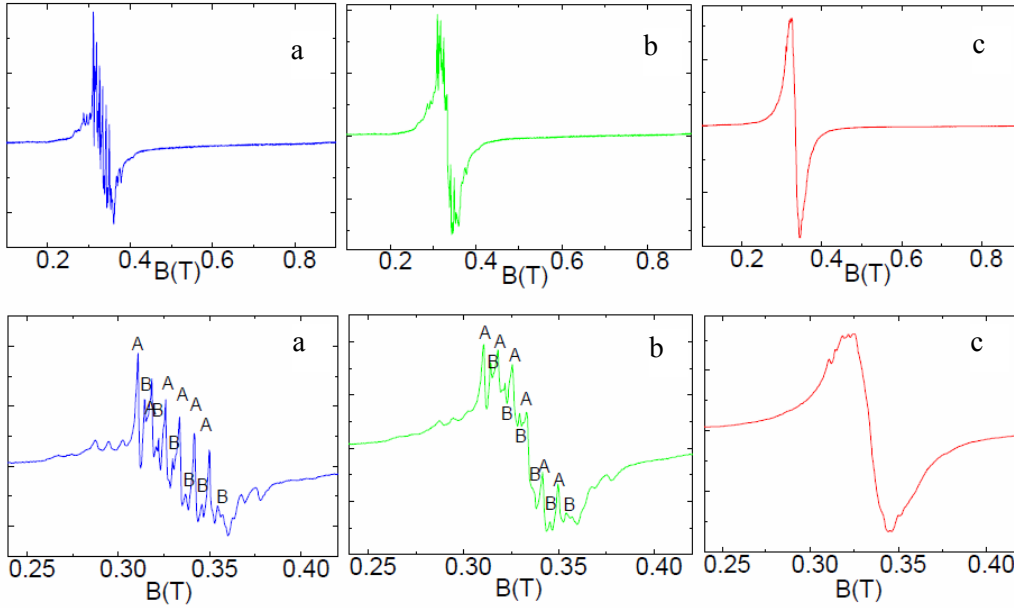


Figure 6.9: Room temperature X-band ESR scans of $\text{Zn}_{1-x}\text{Mn}_x\text{O}$ (a) $x=0.012$, (b) $x=0.016$ and (c) $x=0.018$ made from $(\text{Zn}_{1-x}\text{Mn}_x)_5(\text{OH})_6(\text{CO}_3)_2$ under air. A combined Mn^{2+} and Mn^{4+} hyperfine structure does not get dissolved through Mn-Mn interaction until $x=0.02$.

Curie-Weiss behaviour. The Curie-Weiss temperatures are given at Table 6.1.

While the $x=0.012$ is weakly ferromagnetic $x=0.016$ is closer to be ideally paramagnetic while $x=0.018$ is antiferromagnetic. We attribute the increase of the antiferromagnetic contribution due to the formation of a higher portion of ZnMnO_3 in the system with the addition of Mn species, however the increase could come due to the increased proportion of Mn^{2+} interacting more strongly in ZnO.

The room-temperature ESR measurements of the three HZ-air samples are given in Fig. 6.9. The hyperfine structure of the Mn^{2+} ion gets gradually washed out for the $x=0.016$ sample and gets completely dissolved in the $x=0.018$ sample. This proves a strong increase in

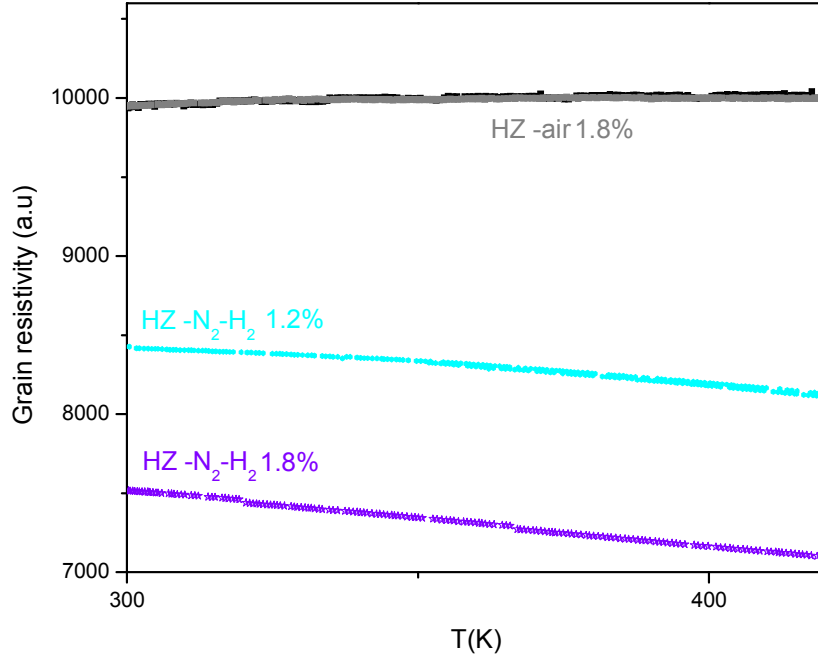


Figure 6.10: AC conductivity measurements of the $x=0.018$ $Zn_{1-x}Mn_xO$ (violet) and $x=0.012$ $Zn_{1-x}Mn_xO$ (cyan) produced by decomposition of $(Zn_{1-x}Mn_x)_5(OH)_6(CO_3)_2$ in N_2H_2 , compared to the AC conductivity of the $x=0.018$ $Zn_{1-x}Mn_xO$ produced by decomposition of $(Zn_{1-x}Mn_x)_5(OH)_6(CO_3)_2$ in air (grey) with the referent undoped sample given in black.

the interaction for these samples with increasing concentration in the studied concentration range $0.012 < x < 0.018$. There is no broad ESR line noted for the samples containing $ZnMnO_3$, as explained in Section 5.2, broad-line stemming from $ZnMnO_3$ component in the room-temperature ESR spectra. The intensity of the lower- g (Mn^{4+}) sextet is lower than in the case of the samples produced from nitrate precursors (See Fig. 5.6). Both traits are confirming that the oxidative conditions of the HZ synthesis are much weaker than in the samples produced by decomposition of nitrate precursors.

The conductivity of the samples, reveals almost unchanged resistivity-temperature curves in the $300\text{ K} < T < 420\text{ K}$ between undoped ($x=0$), $x=0.016$ and $x=0.018$ (shown in Fig. 6.10) region, confirming that the quantity of parasitic $ZnMnO_3$ phase is significantly reduced, and that the quantity of carriers induced is below the threshold conductivity increase needed to be present in order to be documented by the AC conductivity method.

6.2.2 N₂H₂ environment

The reducing atmosphere of the decomposition is favorable for inducing the ferromagnetic response in Zn_{1-x}Mn_xO [90, 95, 120] and has served for direct kinetic correlation between carriers and ferromagnetism in Zn_{1-x}TM_xO. The materials that were synthesized by this method reveal no precipitates of ZnMnO₃ from the absence of it being noticed in XRD, TEM, SQUID, ESR and XPS measurements. The results follow.

Structural properties

The structural properties of Zn_{1-x}Mn_xO produced by thermal decomposition of Mn doped hydrozincite, (Zn_{1-x}Mn_x)₅(OH)₆(CO₃)₂ under the mixture of 94% N₂ and 6% H₂ for 1 hour under 400°C were established using XRD, SADP and XPS. The XRD measurements, given in the Fig. 6.11 have revealed only the reflections of the host semiconductor ZnO. The TEM measurements have proven that the products were of high purity and in the form of ZnO nanocrystallites with diameters of ≈ 20 - 100 nm while the detailed electronic diffraction analysis on many particles showed no reflections from the other phase. The compositional profiling done on the particles of (Zn_{1-x}Mn_x)₅(OH)₆(CO₃)₂ precursor (Chapter 4) and particles of oxides synthesized from these precursors revealed that the initial Mn distribution within the precursor is preserved in the final oxide products.

The landmark work and a useful reference in identifying the valence state of the Mn in ZnO by the method of X-ray photoelectron spectroscopy is the work by Mizokawa et al. [121]. They have studied the n 2p core-level photoemission spectrum of Zn_{1-x}Mn_xO with x=0.13. The broad peak characteristic at ≈ 667 eV is due to Mn L_{2,3}M_{2,3}M_{4,5} Auger emission. The Mn 2p_{3/2} in x=0.018 Zn_{1-x}Mn_xO has the satellite structure on the higher binding-energy side separated by 6.5 eV. The presence of the satellite structure at this site according to the work of Mizokawa et al. indicates Mn²⁺ state. This was calculated by configuration-interaction calculations using the MnY₄ cluster model which gives satellite structure separation of Δ = (6.5±0.1) eV. XPS data that we have used to acquire the Image given in Fig. 6.12 (a) were acquired using Al Kα x-ray radiation source at 1486.6 eV. The XPS spectra were recorded at

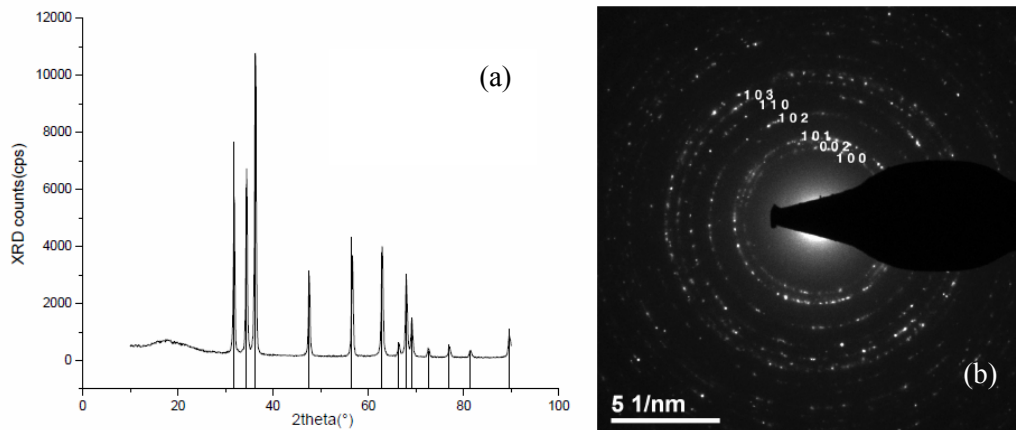


Figure 6.11: a) The θ - 2θ XRD spectra of $\text{Zn}_{1-x}\text{Mn}_x\text{O}$ produced under reducing atmosphere of N_2H_2 exhibiting ZnO reflections, PDF number 05-0664. (b) The SADP diffraction of the pattern of $\text{Zn}_{1-x}\text{Mn}_x\text{O}$ exhibiting polycrystalline rings corresponding to ZnO reflections.

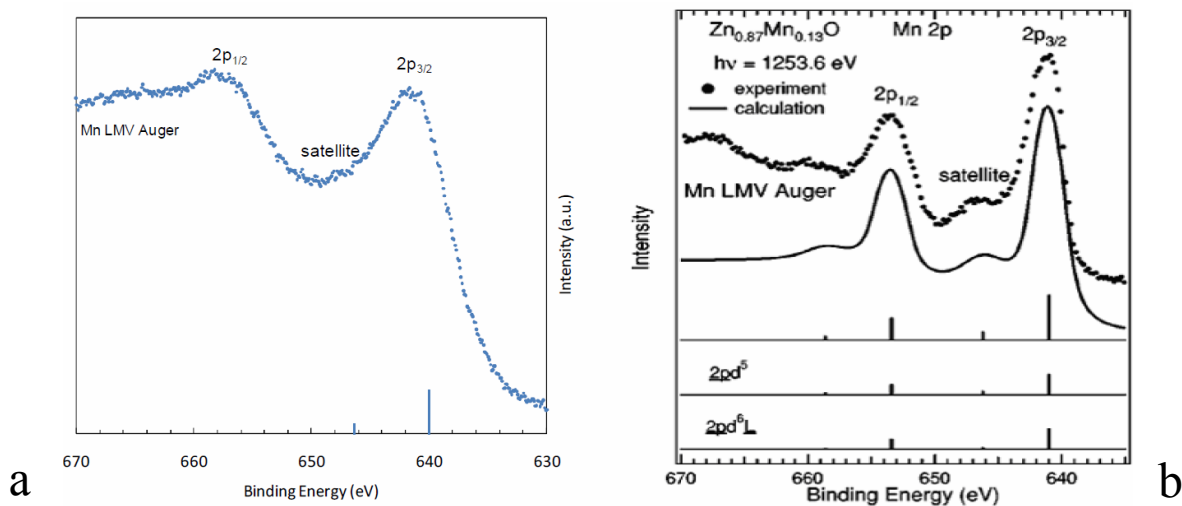


Figure 6.12: (a) XPS spectra of $x=0.018$ $\text{Zn}_{1-x}\text{Mn}_x\text{O}$, the highest doping of $\text{Zn}_{1-x}\text{Mn}_x\text{O}$ in the study, shows that Mn exhibits a satellite structure at 6.5 eV distance from the Mn $2p_{3/2}$ position. (b) The satellite position at the 6.5 eV from the $2p_{3/2}$ Mn edge indicates that $2+$ is the valence state of Mn in ZnO, referring to the study by Mizokawa et al. [121].

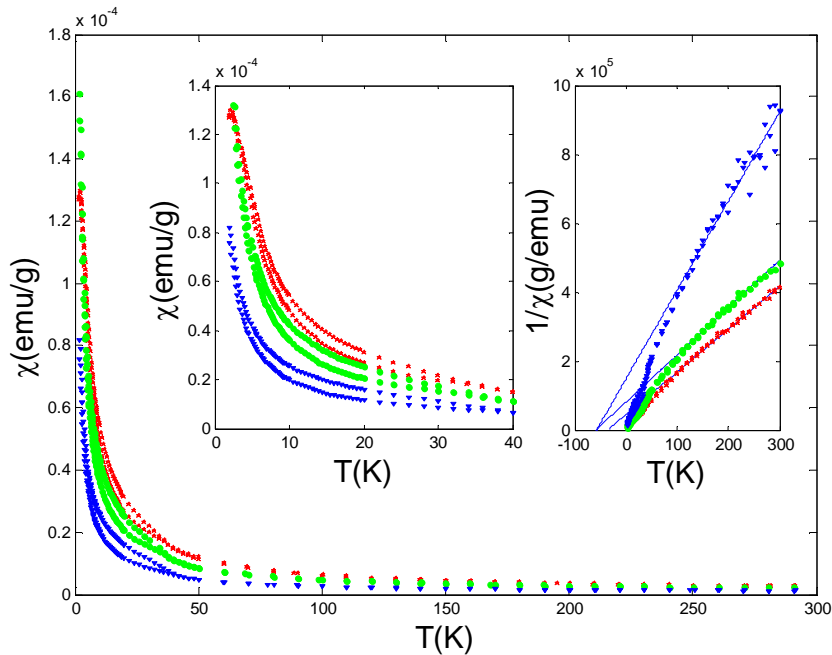


Figure 6.13: SQUID-measured magnetic susceptibility for $\text{Zn}_{1-x}\text{Mn}_x\text{O}$ samples produced by the thermal decomposition of the $(\text{Zn}_{1-x}\text{Mn}_x)_5(\text{OH})_6(\text{CO}_3)_2$ precursor in $\text{N}_2\text{-H}_2$, having three different Mn contents, x , of 0.012 (blue triangle), 0.016 (green circle), 0.018 (red star). Inset A (left): Blow-up of the low-temperature region; Inset B (right): The inverse magnetic susceptibility plots as a function of temperature.

200 eV pass energy, with the energy step for Mn spectra being 100 meV.

Magnetic properties

By changing the synthesis parameters, so as to perform the synthesis in the atmosphere of forming gas $\text{N}_2\text{-H}_2$ the ZFC-FC splitting was induced at 38-40 K in the $x = 0.012$, $x = 0.016$ and $x = 0.018$ samples, as visible from Fig 6.13. No splitting, cusps or kinks are visible at 4.4 K; hence no parasitic phases were produced in $\text{HZ-N}_2\text{-H}_2$ samples. Formation of ferromagnetic domains below 38-40 K has been documented.

The room-temperature ESR scans show smearing out of the hyperfine structure already at the lowest, $x=0.012$ concentration which then proceeds up to the highest concentration of $\text{Zn}_{1-x}\text{Mn}_x\text{O}$. The interactions in $\text{HZ-N}_2\text{-H}_2$ samples are hence stronger as compared to the samples produced in oxidizing atmosphere for the same nominal concentrations. The Curie-Weiss temperature evolution is however different then in the $\text{Zn}_{1-x}\text{Mn}_x\text{O}$ produced in air.

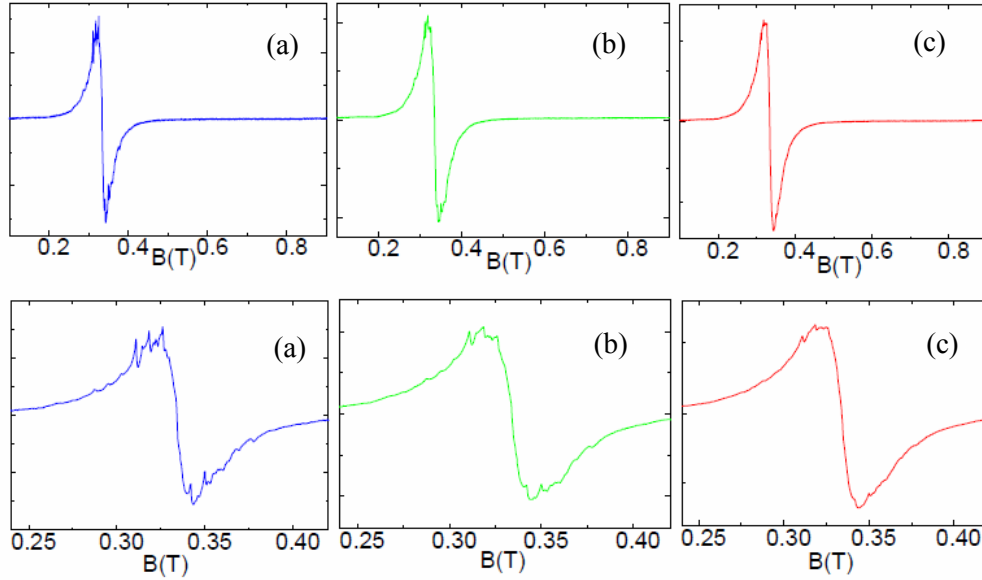


Figure 6.14: Room temperature X-band ESR scans of $\text{Zn}_{1-x}\text{Mn}_x\text{O}$ (a) $x=0.012$, (b) $x=0.016$ and (c) $x=0.018$ made from $(\text{Zn}_{1-x}\text{Mn}_x)_5(\text{OH})_6(\text{CO}_3)_2$ under reducing atmosphere. A combined Mn^{2+} and Mn^{4+} hyperfine structure gets dissolved through Mn-Mn interaction already at $x=0.012$ (cf. Fig. 6.9).

With increasing concentration the interactions move into ferromagnetic direction. This can be explained if we look at the AC conductivity measurements of these samples, given in Figure 6.10.

A drastic increase of the conductivity is visible from the referent undoped ZnO, coinciding with HZ-air sample to $x=0.012$ $\text{Zn}_{1-x}\text{Mn}_x\text{O}$ and from $x=0.012$ $\text{Zn}_{1-x}\text{Mn}_x\text{O}$ to $x=0.018$ $\text{Zn}_{1-x}\text{Mn}_x\text{O}$. Such increase with the Mn concentration means that it is the n-doping with Mn^{4+} that is responsible for the observed conductivity increase. The unintentional, n-type ferromagnetism is the most common form of ferromagnetism observed in ZnO, the theories for ferromagnetism in ZnO often being based on a spin-split impurity band theory (Section 3.3.1), where electrons in hydrogen-like orbitals induced by structural defects, such as oxygen vacancies are mediating the Mn-Mn interaction. Such mediation is here leading to the splitting at 38-40 K, the ferromagnetism present above a certain carrier concentration, as suggested from the fact that the T_C doesn't vary much with the high increase in conductivity noted. An overall antiferromagnetic character more pronounced than in HZ-air samples is due to higher overall

quality of coarsening and compactness in materials that have a number of oxygen vacancies present in the structure. The effect of a significant increase in carrier quantity is visible in the ESR spectra, shown in Fig. 6.14. The hyperfine structure does not persist, except for the remnant peaks in the $x=0.012$ sample, in any of the three samples studied. This is a proof of magnetism enhanced and mediated by the induced carriers, as the samples synthesized in air do not exhibit the smearing out at the lowest concentration, as seen in Fig. 6.9. The absence of the broad-line background seen for the samples produced by nitrate decomposition (Chapter 5) corroborates the absence of a parasitic phase in all the samples studied.

To infer further on the nature of magnetic transition at 40 K in the HZ-N₂H₂ we have performed X-band ESR measurements on the three concentrations studied in the 4-300 K temperature interval. As outlined in Sections 2.3 and 4.1 the main characteristics of the ESR scan are the electronic g-factor, the value of the ΔH_{pp} ESR linewidth and the value of the spin susceptibility which is proportional to the intensity of the ESR signal. In our $x = 0.012$, $x = 0.016$ and $x = 0.018$ Zn_{1-x}Mn_xO the ESR linewidth $(\Delta H)_{pp}$ increases with decreasing temperature in the range from the room temperature to the 40-60 K transition region (Figure 6.15 b). Such behaviour has been observed in DMSs since the 1980s [45] and has caused a considerable theoretical interest due to the fact that dipolar broadening is considered too weak to overcome the strong isotropic exchange narrowing effects expected in DMS. The Dzyaloshinski-Moriya (DM) interaction is often invoked as the underlying broadening mechanism [122] (See Section 2.3). In DM interaction, the anisotropic exchange broadening, is of the form $D(S_i \times S_j)$, where S_i , S_j are the interacting spins and the vector \mathbf{D} reflects the local environment of the magnetic ions and is non-vanishing if there is the lack of inversion symmetry of crystal field with the respect to the centre between two magnetic ions. The line width in these systems can be best described by

$$(\Delta H)_{pp} = (\Delta H)_{\infty}(1 + \Theta/T) \quad (6.2)$$

where $(\Delta H)_{\infty}$ is the infinite temperature linewidth and Θ is the Curie-Weiss temperature. Below 40-60 K, the line width of the Lorentzian feature remains almost constant. It has

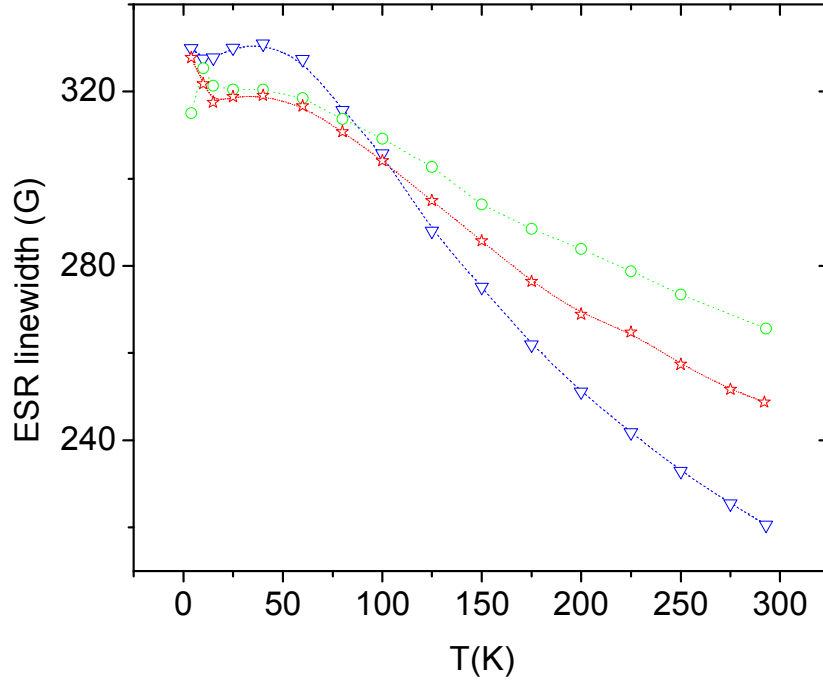


Figure 6.15: Thermal evolution of the ESR line width of the Lorentzian line present in the ESR spectra of the $x=0.012$ (blue triangles), $x=0.016$ (green circles) and $x=0.018$ (red stars) $\text{Zn}_{1-x}\text{Mn}_x\text{O}$ produced by thermal decomposition of $(\text{Zn}_{1-x}\text{Mn}_x)_5(\text{OH})_6(\text{CO}_3)_2$ in reducing atmosphere of $\text{N}_2\text{-H}_2$.

been documented that the constant line width corresponds to a possible paramagnetic-to-spin-glass transition resulting in a state of frozen spins with different regions having different magnetic orders. The different regions will then have resonance frequencies determined by a combination of the local exchange field and the local anisotropy field [51]. In the spin-blocked system these fields are both independent of the temperature, resulting in a line width of the system independent of temperature. This is the trend obtained in Figure 6.15 for all three of the samples studied, $x = 0.012$, $x = 0.016$ and $x = 0.018$.

The temperature evolution of the electronic g-factor is important as the g-factor is sensitive to the local magnetic fields and we can infer the change in magnetic properties of the system with temperature. The observed g-factor measured for the $x=0.012$ sample crosses the 2.0023 free electron value, entering the higher-than-free electron value g-factor region (Figure 6.16). The same trend of moving into the ferromagnetic direction is followed in the case of the $x=0.016$ and $x=0.018$ samples. Thus, the ferromagnetic interactions, mediated by charge

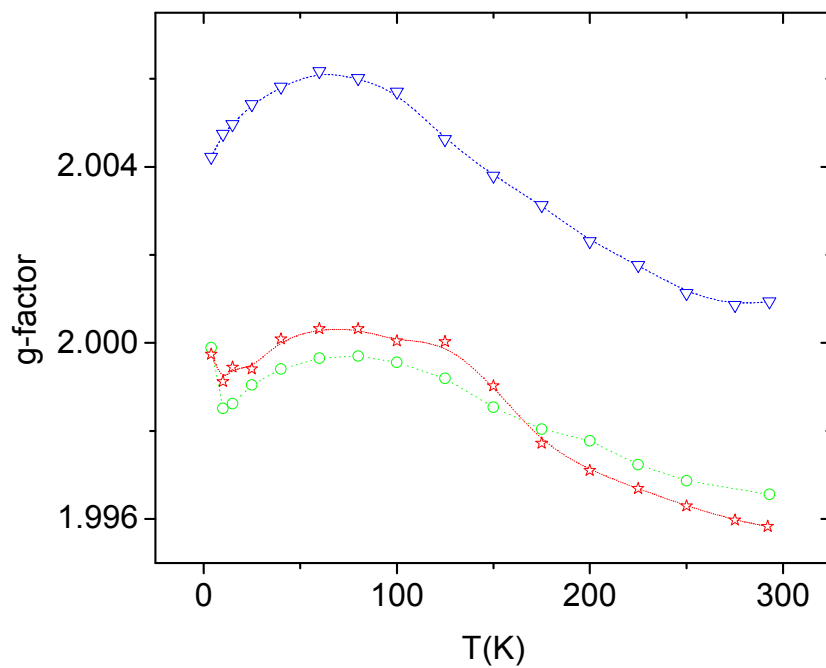


Figure 6.16: Thermal evolution of the g-factor of the Lorentzian line present in the ESR spectra of the $x=0.012$ (blue triangles), $x=0.016$ (green circles) and $x=0.018$ (red stars) $Zn_{1-x}Mn_xO$ produced by the thermal decomposition of the $(Zn_{1-x}Mn_x)_5(OH)_6(CO_3)_2$ in reducing atmosphere of N_2-H_2 .

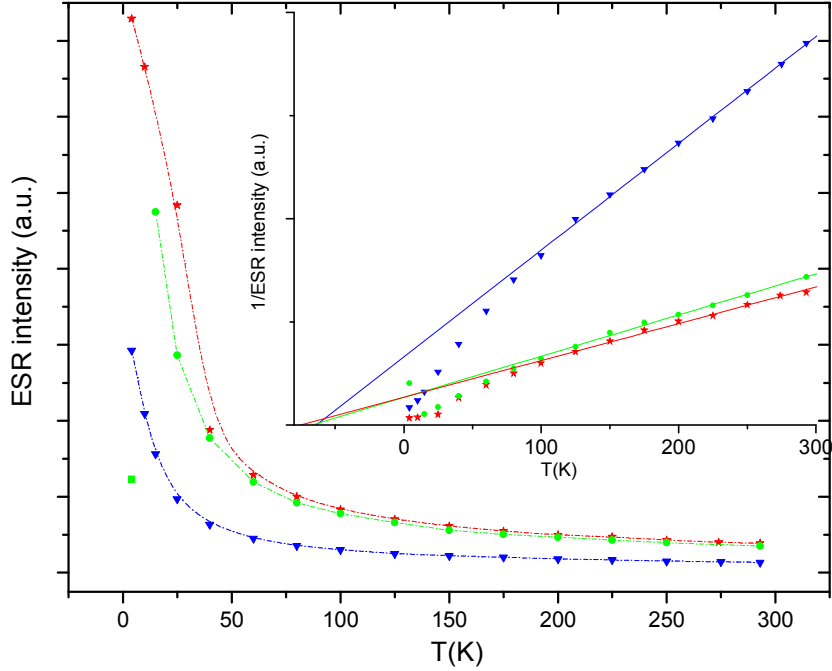


Figure 6.17: The intensity and the inverse intensity of the ESR signal of the $x=0.012$ (blue triangles), $x=0.016$ (green circles) and $x=0.018$ (red stars) $\text{Zn}_{1-x}\text{Mn}_x\text{O}$ produced in reducing atmosphere of $\text{N}_2\text{-H}_2$ reproducing the Curie-Weiss behaviour and antiferromagnetic Curie-Weiss temperatures deduced from the SQUID measurements (cf. Fig 6.13).

carriers [2], become more dominant with the decrease of the temperature until 40-60 K. At temperatures lower than 40 K, the g -factor is again decreasing, thus pointing to an increase in antiferromagnetic correlations. Antiferromagnetic interactions are expected for directly overlapping Mn-Mn orbitals through the mechanism of direct exchange [123] and Mn-Mn coupling through the oxygen atoms (superexchange) [17, 14]. Thus, below the 40-60 K range, the onset of antiferromagnetic couplings would then explain the decrease in the g -factor. From the Figure 6.16 we see that the trend of g -factor elaborated in this paragraph is the same for all the three concentrations studied with the lowest concentration studied having local fields being the most ferromagnetic as inferred from the higher g -factor.

The ESR intensity curves obtained by fitting the signal curves to a Lorentzian are shown in the Fig. 6.13 and tend to follow very well the SQUID intensity curves obtained for the $x=0.012$, $x=0.016$ and $x=0.018$ samples (figure 6.13). The Curie-Weiss temperatures are given in the Table 6.2.

Sample	ESR T_{CW}	SQUID T_{CW}
1.2% Mn	-75 K	-57 K
1.6% Mn	-67 K	-58 K
1.8% Mn	-75 K	-35 K

Table 6.2: Values of Curie-Weiss temperature $\Theta(x)$ for $x=0.012$, $x=0.016$ and $x=0.018$ $Zn_{1-x}Mn_xO$ samples produced under reducing atmosphere of N_2-H_2 as inferred from ESR and SQUID measurements.

The values of the Curie-Weiss temperatures are very close to the ones obtained from SQUID measurements being slightly shifted to the antiferromagnetic (negative) direction. We have hence confirmed the dominant antiferromagnetic interactions in our samples. Once having developed the technology of synthesizing $Zn_{1-x}Mn_xO$ from $(Zn_{1-x}Mn_x)_5(OH)_6(CO_3)_2$ we have focused our attention on production of $Zn_{1-x-y}Li_yMn_xO$ material from (Mn,Li) co-doped hydrozincite. The results of this study are given in the following section.

6.3 The (Mn, Li) co-doping

If one looks at the review papers [59, 124, 65], one can notice the clear disparity between the efforts made in co-doping TM doped ZnO with holes in order to achieve the room-temperature ferromagnetism and the number of papers on TM doped ZnO without the additional co-doping. In the Section 3.1.2 we have covered the issue of defects in ZnO and stated that the dominant defects at room temperatures in ZnO are zinc interstitials and oxygen vacancies, both serving as n-dopants. Another camp of thought is given by stating that the n-type of conductivity of ZnO is only due to hydrogen which acts as a shallow donor with an ionization energy of about 30 meV. Hydrogen can always diffuse into ZnO due to its large mobility. *n*-type doping is significantly easier to achieve in ZnO, and is being performed nominally with group-III elements, such as Al, Ga and I as substitutional elements for Zn and group VII elements Cr and I as substitutional elements for O. *p*-type doping is excessively difficult in wide-band gap semiconductors, such as GaN, ZnSe, and indeed ZnO. *p*-dopants can be compensated by low energy native defects, such as Zn_i or V_O , or background impurities, such as aforementioned H. Deep impurity levels can cause significant resistance to the formation of a shallow acceptor

	Element	Bond length(Å)	E_i (eV)	ΔE
Group I	Li	2.03	0.09	0.21
	Na	2.10	0.17	1.04
	K	2.42	0.32	1.38
Group V	N	1.88	0.40	0.13
	P	2.18	0.93	-0.46
	As	2.23	1.15	-0.18

Table 6.3: Calculated nearest-neighbor bond lengths, the defect energy levels E_i and the energy required ΔE required to form the positively charged AX center from the substitutional acceptors. Taken from [59].

level. The list of acceptors in ZnO follows: lithium (Li), Na, K, and copper (Cu), silver (Ag), Zn vacancies and group V elements such as N, P and As. If one achieves a deep acceptor level one does not contribute significantly to p-type conduction which is the necessary condition for ferromagnetism. Out of the listed acceptors the group I elements seem to have the upper hand regarding the shallowness of acceptor levels. The results are summarized at the Table 6.3. The caveat for the usage of type I elements comes however in the view of group-I having very small radii and thus often occupying the interstitial sites and therefore becoming donors rather than acceptors.

The ideal Zn-O bond length is 1.93 Å, hence the values of bond lengths for Na and K from Table 6.3 are significantly longer, imparting lattice strain which inevitably leads to formation of defects such as vacancies that compensate the dopants. Defects in form of antisites A_{Zn} can also be formed and also lead to compensating effects, themselves being donors as well. This leaves us with N as the best solution for *p*-doping because it has the smallest ionization energy, it does not form the N_{Zn} antisite and the AX center for N is only metastable.

Among work performed on $Zn_{1-x-y}Li_yMn_xO$ a recent work by Zou et al. [125] gave an insight in the properties of p-type $Zn_{0.95-x}Li_{0.05}Mn_xO$ produced by co-sputtering of $Zn_{0.95}Li_{0.05}Mn_xO$ and Mn metal target. By measuring the Hall resistivity on $Zn_{0.90}Li_{0.05}Mn_{0.05}O$ and $Zn_{0.95}Mn_{0.05}O$ they have measured that the presence of Li resulted by the decrease in resistivity for three orders of magnitude (18 Ωcm for the Li treated sample compared to $10^3 \Omega cm$ for the sample free of Li). The co-doping, then, is responsible for the hole concentration of the order of 10^{16} holes/cm² which is too low still for the Dietl model [2], yet the ferromagnetism can be

Sample	T_{CW}
2% Mn, 2% Li, 400°C, air	-9 K
2% Mn, 8% Li, 400°C, N ₂ -H ₂	-64 K
2% Mn, 15% Li, 400°C, N ₂ -H ₂	-51 K

Table 6.4: Values of Curie-Weiss temperature $\Theta(x)$ for (Mn,Li):ZnO powders, with 2% of Mn and different Li concentrations, synthesized at 400°C under different atmospheres.

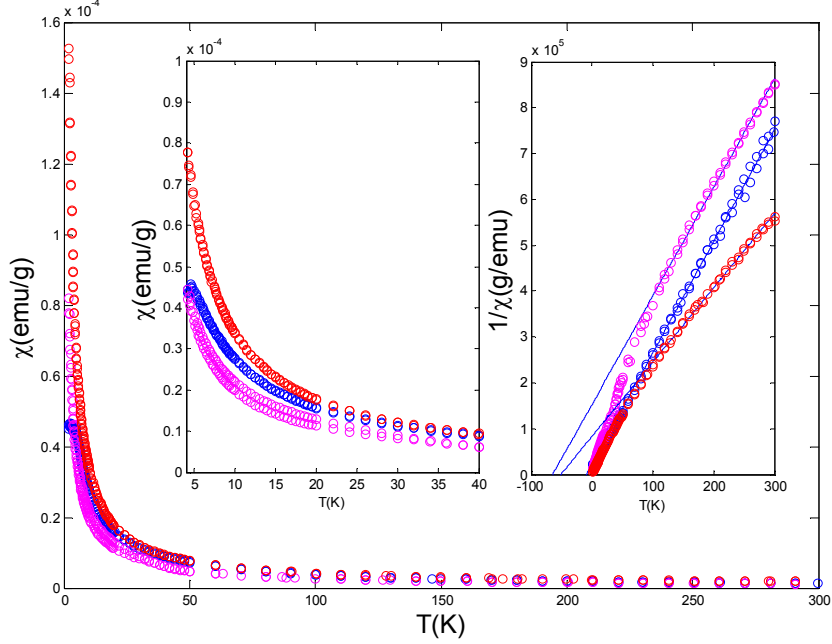


Figure 6.18: The behaviour of the magnetization for the $Zn_{1-x-y}Li_yMn_xO$ samples for $x=0.02$, $y=0.02$ produced at 400°C in air (blue), $x=0.02$, $y=0.08$ produced at 400°C in N₂-H₂ (magenta) and $x=0.02$, $y=0.15$ produced at 400°C in N₂-H₂ (red).

explained by evoking the Coey's model of bound magnetic polarons [94], both presented in the Section 3.3.1.

The structural properties of (Mn,Li) co-doped ZnO are equivalent to those of Mn doped ZnO, i.e. there are no extraneous reflections in the XRD and the TEM characterization does not reveal presence of parasitic phases in the material. Moreover, as EELS is not suitable for very light elements, such as Li, it is difficult to quantify the Li content in our samples. We have however, done an initial study probing for the occurrence of ferromagnetism in this system.

The magnetic properties of the (Mn,Li) co-doped ZnO are given at 6.18. The list of the

Curie-Weiss temperatures is given in the Table 6.4. One can observe a clear move of the Curie-Weiss temperatures away from the paramagnetism, i.e. 0 K, to the antiferromagnetic values for the addition of high concentrations of lithium, i.e. the 8% and 15% concentration of Li in (Mn,Li) co-doped ZnO. Only the sample with 8% Li has exhibited ZFC-FC splitting below 40 K, i.e. ferromagnetic order, with the highest antiferromagnetic temperature as well. This initial study thus shows that (Mn,Li) co-doped ZnO samples reflect to a great extent the properties of non Li treated $Zn_{1-x}Mn_xO$, having antiferromagnetic Curie-Weiss temperatures and the ferromagnetism below 40 K. The p-doping of $Zn_{1-x}Mn_xO$ is in its development and at the time of writing of this Doctoral work the material with such high concentration of holes, namely, 3.5×10^{20} holes per cm^3 needed to render the 5% Mn doped ZnO ferromagnetic has still not been synthesized. This is one of the central problems in the DMS community and will probably be the topic of further studies in the field.

6.4 Co as a dopant

Cobalt doped ZnO has been one of the most studied materials regarding the prediction of its room temperature ferromagnetism at above 300 K. It is also a material that holds advantage when compared to Mn, due to the fact that the ferromagnetism predicted in Co doped ZnO is for ZnO natively n-doped, which is its natural state. At the time of writing of this Doctoral work it is crucial to identify the origin of the ferromagnetism observed, the peculiarity of the $Zn_{1-x}Co_xO$ pertaining to the possibility of precipitates of metallic Co, a ferromagnetic material with the Curie temperature T_C of $1121^\circ C$. The work by Heald et al. [126], although shedding some light on the ferromagnetism of $Zn_{1-x}Co_xO$ has left many questions open for discussion. Heald et al. [126] synthesized $Zn_{1-x}Co_xO$ with high Co concentration and also the samples rich in CoZn, the latter being produced by exposing samples to Zn vapors. Both of the samples were found to be ferromagnetic, however, with magnetization values far from those predicted for bulk Co and bulk CoZn, respectively. This was explained through the likely occurrence of change of magnetic properties for the small magnetic particles, with some of the samples exhibiting the blocking temperature of 50 K.

Cobalt doped ZnO has been synthesized both in reducing and oxidizing atmosphere. As will become apparent from the part of this Section dealing with magnetic properties of our samples, radically different magnetic properties have been observed for the samples produced in the two synthesis conditions. The structural characteristics of the both samples have proven a single-phase in nature in XRD, as is apparent from the Fig. 6.19. STEM-EELS measurements of the $Zn_{1-x}Co_xO$ produced under N_2-H_2 are given in the Fig. 6.20. They are revealing that the system viewed at a nanoscale is not single phase. The images 6.20 (a), (b) and (c) were taken on a single particle with the image on the left side showing the site and the direction of the STEM-EELS scan, while the image on the right side shows the corresponding line profiles extracted from the STEM-EELS scan. This procedure has been performed using Co $L_{2,3}$ (a), Zn $L_{2,3}$ (b) and O ionization edge (c), and taken using a 1 nm electron probe. The y-axis of these line profiles is the electron intensity and the scans are effectively concentration profiles. The scans show that the particle studied in the images (a),(b) and (c) is highly concentrated in Co in some regions, and weakly concentrated in Zn in those very areas. The actual Zn concentration could even be closer to zero but it is influenced by the overlapping ZnO particles which contribute to the Zn signal. The oxygen content given in the Fig. 6.20 (c) stays at the relatively high value pointing to the fact that the formula of the central particle might contain oxygen. This is likely to be ruled out due to the subsequent magnetization measurements that reveal the high-temperature ferromagnetism of the system, that can be explained through the fact that the phase in question is metallic cobalt, ferromagnetic with Curie temperature T_C of 1394 K (1121°C) rather than cobalt(II)- oxide, an antiferromagnet with T_N of 289 K. However, antiferromagnetic particles embedded in a non-magnetic medium can lead to superparamagnetism effects, as shown in the next Section.

We have hinted in Chapter 5 that the phases invisible for detection in very small quantities can be perceived in the same samples produced by the same methods for higher concentration of dopants and higher temperatures. These synthesis conditions have a higher chance for occurrence of higher quantity of precipitate and this can lead to the precipitate being in big enough quantity to be documented by XRD, thereby giving us aid in identifying phase with

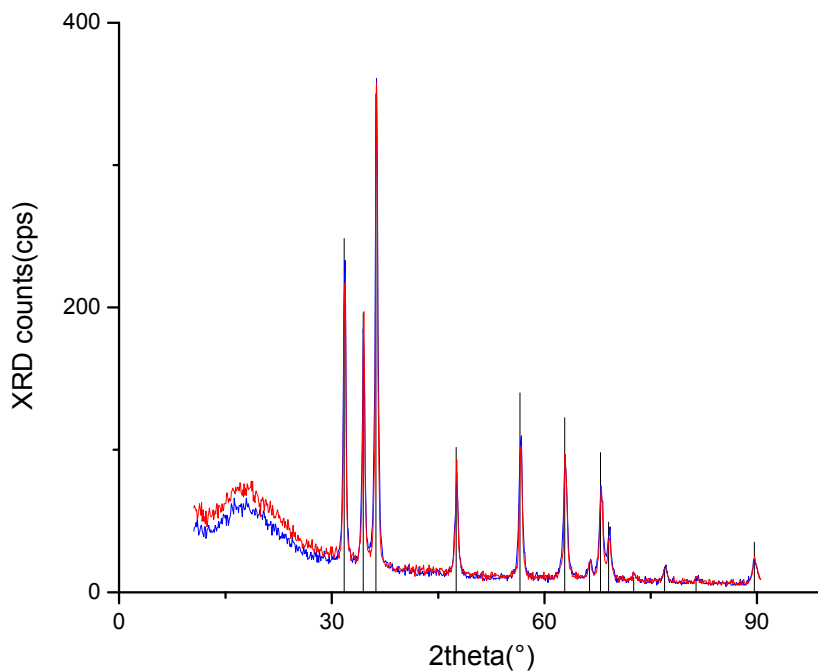


Figure 6.19: XRD scans of $x = 0.08$ $Zn_{1-x}Co_xO$ produced in reducing (red) and oxidizing atmosphere (blue), revealing only the ZnO reflections.

weak reflections in the SADP spectra. Co:ZnO in air is one such example with its SADP scan given in the Fig. 6.21. In Chapter 5, Figure 5.4 we have seen that the phase precipitating from the nitrate precursors is $ZnCo_2O_4$. In the SADP from the sample $x=0.08$ of $Zn_{1-x}Co_xO$ synthesized in air a small extra reflection aside from $Zn_{1-x}Co_xO$ reflections was noted, turning out to be the (400) reflection of $ZnCo_2O_4$. The (220) and (222) $ZnCo_2O_4$ reflections are very close to the (100) and (101) reflections of the ZnO. However, the (400) peak for the $ZnCo_2O_4$ corresponds within 1% to 2%, the accuracy in plane spacings that TEM SADP has, to the (400) peak noted in the XRD spectra of Co:ZnO, as given in the Fig. 5.4.

The occurrence of this phase in $x = 0.08$ of $Zn_{1-x}Co_xO$ synthesized in reducing atmosphere is unlikely as the SADP does not show an extra reflection for this plane spacing, as seen from Fig. 6.22. Together with this the EELS indicates that the phase occurring in the reducing atmosphere sample is very rich in Co. The repeating of the above argument on the closeness of reflections observed in SADP, and the absence of extra reflections, in this case of Co, in the SADP of the sample produced in reducing atmosphere, one reaches a conclusion that,

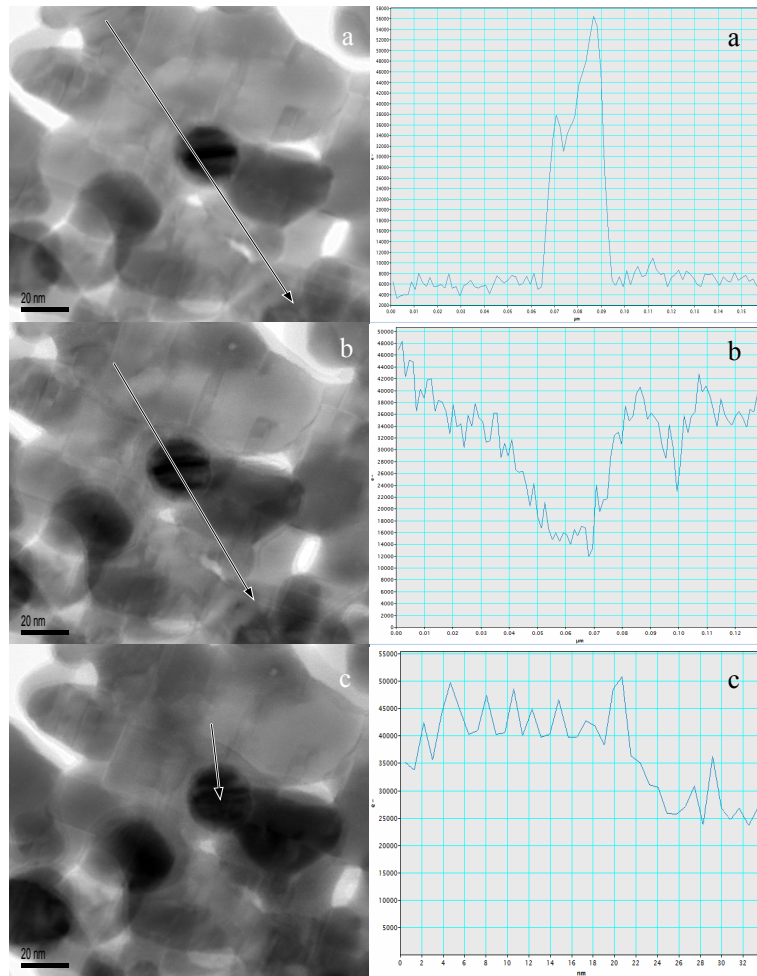


Figure 6.20: STEM-EELS line profiles of a single particle of $\text{Zn}_{0.92}\text{Co}_{0.08}\text{O}$ produced under $\text{N}_2\text{-H}_2$. The scans at the ionization edges of (a)Co $L_{2,3}$ (b)Zn $L_{2,3}$ and (c)oxygen O. Left: the site and the direction of the STEM-EELS scan. Right: line profiles extracted from the STEM-EELS scan. High Co/Zn ratio bears witness to the precipitation of a Co-rich phase.

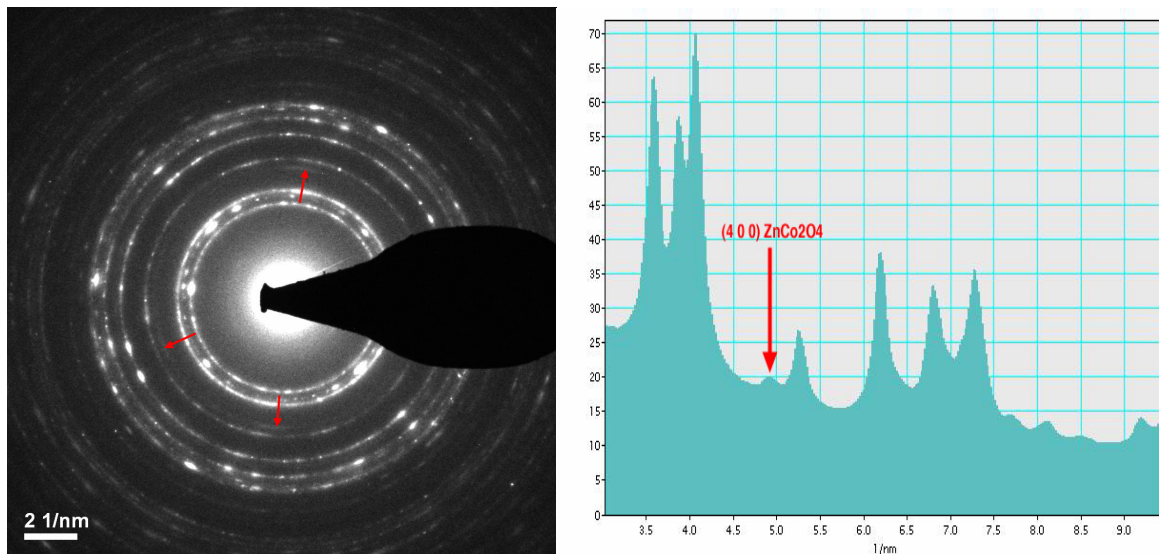


Figure 6.21: Electronic diffraction results for $\text{Zn}_{0.92}\text{Co}_{0.08}\text{O}$ produced under air identifying a small quantity of ZnCo_2O_4 precipitate, marked by red arrows in SADP scan and in radial intensity of the corresponding SADP scan.

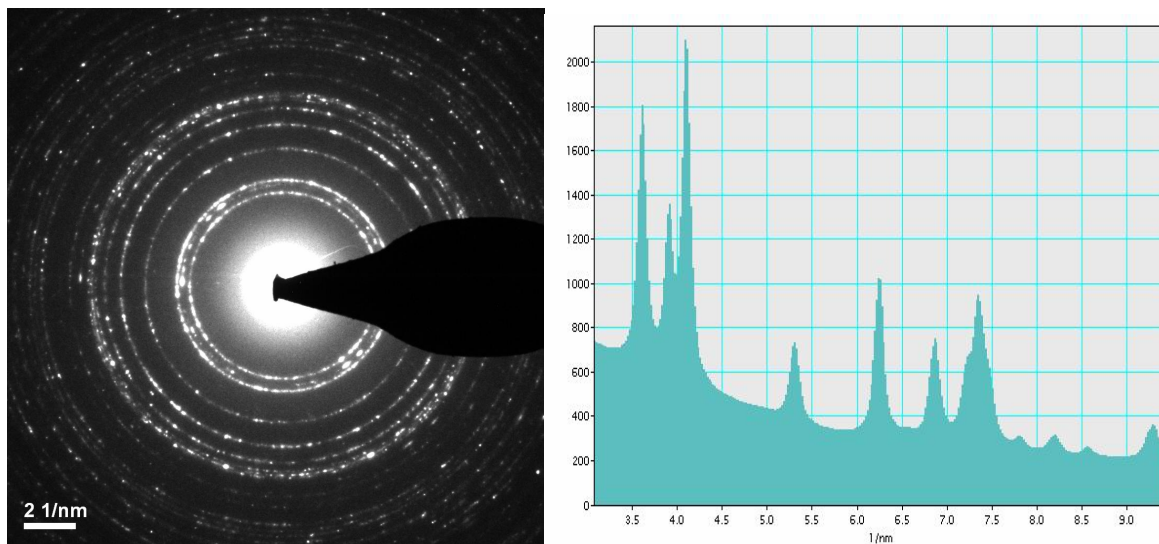


Figure 6.22: Electronic diffraction results for $\text{Zn}_{1-x}\text{Co}_x\text{O}$ produced under reducing atmosphere revealing only ZnO , both in the SADP and the corresponding radial scan. As the CoO reflections coincide well with the ZnO reflections they could be masked with the ZnO reflections, pointing to CoO as the stoichiometry of the existing Co -rich phase. Possible Co reflections would be clearly discernable from the ZnO reflections and are not observed.

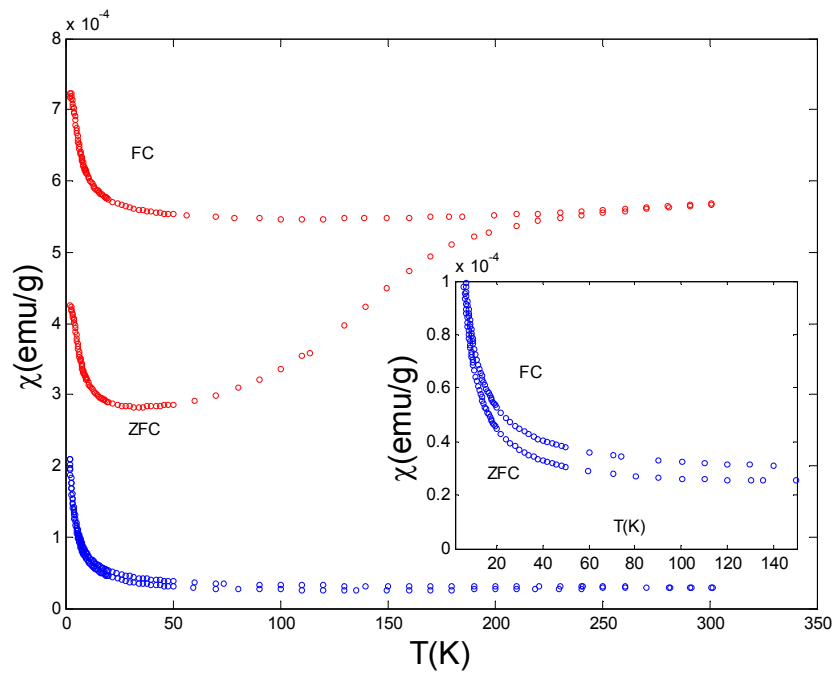


Figure 6.23: ZFC-FC measurements of $x = 0.04$ (blue) $x = 0.08$ (red) $\text{Zn}_{1-x}\text{Co}_x\text{O}$ produced in $\text{N}_2\text{-H}_2$ at 0.1 T applied field revealing a non Curie-Weiss behaviour with ferromagnetic splitting at $T_C \approx 260 \text{ K}$ for the two samples. Inset is the zoom at the low temperature ZFC and FC curves of the $x = 0.04$ $\text{Zn}_{1-x}\text{Co}_x\text{O}$, where clear splitting is present.

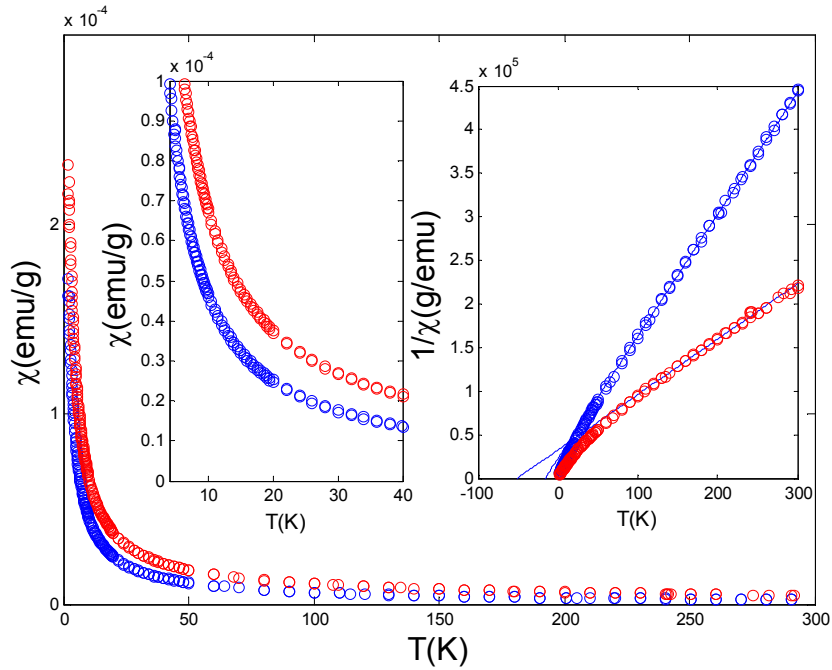


Figure 6.24: ZFC-FC measurements of $x = 0.04$ (blue) $x = 0.08$ (red) $\text{Zn}_{1-x}\text{Co}_x\text{O}$ produced in air at 0.1 T applied field revealing a Curie-Weiss behaviour with the dominant antiferromagnetic interactions reflected in the negative Curie-Weiss temperatures for both samples.

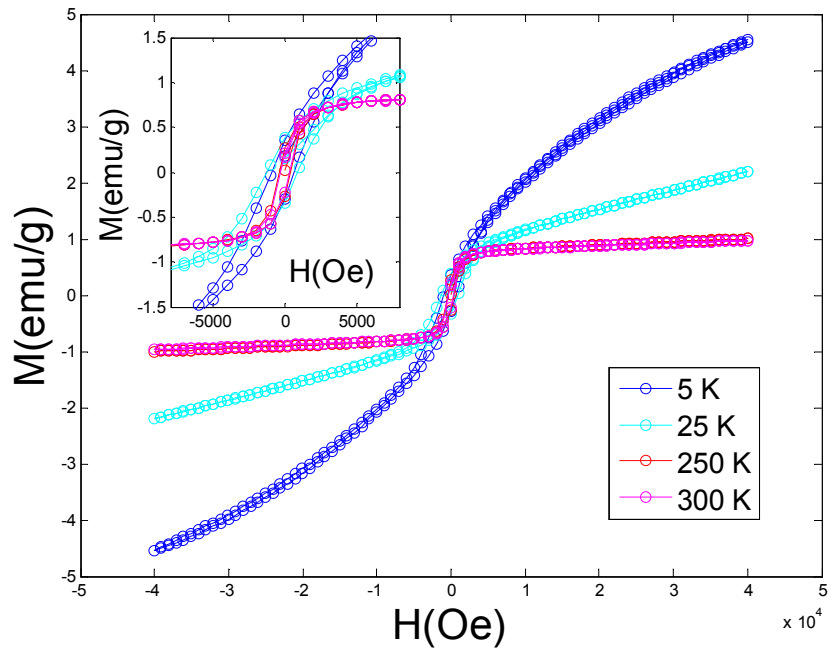


Figure 6.25: A signal revealing a soft-ferromagnetic nature of the $x=0.08$ $\text{Zn}_{1-x}\text{Co}_x\text{O}$ sample produced under $\text{N}_2\text{-H}_2$ at 5 K (blue), 25 K (cyan), 250 K (red) and 300 K (magenta). The inset shows the blow-up of the hysteresis loop for all the temperatures noted.

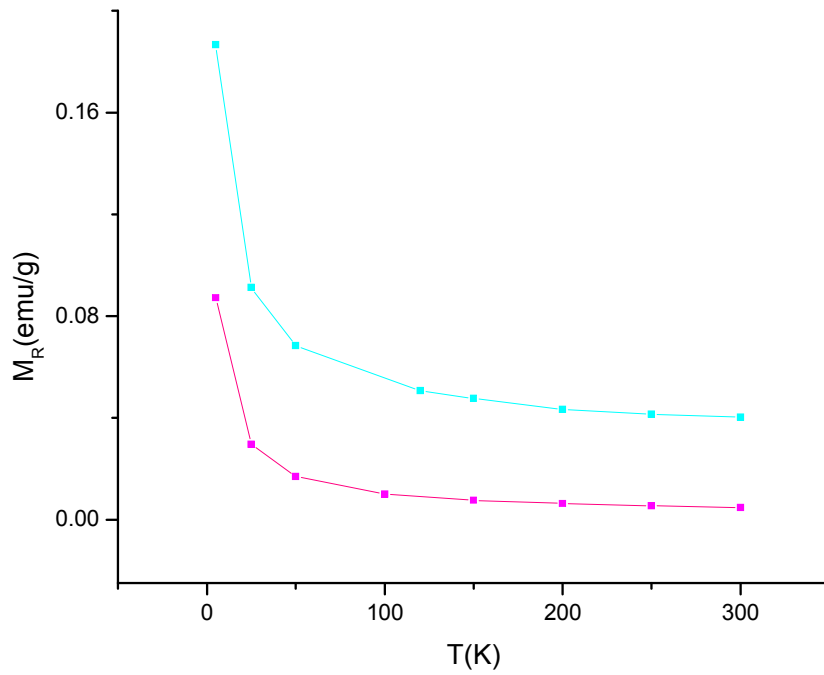


Figure 6.26: The measured magnetic remanence of $x = 0.04$ $\text{Zn}_{1-x}\text{Co}_x\text{O}$ (magenta) and $x = 0.08$ $\text{Zn}_{1-x}\text{Co}_x\text{O}$ (cyan) samples produced in reducing atmosphere measured in the temperature range of 5 - 300 K.

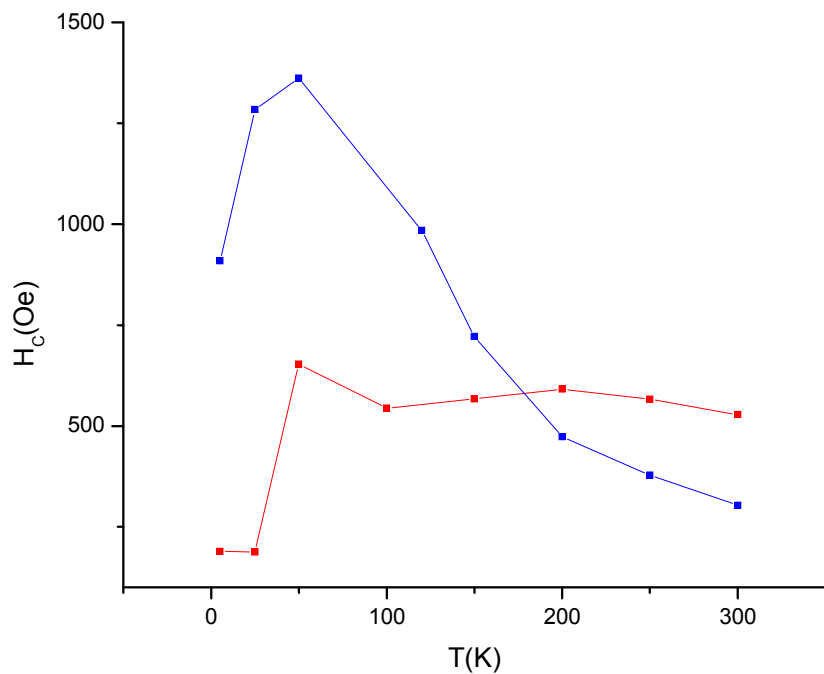


Figure 6.27: The measured magnetic coercivity of $x = 0.04$ $\text{Zn}_{1-x}\text{Co}_x\text{O}$ (red) and $x = 0.08$ $\text{Zn}_{1-x}\text{Co}_x\text{O}$ (blue) samples produced in reducing atmosphere measured in the temperature range of 5 - 300 K.

from the structural point of view, the precipitated phase in the sample produced in reducing atmosphere could be the hexagonal CoO, with reflections coinciding with the ones of ZnO, and therefore likely to be hidden by them. The metallic Co would have exhibited distinctly different and easy to discern reflections from the ones of the host ZnO.

Together with the fact that the ferromagnetism of $\text{Zn}_{1-x}\text{Co}_x\text{O}$ exhibits on-and-off switching when exposed to atmospheres of nitrogen and oxygen, the influence of the synthesis parameters on the structural defects, the chemistry and the magnetic properties of the $\text{Zn}_{1-x}\text{Co}_x\text{O}$ is one of the main reasons to study samples produced under different synthesis conditions.

As shown in Fig. 6.24 $x = 0.04$ $\text{Zn}_{1-x}\text{Co}_x\text{O}$ and $x = 0.08$ $\text{Zn}_{1-x}\text{Co}_x\text{O}$ produced in oxidizing atmosphere (air) showed no splitting in the SQUID ZFC-FC measurement whatsoever hence the absence of ferromagnetism. Instead, a Curie-Weiss behaviour was documented with the dominant antiferromagnetic interactions reflected in the Curie-Weiss temperature of -16 K ($x = 0.04$) and -51 K ($x = 0.08$), respectively. The results for the $x = 0.04$ $\text{Zn}_{1-x}\text{Co}_x\text{O}$ and $x = 0.08$ $\text{Zn}_{1-x}\text{Co}_x\text{O}$ produced in reducing atmosphere are given in the Figure 6.23. In the standard zero-field cooled - field cooled (ZFC-FC) measurement at the applied field of 0.1 T the $x = 0.08$ sample shows a big splitting between the ZFC and FC lines, and $x = 0.04$ a somewhat smaller splitting, yet a ferromagnetic signal below $T_C \approx 260$ K is discerned from these measurements for both of the samples.

As introduced in Section 3.3.2 a standard proof of ferromagnetism is the appearance of the magnetic hysteresis in the field sweep scan of the ferromagnetic material at a given temperature. These sets of measurements are given in Fig. 6.25. The presence of hysteresis is confirmed in the 5 - 300 K range hence the actual Curie temperature of the ferromagnetic sample can prove to be even higher than the $T_C \approx 260$ K deduced from the temperature of the splitting in the results of the ZFC-FC measurement. The strong relation between the magnetic properties and the atmosphere of the synthesis, itself in connection with the defect chemistry and the number of charge carriers in the system is hence clear.

The significantly stronger splitting was found probably due to the fact that the amount of the precipitated Co is higher for a $x = 0.08$ than $x = 0.04$ nominal concentration sample,

especially regarding remanence, as it can be seen in Figs 6.26 and 6.27.

The proof of the high temperature ferromagnetism is the fact that the hysteresis (i.e. the magnetic remanence and coercivity) persists up to the room temperature for both $x = 0.04$ and $x = 0.08$ $\text{Zn}_{1-x}\text{Co}_x\text{O}$, up to 300 K, which was the highest temperature we were able to measure using the SQUID setup.

The samples produced in air exhibit no splitting whatsoever, pointing to the absence of ferromagnetism in these samples. To conclude, the ferromagnetism in $\text{Zn}_{1-x}\text{Co}_x\text{O}$ which is a topic of the current efforts, with the case of ferromagnetism being tackled by advanced spectroscopic synchrotron techniques such as in the very recent work by Ney et al. [127] is likely to occur when there are precipitates of the Co rich phase. At this point in time we have narrowed our candidates for the Co rich phase in $\text{Zn}_{1-x}\text{Co}_x\text{O}$ to metallic cobalt, a high temperature ferromagnet and CoO, which is a high temperature antiferromagnet capable of inducing superparamagnetism. The further structural studies will determine which of the two phases is in question. One can say that our results concur well with the most recent efforts at the time of writing of this Thesis, such as the aforementioned work by Ney et al. that concludes the $\text{Zn}_{1-x}\text{Co}_x\text{O}$ without any precipitates or excessive formation of defects being non-ferromagnetic.

Our work on $\text{Zn}_{1-x}\text{Co}_x\text{O}$ has demonstrated that the samples produced in air tend to be oxidized enough not to form the problematic metallic cobalt phase, yet the concentration that we have worked with was probably too high enabling the formation of the small quantity of the overly oxidized ZnCo_2O_4 phase, which is, as is ZnMnO_3 , the topic of the large part of this Thesis, a cubic spinel. Kim et al. [128] have found that crystal structure of zinc cobalt oxide films changes from wurtzite $\text{Zn}_{1-x}\text{Co}_x\text{O}$ to spinel ZnCo_2O_4 with the increase of the sputtering power ratio between the Co and Zn metal targets. With this in mind, the next step in synthesizing single phase bulk $\text{Zn}_{1-x}\text{Co}_x\text{O}$ is the application of our method with the hydrozincite precursor but with less than 8% Co in concentration.

6.5 Ni as a dopant

Together with Mn and Co, Ni doped ZnO is one of the most studied materials in this field, with its own contribution to the overall controversy surrounding the field. A review by Pan et al. [65] cites two occurrences of studied $\text{Zn}_{1-x}\text{Ni}_x\text{O}$ with diametrically different observed magnetic properties. While the material synthesized on Al (0001) has had paramagnetic properties, the thin film $\text{Zn}_{1-x}\text{Ni}_x\text{O}$ synthesized on Si (100) was found to be ferromagnetic with the T_C in excess of 300 K and the magnetic moment measured to be $0.37 \mu_B/\text{Ni}$ ion. An outstanding work that occurred prior to the avalanche of papers in the DMS/DMO field was the work by Makhlof et al. [129]. They demonstrated the assertion by one of the bards of the ferromagnetism, Louis Néel who conjectured that antiferromagnetic nanoparticles could exhibit superparamagnetic relaxation of their spin lattices as well as permanent moments arising from uncompensated surface spins. This is analogous to the suggested role of Co in $\text{Zn}_{1-x}\text{Co}_x\text{O}$, as explained in the preceding Section. The synthesis of $\text{Zn}_{1-x}\text{Ni}_x\text{O}$ from $(\text{Zn}_{1-x}\text{Ni}_x)_5(\text{OH})_6(\text{CO}_3)_2$ required the use of 400°C to arrive at the optimal decomposition temperature. This was readily inferred by using XRD, as demonstrated in the Fig. 6.28. The heat-treatment at 200°C was not enough to decompose the hydrozincite into zincite completely, as demonstrated in Fig. 6.28. We have tried to infer whether decomposition is simply a time related effect and performed the synthesis for longer time, namely 3 and 6 hours, yet the hydrozincite peaks still persisted.

In order to see what the magnetic properties of the intermediate product were, we have performed magnetic measurements on the samples produced at 200°C and 400°C . Beforehand, we have performed the structural analysis of the samples that were produced at 400°C . The initial TEM analysis of the $x=0.08$ $\text{Zn}_{1-x}\text{Ni}_x\text{O}$ revealed small nanoparticles apparent in some of the ZnO particles, hinting at the nanoscale separation of phases. Due to a small quantity of the precipitates, the compositional analysis using a 1-2 nm size probe in STEM-EELS was not useful in readily reproducing the observed presence of second phases.

In the higher concentration $x=0.2$ $\text{Zn}_{1-x}\text{Ni}_x\text{O}$ we have observed a strong and conspicuous NiO (200) reflection using XRD measurements. NiO has three strong reflections, of which the

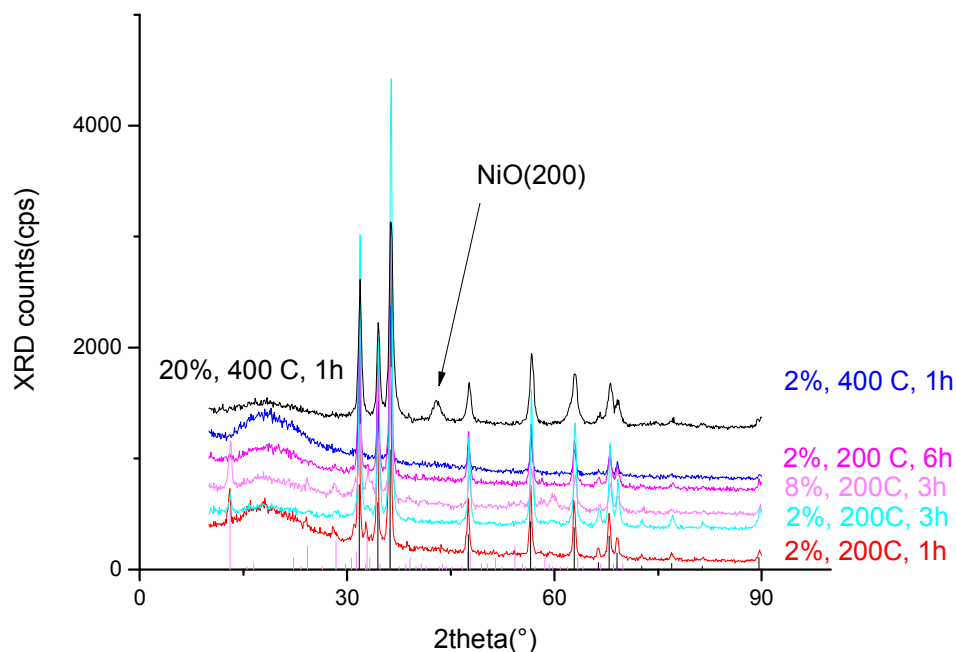


Figure 6.28: XRD signal of $Zn_{1-x}Ni_xO$ synthesized from the decomposition of $(Zn_{1-x}Ni_x)_5(OH)_6(CO_3)_2$ at various temperatures and various annealing times. $400^\circ C$ is the minimal temperature for $(Zn_{1-x}Ni_x)_5(OH)_6(CO_3)_2$ to decompose to $Zn_{1-x}Ni_xO$. For high enough concentration of Ni, NiO is formed.

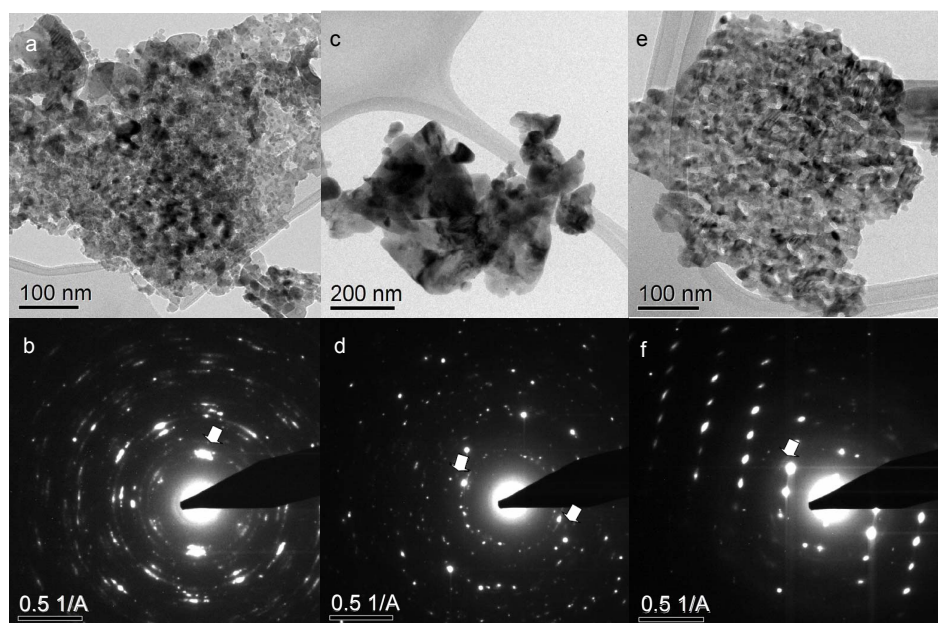


Figure 6.29: TEM and SADP images of the $x=0.08$ $Zn_{1-x}Ni_xO$ (a,b), $x=0.02$ $Zn_{1-x}Ni_xO$ (c,d) and $x=0.02$ $(Zn_{1-x}Ni_x)_5(OH)_6(CO_3)_2$ (e,f) NiO inclusions are present in all three samples and are indicated with white arrows.

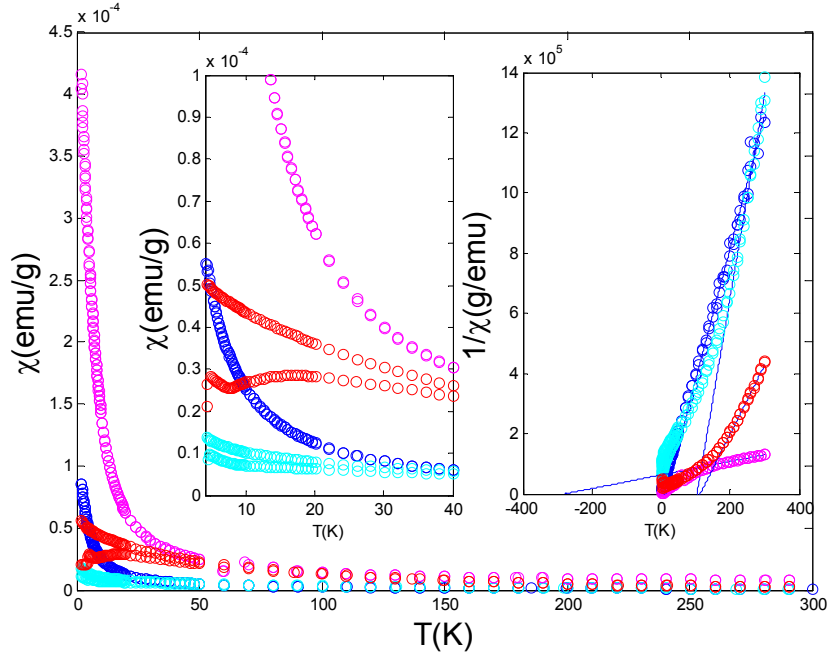


Figure 6.30: ZFC-FC curves measured at 1000 Oe for Ni doped ZnO and Ni doped ZnO/hydrozincite system. The cyan and red line represent the 2% and 8% $\text{Zn}_{1-x}\text{Ni}_x\text{O}$ samples containing NiO precipitates. These samples were produced by the decomposition of the hydrozincites at 400°C. The blue and magenta lines represent the nominal 2% and 8% of the not-completely-decomposed Ni doped hydrozincite/ZnO mixture of phases, synthesized at 200°C.

(111) and the (220) overlap with the ZnO reflections while the (200) reflection can easily be discerned from the ZnO reflections. It has been noticed in the SADP scans of the $x=0.08$ and $x=0.02$ $\text{Zn}_{1-x}\text{Ni}_x\text{O}$ particle and marked by arrows at the Fig 6.29 (b) and (d). The NiO can, however, go unnoticed in the STEM-EELS scan because of the small size of the NiO particles, and NiO being superposed on the ZnO particles.

In the nominal $x=0.02$ $\text{Zn}_{1-x}\text{Ni}_x\text{O}$ two morphologies of particles were observed. Some particles were found to contain NiO nanocrystals with very faint yet present reflections of NiO in SADPs. The ZnO was found to exhibit the same morphology and size characteristics as the higher concentration $x=0.08$ and $x=0.12$ samples. The discerning feature in the $x = 0.02$ sample was the appearance of the *cleaner* particles, that were more effectively doped and with much less NiO. Even in these particles the SADP revealed two faint, this time spots, corresponding to NiO(200) reflections.

Sample	T_{CW}
2% Ni, 200°C	14 K
8% Ni, 200°C	-279 K
2% Ni, 400°C	104 K
8% Ni, 400°C	113 K

Table 6.5: Values of Curie-Weiss $\Theta(x)$ for 2% Ni:ZnO and 8% Ni:ZnO synthesized at 200°C at 400°C. The samples produced at 200°C revealed antiferromagnetic or weakly ferromagnetic Curie-Weiss temperatures, while the samples produced at 400°C exhibited strongly ferromagnetic Curie-Weiss temperatures.

By finding the particle that SADP revealed was a co-existence of hydrozincite and NiO phase, we have revealed that the NiO nanocrystals form before ZnO. Fine dispersion of NiO nanocrystals hence forms first and then the growth of the ZnO crystals is modulated and limited to give the small and ill-defined ZnO grains that one observes in the NiO nanocrystal-containing particles. The opposite case of the ZnO crystals growing first can occur. In this case ZnO is not constrained by NiO and grows to form larger, more well-defined grains that are only slightly Ni-doped. While the two scenarios seem to be equally probable and equally occur in $x=0.02$ sample, the prevalent case for higher concentration samples is the one with NiO growing first.

The magnetism of $Zn_{1-x}Ni_xO$ has shown remarkable transition from the dominantly non-ferromagnetic mixture of $Zn_{1-x}Ni_xO$ and $(Zn_{1-x}Ni_x)_5(OH)_6(CO_3)_2$ produced under 200°C to $Zn_{1-x}Ni_xO$ produced under 400°C in which nanoparticles of NiO precipitated causing the observed ZFC-FC splitting below 120 K. This is shown in Fig. 6.30 where the $Zn_{1-x}Ni_xO$ produced under 200°C are represented with a cyan (2% of Ni) and red (8% of Ni) line and $Zn_{1-x}Ni_xO$ produced under 400°C with blue (2% of Ni) and magenta (8% of Ni) lines, respectively. A very conspicuous move of the Curie-Weiss temperatures from the antiferromagnetic Curie-Weiss temperatures for the samples containing Ni:hydrozincites to ferromagnetic Curie-Weiss temperatures is given in the Table 6.5.

This is in very close relationship with the structural properties of $Zn_{1-x}Ni_xO$ produced by this synthesis method. As the solid state solubility limit of Ni is seemingly much higher in ZnO than in $Zn_5(OH)_6(CO_3)_2$ the excess Ni is either expelled from ZnO in the form of NiO,

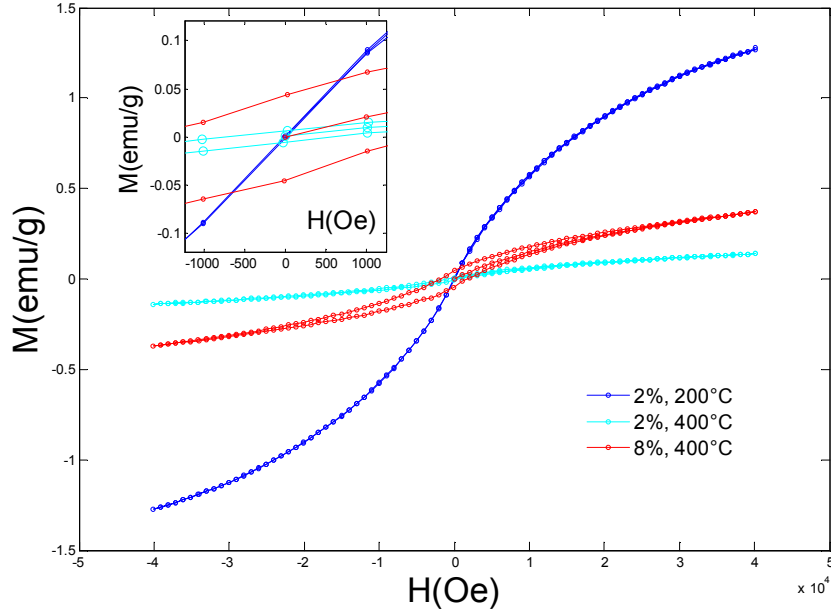


Figure 6.31: -4 T-4 T field sweeps performed on Ni doped ZnO and Ni doped ZnO/hydrozincite system. The cyan and red line represent the 2% and 8% $Zn_{1-x}Ni_xO$ samples with NiO precipitates produced by the decomposition of the corresponding hydrozincites at 400°C. The blue line represents the nominal 2% of the not completely decomposed Ni doped hydrozincite/ZnO mixture of phases, synthesized at 200°C.

or as our earlier discussion claims, simply formed before the ZnO formation. The diameter of NiO is too small to be detected by XRD in $x < 0.08$ as can be inferred from the Fig. 6.28. One can conclude from the analysis in this Section of the Thesis that NiO is synthesized only towards the latter stages of the hydrozincite decomposition, but in many cases before ZnO, and it gives the ferromagnetic, or superparamagnetic on a larger scale, contribution to the magnetism of $Zn_{1-x}Ni_xO$.

The further analysis of the properties of Ni doped ZnO and Ni doped ZnO/hydrozincite system is given in Fig. 6.31. The hysteresis in the field sweep scan confirms the ferromagnetic properties of 2% and 8% $Zn_{1-x}Ni_xO$ samples with NiO precipitates donated by the NiO inclusions to the ZnO system.

The superparamagnetic nature of the NiO contribution is hinted from the behavior of the magnetization of the 8% Ni:ZnO when field sweeps were performed. As explained in Section 5.2 the superparamagnetic behaviour above the blocking temperature of the system is reflected

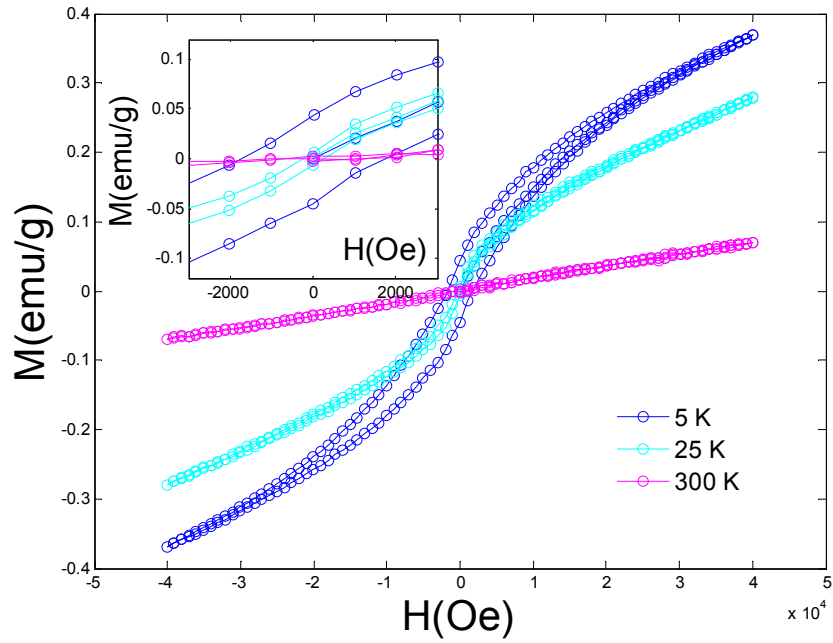


Figure 6.32: -4 T-4 T field sweeps performed on 8% Ni doped ZnO with NiO inclusions in the ZnO matrix. The blue line was measured at 5 K, while the cyan and magenta lines were measured at 25 K and 300 K, respectively.

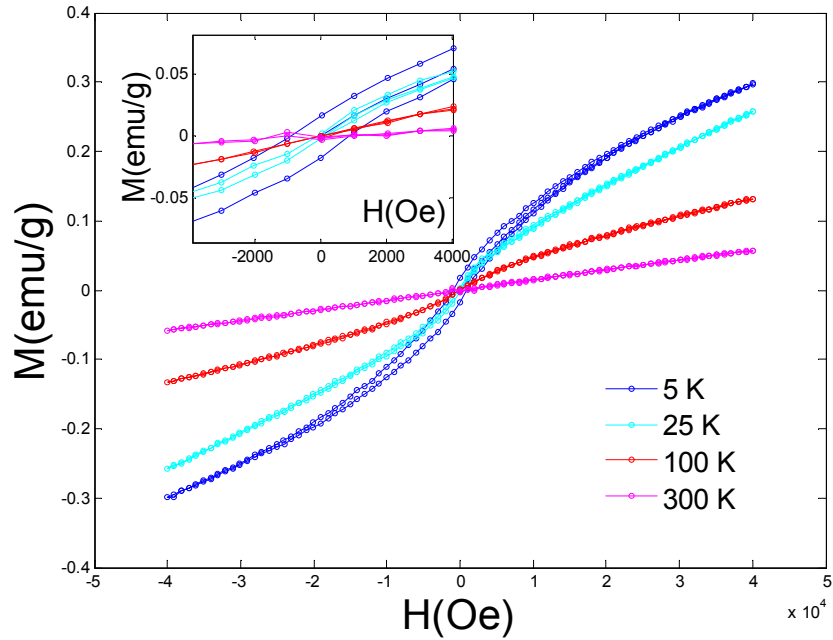


Figure 6.33: -4T-4T field sweeps performed on 4% Ni doped ZnO with NiO inclusions in the ZnO matrix. The blue and cyan line were measured at 5 K and 25 K, respectively, and show a small hysteresis. The red and magenta lines were measured at 100 K and 300 K, respectively and show no traces of the hysteresis.

in the disappearance of the hysteretic features in the field sweep of the magnetization, i.e. the coercive field H_C and the remanence M_R go to zero above the blocking temperature T_B . At 5 K and 25 K there is a clear existence of the hysteresis present while the line at 300 K bears no evidence of the hysteresis. A more persuasive evidence of this is the scan performed on the nominal 4% Ni:ZnO, given in Fig. 6.33 where the scan at 100 K, which is close to the blocking temperature T_B , was performed together with scans at 5 K, 25 K and 300 K. As evident from the Figure 6.33 the disappearance of the hysteresis at 100 K occurred.

In conclusion of this Chapter, we have seen remarkable properties of $Zn_{1-x}TM_xO$ for TM being Mn, Co and Ni synthesized from $(Zn_{1-x}TM_x)_5(OH)_6(CO_3)_2$. $Zn_{1-x}Mn_xO$ was found to exhibit magnetic properties dependent on the atmosphere of synthesis, which is in very close connection with being possible to realize controllable magnetic states by external parameters, one of the premises of spintronics. $Zn_{1-x}Co_xO$ produced in reducing atmosphere was found to be ferromagnetic, yet its magnetism was found to come from magnetic impurities, possibly of cobalt(II)-oxide which in itself is an antiferromagnet, but could yield to high temperature superparamagnetism. Another phase of antiferromagnetic NiO was found to be responsible for the superparamagnetism of the $Zn_{1-x}Ni_xO$ samples, with the blocking temperature of the order of 15 K. (Mn,Li) doping yielded to similar results in terms of magnetization as for $Zn_{1-x}Mn_xO$ samples proving that the prediction of ferromagnetism in highly p-doped ZnO is not realistic, as the ZnO is natively n-doped and it is very difficult to achieve a highly p-doped ZnO and hence the activated ferromagnetism.

Chapter 7

Conclusion and outlook

Scientists are constantly in search for materials suitable for spintronics, spin electronics, the technology that could bring the concept of quantum computing to the realm of everyday application. This could revolutionize the society probably to the extent that the Si based technology did starting from 1960s to the time of the writing of this work. The computer that could boot-up instantaneously or be in stand-by state without any power needed is one of the concepts that spintronics could achieve. The idea of doping semiconductors with magnetic elements is rooted in already developed techniques for semiconductors. Imparting the magnetic, spin degree of freedom to the conventional semiconductors could render them usable for spintronics, where upon the application of magnetic field the energy of spin states becomes different and the electrons can be put into two groups according to the value of their spin. Magnetic semiconductors could also allow for the communication, logic operations and data storage to be merged into a single material.

The road to a functional material is however paved with difficulties and this Thesis work tried to tackle the most common problems regarding its successful synthesis from the chemistry point of view and matching the success in the synthesis with thorough measurements of its physical properties. Our material of choice was $\text{Zn}_{1-x}\text{Mn}_x\text{O}$. The problem in the conventional field of diluted magnetic semiconductors field was soon narrowed down to insufficient characterization and synthesis methods that lead to clustering and parasitic phase formation

within the host semiconducting matrices. As the magnetic signals searched for are easily to be mixed up with the signals coming from clustered magnetic moments or precipitation of parasitic phases one has to characterize the materials thoroughly to infer the real origin of the magnetization. The XRD was the first step in identifying the parasitic phase within our material. Only at $x=0.1$ and higher nominal Mn contents within our $\text{Zn}_{1-x}\text{Mn}_x\text{O}$ material did we notice the reflections of the strongest peak of the ZnMnO_3 impurity. We have therefore used XRD only as an initial *filter* of the quality of our materials. Much more focus has been put on TEM analysis coupled with EDXS and EELS and XPS as the main structural investigation techniques.

Throughout this Thesis we have developed two new synthesis techniques, both relying on the use of novel precursors. The use of nitrate precursors enabled us to obtain the liquid mixture of the precursors and to preserve the mix of the magnetic ions in a non-magnetic matrix. The synthesis of the single-phase nanocrystalline powders was however inhibited by the oxidative activities of the NO_x species during the synthesis process. Staying on the original path of using molten precursors with inherent homogeneity of magnetic species' distribution we have employed synthesis in solutions of nitrates and urea, $\text{CO}(\text{NH}_2)_2$. Urea is the chemical that was used in order to be oxidized by the weakly oxidative species, CO_2 and H_2O , the co-products of the synthesis, thereby leaving the Mn non oxidized and in their original 2+ oxidation state. This method proved a suitable choice for synthesizing powders of single-phase $\text{Zn}_{1-x}\text{Mn}_x\text{O}$ studies with product purity $> 99.9\%$ established by TEM. In other words, less than 1 in 1000 particles observed were found to be an impurity phase, with an estimated volume fraction even lower.

With the two synthesis methods at hand we have proceeded to identify the magnetic and electronic properties of our samples using primarily the SQUID magnetometry, and the ESR measurements at low fields. High-field ESR, the AC susceptibility and AC and DC conductivity together with thermopower have been used to identify the properties of the samples as well.

The synthesis from nitrate precursor enabled us to discover a new compound, ZnMnO_3 . We have been able to identify the contribution of the ZnMnO_3 to the magnetic and electronic

properties of $\text{Zn}_{1-x}\text{Mn}_x\text{O}/\text{ZnMnO}_3$ establishing that ZnMnO_3 itself goes through a short range magnetic transition at ≈ 15 K, but also that it in minute concentrations invokes a 4.4 K superparamagnetic transition in $\text{Zn}_{1-x}\text{Mn}_x\text{O}$. The $\text{Zn}_{1-x}\text{Mn}_x\text{O}$ was additionally found to be the phase responsible for the semiconducting-like conductivity of the $\text{Zn}_{1-x}\text{Mn}_x\text{O}$ samples containing it, while the DC conductivity measurements revealed the activation energy Δ of 0.7 eV and the positive sign of the thermopower mentioned, i.e. the positive sign of the charge carriers. The importance of this result is only beginning to shape with several important publications mapping the low temperature Zn-Mn-O phase diagram and a number of results of high-temperature ferromagnetic properties of $\text{Zn}_{1-x}\text{Mn}_x\text{O}$ being tracked down to spinel structures isostructural with ZnMnO_3 .

The urea route synthesis resulted in a new discovery, hydrozincite $(\text{Zn}_{1-x}\text{Mn}_x)_5(\text{OH})_6(\text{CO}_3)_2$, a form of layered ZnO with the layers interbridged with CO_3 groups. Hydrozincite precursor was studied for Mn, Co, Ni dopants, as well as (Mn,Li) co-dopants. The main results for Mn as a dopant reveal a strong dependence of magnetic signatures on the atmosphere of the decomposition, with the systems not exhibiting any ferromagnetic ordering when synthesized under air, i.e. in oxidative conditions. The stronger interactions, the absence of the ZnMnO_3 precipitation and the ferromagnetic ordering below 40 K were the signatures of the samples produced in reducing atmospheres. The ferromagnetic ordering was however been found to be of short-range and consistent with the spin-glass phenomenon, deduced from ESR measurements through the analysis of ESR intensity, ESR linewidth and the g-factor.

Other TM ions were tried to be introduced in ZnO host. The case of $\text{Zn}_{1-x}\text{Co}_x\text{O}$ is notoriously difficult as the possible precipitate, Co, is ferromagnetic with T_C higher than room temperature. What has been shown in this work is that Co is likely to precipitate when synthesis is performed in reducing atmosphere. This brings about the aforementioned ferromagnetism with $T_C > 300$ K. Synthesis in oxidative conditions, i.e. air, has radically different magnetic signature, the $\text{Zn}_{1-x}\text{Co}_x\text{O}$ being weakly antiferromagnetic but exhibiting a Curie-Weiss behaviour of magnetic susceptibility with no traces of ferromagnetic ordering.

In $\text{Zn}_{1-x}\text{Ni}_x\text{O}$ a significantly lower solid-state solubility of Ni in the ZnO matrix than in

$\text{Zn}_5(\text{OH})_6(\text{CO}_3)_2$ has been shown. The Ni was hence found to precipitate and form NiO second phase even for $x < 0.02$ concentrations of Ni in ZnO. The weak ferromagnetism of Ni doped ZnO was found to stem from the NiO inclusions in the ZnO matrix. As an empirical rule throughout this work the parasitic phases were not identified using XRD, but only through TEM inspection. The superparamagnetic state exists below 120 K and exhibited a remanence of 0.05 emu/g and coercivity of 2000 Oe at 2 K.

The originally proposed theory for high T_C ferromagnetism in ZnO requires a highly p-doped material. The latter is not a trivial task as the dominant defects in zinc oxide are the zinc interstitials and oxygen vacancies both bringing an unintentional, n-doping to the system. The case of (Mn,Li) co-doped ZnO did not show significant differences to Mn doped ZnO and no long-range ferromagnetic ordering was found in the (Mn,Li) co-doped ZnO samples. The investigations have to be continued in the view of qualifying the conductivity and the species of charge carriers in this system.

The main result of this Ph.D work is that a new synthesis route was elaborated for a homogeneous magnetic semiconductor. This settles a solid starting point for the amelioration of the material with additional dopings to tune the magnetic properties of the material towards room temperature. However, the very next step will be to transfer this homogeneous microcrystalline material by sputtering technique into a thin film form and check if the homogeneity is maintained. We are confident that this will be the case, and with new doping procedures it will settle the program for further doctoral studies.

Bibliography

- [1] Chennupati, J. and Pearton, S., editors. *Zinc Oxide Bulk, Thin Films and Nanostructures*. Elsevier Limited, (2006).
- [2] Dietl, T., Ohno, H., Matsukura, F., Cibert, J., and Ferrand, D. *Science* **287**, 1019–1022 (2000).
- [3] Tsai, Y. L., Huang, C. L., and Wei, C. C. *Journal of Materials Science Letters* **4**, 1305–1307 (1985).
- [4] Lee, S. H., Lee, S. S., Choi, J. J., Jeon, J. U., and Ko, R. *Advances in Nondestructive Evaluation, Pt 1-3* **270-273**, 1095–1100 (2004).
- [5] Lee, S. H., Lee, S. S., Choi, J. J., Jeon, J. U., and Ro, K. *Microsystem Technologies-Micro-and Nanosystems-Information Storage and Processing Systems* **11**(6), 416–423 (2005).
- [6] Sato, K. and Katayama-Yoshida, H. *Japanese Journal of Applied Physics Part 2-Letters* **39**(6B), L555–L558 (2000).
- [7] Sato, K. and Katayama-Yoshida, H. *Japanese Journal of Applied Physics Part 2-Letters* **40**(4A), L334–L336 (2001).
- [8] Datta, S. and Das, B. *Applied Physics Letters* **56**(7), 665–667 (1990).
- [9] Kittel, C. *Physical Review* **71**(4), 270–271 (1947).
- [10] Kittel, C. *Physical Review* **72**(6), 529–529 (1947).

- [11] Kittel, C. *Introduction to solid state physics*. John Wiley & Sons, Inc., (2005).
- [12] Vanvleck, J. H. *Physical Review* **78**(3), 266–274 (1950).
- [13] Anderson, P. W. and Weiss, P. R. *Reviews of Modern Physics* **25**(1), 269–276 (1953).
- [14] Anderson, P. W. *Physical Review* **79**(2), 350–356 (1950).
- [15] Crangle, J. *The magnetic properties of solids*. Edward Arnold, (1976).
- [16] Blundell, S. *Magnetism in condensed matter*. Oxford Master Series in Condensed Matter Physics, (2008).
- [17] Kramers, H. A. *Physica* **1**, 182–192 (1934).
- [18] Goodenough, J. B. and Loeb, A. L. *Physical Review* **98**(2), 391–408 (1955).
- [19] Goodenough, J. B. *Physical Review* **100**(2), 564–573 (1955).
- [20] Kanamori, J. *Journal of Physics and Chemistry of Solids* **10**(2-3), 87–98 (1959).
- [21] Dzyaloshinsky, I. *Journal of Physics and Chemistry of Solids* **4**(4), 241–255 (1958).
- [22] Moriya, T. *Physical Review Letters* **4**(5), 228–230 (1960).
- [23] Furdyna, J. K. and Kossut, J. *Semiconductors and semimetals, vol.25: Diluted Magnetic Semiconductors*. Academic Press Inc., Harcourt Brace Jovanovich, Publishers., (1988).
- [24] Fischer, K. H. and Hertz, J. A. *Spin glasses*. Cambridge University Press, (1991).
- [25] Zutic, I., Fabian, J., and Das Sarma, S. *Reviews of Modern Physics* **76**(2), 323–410 (2004).
- [26] Baibich, M. N., Broto, J. M., Fert, A., Vandau, F. N., Petroff, F., Eitenne, P., Creuzet, G., Friederich, A., and Chazelas, J. *Physical Review Letters* **61**, 2472–2475 (1988).
- [27] Esaki, L., Stiles, P. J., and Molnar, S. V. *Physical Review Letters* **19**, 852–854 (1967).
- [28] Julliere, M. *Physics Letters A* **54**, 225–226 (1975).

- [29] Feher, G. *Physical Review Letters* **3**(3), 135–137 (1959).
- [30] Lampel, G. *Physical Review Letters* **20**(10), 491–493 (1968).
- [31] Kastler, A. *Journal De Physique Et Le Radium* **11**(6), 255–265 (1950).
- [32] Dyakonov, M. I. and Perel, V. I. *Jetp Letters-Ussr* **13**(11), 467 (1971).
- [33] Coleman, P. *Physics* **2**, 9 (2009).
- [34] Aronov, A. G. *Zhurnal Eksperimentalnoi I Teoreticheskoi Fiziki* **71**(7), 370–376 (1976).
- [35] Dzhioev, R. I., Kavokin, K. V., Korenev, V. L., Lazarev, M. V., Meltser, B. Y., Stepanova, M. N., Zakharchenya, B. P., Gammon, D., and Katzer, D. S. *Physical Review B* **66**(24), 245204 (2002).
- [36] Bir, G. L., Aronov, A. G., and Pikus, G. E. *Zhurnal Eksperimentalnoi I Teoreticheskoi Fiziki* **69**(4), 1382–1397 (1975).
- [37] Dyakonov, M. I., editor. *Spin physics in semiconductors*. Springer Verlag, (2008).
- [38] Stoehr, J. Siegmann, H. C. *Magnetism From Fundamentals to Nanoscale Dynamics*. Springer Verlag Berlin Heidelberg, (2006).
- [39] Felser, C., Fecher, G. H., and Balke, B. *Angewandte Chemie-International Edition* **46**(5), 668–699 (2007).
- [40] Mohn, P. *Magnetism in the Solid State: An Introduction*. Springer-Verlag Berlin Heidelberg, (2003, 2006).
- [41] Katayama-Yoshida, H. and Sato, K. *Physica B-Condensed Matter* **327**(2-4), 337–343 (2003).
- [42] Fabian, J., Matos-Abiague, A., Ertler, C., Stano, P., and Zutic, I. *Acta Physica Slovaca* **57**(4-5), 565–907 (2007).
- [43] Kasuya, T. and Yanase, A. *Reviews of Modern Physics* **40**(4), 684–696 (1968).

- [44] Baltzer, P. K., Lehmann, H. W., and Robbins, M. *Physical Review Letters* **15**(11), 493–& (1965).
- [45] Furdyna, J. K. *Journal of Applied Physics* **64**(4), R29–R64 (1988).
- [46] Ohno, H., Munekata, H., Penney, T., Vonmolnar, S., and Chang, L. L. *Physical Review Letters* **68**(17), 2664–2667 (1992).
- [47] Munekata, H., Ohno, H., Vonmolnar, S., Segmuller, A., Chang, L. L., and Esaki, L. *Physical Review Letters* **63**(17), 1849–1852 (1989).
- [48] Ohno, H., Shen, A., Matsukura, F., Oiwa, A., Endo, A., Katsumoto, S., and Iye, Y. *Applied Physics Letters* **69**(3), 363–365 (1996).
- [49] Oseroff, S. B. *Physical Review B* **25**(11), 6584–6594 (1982).
- [50] Spalek, J., Lewicki, A., Tarnawski, Z., Furdyna, J. K., Galazka, R. R., and Obuszko, Z. *Physical Review B* **33**(5), 3407–3418 (1986).
- [51] Ben Mahmoud, A., von Bardeleben, H. J., Cantin, J. L., Chikoidze, E., and Mauger, A. *Journal of Applied Physics* **101**(1), 013902 (2007).
- [52] Mulder, C. A. M., Vanduyneveldt, A. J., and Mydosh, J. A. *Physical Review B* **23**(3), 1384–1396 (1981).
- [53] Han, J. P., Mantas, P. Q., and Senos, A. M. R. *Journal of the European Ceramic Society* **22**(1), 49–59 (2002).
- [54] Vogel, D., Kruger, P., and Pollmann, J. *Physical Review B* **52**(20), 14316–14319 (1995).
- [55] Van de Walle, C. G. *Physical Review Letters* **85**(5), 1012–1015 (2000).
- [56] Look, D. C., Reynolds, D. C., Sizelove, J. R., Jones, R. L., Litton, C. W., Cantwell, G., and Harsch, W. C. *Solid State Communications* **105**, 399–401 (1998).
- [57] Costa, M. E. V., Mantas, P. Q., and Baptista, J. L. *Sensors and Actuators B-Chemical* **27**(1-3), 312–314 (1995).

- [58] Joanni, E. and Baptista, J. L. *Sensors and Actuators B-Chemical* **17**(1), 69–75 (1993).
- [59] Ozgur, U., Alivov, Y. I., Liu, C., Teke, A., Reshchikov, M. A., Dogan, S., Avrutin, V., Cho, S. J., and Morkoc, H. *Journal of Applied Physics* **98**(4) (2005).
- [60] Dalcorso, A., Posternak, M., Resta, R., and Baldereschi, A. *Physical Review B* **50**(15), 10715–10721 (1994).
- [61] Nye, J. F. *Physical Properties of Crystals*. Clarendon, Oxford, (1975).
- [62] Hill, N. A. and Waghmare, U. *Physical Review B* **62**(13), 8802–8810 (2000).
- [63] Kuroda, S., Nishizawa, N., Takita, K., Mitome, M., Bando, Y., Osuch, K., and Dietl, T. *Nature Materials* **6**(6), 440–446 (2007).
- [64] Dietl, T. *Journal of Applied Physics* **103**(7), 07D111 (2008).
- [65] Pan, F., Song, C., Liu, X. J., Yang, Y. C., and Zeng, F. *Materials Science & Engineering R-Reports* **62**(1), 1–35 (2008).
- [66] Mandal, S. K., Das, A. K., Nath, T. K., Karmakar, D., and Satpati, B. *Journal of Applied Physics* **100**(10), 104315 (2006).
- [67] Song, C., Geng, K. W., Zeng, F., Wang, X. B., Shen, Y. X., Pan, F., Xie, Y. N., Liu, T., Zhou, H. T., and Fan, Z. *Physical Review B* **73**(2), 024405 (2006).
- [68] Gu, Z. B., Lu, M. H., Wang, J., Du, C. L., Yuan, C. S., Wu, D., Zhang, S. T., Zhu, Y. Y., Zhu, S. N., and Chen, Y. F. *Thin Solid Films* **515**(4), 2361–2365 (2006).
- [69] MacManus-Driscoll, J. L., Khare, N., Liu, Y. L., and Vickers, M. E. *Advanced Materials* **19**(19), 2925–2929 (2007).
- [70] Lin, Y. B., Lu, Z. H., Zou, W. Q., Lu, Z. L., Xu, J. P., Ji, J. T., Liu, X. C., Wang, J. F., Lv, L. Y., Zhang, F. M., Du, Y. W., Huang, Z. G., and Zheng, J. G. *Chinese Physics Letters* **24**(7), 2085–2087 (2007).

- [71] Jin, Z. W., Fukumura, T., Kawasaki, M., Ando, K., Saito, H., Sekiguchi, T., Yoo, Y. Z., Murakami, M., Matsumoto, Y., Hasegawa, T., and Koinuma, H. *Applied Physics Letters* **78**(24), 3824–3826 (2001).
- [72] Pakhomov, A. B., Roberts, B. K., and Krishnan, K. M. *Applied Physics Letters* **83**(21), 4357–4359 (2003).
- [73] Guo, J. H., Gupta, A., Sharma, P., Rao, K. V., Marcus, M. A., Dong, C. L., Guillen, J. M. O., Butorin, S. M., Mattesini, M., Glans, P. A., Smith, K. E., Chang, C. L., and Ahuja, R. *Journal of Physics-Condensed Matter* **19**(17), 172202 (2007).
- [74] Mandal, S. K. and Nath, T. K. *Thin Solid Films* **515**(4), 2535–2541 (2006).
- [75] Peiteado, M., Caballero, A. C., and Makovec, D. *Journal of Solid State Chemistry* **180**(9), 2459–2464 (2007).
- [76] Thota, S., Dutta, T., and Kumar, J. *Journal of Physics-Condensed Matter* **18**(8), 2473–2486 (2006).
- [77] Schwartz, D. A., Norberg, N. S., Nguyen, Q. P., Parker, J. M., and Gamelin, D. R. *Journal of the American Chemical Society* **125**(43), 13205–13218 (2003).
- [78] Deka, S., Pasricha, R., and Joy, P. A. *Chemistry of Materials* **16**(7), 1168–1169 (2004).
- [79] Bouloudenine, M., Viart, N., Colis, S., Kortus, J., and Dinia, A. *Applied Physics Letters* **87**(5), 052501 (2005).
- [80] Biswick, T., Jones, W., Pacula, A., Serwicka, E., and Podobinski, J. *Solid State Sciences* **11**(2), 330–335 (2009).
- [81] Lakshmi, Y. K., Srinivas, K., Sreedhar, B., Raja, M. M., Vithal, M., and Reddy, P. V. *Materials Chemistry and Physics* **113**(2-3), 749–755 (2009).
- [82] Liu, C., Yun, F., and Morkoc, H. *Journal of Materials Science-Materials in Electronics* **16**(9), 555–597 (2005).

- [83] Sharma, P., Gupta, A., Rao, K. V., Owens, F. J., Sharma, R., Ahuja, R., Guillen, J. M. O., Johansson, B., and Gehring, G. A. *Nature Materials* **2**(10), 673–677 (2003).
- [84] Seshadri, R. *Current Opinion in Solid State & Materials Science* **9**(1-2), 1–7 (2005).
- [85] Kundaliya, D. C., Ogale, S. B., Lofland, S. E., Dhar, S., Metting, C. J., Shinde, S. R., Ma, Z., Varughese, B., Ramanujachary, K. V., Salamanca-Riba, L., and Venkatesan, T. *Nature Materials* **3**(10), 709–714 (2004).
- [86] Gajbhiye, N. S., Bhattacharya, U., and Darshane, V. S. *Thermochimica Acta* **264**, 219–230 (1995).
- [87] Dollimore, D. *Journal of Thermal Analysis* **11**(2), 185–200 (1977).
- [88] Zener, C. *Physical Review* **81**(3), 440–444 (1951).
- [89] Zener, C. *Physical Review* **82**(3), 403–405 (1951).
- [90] Kittilstved, K. R. and Gamelin, D. R. *Journal of the American Chemical Society* **127**, 5292–5293 (2005).
- [91] Coey, J. M. D. *Current Opinion in Solid State & Materials Science* **10**(2), 83–92 (2006).
- [92] Zener, C. *Physical Review* **83**(2), 299–301 (1951).
- [93] Dietl, T., Awschalom, D., Kaminska, A., and Ohno, H. *Spintronics*. Academic Press, (2008).
- [94] Coey, J. M. D. *Journal of Applied Physics* **97**, 10D313 (2005).
- [95] Kittilstved, K. R., Norberg, N. S., and Gamelin, D. R. *Physical Review Letters* **94**(14), – (2005).
- [96] Ochsenein, S. T., Feng, Y., Whitaker, K. M., Badaeva, E., Liu, W. K., Li, X., and Gamelin, D. R. *Nature Nanotechnology* **4**(10), 681–687 OCT (2009).

- [97] Hausmann, A. and Huppertz, H. *Journal of Physics and Chemistry of Solids* **29**(8), 1369–1375 (1968).
- [98] Dorain, P. B. *Physical Review* **112**(4), 1058–1060 (1958).
- [99] Schneider, E. E. and England, T. S. *Physica* **17**(3-4), 221–233 (1951).
- [100] Chikoidze, E., Dumont, Y., Von Bardeleben, H. J., Gleize, J., Jomard, F., Rzepka, E., Berrerar, G., Ferrand, D., and Gorochoy, O. *Applied Physics a-Materials Science & Processing* **88**(1), 167–171 (2007).
- [101] Ghose, S. *Acta Crystallographica* **17**(8), 1051–1057 (1964).
- [102] Zhou, H., Hofstaetter, A., Hofmann, D. M., and Meyer, B. K. *Microelectronic Engineering* **66**(1-4), 59–64 (2003).
- [103] Blasco, J. and Garcia, J. *Journal of Solid State Chemistry* **179**(7), 2199–2205 (2006).
- [104] Hayashi, K., Ando, A., Hamaji, Y., and Sakabe, Y. *Japanese Journal of Applied Physics Part 1-Regular Papers Short Notes & Review Papers* **37**(9B), 5237–5240 (1998).
- [105] Mydosh, J. A. *Spin Glasses: an experimental introduction*. Taylor and Francis, (1993).
- [106] Kolesnik, S., Dabrowski, B., and Mais, J. *Journal of Superconductivity* **15**(4), 251–255 (2002).
- [107] Zhou, S. Q., Potzger, K., von Borany, J., Grotzschel, R., Skorupa, W., Helm, M., and Fassbender, J. *Physical Review B* **77**(3) (2008).
- [108] Shinde, S. R., Ogale, S. B., Higgins, J. S., Zheng, H., Millis, A. J., Kulkarni, V. N., Ramesh, R., Greene, R. L., and Venkatesan, T. *Physical Review Letters* **92**(16), 166601 (2004).
- [109] Bates, C. H., White, W. B., and Roy, R. *Journal of Inorganic & Nuclear Chemistry* **28**(2), 397–405 (1966).

- [110] Han, S. J., Jang, T. H., Kim, Y. B., Park, B. G., Park, J. H., and Jeong, Y. H. *Applied Physics Letters* **83**(5), 920–922 (2003).
- [111] Peiteado, M., Makovec, D., Villegas, M., and Caballero, A. C. *Journal of Solid State Chemistry* **181**(9), 2456–2461 (2008).
- [112] Saraf, L., Nachimuthu, P., Engelhard, M. H., and Baer, D. R. *J Sol-Gel Sci Technol* **53**, 141–147 (2010).
- [113] Sagredo, V., Goya, G. F., Silva, P., and de Chalbaud, L. M. *Journal of Magnetism and Magnetic Materials* **226**, 1323–1325 (2001).
- [114] Wilson, A. H. *Proceedings of the Royal Society of London Series a-Containing Papers of a Mathematical and Physical Character* **134**(823), 277–287 (1931).
- [115] Mollwo, E. *Z. Angew. Phys.* **6**, 257 (1954).
- [116] Seeger, K. *Semiconductor Physics*. Springer, (1982).
- [117] Schmid, H. K. and Mader, W. *Micron* **37**(5), 426–432 (2006).
- [118] Fultz, B. and Howe, J. M. *TEM and diffractometry of materials*. Springer-Verlag Berlin Heidelberg, (2001,2003,2008).
- [119] Rubi, D., Fontcuberta, J., Calleja, A., Aragonés, L., Capdevila, X. G., and Segarra, M. *Physical Review B* **75**(15), 155322 (2007).
- [120] Kittilstved, K. R., Schwartz, D. A., Tuan, A. C., Heald, S. M., Chambers, S. A., and Gamelin, D. R. *Physical Review Letters* **97**(3), 037203 (2006).
- [121] Mizokawa, T., Nambu, T., Fujimori, A., Fukumura, T., and Kawasaki, M. *Physical Review B* **65**(8), 085209 (2002).
- [122] Samarth, N. and Furdyna, J. K. *Solid State Communications* **65**(8), 801–804 (1988).
- [123] Blundell, S. *Magnetism in condensed matter*. Oxford master series in condensed matter physics. Oxford University Press, Oxford, (2001).

- [124] Pearton, S. J., Norton, D. P., Ip, K., Heo, Y. W., and Steiner, T. *Journal of Vacuum Science & Technology B* **22**, 932–948 (2004).
- [125] Zou, C. W., Wang, H. J., Yi, M. L., Li, M., Liu, C. S., Guo, L. P., Fu, D. J., and Kang, T. W. *Applied Surface Science* **256**(8), 2453–2457 (2010).
- [126] Heald, S. M., Kaspar, T., Droubay, T., Shutthanandan, V., Chambers, S., Mokhtari, A., Behan, A. J., Blythe, H. J., Neal, J. R., Fox, A. M., and Gehring, G. A. *Physical Review B* **79**(7), 075202 (2009).
- [127] Ney, A., Opel, M., Kaspar, T. C., Ney, V., Ye, S., Ollefs, K., Kammermeier, T., Bauer, S., Nielsen, K. W., Goennenwein, S. T. B., Engelhard, M. H., Zhou, S., Potzger, K., Simon, J., Mader, W., Heald, S. M., Cezar, J. C., Wilhelm, F., Rogalev, A., Gross, R., and Chambers, S. A. *New Journal of Physics* **12**, 013020 (2010).
- [128] Kim, H. J., Song, I. C., Sim, J. H., Kim, H., Kim, D., Ihm, Y. E., and Choo, W. K. *Solid State Communications* **129**(10), 627–630 (2004).
- [129] Makhlouf, S. A., Parker, F. T., Spada, F. E., and Berkowitz, A. E. *Journal of Applied Physics* **81**(8), 5561–5563 (1997).

CURRICULUM VITAE

Zlatko Micković

Date of birth: 20th April, 1981

Place of birth: Slavonski Brod, Croatia

Nationality: Croatian

Ecole Polytechnique Fédérale de Lausanne

zlatko.mickovic@gmail.com

Lausanne, Vaud, Switzerland

<http://lnnme.epfl.ch/>

Education

- Ecole Polytechnique Fédérale de Lausanne, Switzerland, Ph.D. Physics, 2006 - 2010
Ph.D. Thesis: The synthesis, structural, electronic and magnetic properties of $Zn_{1-x}Mn_xO$
Thesis advisor: Laszlo Forró, Thesis co-advisor: Arnaud Magrez
Thesis committee: Ø. Fischer, H. M. Rønnow, J. W. Seo, G. Meylan, A. Magrez and L. Forró
- University of Zagreb, Croatia, Diploma Engineer, Physics, 1999 - 2005
Diploma Thesis: Synthesis and electrical conductivity of the polyaniline in dissolved form, in Croatian.
Thesis advisor: Dinko Babić
Thesis committee: I. Batistić, A. Tonejc, and D. Babić
Graduated with the grade average of 4.57 (2.00(pass)-5.00(highest))

Teaching

- *Metrologie for 1st year Physics Students*, R. Schaller and G. Gremaud, assistant
- *Physics for 1st year Life Science Students*, R. Schaller and G. Gremaud, assistant

Publications

- **2010:** Z. Micković, D.T.L. Alexander, A. Sienkiewicz, M. Mionić, L. Forró and A. Magrez, *Synthesis of Nanosized Mn-doped ZnO by Low Temperature Decomposition of Hydrozincite Precursors*, submitted to Crystal Growth and Design
- **2010:** J. Jaćimović, Z. Micković, R. Gaal, C. Vaju, R. Smajda, A. Magrez and L. Forró, *The conductivity and thermoelectric power of ZnMnO₃*, in preparation, to be submitted to Solid State Communications
- **2010:** Z. Micković, A. Sienkiewicz, D.T.L. Alexander, L. Forró, A. Magrez, D. Quintavalle, T. Feher, Z. Szatmari and A. Jánossy, *Short-range magnetic order in the diluted magnetic semiconductor Zn_{1-x}Mn_xO obtained by thermal decomposition of inorganic precursors*, in preparation

Conference talks

- **2009:** Z. Micković, *Synthesis, magnetic and electronic properties of diluted magnetic semiconductor Zn_{1-x}Mn_xO*, a 15 minute oral presentation at 2009 Swiss Workshop on Materials with Novel Electronic Properties (MANEP), Les Diablerets, Switzerland, August 26-27-28, 2009.

Posters

- **2010:** Z. Micković, D. T. L. Alexander, A. Sienkiewicz, L. Forró and A. Magrez, *Magnetism of Ni and Co-doped ZnO Produced by Low Temperature Synthesis Process*, Annual Meeting of the Swiss Physical Society, Basel, Switzerland, June 21st-22nd, 2010.
- **2010:** G. J. Nilsen, J. O. Piatek, D. Kasinathan, A. Raja, Z. Micković, H. Mutka, A. Harrison and H. M. Rønnow, *Frustrated Magnetism in the Titanium Alum Family: KTi(SO₄)₂ and KTi(SO₄)₂·H₂O*, Perspectives in Highly Frustrated Magnetism, International Workshop, Dresden, Germany, April 19th-23rd, 2010.
- **2009:** Z. Micković, A. Magrez, A. Sienkiewicz, D. T. L. Alexander, D. Quintavalle, A. Janossy and L. Forro, *Structural, Magnetic and Electronic Properties of Dilute*

Magnetic Semiconductor $Zn_{1-x}Mn_xO$, 5th International School and Conference on Spintronics and Quantum Information Technology, Krakow, Poland, July 7th-11th, 2009.

- **2008:** D. T. L. Alexander, Z. Micković, A. Magrez and L. Forro, *In-situ vs. Ex-situ nanocrystallization of Mn doped ZnO* , Microscopy & Microanalysis 2008 Meeting, Albuquerque, New Mexico, United States, August 3rd-7h, 2008.

Languages

- **Fluent:** English, French, German, Croatian(Mother Tongue)
- **Basic:** Italian